UNIVERSITÉ DE GENÈVE

Groupe de Physique Appliquée - Optique

FACULTÉ DES SCIENCES

Professeur Nicolas GISIN

Exploring storage capability of a solid-state quantum memory for light

THÈSE

présentée à la Faculté des Sciences de l'Université de Genève
pour obtenir le grade de Docteur ès Sciences, mention Physique

par

Alexey TIRANOV

de Kazan (Russie)

Thèse N° 4993

GENÈVE

2016

UNIVERSITÉ DE GENÈVE

FACULTÉ DES SCIENCES

Doctorat ès sciences
Mention physique

Thèse de *Monsieur Alexey TIRANOV*

intitulée :

"Exploring Storage Capability of a Solid-state Quantum Memory for Light"

La Faculté des sciences, sur le préavis de Monsieur N. GISIN, professeur ordinaire et directeur de thèse (Groupe de Physique Appliquée - Optique), Monsieur M. AFZELIUS, docteur (Groupe de Physique Appliquée - Optique), Monsieur F. BUSSIERES, docteur (Groupe de physique appliquée et ID Quantique S.A. Genève), Monsieur K. ENSSLIN, professeur (Solid State Physics Laboratory, Swiss Federal Institute of Technology Zurich, Switzerland) et Monsieur A. LVOVSKY, professeur (Department of Physics and Astronomy, University of Calgary, Canada), autorise l'impression de la présente thèse, sans exprimer d'opinion sur les propositions qui y sont énoncées.

Genève, le 6 octobre 2016

Thèse - 4993 -

Le Doyen

Abstract

Quantum physical phenomena are important not only from a fundamental point of view allowing to probe the limits of our understanding. Their application in modern technologies provides us with uniquely precise tools and has great potential for quantum information science. In this context, quantum key distribution, which allows one to exchange cryptographic keys in a fundamentally secure way, is just one of the examples how quantum phenomena could change our everyday life. The future impetuous breakthrough in this direction is attributed to the scalable quantum technologies which will allow one to build quantum information network and to realize quantum computing over long (potentially intercontinental) distances.

The scalability condition can be efficiently achieved using light as the carrier to distribute quantum information between two distant points. However, finite transmission of modern communication channels (optical fibers) makes the probability of a single photon to reach the end of the fiber exponentially low. This fact imposes strong restrictions on the possible distances (few hundreds kilometres) and enforces to develop novel techniques to overcome this limitation. One solution is to realize a quantum repeater, in analogy to the classical one, which is based on quantum teleportation phenomena and entanglement swapping techniques.

In this context, optical quantum memories became one of the essential building blocks necessary for future practical implementation of quantum repeaters. Such a quantum memory allows coupling between flying qubits (carried by photons) and stationary qubits which can store, process and release quantum information. One of the best candidates for this purpose is a light-matter interface consisting of large atomic ensembles which can be optically manipulated and can preserve quantum information. Rare-earth ion-doped crystals are one of the examples of such an interface. Particularly, these materials proved to be a great tool to transfer quantum information from single-photon carrier to the atomic excitation and back without loss of coherence. Mapping photons to the atomic frequency combs prepared in these materials is also compatible with multiplexing techniques greatly enhancing the overall efficiency of a quantum repeater.

The present thesis includes a series of experiments exploring the potential of using rare-earth ion-doped crystals as a light-matter quantum interface using different quantum states of light as a probe resource. We start with the realization of an elementary quantum repeater block, implementing quantum teleportation of a polarization qubit into a solid-state quantum memory based on a yttrium-orthosilicate crystal doped with neodymium

ions. The storage of an hyperentangled (entangled in more than one degree of freedom) state of light compatible with long-distance quantum communication was demonstrated to show the potential of using this quantum memory for quantum purification techniques. To explore the temporal multiplexing capability of atomic frequency combs in atomic ensembles we performed temporal multimode storage of multi-photon entangled state of light. Such a temporal multimode capacity together with the developed novel theoretical techniques allowed us to show the storage of more than one bit of entanglement (*e*bit) using multi-photon and multi-dimensional entangled photon states.

In addition, we demonstrate the potential of our quantum memory to test the validity of quantum theory at macroscopic scales. For this purpose, we generated a quantum state that involves the superposition of two macroscopically distinguishable components entangled with a single photon. The observed quantum correlations stemmed from a light-matter micro-macro entangled state where the micro part included a single photon, while the macro part was composed of several tens of atomic excitations. This approach based on quantum memory techniques can be used in other systems to expand the size of quantum superpositions in matter.

Together, all these experiments demonstrate the universality of solid-state light-matter quantum interfaces based on rare-earth ion-doped crystal and atomic frequency combs not only for quantum communication applications but also their strong potential for exploring fundamental questions of modern quantum physics.

Résumé

Les phénomènes physiques quantiques sont importants d'un point de vue fondamental car ils nous permettant de sonder les limites de notre compréhension. Leur application dans les technologies modernes nous fournit des outils précis et uniques avec un grand potentiel pour l'information quantique. Dans ce contexte, la distribution quantique de clés, permettant d'échanger de clés cryptographiques de manière fondamentalement sécurisée, est juste un des exemples de comment les phénomènes quantiques pourraient changer notre vie de tous les jours. Les progrès dans cette direction sont attribués aux technologies quantiques extensibles qui permettront de construire des réseaux d'information quantique et de réaliser le calcul quantique sur de longues distances (potentiellement intercontinentales).

La condition d'échelle variable peut être efficacement réalisé en utilisant la lumière comme support pour distribuer l'information quantique entre deux points éloignés. Cependant, la transmission finie des canaux de communication modernes (fibres optiques) implique que la probabilité qu'un photon unique atteigne l'extrémité de la fibre devient exponentiellement faible. Ce fait impose de fortes restrictions sur les distances possibles (quelques centaines de kilométres) et implique la nécessité de développer de nouvelles techniques pour surmonter cette limitation. Une solution consiste à réaliser un répéteur quantique, de manière analogue à la communication classique, qui est basé sur des phénomènes de téléportation quantique et des techniques de permutation d'intrication.

Dans ce contexte, les mémoires quantiques optiques sont devenus l'un des éléments essentiels nécessaires à la mise en œuvre pratique des répéteurs quantiques. Une telle mémoire quantique permet le couplage entre les qubits volants (portés par les photons) et qubits stationnaires qui peuvent stocker, traiter et libérer l'information quantique. L'un des meilleurs candidats dans ce but sont les interfaces lumière-matière constitués de grands ensembles atomiques qui peuvent être optiquement manipulés et peuvent préserver l'information quantique. Les cristaux dopés aux ions terre rare sont un exemple possible d'une telle interface. En particulier, ces matériaux se sont avérés un excellent outil pour transférer l'information quantique d'un photon unique à une excitation atomique et vice-versa sans perte de cohérence. Le couplage des photons aux peignes de fréquence atomique préparés dans ces matériaux est également compatible avec des techniques de multiplexage qui améliore grandement l'efficacité globale d'un répéteur quantique.

La présente thèse comprend une série d'expériences qui explorent la possibilité d'utiliser des cristaux dopés aux ions terre rare comme une interface quantique lumière-matière en utilisant différents états quantiques de la lumière comme une sonde. Nous commençons avec la réalisation d'un bloc élémentaire de répéteur quantique, la mise en œuvre de la téléportation quantique d'un qubit de polarisation dans une mémoire quantique dans l'état solide basée sur un cristal d'yttrium-orthosilicate dopé avec des ions néodyme. Le stockage d'un état hyper-intriqué (intriqué dans plus d'un degré de liberté) de la lumière compatible avec communication quantique de longue distance a été démontrée pour montrer la possibilité d'utiliser cette mémoire quantique pour les techniques de purification quantique. Pour explorer la capacité de multiplexage temporel des peignes en fréquence dans des ensembles atomiques nous avons effectués le stockage temporellement multimode d'états intriqués avec plusieurs photons. Une telle capacité multimode temporelle ainsi que des nouvelles techniques théoriques développées nous ont permis de montrer le stockage de plus d'un bit d'intrication (*e*bit) en utilisant plusieurs photons et états de photons multidimensionnellement intriqués.

En outre, nous démontrons le potentiel de notre mémoire quantique à tester la validité de la théorie quantique à l'échelle macroscopique. Dans ce but, nous avons généré un état quantique qui implique la superposition de deux composantes macroscopiques distinguables intriquées avec un seul photon. Les corrélations quantiques observées provenaient d'un état micro-macro, lumière-matière, intriqué où la partie micro désigne le photon unique, tandis que la partie d'était macro composée de plusieurs dizaines d'excitations atomiques. Cette approche basée sur les techniques de mémoire quantique peut être utilisée dans d'autres systémes pour augmenter la taille des superpositions quantiques dans la matière.

Dans l'ensemble, toutes ces expériences démontrent l'universalité des interfaces quantiques lumière-matière dans l'état solide à base des cristaux dopés aux ions terre rare et des peignes atomique en fréquence non seulement pour des applications de communication quantique, mais aussi pour explorer les questions fondamentales de la physique quantique moderne.

Introduction

Quantum information is one of the most intriguing modern fields of research which gave rise to many new and attractive experimental and theoretical concepts. In the last decades it has become the source of revolutionizing technologies and their great potential for applications in our everyday life. The idea of using quantum mechanical concepts like entanglement and superposition as resources to build a machine which could directly simulate Nature became the foundation of modern technological innovations which go far beyond this elegant idea. Nowadays, they are widely used as a resource to improve the existing information processing protocols.

The start-point is 1935, when Einstein, Podolsky and Rosen (EPR) argued that quantum mechanics was an incomplete theory (Einstein et al. 1935). Their so-called EPR-paradox was based on the basic assumption that two systems cannot influence each other when they are not interacting (locality) which means that quantum mechanics is incomplete and that more universal theory (with hidden variables) has to be formulated.

This paradox remained until John Bell in 1964 derived correlation inequalities (Bell 1964) that must be satisfied within all hidden variable theories but can be violated in quantum mechanics. After, Clauser, Horne, Shimony and Holt proposed an experimental test of local hidden variable models based on Bell's inequality, through the violation of a CHSH inequality (Clauser et al. 1969). The experiments in the 70'ies and the 80'ies such as e.g. (Freedman et al. 1972; Lamehi-Rachti et al. 1976; Aspect et al. 1982; Ou et al. 1988) finally verified the foundations of quantum mechanics. Modern experiments were able to repeat this without loopholes allowing for a local-realistic explanation, such as low detection efficiency or time-space separation between the detection events (Hensen et al. 2015; Shalm et al. 2015; Giustina et al. 2015).

Most of these experiments were performed using optical quantum systems. The concept of a photon as a light quanta and the possibility to use it as a carrier to transfer quantum information now became a basic tool for modern quantum information studies. One of the examples is quantum cryptography which is based on the impossibility to clone unknown quantum states (Wootters et al. 1982; Dieks 1982) and guaranties the secure transmission of the encrypted messages (Bennett et al. 1984). A protocol based directly on the entanglement distribution was proposed by Ekert 1991.

Quantum mechanical concepts offer not only absolute security in contrast with classical encryption but also can give an enormous computational power to make classical encryption schemes such as e.g. RSA (Rivest et al.

1978) insecure (Deutsch 1985; Shor 1994). This can be done by taking advantage of the quantum parallelism arising when several particles existing in superpositions are entangled.

Quantum communications over long distances face serious technological limitations due to the finite transmission (up to 0.16 dB/km for telecommunication wavelengths) of commercial optical fiber, which is the best way to transfer information today. This makes the direct transmission of entangled carriers over distances more than few hundred kilometres inefficient and impractical.

One solution is the quantum state transfer from one location to another, without physical transfer of a carrier, proposed by Bennett et al. 1993. This process is known as quantum teleportation and based on entanglement distribution followed by joint quantum measurement was experimentally demonstrated using postselection (Bouwmeester et al. 1997) and unconditionally (Furusawa et al. 1998). This scheme became a basis for the concept of a quantum repeater (Briegel et al. 1998) which should enable to overcome the problem of entanglement distribution over continental and intercontinental distances.

The basic idea relies on entanglement swapping technique which use EPR pairs to distribute entanglement between distant nodes. For this, the whole distance is divided into several elementary links where each one is connected by a direct transmission link with the sources of EPR pairs. By performing a sequential joint measurement with each EPR pair an entanglement swapping operation can be realized distributing entanglement link by link over a larger and larger distances.

To make this process more efficient the storage of entangled state has to be realized to synchronize different links using quantum memories. Doing this one can change the scaling of the rate as a function of distance. But there is still a power law dependence on the efficiency of the memory to the power of how many memories are used. This explains why one needs very efficient memories in order to build efficient quantum communication link.

Further processing including entanglement distillation and purification techniques, allows one to restore the fidelity of a quantum state. This drastically reduces the transfer time for long-range transmission and allows one to use repeat-until-success strategies to transfer the entanglement over the whole chain of links.

The implementation of quantum memories is mostly based on the coherent interaction between light and matter. Promising physical systems include single atoms and ions, hot and ultracold atomic ensembles, solid-state systems like quantum dots, defects in diamonds and impurities in the crystalline media (Lvovsky et al. 2009; Hammerer et al. 2010; Simon et al. 2010; Bussières et al. 2013). For this, various quantum memory protocols were developed and successively implemented showing their great potential.

One of the main problems of the quantum memory based on single atoms/ions or atomic ensembles is its capability to store many different modes using various photonic degrees of freedom. Temporal or frequency

multiplexing in these systems is hardly achievable, while these techniques form a basic tool for efficient classical communication. To overcome this problem one usually uses polarization or spatial (orbital angular momentum) degrees of freedom.

In this context, rare-earth ion-doped crystals showed their great potential due to notable optical and nuclear coherent properties, long storage times and capability to perform efficient multiplexing both in time and frequency space. Based on the special features of this system (like large inhomogeneous broadening) a new quantum memory protocol based on atomic frequency combs was developed (Afzelius et al. 2009) and efficiently implemented for entanglement storage shared by single photons (Clausen et al. 2010). The capability of efficient temporal multiplexing makes this solid-state light-matter interface one of the most promising to realize an efficient full quantum repeater scheme (Sangouard et al. 2011).

A goal of this thesis is to explore and demonstrate that rare-earth materials have a particular high potential of "universal" quantum storage involving many different degrees of freedom (polarization, time, photon number space). Here we describe a series of experiments which were performed to demonstrate the potential of solid-state light-matter interfaces for efficient long-distance quantum communication and its suitability to perform multiplexing using quantum states of light. It covers the steps from material spectroscopy to proof-of-principle demonstrations of key features of a multimode quantum memory.

In particular, an elementary link of a quantum repeater was implemented by performing quantum teleportation of a polarization qubit into the solid-state quantum memory. The compatibility of our quantum memory with quantum purification schemes for long-distance communication was demonstrated by performing quantum storage of the hyperentanglement (simultaneous entanglement in more than one degrees of freedom).

To show the temporal multiplexing capability of the atomic frequency combs we implemented temporal multimode storage of entangled photon pairs. A novel theoretical method allowed us to verify the storage of two entangled photons. The temporal multimode capacity gives the possibility to increase the amount of entanglement (number of entanglement bits or $e$bits) which can be stored in the quantum memory. To demonstrate this we generated a multi-dimensional energy-time entangled state and certified more than one $e$bit of information shared by two photons after storing one of them in the crystal.

At the end, we showed the capability of our solid-state interface to be used for fundamental tests of quantum theory at the macroscopic scale. For this we analysed entangled state involving micro-macro quantum state shared between light and a solid-state atomic ensemble. The micro part consisted of a single photon which was entangled with the macro part composed of several tens of atomic excitations. Detected quantum correlations proved to stem from the generated quantum state. Such a state potentially can be detected using classical detectors based on coarse-grained measurement revealing quantum properties, such as quantum superpositions, at the

macroscopic scale.

The thesis is organized as follows:

- Chapter 1 reviews the original idea of the quantum repeater, based on the use of atomic ensembles;

- Chapter 2 covers quantum memory protocols based on atomic ensembles and particularly the atomic frequency comb protocol, used in this thesis;

- Chapter 3 describes the source of entangled photons that has been characterized and used during this thesis;

- Chapter 4 describes the physical system in which quantum memory was implemented, rare earth ion-doped crystal together with it's spectroscopic studies;

- Chapter 5 describes quantum storage of the single photon state together with the experiment involving quantum teleportation of a polarization qubit into the solid-state quantum memory;

- Chapter 6 describes the results of probing multimode capacity of the quantum memory using entangled excitations in multiphoton and hyperentangled quantum states. It also contains novel theoretical techniques which were used to analyse multiphoton entanglement;

- Chapter 7 presents the results of multi-dimensional entangled state storage. The novel theoretical method to quantify entanglement using incomplete data is described;

- Chapter 8 presents the demonstration of light-matter micro-macro quantum correlations;

- The conclusion and outlook are given in Chapter 9.

Contents

List of Figures

xviii

1 Long-distance Quantum Communication

1.1 Quantum information basics

Entanglement is a key resource in quantum information science. The motivation of the research in this thesis starts with the desire to create and distribute entanglement over large distances in order to extend the range of quantum networks (Kimble 2008). The concept of entanglement was at the heart of the famous EPR argument that quantum mechanics is incomplete (Einstein et al. 1935).

In this paper (Einstein et al. 1935), a source produces a pair of particles, A and B, in a quantum state, and then the particles move apart. Strong correlations exist between the position and momentum of the separated particles such that a measurement of the position of particle A allows the prediction of the position of particle B with certainty due to the correlation they share regardless of spatial separation. This is the key feature of entanglement motivating much research toward exploiting it as a resource for communication.

1.1.1 Qubits

In the simplest case, the smallest bit of quantum information, the qubit, can be described as a quantum superposition of 0s and 1s. The word qubit stands for «quantum-bit» and it was first introduced by Schumacher 1995. A qubit can be represented in Dirac notation (Dirac 1939) as,

$$|\psi\rangle = \alpha |0\rangle + \beta |1\rangle \tag{1.1}$$

where, α and β are the complex probability amplitudes normalized by $|\alpha|^2 + |\beta|^2 = 1$. One convenient way to visualize a qubit state is to use the Bloch sphere representation shown in Fig. 1.1. Any point on the Bloch sphere is defined by angles θ (polar) and ϕ (azimuthal) and corresponds to a pure quantum state. In this case, a qubit state can be expressed by probability amplitudes $\cos(\theta/2) \equiv \alpha$ and $e^{i\phi}\sin(\theta/2) \equiv \beta$. Using these parameters, a qubit state can be written in the following form:

$$|\psi\rangle = \cos(\theta/2) |0\rangle + e^{i\phi}\sin(\theta/2) |1\rangle \,, \tag{1.2}$$

represented by the vector touching the sphere with unity radius (Fig. 1.1). For example, the points on the poles of the Bloch sphere correspond to states
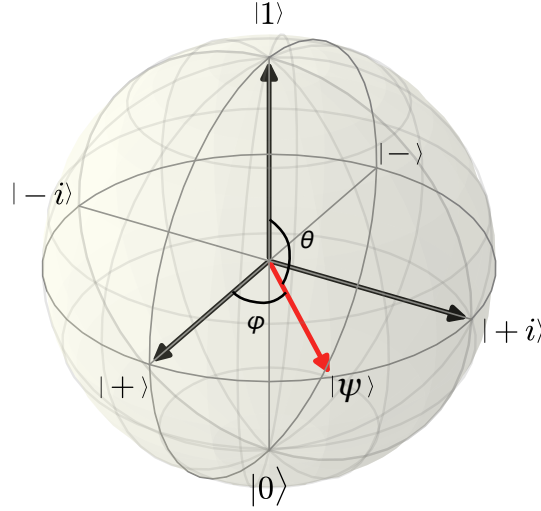
FIGURE 1.1: Bloch sphere. Any arbitrary pure state $|\psi\rangle$ is represented by a point, defined by angles θ and ϕ, on the Bloch sphere. Pure states represented by diametral (opposing) points on the Bloch sphere are orthogonal, e.g. $|0\rangle$ and $|1\rangle$, $|\pm\rangle = (|0\rangle \pm |1\rangle)/\sqrt{2}$ or $|\pm i\rangle = (|0\rangle \pm i\,|1\rangle)/\sqrt{2}$.

$|0\rangle$ and $|1\rangle$, while the equator points represent equal superpositions of these states. The pair of states that are represented on each side of any defined axis through the center of the Bloch sphere, for example $|0\rangle$ and $|1\rangle$, $|\pm\rangle = (|0\rangle \pm |1\rangle)/\sqrt{2}$ or $|\pm i\rangle = (|0\rangle \pm i\,|1\rangle)/\sqrt{2}$ are orthogonal states. A set of orthogonal states forms a basis for any qubit state, meaning that any qubit state can be written as their linear combination.

This representation is universal and can be applied to describe any two-level physical system. One of the classical examples is polarization state of the single photon, but it can be extended to other degrees of freedom: frequency, spatial and temporal modes or orbital angular momentum. Solid-state qubits can be implemented using electronic or nuclear energy levels of single atoms and ions, charge or flux qubits in superconducting circuits (Xiang et al. 2013).

The points inside the Bloch sphere correspond to mixed states which are described by the notion of the density matrix ρ. A quantum state in this case can be written as a linear combination in the orthogonal basis of the pure states $|\psi\rangle_i$

$$\rho = \sum_i p_i \, |\psi\rangle_{ii}\langle\psi| , \tag{1.3}$$

where p_i is the probability to find the system in the the state $|\psi\rangle_i$ expressed as a result of projective measurement $p_i = \text{Tr}(\rho A)$ where A is the projective operator $A = |\psi\rangle_{ii}\langle\psi|$. The normalization in this case is $\sum_i p_i = 1$. Using the notion of Pauli matrices

$$\mathbb{1} = \begin{pmatrix} 1 & 0 \\ 0 & 1 \end{pmatrix}, \quad \sigma_x = \begin{pmatrix} 0 & 1 \\ 1 & 0 \end{pmatrix}, \quad \sigma_y = \begin{pmatrix} 0 & -i \\ i & 0 \end{pmatrix}, \quad \sigma_z = \begin{pmatrix} 1 & 0 \\ 0 & -1 \end{pmatrix} \tag{1.4}$$

any density matrix can be written as

$$\rho = \frac{1}{2}(\mathbb{1} + \vec{\mathbf{r}}\vec{\sigma}), \qquad \vec{\mathbf{r}} = (r_x, r_y, r_z), \qquad \vec{\sigma} = (\sigma_x, \sigma_y, \sigma_z) \qquad (1.5)$$

To quantify the purity of the quantum state ρ the scalar value called purity P defined as $P = \mathrm{Tr}(\rho^2)$ is used. The purity is limited by $1/2 \leq P \leq 1$, where maximum corresponds to the pure states for which $\rho = \rho^2$. In general case, where dimension of ρ is bigger than 2 (which is true for qubits) and equal to d the range is modified accordingly $1/d \leq P \leq 1$.

The fidelity term is used for quantitative description on how two quantum states ρ_a and ρ_b are close to each other and is defined as $F = \left(\mathrm{Tr}\sqrt{\sqrt{\rho_a}\rho_b\sqrt{\rho_a}}\right)^2$ varying in the range $0 \leq F \leq 1$ for orthogonal and identical states, respectively. When one of the states is pure the fidelity is expressed by $F = \langle\psi|\rho|\psi\rangle$.

Similar to classical information which is usually divided in two different types of encoding known as digital and analog information processing, quantum information processing can be based on discrete (Nielsen et al. 2000) and continuous variables (Braunstein et al. 2005) depending on the eigenvalue spectrum of the observable. A qubit encoded using polarization of a single photon is the simplest example of discrete quantum information.

To characterize the preservation of the information in the quantum interface (for example quantum memory) the fidelity between the input and output states can be measured. In order to distinguish between classical and quantum regimes of the interface the boundary fidelities have to be defined. The maximum classical fidelity of $F = 2/3$ (Massar et al. 1995) is used in the case of discrete variable measurement, while for the continuous variables the critical fidelity is $F = 1/2$ (Hammerer et al. 2005).

1.1.2 Entanglement

The "spooky action at a distance" described by the EPR-paradox was later formulated in more mathematical form using the term *entanglement* by Schrödinger 1935. The entangled state there was defined as a state of the system which can not be factorized to the individual states of it's different parts. This property is usually called separability criteria and is expressed as

$$\rho_{ab} \neq \sum_i p_i \rho_a^i \otimes \rho_b^i \qquad (1.6)$$

Separable states are classically correlated. This means that for the production of a separable state only local operations and classical communication (LOCC) are necessary. Non separability condition (Eq. 1.6) can lead to the correlations between measurement outcomes which can not be explained using classical models. This fact was successfully used to formulate criteria to test nonlocal properties of quantum physics by Bell 1964 referred to as Bell-inequalities. For example, the following joint quantum states of two

spin 1/2 particles are examples of entangled states:

$$\left|\Psi_{ab}^{\pm}\right\rangle = (\left|\uparrow\right\rangle_a \left|\downarrow\right\rangle_b \pm \left|\downarrow\right\rangle_a \left|\uparrow\right\rangle_b)/\sqrt{2}, \quad \left|\Phi_{ab}^{\pm}\right\rangle = (\left|\uparrow\right\rangle_a \left|\uparrow\right\rangle_b \pm \left|\downarrow\right\rangle_a \left|\downarrow\right\rangle_b)/\sqrt{2} \quad (1.7)$$

These states form an orthogonal basis for two-qubit systems. Due to the perfect correlations (or anticorrelations) between individual spin a and spin b these states lead to the strongest violation of Bell inequalities and thereafter called Bell states. They are maximally entangled, in the sense that any other entangled state can be generated from each of them by local operations. The state $\left|\Psi_{ab}^{-}\right\rangle$ is known as the singlet state.

In addition to their importance in the foundations of quantum theory, two-qubit entangled systems are the main ingredients in quantum communication. The distribution of entanglement over long distances is one of the main goals in this area of research. For this, Bell states measurements, consisting of a projection onto the Bell states (Eqs. 1.7) are used to perform entanglement swapping. This technique can be used to extend entanglement over long distances and to realize quantum repeater.

1.1.3   Schmidt decomposition

Schmidt decomposition is very useful tool in the description of entanglement for bipartite systems. It allows one to decompose arbitrary bipartite state $|\psi\rangle = \sum_{i,j} c_{i,j} |a_i, b_j\rangle \in \mathcal{H}_A \otimes \mathcal{H}_B$ in the tensor product of two Hilbert spaces. Then there exist an orthonormal basis $|\alpha_i\rangle$ of $\mathcal{H}_A$ and an orthonormal basis $|\beta_i\rangle$ of $\mathcal{H}_B$ such that

$$|\psi\rangle = \sum_{k}^{R} \lambda_k |\alpha_k, \beta_k\rangle, \quad (1.8)$$

holds, with positive real coefficients λ_k. The λ_k are uniquely determined as the square roots of the eigenvalues of the matrix $CC^\dagger$, where $C = \{c_{ij}\}$. The number R is called the Schmidt rank of $|\psi\rangle$.

The mixed state have Schmidt number k if it can be written as a convex combination of pure states of Schmidt rank k or smaller (Terhal et al. 2000). Or, in other words, Schmidt number is the minimum Schmidt rank of the pure states needed to construct the mixed state.

1.2   Entanglement criteria

The problem of entanglement certification and quantification is of great importance for quantum information processing. This topic is actively studied since it can greatly enhance different applications where entanglement has to be efficiently detected and characterized. Depending on the type of quantum information processing based on discrete or continuous variables different criteria has to be applied. Further, we describe some approaches which are used for discrete variables, while continuous variable techniques are also actively utilized (Duan et al. 2000; Simon 2000).
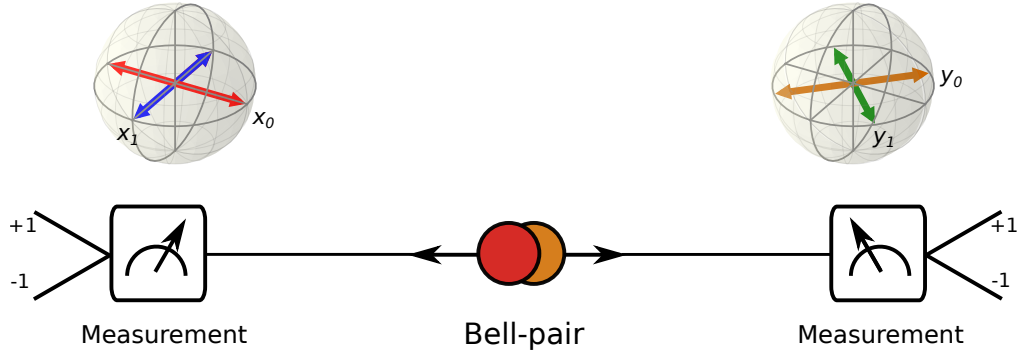
FIGURE 1.2: CHSH inequality violation. A measurement apparatus to find the correlations between entangled particles: The Bloch spheres on each particles side depict the projection settings required for a CHSH Bell-inequality test.

1.2.1 Bell's theorem. CHSH inequality

One of the standard tools to verify entanglement is a Bell inequality test, explored by Bell 1964. This test reveals the non-local nature of bipartite states and constitutes a cornerstone in the interpretation of quantum mechanics.

This criterion is stronger than the one of being entangled but due to it's convenience Bell inequality is broadly used for entanglement certification. The main procedure in a Bell test is to quantify the correlations between entangled particles for different projection measurement settings. The CHSH (Clauser-Horne-Shimony- Holt) inequality is one of the most well-known forms of the Bell inequalities (Clauser et al. 1969). It requires four different predefined sets of joint projective measurements $x, y = 0, 1$ with two outcomes $+1$ and -1 for each measurement (Fig. 1.2).

The CHSH parameter S can be defined as

$$S = \sum_{x,y=0,1} (-1)^{xy} E_{xy}, \qquad E_{xy} = \sum_{a,b=\pm 1} ab\, p(ab|xy). \qquad (1.9)$$

From each measurement result a correlation coefficient E_{xy} is determined, where $p(ab|xy)$ are the probabilities of the correlated outcomes which Alice and Bob measure simultaneously. An example of a projective measurement is the following: using Bloch vector notation, Alice's measurements are given by observables $\hat{\sigma}_x$ (for $x = 0$) and $\hat{\sigma}_y$ (for $x = 1$), while Bob's measurements are $(\hat{\sigma}_x + \hat{\sigma}_y)/\sqrt{2}$ (for $y = 0$) and $(\hat{\sigma}_x - \hat{\sigma}_y)/\sqrt{2}$ (for $y = 1$).

Classical (local) models based on the assumption of locality (generally referred to as local hidden-variable theories) predict that the S-parameter has a maximum value of 2. While for quantum mechanics the maximum predicted value is $2\sqrt{2}$ which can be obtained using Bell states. Thus measuring S-parameter in the range $2 < S \leq 2\sqrt{2}$ one can prove the non-local character of the observed correlations which can not be explained by any classical models. At the same time, thus, a violation of a Bell inequality implies that the state is entangled.

However, violation of a Bell inequality and entanglement are not the equivalent. Assuming two-qubit state one can reduce the lower limit of the S-parameter to certify entanglement from 2 to $\sqrt{2}$. Thus the value measured between $\sqrt{2} < S \le 2\sqrt{2}$ (Roy 2005) will prove the presence of entanglement. Both tests were used many times in this thesis to certify the storage of photonic entanglement and demonstrate micro-macro quantum correlations.

1.2.2   Entanglement witness

Entanglement witnesses (Gühne et al. 2009) provide a simple and useful entanglement criterion. Since any mixtures of separable states will remain separable, the set of all separable states is called convex. However, the set of entangled states is not convex. Due to this property there exists (Horodecki et al. 1996) a hermitian operator $\mathcal{W}$, called the entanglement witness or witness operator, such that if the state ρ is entangled, then

$$\begin{cases} \operatorname{Tr}(\mathcal{W}\rho) \ge 0 \text{ for all separable } \rho \\ \operatorname{Tr}(\mathcal{W}\rho) < 0 \text{ for at least one entangled } \rho \end{cases}$$

holds. Thus, if we measure $\operatorname{Tr}(\mathcal{W}\rho) < 0$ we know for sure that the state ρ is entangled. For each entangled state ρ there exist an entanglement witness $\mathcal{W}$ detecting it.

Entanglement witnesses provide us with an entanglement criterion, which is directly related to expectation values of observables. However there are many experimental situations when the observables can not be constructed due to technical limitations and limited number of outcomes. In Chapter 6 we introduced a novel indirect entanglement witness technique which helps to overcome this problem and construct entanglement witness in these cases. This technique was applied to show storage of two entangled photon pairs inside our quantum memory.

In analogy with entanglement witness the Schmidt number witness can be defined (Sanpera et al. 2001). It is possible because Schmidt number is an entanglement monotone and can thus be used to quantify the degree of entanglement (Terhal et al. 2000).

1.2.3   Quantum state tomography

Another method to detect entanglement is to perform quantum state tomography. This method is straightforward and requires the detection all the outcomes from the measured quantum state. This technique is well established and widely applied for states in low dimensional Hilbert space. This technique becomes less efficient when the dimension of the Hilbert space d grows. It happens due to the fast increase of the required number of measurement outcomes, d^4, in order to collect a complete set of measurements without strong assumptions on the quantum state.

During this thesis, quantum state tomography using maximum likelihood estimation (James et al. 2001) was performed to analyse photonic entanglement stored in the crystal and reveal quantum micro-macro correlations between light and matter. The results are discussed in Chapter 8.

1.3   Quantum repeater

The problem of transferring quantum information between two distant nodes is strongly connected to the technical limitations of the existing communication channels. Inevitably present photon loss inside modern optical fibers strictly limits the possible distances to implement quantum communication.

In general, this is not an issue for classical optical communication because optical signals can be amplified at intermediate stages of a communication channel so that loss can be compensated. However, this solution cannot be applied directly for quantum communication due to the no-cloning theorem (Wootters et al. 1982) prohibiting to perfectly copy quantum information without destroying quantum state. One solution to this problem is to use quantum relay stations to transmit the quantum information over long distances (Aspelmeyer et al. 2003). Another solution is to implement quantum repeaters proposed by Briegel et al. 1998. The second approach will be further discussed in details.

1.3.1   Entanglement swapping

The idea of quantum repeater is based on quantum teleportation phenomena (Bennett et al. 1993) and entanglement swapping (Żukowski et al. 1993) and was proposed to overcome decoherence during the transmission of quantum states. However, the same technique can be used directly to overcome the problem of losses and extend quantum communication over longer distances.

Entanglement swapping requires few entangled photon pairs and the possibility to perform a full joint Bell-state measurement on one of the qubits from each entangled pair. Suppose we start from two initially fully independent entangled pairs $|\Phi^+\rangle_{12}$ and $|\Phi^+\rangle_{34}$:

$$\left|\Phi^+\right\rangle_{12} = (|\uparrow\rangle_1 |\uparrow\rangle_2 + |\downarrow\rangle_1 |\downarrow\rangle_2)/\sqrt{2}, \quad \left|\Phi^+\right\rangle_{34} = (|\uparrow\rangle_3 |\uparrow\rangle_4 + |\downarrow\rangle_3 |\downarrow\rangle_4)/\sqrt{2}.$$
(1.10)

The Bell states form a complete orthogonal basis for the Hilbert-subspace of those 2 qubits. In this case the insertion of the Bell states of qubits 2 and 3 leads formally to the following result

$$|\Phi\rangle = |\Phi^+\rangle_{12} \otimes |\Phi^+\rangle_{34} =$$
$$= (|\Phi^+\rangle_{23} |\Phi^+\rangle_{14} + |\Psi^+\rangle_{23} |\Psi^+\rangle_{14} + |\Psi^-\rangle_{23} |\Psi^-\rangle_{14} + |\Phi^-\rangle_{23} |\Phi^-\rangle_{14})/2.$$
(1.11)

This purely mathematical trick clearly shows that by projecting on one of the Bell states involving qubits 2 and 3 one can switch (i.e. swap) entanglement
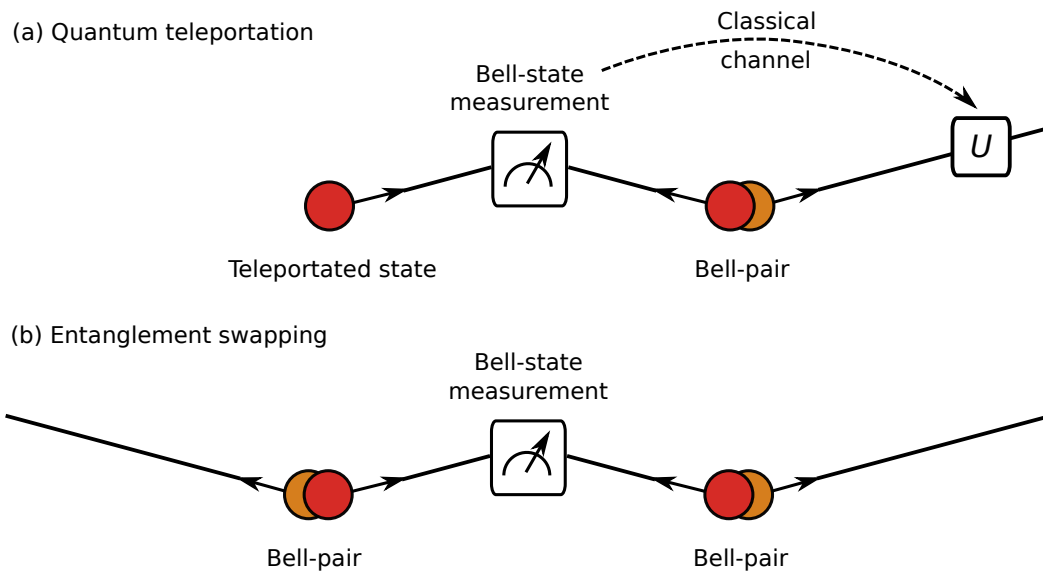
FIGURE 1.3: Entanglement swapping. (a) Quantum teleportation. The Bell state measurement (BSM) between the teleported state and one of the particles from the Bell-pair, which is entangled with another particle, leads to the transformation of the state of the particle. The unitary transformation U based on the results of the BSM has to be applied to finish quantum teleportation. (b) Two pairs of entangled Bell-pairs are involved in the process. One member of each entangled pair participate in the projection to one of the Bell-states (BSM). After applying unitary transformations U the initial entangled state of each photon pair can be established.

to qubits 1 and 4 without their direct interaction.

Quantum teleportation is based on the same approach (Bennett et al. 1993). By replacing one entangled pair by the arbitrary qubit state $\alpha \left|\uparrow\right\rangle_1 + \beta \left|\downarrow\right\rangle_1$ one can use the same trick and write the state as

$$
\begin{aligned}
\left|\Phi\right\rangle &= (\left|\phi\right\rangle_1) \otimes \left|\Phi^+\right\rangle_{23} = (\alpha \left|\uparrow\right\rangle_1 + \beta \left|\downarrow\right\rangle_1) \otimes \left|\Phi^+\right\rangle_{23} = \\
&= (\left|\Phi^+\right\rangle_{12}(\alpha \left|\uparrow\right\rangle_3 + \beta \left|\downarrow\right\rangle_3) + \left|\Psi^+\right\rangle_{12}(\alpha \left|\downarrow\right\rangle_3 + \beta \left|\uparrow\right\rangle_3) + \\
&+ \left|\Phi^-\right\rangle_{12}(\alpha \left|\uparrow\right\rangle_3 - \beta \left|\downarrow\right\rangle_3) + \left|\Phi^+\right\rangle_{12}(\alpha \left|\downarrow\right\rangle_3 - \beta \left|\uparrow\right\rangle_3))/2. = \\
&= (\left|\Phi^+\right\rangle_{12} U_{\Phi^+} \left|\phi\right\rangle_3 + \left|\Psi^+\right\rangle_{12} U_{\Psi^+} \left|\phi\right\rangle_3 + \\
&+ \left|\Phi^-\right\rangle_{12} U_{\Phi^-} \left|\phi\right\rangle_3 + \left|\Phi^+\right\rangle_{12} U_{\Psi^-} \left|\phi\right\rangle_3)/2.
\end{aligned}
\tag{1.12}
$$

where U_Ψ refers to single qubit rotations on qubit 3, conditional on the joint Bell-state measurement between qubits 1 and 2. In this form, the teleportation is obvious: depending on the Bell-state measurement outcome, a particular single-qubit operation needs to be applied to the third qubit, after which the third qubit becomes a perfect copy of the first one, without ever being measured. As two bits of classical information needs to be transferred from the location of qubits 1,2 to qubit 3 (Fig. 1.3), no superluminal communication is possible, and therefore no violation of special relativity occurs.

1.3.2 Entanglement purification

In reality there are no perfectly pure states that can be prepared. The imperfections due to the decoherence and/or statistical mixtures lead to errors and reduced fidelities during the communication. Let's assume that the decoherence can be modelled by white noise such that a 2-qubit state can be written as a Werner state (Werner 1989) $\rho = V \left|\Psi\right\rangle \left\langle\Psi\right| + (1 - V)\mathbb{1}/4$ where V is the visibility. Then violation of the CHSH inequality (Clauser et al. 1969) in this case requires $V > 1/\sqrt{2}$ or fidelity $F > 0.85$ (Cirel'son 1980).

Fortunately, entangled states (except some special cases (Vedral 1999)) can be used in a protocol known as entanglement purification: an initial set of partially entangled states can, under certain conditions, be transformed to a new reduced set with improved entanglement properties. (Bennett et al. 1996b; Bennett et al. 1996a). As all quantum operations are imperfect, none of the pre-established entangled pairs would have perfect fidelity. Entanglement purification starts from these imperfectly entangled pairs, and combines 2-qubit, entangling gates with single-qubit operations to obtain higher-fidelity pairs (Pan et al. 2001; Simon et al. 2002; Pan et al. 2003). The way to extract a subset of states of high entanglement and high purity from a large set of less entangled states is thus needed to overcome decoherence in quantum repeater channels involving quantum memories (Li et al. 2014)

The use of hyperentanglement can greatly simplify the optical realization of the purification procedure (Simon et al. 2002). Hyperentanglement is a type of entangled state which involves few degrees of freedom of the same quantum system. For example, two photons can share entanglement in polarization and energy-time at the same time. In this case the state can

be written as

$$|\Phi\rangle = \left|\Phi_\pi^+\right\rangle \otimes \left|\Phi_\tau^+\right\rangle = \underbrace{|HH\rangle + |VV\rangle}_{\text{polarization}} \otimes \underbrace{|EE\rangle + |LL\rangle}_{\text{energy-time}}. \qquad (1.13)$$

The projection on one degree of freedom together with the single-qubit operation can increase the fidelity of the entangled state in other degree of freedom (Simon et al. 2002). In this thesis we demonstrated all prerequirements to realize entanglement purification compatible with long-distance quantum communication and involving storage in a quantum memory. These results are discussed in Chapter 5.

1.3.3   Elementary link: multimode approach

The further idea to realize long-distance quantum communication using entanglement swapping is to divide the whole distance into shorter segments and to distribute entanglement in between end nodes of these segments using the techniques described above (Fig. 1.4). By repeating this procedure many times entanglement is extended over the entire distance.

The probabilistic nature of entanglement generation and intrinsic losses during its distribution greatly reduce the rate of entanglement distribution over long distances. This happens because the rate of entanglement swapping (Bell-state measurement) over the whole distance is given by the product of the swapping rates for each elementary link. Which makes the total probability of entanglement distribution polynomially low. To increase the whole rate one have to enhance the probability for each part to swap entanglement. To increase the probability of successful Bell-state measurement one have to synchronize photons from different entangled photon pairs in time.

One of the solutions is to use quantum memories which can store separate entangled photons until the entanglement is successfully distributed over the given link. As a result, after a certain time the retrieved photon can be synchronized with the photon stored in another quantum memory to perform Bell-state measurement (Fig. 1.4). The synchronization implemented using optical quantum memories can greatly enhance entanglement distribution rates over long distances (Sangouard et al. 2011).

Further, different multiplexing schemes can be applied which allow one to efficiently parallelize the performance of the quantum repeater. In this context, multimode quantum memories (Afzelius et al. 2009) are of a great interest in modern studies, especially for quantum repeaters based on solid-state quantum memories. The potential for massive parallelism and high operation speed that make solid-state quantum repeaters an important yet challenging goal within the quantum information processing community. The work presented in this thesis falls within this framework.

The whole procedure describing the principle of quantum repeater can be divided into few steps (Fig. 1.4):

(a) Entanglement

Multimode QMs

(b) Swapping

BSM

(c) Entanglement purification

(c) Synchronized swapping
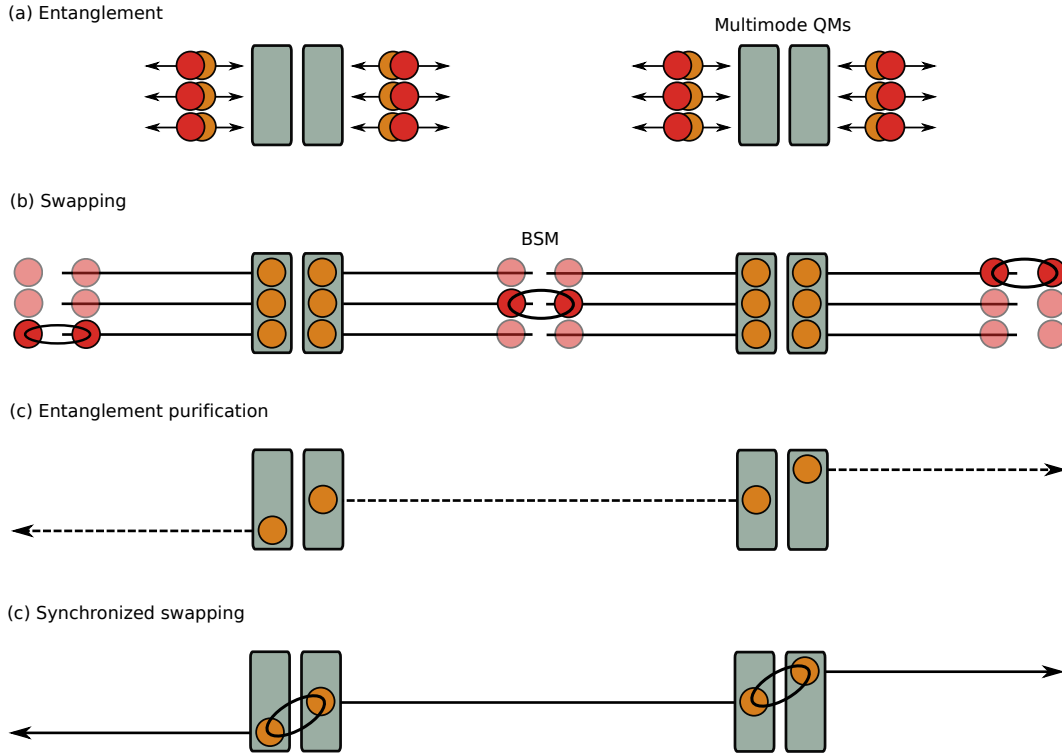
FIGURE 1.4: Elementary link of a quantum repeater. (a) One of the implementations of a quantum repeater (Simon et al. 2007) involves the use of probabilistic sources of entangled photon pairs and multimode quantum memories which can simultaneously store many temporal modes of the generated photon pairs. One of the photons from each photon pair (which are generated in parallel) is stored in the quantum memory, while another photon is sent towards the adjacent node where a Bell-state measurement (BSM) is performed. (b) Successful BSM between a pairs of photons that were not lost leads to the swapping of entanglement and heralds entanglement between quantum memories. (c) Quantum purification of the entangled state could be performed using different schemes. Entanglement can be stored until the neighbouring memories have also successfully stored entanglement. (d) Once neighbouring quantum memories have both stored one photon, they are synchronized in order to perform BSM that swaps entanglement to further nodes. This process is repeated until entanglement is generated over the desired distance (Bussières et al. 2013).

- massive generation of entangled qubit pairs and their distribution over the quantum channels using multiplexing schemes. Half of the entangled state is stored in multimode quantum memories while the other half travels towards the Bell-state measurement;

- the previous step is applied using repeat-until-success strategy such that an entangled pair will be established for every link. This can be done in parallel for all links with the total required time approximately equal to the average time needed for a single link to be established;

- the state of the entangled pairs can be purified and distilled in order to improve the fidelity reduced by the losses or decoherence;

- entanglement swapping can then be used to distribute entanglement possibly combined with other, intermediate purification steps that compensate for errors during the swapping.

The result is a longer-distance, high-fidelity entangled EPR-Bell pair, that could be used for secure quantum communication.

2   Light-matter quantum interface

As discussed in the previous chapter, quantum memory are essential tools to realize long-distance quantum communication. Due to their ability to store quantum information and preserve entanglement they were intensively studied during the last years. Most of the quantum memory protocols are based on the interaction between light and matter. However, light-matter interaction is not the only way to realize a quantum memory. All-optical systems can also be used for this purposes (Yoshikawa et al. 2013).

2.1   Optical quantum memory

It has been shown that light can be significantly slowed down by the presence of a media or even "stopped" inside it. These phenomena gave rise to many different protocols which utilize different properties of the light-matter interaction. The general idea is to map the quantum state of light into the quantum state of the media with the possibility to map it back (reversible). This approach is based on absorption and further reemission of light carrying quantum information. Another approach is to use the quantum memory as an emissive media to realize a delayed source of entangled photon pairs (Duan et al. 2001; Sekatski et al. 2011). In this case, a first emitted single photon is entangled with an internal degree of freedom of the memory which can then be readout on-demand emitting a second photon. Both approaches have great potential for quantum communication technologies (Sangouard et al. 2011).

In the context of quantum communication, a quantum memory is a device that can store a quantum state of light at the single photon level which then can be extracted on-demand. The variable delay that can be applied should allow one to synchronize different parts of the communication links to increase the whole efficiency and to make quantum repeater practical. Optical quantum memories have to fulfil certain requirements in order to be used for quantum communications:

2.1.1   Fidelity

The ability to preserve quantum information during the storage is characterized using the fidelity F. Any additional noise will reduce the value of fidelity and destroy quantum correlations. Assuming a single qubit, the largest fidelity achievable using measure and prepare strategy is $F = 2/3$

(Massar et al. 1995). While the minimal fidelity which is required to show nonlocal nature of a retrieved photon is 85.4% (Cirel'son 1980). However, these bounds are not sufficient to beat direct transmission with a quantum repeater, since noisy storage has to be compensated by entanglement purification or error correction, which reduces the entanglement distribution rate.

High recall fidelities exceeding 99% using polarization qubits were realized using solid-state system (Zhou et al. 2012b).

2.1.2   Efficiency

Another important parameter which characterizes the quality of a quantum memory is the efficiency η. It can be defined as a probability of the input single photon excitation to be stored and emitted from the quantum memory. It has been shown that probabilities of 90% has to be achieved to build practical quantum repeater. While the 1% increase in storage efficiency can increase the entanglement distribution rate from 7 to 18% (Sangouard et al. 2011).

Enhanced light-matter interaction can increase the optical memory efficiency. For this purpose, optical cavities and/or large atomic ensembles have been shown to be very useful (Sabooni et al. 2013; Jobez et al. 2014). Highest storage efficiencies of up to 76% were realized using solid-state (Schraft et al. 2016), up to 87% using warm vapors (Hosseini et al. 2011a) and 87% with cold atomic ensemble quantum memories (Cho et al. 2016).

2.1.3   Storage time

Ideally the storage time of the quantum memory in the architecture of a quantum repeater should be defined by the entanglement distribution time over the whole distance. For 1000 km optical fiber link, it can be few seconds (Sangouard et al. 2011). However, it has bee shown that this time could be defined by the elementary link only (Munro et al. 2010).

This time can be efficiently decreased applying various multiplexing schemes, but the maximum storage time is desirable. The longest storage time reported in the quantum regime has been implemented in cold atomic ensembles and reached 100 ms (Radnaev et al. 2010). While for classical regime it can reach a minute (Heinze et al. 2013).

2.1.4   Bandwidth

The bandwidth of the quantum memory defines the maximum spectral bandwidth of the photon that can be stored in it. Narrowband single photons have long coherence times, meaning that less photons can be sent in a given time. It is therefore an important practical advantage to distribute broadband photons. However, dispersion effects start to be important and have be considered and compensated.

Broadband quantum memories can greatly increase the temporal multimode capacity and use full spectrum of spontaneous parametric downconversion sources of entangled photon pairs. Large bandwidth of few GHz can be achieved using atomic vapors (Reim et al. 2010), hundreds of GHz in rare-earth ion-doped materials (Saglamyurek et al. 2012; Saglamyurek et al. 2015a), up to THz with diamonds (Lee et al. 2011) and 100 THz with hydrogen molecules (Bustard et al. 2013).

2.1.5   Multimode Capacity

The multiplexing scheme implies the possibility to store many modes inside the quantum memory at the same time. For this, different degrees of freedom of input light can be used: spectral, temporal, spatial and polarization modes. This could greatly enhance the distribution rate over the elementary link and over the whole distance of the quantum repeater (Simon et al. 2007). The storage of N Bell states simultaneously lead to N-fold increase in the quantum repeater operation rate.

Simultaneous storage of several temporal (Usmani et al. 2010; Bonarota et al. 2011; Jobez et al. 2016), spectral (Saglamyurek et al. 2014) modes and multidimensional quantum system (Zhou et al. 2015) have been implemented in this direction.

2.1.6   Other criteria

To realize entanglement distribution over long distances using optical fiber links, quantum memory has to operate at telecommunication wavelengths (C-band around 1550 nm) where transmission of optical fibers is maximal (the minimal loss 0.16 dB/km for Corning SMF-28 ULL optical fiber). This problem can be resolved using efficient frequency conversion to telecommunication wavelengths using nonlinear waveguides (see for example (Curtz et al. 2010; Zaske et al. 2012; Albrecht et al. 2014)) or in atomic ensembles (Radnaev et al. 2010). In this thesis our approach is based on using sources of entangled photons, where one photon of each pair is at a telecommunication wavelength, with the storage and recall of the other photon in an optical quantum memory (Simon et al. 2007).

To make the quantum repeater more practical integrated quantum memory directly into the quantum network is also desirable. In this context, quantum storage of light in waveguides or optical fibers doped by rare-earth ions is promising (Saglamyurek et al. 2011; Saglamyurek et al. 2015b).

The ability of the quantum memory to release stored quantum state on-demand is a basic feature to synchronize Bell-state measurement for efficient entanglement swapping. There are some proposals for quantum repeater which uses frequency multiplexing scheme where this feature is not necessary (Sinclair et al. 2014).

All necessary requirements introduced so far were successfully realized with different physical systems, but mostly separately. The main challenge nowadays is to combine all the best values (of efficiency, storage time, bandwidth and multimode capacity) that have been demonstrated using one

physical system. As an example, the best combination of high efficiency (up to 87%) and long storage times (1 ms) were implemented using cold atomic ensembles (Bao et al. 2012; Cho et al. 2016), however, the narrow bandwidth and single temporal mode in this case greatly restrict the multimode capacity which can be realized. Some other examples with high potential will be described further.

2.2   Single quantum systems

The experimental control of single atoms, ions or single solid-state emitters gave the possibility to use them as elementary building blocks of quantum networks (Cirac et al. 1997). The naturally limited multimode capacity for this system can be compensated by the possible deterministic Bell-state measurement (Reiserer et al. 2015).

Single Rb atoms together with high-finesse cavities gave retrieval efficiencies up to 9% and storage times of 180 μs (Specht et al. 2011). Several sub-parts of a quantum-repeater protocol have been successfully implemented with these systems at near-infrared wavelengths. Quantum teleportation between two distant trapped Yb^+ ions have been realized (Olmschenk et al. 2009). An elementary quantum network using two single-atom quantum memories in separate atom traps distant by 21 m (Ritter et al. 2012) and heralded entanglement between two single atoms sitting in dipole traps and separated by 20 m (Hofmann et al. 2012) were demonstrated. An atom-photon quantum gate (Reiserer et al. 2014), and the heralded storage of a photonic quantum bit (Kalb et al. 2015) were realized. It has also been demonstrated with solid-state single-spin qubits based on a single nitrogen-vacancy center (Togan et al. 2010; Sipahigil et al. 2012) and quantum dots (Gao et al. 2012).

2.3   Atomic ensembles

The experimental control of single atoms and ions trapped and coupled to high-finesse optical cavities is very challenging which makes the direct implementation of the quantum repeater barely practical. The first proposal for a practical quantum repeater based on ensembles of atoms and linear optics was done by Duan et al. 2001, now often referred to as the DLCZ (Duan-Lukin-Cirac-Zoller) protocol.

Light-matter and conversion usually requires the strong interaction between light and matter in order to improve the interface between them. By increasing the number of interacting particles in the systems one can sufficiently increase the optical depth and enhance light-matter interactions. These systems can be realized using warm atomic vapors, cold atomic ensembles, Bose-Einstein condensates and rare earth ion-doped systems. The last one was used in this thesis and described in more details in Chapter 4.

Most of them are based on the preparation of collective atomic states to map single photons into the quantum state of matter and, after certain

time, map it back (Fig. 2.1). In the case of two-level atomic system consisting of ground $|g\rangle$ and excited $|e\rangle$ state, collective atomic excitations can be described as the Dicke state (Dicke 1954). The absorbed single photon on the transition $|g\rangle - |e\rangle$ will produce the delocalized atomic excitation which can be written as

$$|\Psi_D\rangle = \frac{1}{\sqrt{N}} \sum_{i=1}^{N} c_i |g_1...e_i...g_N\rangle, \tag{2.1}$$

where N is the number of atoms and c_i is the phase coefficient corresponding to the i-th atom. Physical manipulation of c_i phase coefficients defines the variety of different quantum memory protocols which could be realized in different physical systems.

2.3.1 Electromagnetically-induced transparency

Electromagnetically induced transparency (EIT) was first experimentally observed in warm strontium vapour (Boller et al. 1991). It is based on the quantum interference between different excitations pathways that creates a narrow spectral transparency window and fast varying susceptibility (Fig. 2.1(b)). Based on this an ultralow group velocity and full transparency in an otherwise opaque medium were observed (Hau et al. 1999).

Inside the transparency window the group velocity of the light is reduced by a factor proportional to $d\Gamma/(4\Omega^2)$ with Γ the linewidth of the transition, Ω the Rabi frequency of the control field, L is the length of the medium with optical depth d. Storage is achieved by adiabatically reducing the control field intensity to zero before the pulse leaves the medium (Fig. 2.1(b)). The protocol to stop light inside the medium was proposed (Fleischhauer et al. 2000) and also realized in atomic Rb vapour (Liu et al. 2001) and rare-earth ion-doped crystal (Phillips et al. 2001).

Modern experiments involve an attenuated laser field as an input signal, interacting with a dense atomic ensemble with variable optical depth up to 1000. They achieved storage efficiencies up to 96% with Cs atomic ensemble (Hsiao et al. 2016) and 78% using bright pulses in cold ^{87}Rb ensemble (Chen et al. 2013) and 76% in $Pr^{3+}:Y_2SiO_5$ crystal (Schraft et al. 2016). High-efficiency EIT storage up to 49% of single photons generated using a cold atomic ensemble has also been recently demonstrated in a cold atomic ensemble (Zhou et al. 2012a).

The bandwidth of the EIT protocol is typically limited to few MHz and depends on the Rabi frequency of the control field. In this case the maximum duration of the input that can be entirely compressed in the medium is defined as $d\Gamma/(4\Omega^2)$. The bandwidth of the input light is limited by the width of the transparency window $4\Omega^2/(\Gamma\sqrt{d})$. This means that the temporal multimode capacity scales as $\propto \sqrt{d}$ (Lukin 2003). Another limitation comes from the resonant character of the technique which can lead to additional noise and therefore reduce the maximum achievable quantum fidelity (Hsu et al. 2006).
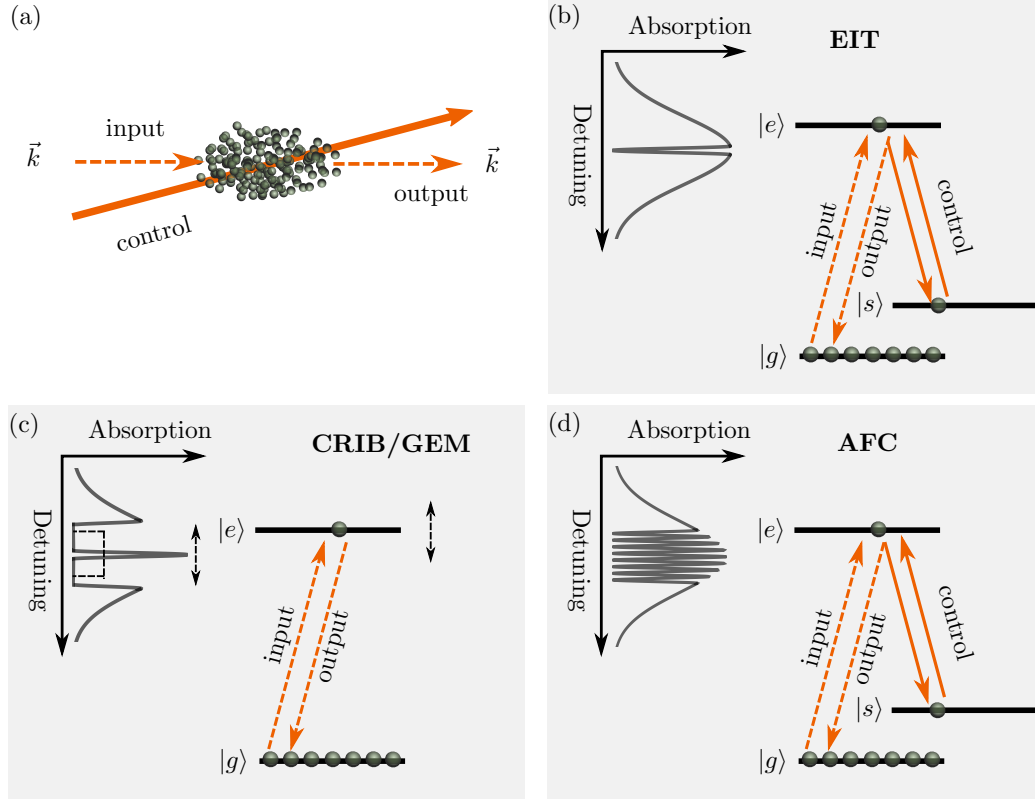
FIGURE 2.1: Quantum memory protocols. (a) Light-matter interaction can be enhanced using large atomic ensembles to realize a quantum memory. The interaction of a single photon at the input leads to the generation of a collective atomic state which can be manipulated using a control field in different regimes. (b) A strong control field applied to the homogeneous atomic system on the $|e\rangle \longleftrightarrow |s\rangle$ transition creates a narrow transmission window in the ensemble's absorption spectrum at the frequency corresponding to the energy difference between states $|g\rangle$ and $|e\rangle$. This effect is called electromagnetically induced transparency (EIT). Input photons with a spectral bandwidth comparable to the transmission window are slowed down and spatially compressed due to the strong dispersion. By turning off the control field, the input photon can be stored as a coherent spin wave and then retrieved after a certain time by turning the control field on again. (c) The artificial inhomogeneous broadening which can be created and reversed using external gradient fields can be used to manipulate a stored excitation. During the absorption of an input photon the gradient field is applied to store the input light as an excitation on the inhomogeneously broadened $|g\rangle \longleftrightarrow |e\rangle$ transition. The reversed gradient field will lead to the retrieval process. (d) Natural inhomogeneous broadening can be used to create a periodic structure in the absorption profile i.e. an atomic frequency comb (AFC) using optical pumping techniques. After a single input photon with a spectrum broader than the period is absorbed, a strong control pulse transfers the coherence from the excited state to a long-lived spin state. To read out, a second control pulse transfers the coherence back to the excited state and the rephasing process continues and leads to an output.

2.3.2 Controlled reversible inhomogeneous broadening

Controlled reversible inhomogeneous broadening (CRIB) was originally proposed as an optical quantum memory protocol based on the manipulation of the inhomogeneous broadening of the optical transition in atomic gases (Moiseev et al. 2001) or rare-earth ion-doped crystals (Nilsson et al. 2005; Alexander et al. 2006).

CRIB implementations usually involve the creation of a narrow absorption line of width γ and optical depth d (Fig. 2.1(c)). During the absorption of single photon at the input artificial inhomogeneous broadening Γ is created by the external gradient fields. This leads to the mapping of the single photon state into the collective atomic state

$$|\Psi_D\rangle = \frac{1}{\sqrt{N}} \sum_{i=1}^{N} c_i e^{j(\vec{k}\vec{r}_i - 2\pi\delta_i t)} |g_1...e_i...g_N\rangle, \qquad (2.2)$$

where each ion i has detuning δ_i which is modulated by external field. Due to this gradient in frequencies atomic state is rapidly dephased. However, at given time $t/2$ the external field can be reversed by changing the time order, i.e. letting $\delta_i \to -\delta_i$. In this case due to rephasing of the collective atomic state the photon echo signal can be observed at time t.

The efficiency of CRIB can be expressed as

$$\eta_{\text{CRIB}}(t) = (d\gamma/\Gamma)^2 e^{-d\gamma/\Gamma} e^{-4\pi^2 t^2 \gamma^2}. \qquad (2.3)$$

The main assumption here is that the spectral width of the absorption peak Γ is much wider than the spectral bandwidth of the photon to be stored. The maximum storage time in this case is defined by the initial width of the narrow absorption peak γ ans is given by $1/\gamma$.

From expression (2.3) one can see that in order to keep the efficiency η constant when increasing the number of modes, the optical depth d needs to be increased proportionally. Indeed, by doubling the bandwidth Γ to double the number of temporal modes that can be stored using CRIB one has to double the optical depth d to reach same efficiency η. As a result the multimode capacity scales linearly with the optical depth $N \propto d$.

The first experiments in solid-state media were executed using transverse electrical field to imply controlled linear Stark effect and classical pulses, but later the results were extended to the single-photon level (Lauritzen et al. 2010; Hedges et al. 2010).

The efficiency of this method is limited to 54% due to the reabsorption process during the reemission. In order to overcome this problem the longitudinal CRIB, also known as gradient echo memory (GEM) (Fig. 2.1(c)) was proposed (Alexander et al. 2006) and implemented using $Pr^{3+}:Y_2SiO_5$ crystal with storage efficiencies up to 69% (Hétet et al. 2008; Hedges et al. 2010).

2.3.3   Atomic frequency combs

The atomic frequency comb (AFC) quantum memory protocol is based on the rephasing of atomic coherences analogous to photon echo phenomena. Due to the prepared periodically shaped absorption profile, the rephasing happens at a predetermined moment in time inversely, proportional to the period of the structure (Fig. 2.1(d)). The implementation for quantum memories has been proposed by (Afzelius et al. 2009) in Geneva.

The simplest scheme requires the creation of a periodic absorption structure on the optical transition $|g\rangle \longleftrightarrow |e\rangle$. This structure can be created by various optical pumping techniques which usually involve the use of the third level $|aux\rangle$ to transfer the residual atomic population (Fig. 2.2(a)). The absorption of a single photon with wavevector $\vec{k}$ by such atomic ensembles leads to the generation of the collective atomic state

$$|\Psi_D\rangle = \frac{1}{\sqrt{N}} \sum_{i=1}^{N} c_i e^{j(\vec{k}\vec{r}_i - 2\pi\delta_i t)} |g_1...e_i...g_N\rangle, \qquad (2.4)$$

where a single atomic excitation is delocalized among N atoms. Here $\vec{r}_i$ is the position of the ith atom, δ_i is the frequency detuning of the ith atom with respect to the central frequency of the input photon and c_i is the complex amplitude depending on the frequency and position of the specific atom. Due to the inhomogeneous broadening of the atomic ensemble (large distribution of the frequency detunings δ_i) the collective state quickly dephases after the absorption of a single photon (Fig. 2.2(b,c)). However, such an inhomogeneous dephasing can be reversed in the presence of equally distributed absorption peaks such that $\delta_i = m_i\Delta$ where m_i are integers. This leads to the collective rephasing of the single atomic coherences after the storage time $\tau = 1/\Delta$. The efficiency in this case can be written as

$$\eta_{\text{AFC}} = (d/F)^2 e^{-d/F} \eta_{\text{deph}}, \qquad (2.5)$$

where d is the optical depth corresponding to the amplitude of the absorption peak, $F = \Delta/\gamma$ is the finesse of the comb, γ is the width of the single absorption peak and η_{deph} is the rephasing efficiency which depends on the AFC shape (Bonarota et al. 2010). The first term corresponds to the absorption and reemission efficiency , while the second describes the reabsorption process. Due to the presence of this term the efficiency in forward direction is limited to 54%.

In order to reach 100% retrieval efficiency a complete AFC scheme can be used (Afzelius et al. 2009). For this, the stored excitation is transferred to the third spin level $|s\rangle$ where it can be stored for a longer time in the form of a spin-wave and retrieved back on-demand (Fig. 2.2(b,d)). This is done by applying two control π-pulses which transfer the atomic population on the $|e\rangle - |s\rangle$ transition.

In the case when the control pulses are applied in a counter propagating direction to the input pulse a storage and retrieval efficiency can reach unity (Afzelius et al. 2009). Assuming perfect transfer efficiency the efficiency in

(a) AFC preparation

(b) Storage and retrieval

(c) Timing. AFC delay line

(d) Timing. Full AFC scheme
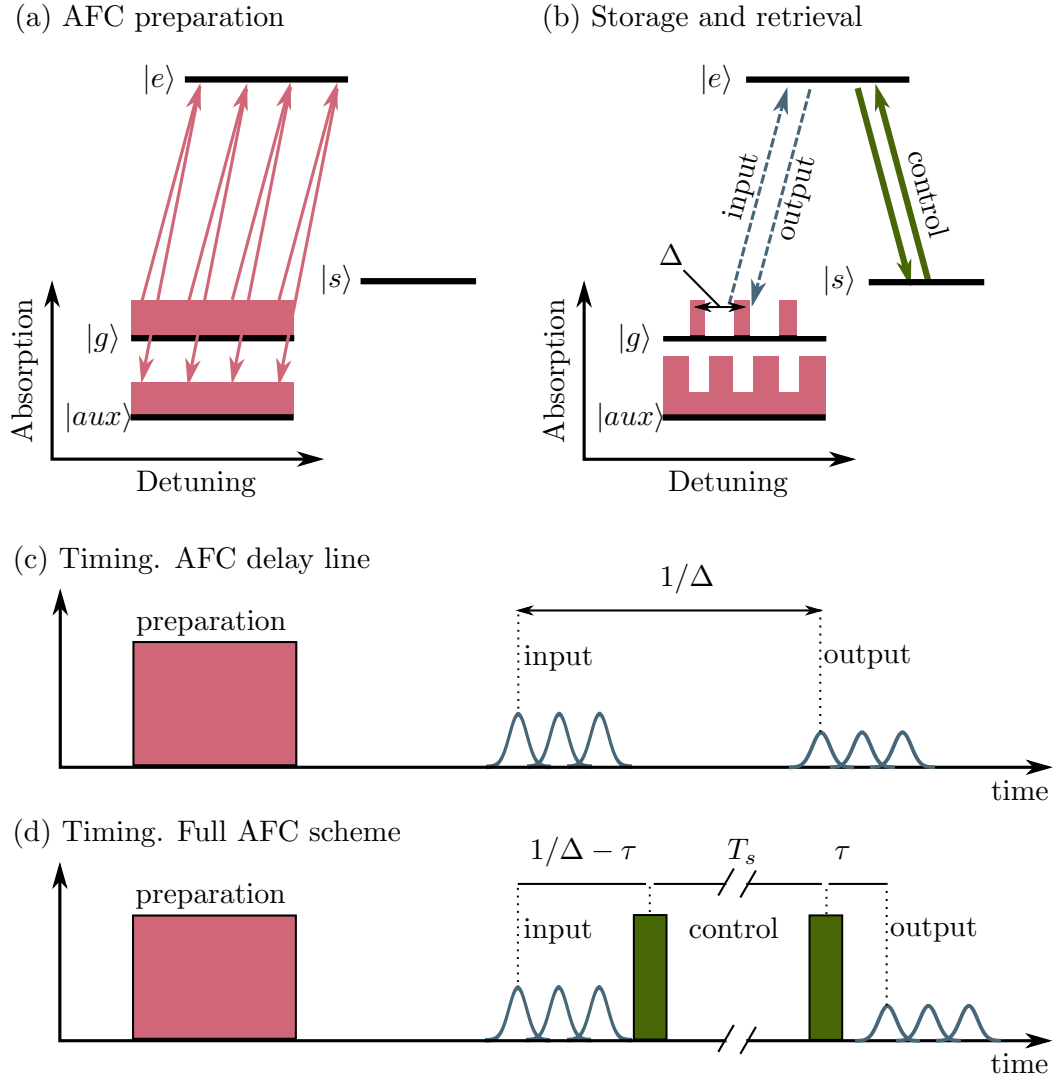
FIGURE 2.2: AFC quantum memory protocol. (a) First, the atomic frequency comb structure with period Δ is prepared on the $|g\rangle \longleftrightarrow |e\rangle$ using frequency selective optical pumping. (b) The excitation at the input produces a collective atomic state which can be transferred to the prepared spin state $|s\rangle$ using control field $|e\rangle \longleftrightarrow |s\rangle$. (c) Without the use of control pulses the stored excitation will be reemitted after time $1/\Delta$. Multimode capacity allows one to store many excitations in different temporal modes. (d) Applying control pulses allows the storage time to be extended by storing excitation as a spin-wave in the media. The on-demand retrieval is done by a second control pulse after time T_s that transfers the excitations back to $|e\rangle$. This leads to the reemission of the stored single photon after time $1/\Delta + T_s$.

this case can be written as

$$\eta_{\text{AFC}} = (1 - e^{-d/F})^2 \eta_{\text{deph}} \tag{2.6}$$

and does not include losses due to reabsorption. The main advantage of the AFC protocol is it's temporal multimode capacity which defines the number of stored modes N (Fig 2.1(c,d)). For AFC, it does not depend on the optical depth d and scales only with the number of absorption peaks in the atomic structure. For the AFC with total spectral bandwidth Γ and period Δ we have that $N \propto \Gamma/\Delta$. The absorption caused by the background optical depth d_0 usually limits the maximum achievable efficiency and is attributed to the imperfect state preparation.

The implementation of the AFC quantum memory is mostly based on rare-earth ion-doped crystals. AFC structure in these materials can be efficiently created using spectral hole burning techniques. The hyperfine splitting of the ground state offers the possibility to implement a complete AFC scheme and long storage times. The first two-level AFC (Fig. 2.2(c)) demonstration was realized at the single photon level (Riedmatten et al. 2008) and later using entangled single photons (Clausen et al. 2010) using Nd^{3+} ions. The storage in this case was done up to 200 ns with 5% efficiency. This configuration was further used to demonstrate storage of the polarization qubits (Clausen et al. 2012) and to demonstrate heralded entanglement between two crystals (Usmani et al. 2012). The storage time using two-level AFC scheme and heralded single photons was extended up to 4.5 μs in Pr^{3+}:Y_2SiO_5 with 1% efficiency (Rielander et al. 2014).

A complete AFC protocol (Fig. 2.2(d)) has been demonstrated using strong coherent states as input (Afzelius et al. 2010a) and at the single photon level (Timoney et al. 2013) for up to 30 μs storage times. Later the storage of photonic qubits encoded using time-bins (Gündoğan et al. 2015) and polarization together with 5 temporal modes (Laplane et al. 2016b) have been demonstrated. Quantum storage of true single photons using full AFC scheme has not been realized yet.

A temporal multimode capacity with the two-level AFC scheme of up to 1060 has been demonstrated using classical light (Bonarota et al. 2011), 64 modes have been stored at the single photon level (Usmani et al. 2010). With full AFC scheme, the storage of 50 modes for 500 μs has been realized (Jobez et al. 2016).

The use of impedance-matched optical cavity helps to overcome the limitation on the maximum efficiency (Afzelius et al. 2010a). The first demonstrations showed the possibility to reach 58% with weakly absorbing Pr^{3+}:Y_2SiO_5 and 53% with Eu^{3+}:Y_2SiO_5 crystals with μs storage times (Sabooni et al. 2013; Jobez et al. 2014).

All the storage experiments presented in this thesis are performed using two-level AFC quantum memory protocol. The features that allow storage of the different states of lights that have been investigated only depend on the AFC two-level memory, hence they can also be stored using the full AFC spin-wave memory.

2.3.4   Raman based memory

Raman type process enables broadband, sub-nanosecond photon storage (Fig. 2.3(a)). It has been proposed and demonstrated in hot atomic vapours with 1 GHz bandwidth (Reim et al. 2010), diamonds up to 1 THz (Lee et al. 2011; England et al. 2013) and hydrogen molecules up to 125 THz bandwidth (Bustard et al. 2013). The large bandwidth is the main advantage of this approach, while the scaling with the number of modes is analogous to EIT protocol and storage times are extremely small (up to 1 ns).

Significant progresses are associated with applying GEM technique to induce a controlled broadening of the spin transition memory (Λ-GEM). For this, one uses an off-resonant stimulated Raman interaction to map the light field onto an atomic spin wave (Fig. 2.3(a)). This scheme was implemented in warm atomic Rb vapours with a storage and retrieval efficiency of up to 89% (Hosseini et al. 2009; Hosseini et al. 2011a) and tens of microseconds storage times. The bandwidth in this case is much smaller and reaches few MHz, while the scaling for the number of modes is the same as for usual CRIB and GEM.

Other significant results with Λ-GEM include coherent pulse sequencing (Hosseini et al. 2012) and highly efficient 84% unconditional quantum memory for weak coherent pulses (Hosseini et al. 2011b). The control of the single collective spin excitations was also demonstrated (Albrecht et al. 2015).

2.3.5   DLCZ-type quantum memory

DLCZ protocol (Duan et al. 2001) is based on using collective atomic states to generate and swap entanglement. In this scheme, entanglement is created between a single photon and a collective atomic excitation. This excitation can be read out as a photon to perform a Bell-state measurement and distribute entanglement between a network of atomic ensembles.

In this case, the atomic ensemble can be considered as a source of entangled photon pairs with controllable delay line between them (Fig. 2.3(b)). Such type of quantum memory is usually referred to as *emissive* in contrast to the absorptive quantum memories described above.

The implementation of the DLCZ scheme using cold Rb atomic ensembles became a work horse for a great number of impressive experiments. The longest quantum storage of 100 ms involving frequency conversion to telecommunication wavelengths was reported by (Radnaev et al. 2010). An optical cavity around Rb atomic ensemble helped to achieve 73% readout efficiency together with 3.2 ms storage time (Bao et al. 2012). Based on this, entanglement among four quantum memories has been demonstrated (Choi et al. 2010). Further improvements helped to achieve an initial retrieval efficiency of 76% together with an $1/e$ lifetime of 0.22 s (Yang et al. 2016).

The realization of the DLCZ-like scheme in solid states can offer great advantages based on the temporal multimode capacity. The proposed rephased
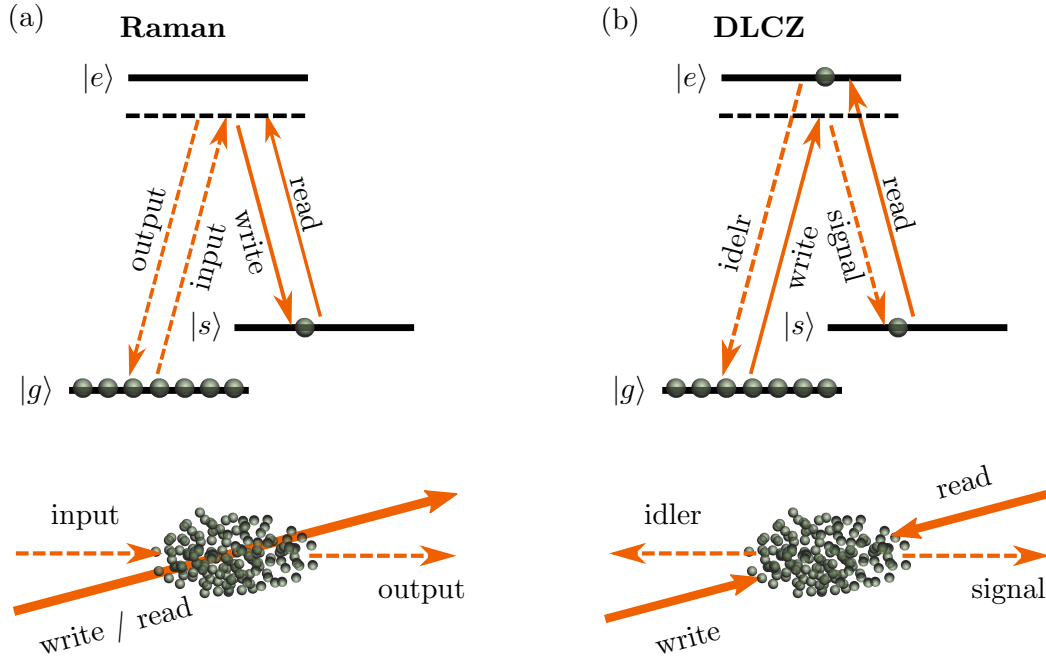
FIGURE 2.3: Off-resonant quantum memory protocols. (a) One of the im-
plementations of the quantum memory based on off-resonant Raman scat-
tering. An input signal photon together with a strong write pulse stimulate
Raman scattering on the $|g\rangle \longleftrightarrow |e\rangle$ transition and forms a collective exci-
tation on the storage state $|s\rangle$. The application of the read pulse on the same
transition leads to the emission of an anti-Stokes photon and read-out from
the memory. (b) Energy level scheme used for the DLCZ (Duan et al. 2001)
memory. The write pulse off-resonantly couples the ground state $|g\rangle$ to the
excited level $|e\rangle$. A Stokes photon is emitted with small probability, thus
creating a single collective excitation to the storage state $|s\rangle$. During the
retrieval process, a pulse resonant with the $|s\rangle \longrightarrow |e\rangle$ transition (read) col-
lectively transfers back the atom to the initial state $|g\rangle$ while emitting an
anti-Stokes single photon in a well-defined spatio-temporal mode.

spontaneous emission (RASE) (Ledingham et al. 2010) has been demonstrated in rare-earth ion-doped crystals involving classical correlations (Beavan et al. 2012), entanglement (Ledingham et al. 2012) and non classical correaltions (Ferguson et al. 2016). It has been demonstrated using homodyne measurement based on Duan's criteria (Duan et al. 2000). We note that no non-classical correlations using discrete variables has been published yet.

The combination of the DLCZ and AFC schemes (AFC-DLCZ) was proposed by Sekatski et al. 2011 and offers great temporal multimode capacity combined with the narrowband photon pair sources compatible for quantum communication.

3   Source of entangled photon pairs

This chapter is partly based on the results published in

C. Clausen, F. Bussières, A. Tiranov, H. Herrmann, C. Silberhorn, W. Sohler, M. Afzelius & N. Gisin, **"A source of polarization-entangled photon pairs interfacing quantum memories with telecom photons"**, New Journal of Physics 16, 093058 (2014) (pages 143-172)

The source of entangled photon pairs used in this thesis based on spontaneous parametric down conversion (SPDC) in nonlinear waveguides. It was aligned and characterized for experiments involving an AFC two-level quantum memory introduced in Chapter 2. This quantum memory protocol was implemented in a Nd^{3+}:Y_2SiO_5 crystal described in Chapter 4. The signal photon from the photon pair has to be in resonance with the transition from the ${}^4I_{9/2}$ ground state to the ${}^4F_{3/2}$ excited state of the Nd^{3+} ion at $\lambda_s = 883$ nm.

To realize long-distance quantum communication the wavelength of the idler photon of a pair has to be in the region from 1300 nm to 1700 nm in order to take advantage of high transmission in optical fibres at these wavelengths. This condition can be conveniently satisfied using a pump wavelength of $\lambda_p = 532$ nm, for which high-quality solid-state lasers are readily available. This places the idler wavelength at $\lambda_i = (\lambda_p^{-1} - \lambda_s^{-1})^{-1} = 1338$ nm due to energy conservation.

In this chapter we give a brief introduction to the theory of SPDC and present experimental details about the realization and characterization of the source of entangled photons used in this thesis.

3.1   Spontaneous parametric down conversion

Spontaneous parametric down-conversion (SPDC) can be considered as the inverse process of sum-frequency generation in non-linear optics. It is the process taking place inside a medium with $\chi^{(2)}$-nonlinearity when a pump photon spontaneously decays into a pair of photons, such that energy and momentum are conserved. In the simplest case, SPDC process is usually described by the interaction Hamiltonian

$$\hat{H}_I = \hbar\chi^{(2)}(\xi a_s^\dagger a_i^\dagger a_p + \xi^* a_s a_i a_p^\dagger), \tag{3.1}$$

where a_p, a_s and a_i denote the annihilation operators for the pump, signal and idler modes, respectively, and ξ depends on the properties of the pump, among other things. Under this Hamiltonian, the vacuum state evolves into

a two-mode squeezed state,

$$|\Psi\rangle = e^{i\hat{H}_I t/\hbar} |vac\rangle = \sqrt{1-p} \sum_{n=0}^{\infty} p^{n/2} |n_s, n_i\rangle, \tag{3.2}$$

where $p = \tanh^2(\chi^{(2)}|\xi|t)$, which in the case $p \ll 1$ can be interpreted as the probability to create a single photon pair.

The two-mode squeezed state (Eq. (3.2)) has a series of properties of interest that are important for most of the quantum optics experiments.

3.1.1 Thermal statistics of the signal and idler modes

When considered individually, the signal and idler modes exhibit thermal statistics. This can be seen directly by expressing the photon number distribution in terms of the mean photon number,

$$P(n) = \frac{\mu^n}{(1+\mu)^{n+1}}, \text{ where } \mu = \langle n_s \rangle = \langle n_i \rangle = \frac{p}{1-p}. \tag{3.3}$$

Additionally, the thermal bunching is reflected in the second-order autocorrelation function of the signal and idler modes,

$$g^{(2)} = \frac{\langle a^\dagger a^\dagger a a \rangle}{\langle a^\dagger a \rangle^2}, \tag{3.4}$$

which reaches 2 for two-mode squeezed state containing only one mode.

3.1.2 Multimode properties

The existence of several two-mode squeezed states in parallel can have a strong effect on the measurements. Consider, for instance, a measurement of $g_{s,s}^{(2)}$, which requires a coincidence detection of two signal photons. If the photons stem from different squeezed states, there are no correlations between them, and the value of the auto-correlation function is reduced. An auto-correlation value close to the maximum of 2 can only be obtained if the probability is high that both photons belong to the same mode, that is, if the total number of modes is small. Indeed, one can show that the value of the auto-correlation function in the multimode case is given by

$$g^{(2)} \approx 1 + \frac{1}{K} \tag{3.5}$$

where $K \geq 1$ is the effective number of modes (Christ et al. 2011).

Multimode photon-pair sources can be turned into single-mode sources by applying filtering in the time and/or frequency domains, such that the detected photons always belong to the same mode. In our case, filtering in the time domain amounts to having a detector with a temporal resolution that is much shorter than the coherence time of the generated photons.

The effective number of modes hence depends on the combined system of source and detector.

3.1.3 Nonclassical correlations

While the signal and idler modes seem perfectly classical individually, there are strong quantum correlations between them. The quantumness stems from the fact that the number of photons in the signal and idler modes are always exactly identical (Eq. (3.2)). Experimentally, this can be demonstrated using different methods. Here we discuss only technique based on the single photon counting.

The first way to prove that the correlations between signal and idler are non-classical is by the violation of a Cauchy-Schwartz inequality that relates the cross-correlation function $g_{s,i}^{(2)}$ to the auto-correlation functions $g_{s,s}^{(2)}$ and $g_{i,i}^{(2)}$ (Kuzmich et al. 2003),

$$g_{s,i}^{(2)} \leq \sqrt{g_{s,s}^{(2)} g_{i,i}^{(2)}} \tag{3.6}$$

for classical fields.

For the two-mode squeezed state one find correlation function

$$g_{s,i}^{(2)} = \frac{\langle a_s^\dagger a_i^\dagger a_s a_i \rangle}{\langle a_s^\dagger a_s \rangle \langle a_i^\dagger a_i \rangle} = 1 + \frac{1}{p} \tag{3.7}$$

which violates inequality (3.6)for all $p < 1$.

The second way to show non-classicality is related to the use of photon-pair sources as heralded sources of single-photons. The identifying property of a single-photon source is its vanishing auto-correlation function $g^{(2)} = 0$, while classical fields always have $g^{(2)} \geq 1$. A source generating a two-mode squeezed state (Eq. (3.2)) can be an almost ideal source of heralded single photons, because the ratio of double-pair to single-pair emission can be made arbitrarily small when $p \ll 1$. This fact can be reflected in an auto-correlation function that is conditioned on the detection of the idler photon (Clausen 2013),

$$g_{s,s|i}^{(2)} = \frac{\langle a_i^\dagger a_i \rangle \langle a_i^\dagger a_s^\dagger a_s^\dagger a_s a_s a_i \rangle}{\langle a_i^\dagger a_s^\dagger a_s a_i \rangle^2} = 2p \frac{2 + p}{(1 + p)^2} \tag{3.8}$$

which for $p \ll 1$ can be approximated by $g_{s,s|i}^{(2)} \approx 4p$.

3.1.4 Temporal inversion

SPDC process can be used to herald single photons with arbitrary controlled time waveform. This fact can be used for different applications involving interaction of the single photons with the single emitters.

The conditions for the perfect absorption of an incident single photon by a single atom can be found from the reversed process: the spontaneous emission of a photon from an atom prepared in an excited state. This feature
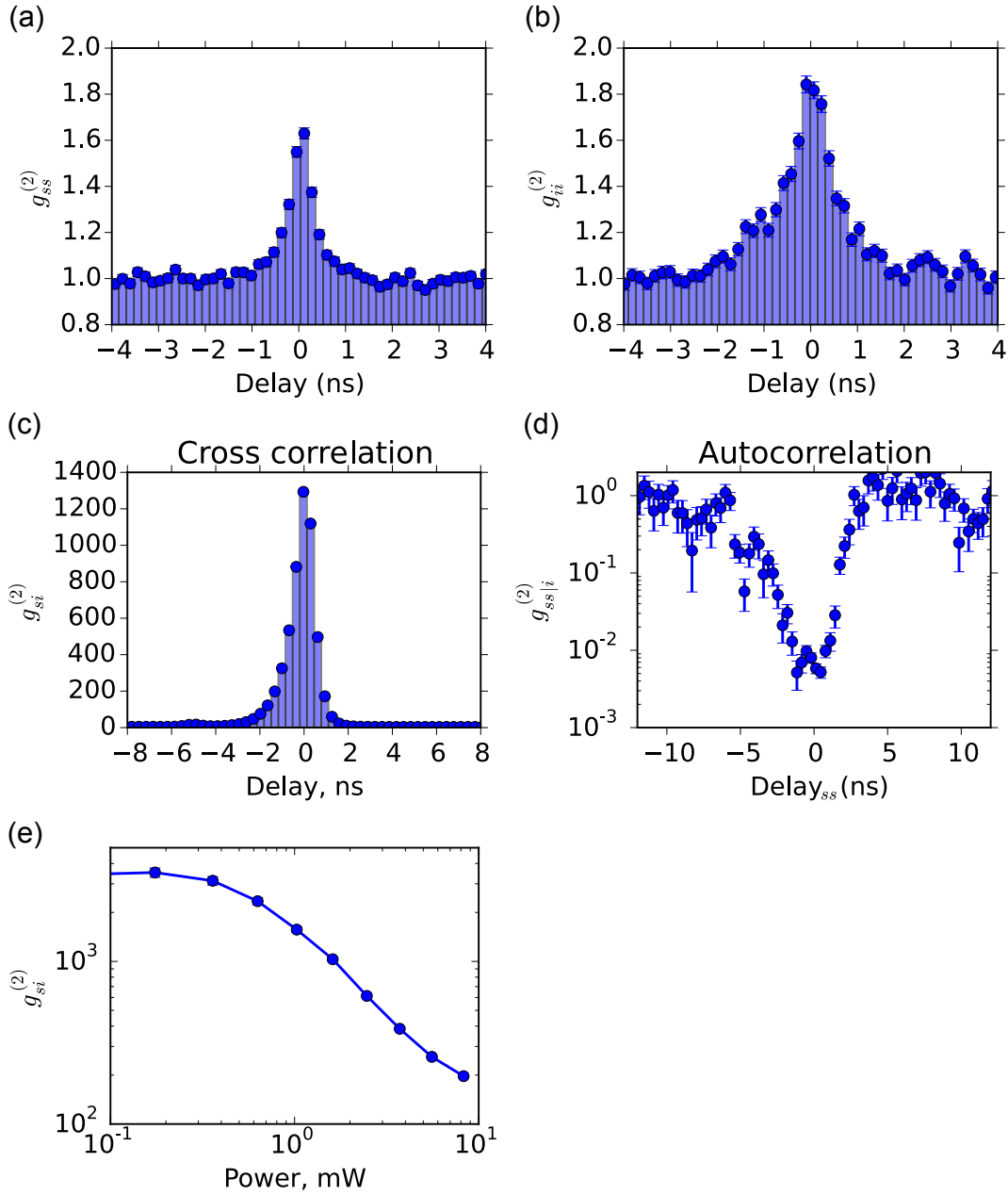
FIGURE 3.1: Second order correlation functions of the SPDC source. (a) -(b) Autocorrelation functions of the signal $g_{ss}^{(2)}$ and idler mode $g_{ii}^{(2)}$. (c) Cross-correlation function $g_{si}^{(2)}$ between signal and idler modes. (d) Auto-correlation function of the heralded single photon in the signal mode $g_{ss|i}^{(2)}$ heralded by the detection of the idler photon. (e) Cross-correlation function $g_{si}^{(2)}$ measured as the function of the SPDC pump power. At low pump powers $g_{si}^{(2)}$ starts to be limited by the dark count of the detectors.

is induced by the time-reversal symmetry of Schrödinger's and Maxwell's equations. Therefore, to enhance the coupling between atom and single photon the incident photon should have an exponentially rising temporal envelope with a matching time constant (Aljunid et al. 2013). This principle is general and it is applicable for the optimization of the light matter interfaces (Gorshkov et al. 2007).

To temporally inverse the exponentially decaying waveform the reflection from the asymmetric cavity can be used (Srivathsan et al. 2014). Recently, efficient coupling with the single atom has been demonstrated using a single photon generated via four-wave-mixing in the Rb atomic ensemble (Leong et al. 2016).

For this purpose, SPDC process also can be used applying spectral filtering based on standard cavities. The state of the single photon pair generated by the multimode SPDC process can be written as

$$|\Psi\rangle \propto \int \int d\omega_s d\omega_i \Phi(\omega_s, \omega_i) \alpha(\omega_s + \omega_i) a^\dagger_{\omega_s} a^\dagger_{\omega_i} |\text{vac}\rangle \tag{3.9}$$

The product of $\alpha(\omega_s + \omega_i)$ and $\Phi(\omega_s, \omega_i)$ is often called the joint spectral amplitude. Applying spectral filtering to the idler mode which is much narrower than for the signal photon and assuming monochromatic pump laser ω_p one can write the state as

$$|\Psi\rangle \propto \int d\Delta I(\Delta) a^\dagger_{\omega_s^0 - \Delta} a^\dagger_{\omega_i^0 + \Delta} |\text{vac}\rangle \tag{3.10}$$

where Δ is the detuning from the central frequency of the filter ω_0^0 with transmission amplitude $I(\Delta)$ applied to the idler mode and $\omega_p = \omega_i^0 + \omega_s^0$. The detection of the idler mode at time moment t_0 heralds the single photon wavepacket in the signal mode with spectral amplitude $I(-\Delta)$. For the case when $I(-\Delta) = I^*(\Delta)$ this will correspond to the inversion in time. For example, in the simplest case the lorentzian filter (standard cavity or etalon) with spectral amplitude $I(\Delta) = 1/(1 - i\Delta\tau_i)$ which corresponds to the exponentially falling temporal envelope with decay time τ_i. Thanks to the anticorrealtion in energy shown above (Eq. (3.10)), by detecting the idler photon after the lorentzian filter the signal photon with exponentially rising waveform is heralded. The temporal shape can be revealed by measuring the cross-correlation function $g^{(2)}_{si}$ (Fig. 3.1(c)).

3.1.5 Entanglement

The SPDC process provides a tool to generate entanglement between the signal and idler photons. The entanglement can be established using various photonic degrees of freedom. In particular, energy-time entanglement and polarization entanglement were used during our experiments to demonstrate efficient interface between solid-state quantum memories and SPDC sources (Chapters 5 and 6).

Energy-time entanglement

In the case of a highly coherent continuous-wave pump laser, the spectrum of the pump laser is very narrow as compared to the spectrum of the idler or signal photons. Consequently, the sum of the energies of signal and idler photons is perfectly well-defined, and we can approximate it by

$$\alpha_{\text{cw}}(\omega_s + \omega_i) \approx \delta(\omega_s + \omega_i - \omega_p). \tag{3.11}$$

In this case, the joint spectral amplitude is given only by the phase-matching condition. In such extreme case, spectral correlations between two photons can not be destroyed by the spectral filtering. Instead, temporal filtering is needed to introduce some uncertainty in the total energy of the photon pair.

The situation of a highly coherent pump that we have just described is nothing but entanglement in energy and time (Franson 1989). An arguably more intuitive picture is given by the time-domain description: A narrow-band pump laser can have a coherence time that is many orders of magnitude longer than the coherence time of the photons created by SPDC. Energy conservation tells us that the signal and idler photons must be created at the same time to within their coherence length, but the exact time has an uncertainty on the order of the coherence time of the pump laser.

The coherence time in this case is defined by the filtering system of both photons which has to be still much bigger than the spectrum of the pump to still keep energy/time entanglement between two photons (Fig. 3.2(a)).

The state of the energy-time entangled photon pair with certain coherence time $|t\rangle$ can be described as

$$|\Phi_t\rangle \sim \int dt\tilde{\alpha}(t) |t_s\rangle |t_i\rangle, \tag{3.12}$$

where $\tilde{\alpha}(t)$ is the temporal envelope of the pump photon.

Energy-time entanglement can be probed by Franson interferometry using the series of Mach-Zender interferometers on each side of the experiment (Franson 1989). While the travel-time difference between the short (early $|E\rangle$) and long (late $|E\rangle$) arms is greater than the coherence time of the photon pair τ_c there is no single-photon interference. Due to the large uncertainty in the creation time, a coincidence stemming from both photons traveling the short arms ($|E_s E_i\rangle$) is indistinguishable from one where both photons traveling the long arms ($|L_s L_i\rangle$), leading to quantum interference (Fig. 3.3(a)). These coincidences can be seen as stemming from a time-bin maximally entangled Bell state

$$|\Phi\rangle = (|E_s E_i\rangle + |L_s L_i\rangle)/\sqrt{2}. \tag{3.13}$$

By varying the time separation between early $|E\rangle$ and $|L\rangle$ paths one can probe the energy-time entanglement of the state (3.12) at different time scale (Thew et al. 2004).
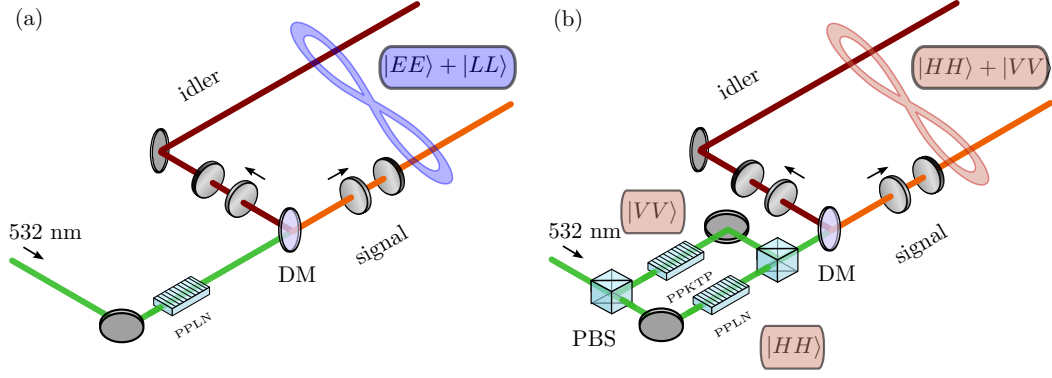
FIGURE 3.2: Generation of entangled photon pairs. (a) Generation if energy-time entanglement between two photons (signal and idler) using monochromatic pump laser at 532 nm. Uncertainty in time creation of the photon pair is given by the coherence time of the pump laser. Considering two temporal modes where photon pair can be created one can approximate the resulting state as $|\Phi\rangle = (|E_s E_i\rangle + |L_s L_i\rangle)/\sqrt{2}$ (Eq. (3.13)). (b) Creation of polarization-entangled photon pairs using two waveguides inside a polarization interferometer. A polarization beam splitter (PBS) coherently divides the pump photons, where each polarization component has a certain probability to be converted into a photon pair with the same polarization. The two polarization components of the photon pair are then recombined into the same spatial mode by a second PBS. By adjusting the phase of the interferometer the state can be written as $|\Phi\rangle = (|H_s H_i\rangle \pm |V_s V_i\rangle)/\sqrt{2}$ (Eq. (3.15)).

The state can be seen as multidimensional entangled state by discretizing the state (3.12) in time using d time bins and can be written as

$$|\Phi_d\rangle = \frac{1}{\sqrt{d}} \sum_{j=1}^{d} \tilde{\alpha}_j |j_s\rangle |j_i\rangle. \tag{3.14}$$

Entangled two-photon time-bin qudits states with the dimension up to 4 were certified and used to violate CGLMP inequality (Ikuta et al. 2016). This state was used to demonstrate multi-dimensional entanglement storage in Chapter 7.

Polarization entanglement

Various schemes have been devised to generate polarization-entangled photon pairs through SPDC. These schemes include selective collection of photon pairs emitted at specific angles for non-collinear type-II phasematching (Kwiat et al. 1995), collinear SPDC in two orthogonally oriented crystals (Kwiat et al. 1999; Trojek et al. 2008), and SPDC in Sagnac interferometers (Kim et al. 2006; Hentschel et al. 2009).

To create polarization entanglement using two different waveguides we follow the ideas of (Kwiat et al. 1994; Kim et al. 2001) that suggest using each of them in different arm of a polarization interferometer (Fig. 3.2(b)).
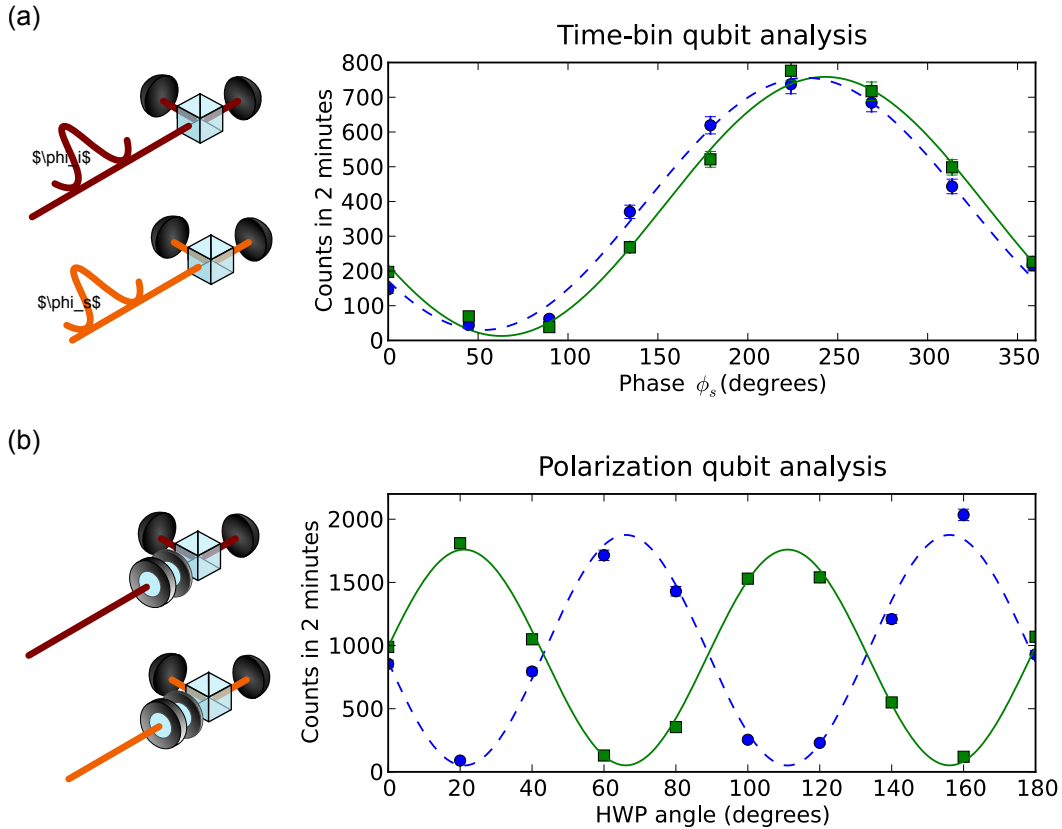
FIGURE 3.3: Visibility curves measured for polarization and energy-time degree of freedom. (a) Rates of the coincidence peak plotted as a function of the sum of the phases of each interferometer. The small phase shift between the curves appears due to a residual phase difference between $|H\rangle$ and $|V\rangle$ components at the output of the interferometer on the signal side. (b) Rates of the coincidence peak as a function of polarization analyzer's half-wave plate (HWP) angle of the signal photon (with the half-wave plate at 45°), for different pairs of detectors at the outputs of the PBSs, as a function of the HWP angle, from which the phase of the polarization Bell state can be extracted from the horizontal offset.

We use type-I phasematching for both waveguides. A polarizing beam splitter at the entrance of the interferometer splits the two coherent state components in two paths. In the horizontal path the photons can be converted into a photon pair $|HH\rangle$ with a probability amplitude α by a first nonlinear waveguide. A second waveguide rotated by $90°$ in the vertical path can produce a photon pair $|VV\rangle$ with probability amplitude β. Another PBS recombines the two paths, and the final single-pair state $|\psi_1\rangle$ is given by $\alpha|H_sH_i\rangle + \beta e^{i\phi}|V_sV_i\rangle$. The phase ϕ depends on the path-length difference of the interferometer (Fig. 3.3(b)).

By choosing the pump polarization such that it compensates the efficiency difference, and by slightly varying the position of one of the mirrors to obtain $e^{i\phi} = \pm 1$, the single-pair state becomes equivalent to one of the two Bell-states

$$\left|\Phi^\pm\right\rangle = (|H_sH_i\rangle \pm |V_sV_i\rangle)/\sqrt{2}. \tag{3.15}$$

3.2 Experimental characterization

The strong filtering was applied for both modes of the SPDC process to reach 200 MHz bandwidth of the photon pair. For this the series of the cavities and volume Bragg gratings were used on each side of the experiment. The cavity with the full-width half-maximum of 240 MHz was used to filter idler photon while for the signal mode 600 MHz filtering was applied. This leads to the strong reduction of the uncertainty in energy of the idler and signal mode comparing with the initial spectrum which reaches 500 GHz.

3.2.1 Correlation functions

To characterize the SPDC process and to reveal nonclassical properties of the emitted light different correlation functions have been measured (Fig. 3.1). The thermal properties of the signal and idler mode were verified using autocorrelation functions $g_{ss}^{(2)}$ and $g_{ii}^{(2)}$ (Fig. 3.1(a,b)). The values bigger than 1.5 were measured for both modes and are limited by jitter of the detectors and contribution from the other spectral modes of the respective filtering cavities.

The cross correlation function $g_{si}^{(2)}$ values up to almost 4000 was measured using coincidence detection between signal and idler mode (Fig. 3.1 (c,e)) and for low pump powers was limited by the detection system noise. This value is much bigger than 2 which together with the autocorrealtion functions demonstrates strong non-classicality of the generated light using Cauchy-Schwarz inequality (Eq. (3.6)).

The single photon character was demonstrated using heralded autocorrelation function $g_{ss|i}^{(2)}$ measurement (Fig. 3.1(d)). The value close to 10^{-3} was measured showing the possibility to generate the state which is close to the single photon using the SPDC process and heralding one of its modes.

3.2.2   Entanglement

To characterize entanglement between two photonic modes one has to probe the two-photon state in different bases on each side of the experiment. In our case we used two different photonic degrees of freedom (polarization and time).

The measurement that verifies the coherent nature for the state entangled in polarization (or energy-time) is illustrated in Figure 3.3. First, the idler photon is measured in the basis $|+\rangle = (|H\rangle + |V\rangle)/\sqrt{2}$ $((|E\rangle + |L\rangle)/\sqrt{2})$ using a half-wave plate and a PBS (or using interferometer and phase controller). If a photon is projected on $|+\rangle$ state, the signal photon is also projected onto the state $|+\rangle = (|H\rangle + |V\rangle)/\sqrt{2}$ (or $(|E\rangle + |L\rangle)/\sqrt{2}$). Measuring it using the states on the equator of the Bloch sphere $(|H\rangle + e^{i\phi}|V\rangle)/\sqrt{2}$ (or $(|E\rangle + e^{i\phi}|L\rangle)/\sqrt{2}$) one should obtain sinusoidal fringes by varying the phase ϕ (Fig. 3.3). In contrast, if the photon pairs are generated in a maximally mixed state one will not see any dependence on ϕ. A fringe visibility larger than 33% is necessary to infer the presence of entanglement in this case (Peres 1996).

In Figure 3.3 we show the results of the described measurement procedure for each degree of freedom. The number of measured coincidences oscillates as a function of ϕ, as expected. A sinusoidal fit reveals an average visibility 96% and 92% for polarization and energy-time entanglement, respectively, which indicates that the source generates photon pairs that are close to maximally entangled in polarization and energy-time.

To unequivocally prove the presence of entanglement we performed a violation of the Clauser–Horne–Shimony–Holt (CHSH) inequality (Clauser et al. 1969) described in Chapter 1. We find a CHSH parameter of 2.716(11) and 2.571(11) for polarization and energy-time degree of freedom, respectively. These values are both above the bound for separable states of $S \leq 2$.

By measuring both degrees of freedom simultaneously and independently one can analyze hyperentangled state consisting of polarization and energy-time entanglement (Eq. (1.13)) (Chapter 6).

3.2.3   Hong-Ou-Mandel interference

The simplest implementation of the Bell-state measurement is based on beamsplitter-interference and therefore lends itself well for photonic implementations (Pan et al. 1998; Knill et al. 2001). Fig. 3.4(a) illustrates the convention used in the description of the beamsplitter: ports a and b as inputs, and c and d as outputs. For single photon input states $|\phi\rangle$ or $|\psi\rangle$ at inputs a or b, the beamsplitter coherently mixes the inputs to yield the following results:

$$|\phi_a\rangle \rightarrow \frac{1}{\sqrt{2}}(|\phi_c\rangle + |\phi_d\rangle), \ \ |\psi_b\rangle \rightarrow \frac{1}{\sqrt{2}}(|\psi_c\rangle - |\psi_d\rangle). \qquad (3.16)$$

Only when two states $|\phi\rangle$ or $|\psi\rangle$ are indistinguishable the destructive interference between the respective pathways from input a and b to the outputs results in bunching behaviour for the photons: both photons will
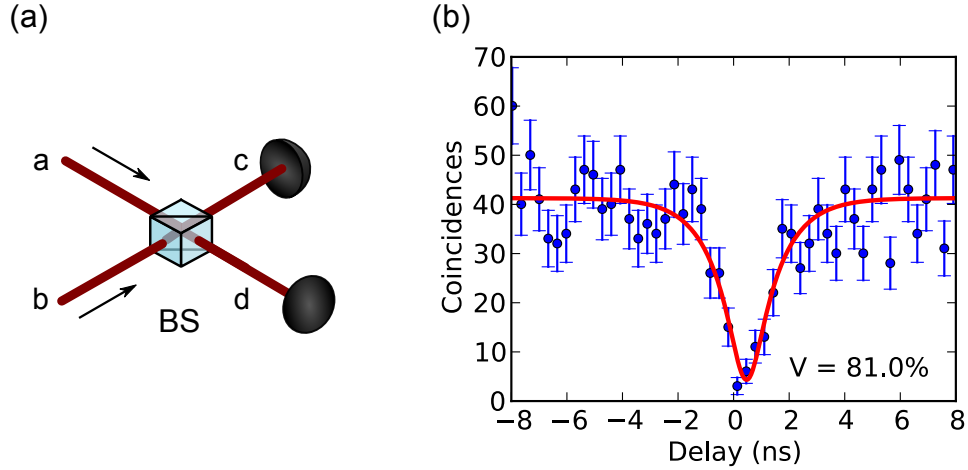
(a)   (b)

FIGURE 3.4: Hong-Ou-Mandel (HOM) interference. (a) The conceptual setup to observe HOM interference between two photonic modes a and b combined o the 50/50 beamsplitter. If two states at the input are indistinguishable than due to the quantum interference only the cases where both states will emerge at the same output (c or d) will be present. (b) HOM dip measured between heralded single photon from SPDC process and continuous weak coherent state. The coincidences as a function of delay between two detectors reveal destructive interference between the states of the single photon and coherent state. The visibility defined as $N_{\mathrm{max}}/N_{\mathrm{min}}$ of 81% was estimated from the fit (solid line).

emerge at the same output (Hong et al. 1987)

$$|\phi_a\rangle |\phi_b\rangle \rightarrow \frac{1}{2}(|\phi_c\rangle |\phi_c\rangle - |\phi_d\rangle |\phi_d\rangle). \tag{3.17}$$

One of requirements to perform perfect quantum teleportation is complete indistinguishability between two states involved into a Bell-state measurement. However, complete indistinguishability is hardly achievable due to the technical limitations.

Instead of using two single photon states Hong-Ou-Mandel interference can be observed between single photon and coherent state. The interference in this case can not be perfect and is limited by the different photon statistics. However, with low enough mean photon numbers of the coherent states the visibilities more than 80% are still achievable (Fig. 3.4(b)). This fact allowed us to perform close to the Bell-state measurements and realize quantum teleportation of the qubit encoded into it's polarization state (Chapter 5).

4   Rare-earth ion-doped crystals

The discovery of rare-earth elements started in 1794 from a black metal mineral called Yttria found in Ytterby in Sweden, which was a mixture of several elements. It took almost 100 years to isolate the first six rare earths (Y, Ce, La, Tb, Er, Yb). The use of the optical flame spectroscopy greatly accelerated their investigation. Only seven years after the first time that this new technique was applied to rare-earth compounds, researchers had discovered another eight rare-earth elements (Sm, Sc, Tm, Ho, Dy, Gd, Pr, Nd).

Unusually narrow spectral lines at visible wavelengths were observed by Vleck 1937 and were attributed to the $4f$ intrashell electronic transitions. This was an indication of a weak interaction between RE elements and their environment. High-resolution spectroscopy was performed only after invention of the dye lasers and finally confirmed this hypothesis (Macfarlane et al. 1987b). The results gave first quantitative description of emitter-emitter and emitter-matrix interactions in rare-earth compounds.

In this chapter, we will start with an outline about electronic level structure of the rare-earth ions doped in crystals. We also describe different sources of spectral broadening and discuss coherent optical properties of some materials which are important for quantum information applications. Spectroscopy of the Nd^{3+}:Y_2SiO_5 crystal which was used as a quantum memory is presented. Optical pumping technique which is required to implement AFC quantum memory protocol (described in Chapter 2) is discussed together with it's limitations.

4.1   Energy structure

As there are many elements in the lanthanide series, different metals give rise to different transition wavelengths ranging from the visible to the infrared. In the context of quantum information processing, experiments focus on the use of europium (Eu), praseodymium (Pr) , thulium (Tm), neodymium (Nd), and erbium (Er) as the dopants for often yttrium orthosilicate (YSiO), yttrium aluminium garnet (YAG) or lithium niobate (LiNbO). These metals have transition wavelengths of 580 nm, 606 nm, 790 nm, 880 nm and 1530 nm, respectively.

All these elements are characterized by $[Xe]4f^j$ electron configuration where j ranges between 0 (La) and 14 (Lu). The sharp spectral lines of

1	2	3	4	5	6	7	8	9	10	11	12	13	14	15	16	17	18
1 **H** 1.0079 Hydrogen																	2 **He** 4.0025 Helium
3 **Li** 6.941 Lithium	4 **Be** 9.0122 Beryllium											5 **B** 10.811 Boron	6 **C** 12.011 Carbon	7 **N** 14.007 Nitrogen	8 **O** 15.999 Oxygen	9 **F** 18.998 Flourine	10 **Ne** 20.180 Neon
11 **Na** 22.990 Sodium	12 **Mg** 24.305 Magnesium											13 **Al** 26.982 Aluminium	14 **Si** 28.086 Silicon	15 **P** 30.974 Phosphorus	16 **S** 32.065 Sulphur	17 **Cl** 35.453 Chlorine	18 **Ar** 39.948 Argon
19 **K** 39.098 Potassium	20 **Ca** 40.078 Calcium	21 **Sc** 44.956 Scandium	22 **Ti** 47.867 Titanium	23 **V** 50.942 Vanadium	24 **Cr** 51.996 Chromium	25 **Mn** 54.938 Manganese	26 **Fe** 55.845 Iron	27 **Co** 58.933 Cobalt	28 **Ni** 58.693 Nickel	29 **Cu** 63.546 Copper	30 **Zn** 65.39 Zinc	31 **Ga** 69.723 Gallium	32 **Ge** 72.64 Germanium	33 **As** 74.922 Arsenic	34 **Se** 78.96 Selenium	35 **Br** 79.904 Bromine	36 **Kr** 83.8 Krypton
37 **Rb** 85.468 Rubidium	38 **Sr** 87.62 Strontium	39 **Y** 88.906 Yttrium	40 **Zr** 91.224 Zirconium	41 **Nb** 92.906 Niobium	42 **Mo** 95.94 Molybdenum	43 **Tc** 96 Technetium	44 **Ru** 101.07 Ruthenium	45 **Rh** 102.91 Rhodium	46 **Pd** 106.42 Palladium	47 **Ag** 107.87 Silver	48 **Cd** 112.41 Cadmium	49 **In** 114.82 Indium	50 **Sn** 118.71 Tin	51 **Sb** 121.76 Antimony	52 **Te** 127.6 Tellurium	53 **I** 126.9 Iodine	54 **Xe** 131.29 Xenon
55 **Cs** 132.91 Caesium	56 **Ba** 137.33 Barium	57-71 **La-Lu** Lanthanide	72 **Hf** 178.49 Hafnium	73 **Ta** 180.95 Tantalum	74 **W** 183.84 Tungsten	75 **Re** 186.21 Rhenium	76 **Os** 190.23 Osmium	77 **Ir** 192.22 Iridium	78 **Pt** 195.08 Platinum	79 **Au** 196.97 Gold	80 **Hg** 200.59 Mercury	81 **Tl** 204.38 Thallium	82 **Pb** 207.2 Lead	83 **Bi** 208.98 Bismuth	84 **Po** 209 Polonium	85 **At** 210 Astatine	86 **Rn** 222 Radon
87 **Fr** 223 Francium	88 **Ra** 226 Radium	89-103 **Ac-Lr** Actinide	104 **Rf** 261 Rutherfordium	105 **Db** 262 Dubnium	106 **Sg** 266 Seaborgium	107 **Bh** 264 Bohrium	108 **Hs** 277 Hassium	109 **Mt** 268 Meitnerium	110 **Ds** 281 Darmstadtium	111 **Rg** 280 Roentgenium	112 **Uub** 285 Ununbium	113 **Uut** 284 Ununtrium	114 **Uuq** 289 Ununquadium	115 **Uup** 288 Ununpentium	116 **Uuh** 293 Ununhexium	117 **Uus** 292 Ununseptium	118 **Uuo** 294 Ununoctium

57 **La** 138.91 Lanthanum	58 **Ce** 140.12 Cerium	59 **Pr** 140.91 Praseodymium	60 **Nd** 144.24 Neodymium	61 **Pm** 145 Promethium	62 **Sm** 150.36 Samarium	63 **Eu** 151.96 Europium	64 **Gd** 157.25 Gadolinium	65 **Tb** 158.93 Terbium	66 **Dy** 162.50 Dysprosium	67 **Ho** 164.93 Holmium	68 **Er** 167.26 Erbium	69 **Tm** 168.93 Thulium	70 **Yb** 173.04 Ytterbium	71 **Lu** 174.97 Lutetium
89 **Ac** 227 Actinium	90 **Th** 232.04 Thorium	91 **Pa** 231.04 Protactinium	92 **U** 238.03 Uranium	93 **Np** 237 Neptunium	94 **Pu** 244 Plutonium	95 **Am** 243 Americium	96 **Cm** 247 Curium	97 **Bk** 247 Berkelium	98 **Cf** 251 Californium	99 **Es** 252 Einsteinium	100 **Fm** 257 Fermium	101 **Md** 258 Mendelevium	102 **No** 259 Nobelium	103 **Lr** 262 Lawrencium

FIGURE 4.1: Periodic table of the chemical elements. The rare-earth elements are highlighted with a background. Lanthanides together with scandium (Sc) and yttrium (Y) are considered as rare earth elements.

these elements originate from the shielding of the $4f$ electrons by higher energy levels and the spatially outer-lying $5s$, $5p$ and $6s$ electronic shells. This means that all the processes taking place within the $4f$ shell are thus weakly disturbed by the immediate environment surrounding Re^{3+}-ion. Respective optical linewidths may approach the lifetime limit even in chemical compounds.

Due to this fact the free-ion Hamiltonian $\hat{H}_{free}$ is more dominant than the crystal field Hamiltonian $\hat{H}_{CF}$. The Hamiltonian $\hat{H}$ of a trivalent rare-earth ion Re^{3+}-ion doped into the crystal can be decomposed into several components:

$$\hat{H} = \hat{H}_{free} + \hat{H}_{CF} + \hat{H}_Z + \hat{H}_{HF} + \hat{H}_Q, \tag{4.1}$$

where smaller contributions are related to electronic Zeeman interactions $\hat{H}_Z$, to hyperfine interaction $\hat{H}_{HF}$ and nuclear electric quadrupole interaction $\hat{H}_Q$. The interaction with crystal phonons usually can eliminated by using cryogenic temperatures for the crystal (< 4K).

Free-ion Hamiltomian $\hat{H}_{free} = \hat{H}_0 + \hat{H}_C + \hat{H}_{SO}$ contains the kinetic and potential energies of all the electrons in the field of the nucleus $\hat{H}_0$, the Coulomb interactions between them $\hat{H}_C$ and their spin-orbit coupling $\hat{H}_{SO}$. In this context, depending on the Re^{3+} ion LS (Russell-Saunders $\hat{H}_C \gg \hat{H}_{SO}$) coupling, jj ($\hat{H}_C \ll \hat{H}_{SO}$) or intermediate regime ($\hat{H}_C \approx \hat{H}_{SO}$) can be used (Sun 2005). From the Russell-Saunders coupling scheme using n (principal quantum number), l (azimuthal quantum number), and J (total angular momentum) quantum numbers for $\hat{H}_{free}$ the free-ion eigenstates can be written as

$$|\Psi_{nIJ}\rangle = \sum_{LSM} a_{LSJ} |nILSJM\rangle . \tag{4.2}$$

There are $2J + 1$ Russell-Saunders eigenstates ($M = -J...+J$) contributing to a new free-ion eigenstate which is thus $2J + 1$-fold degenerate. Coulomb interactions alone cause energy splittings on the order of $\approx$100 THz corresponding to optical transitions, while for spin-orbit interactions the average value is around $\approx$10 THz.

4.1.1 Crystal field

A Re^{3+} ion that is embedded into a crystalline environment experiences electrostatic perturbations which will lift the spherical symmetry of the free-ion potential and, as a consequence, also the $2J + 1$ fold degeneracy of the $\hat{H}_{free}$ eigenstates. It is relatively easy to predict the degree to which this degeneracy is lifted since this depends exclusively on the point symmetry of the crystal site where the Re^{3+} resides. It is difficult, however, to obtain actual values for the respective crystal-field splittings because there are a number of interactions influencing the electronic states are difficult to account for in ab initio calculations (Liu 2005).

It is not clear from the very beginning how to correctly model the crystal-field interactions mathematically. However, since the crystal-field interaction may be approximated as point charge perturbations, one may define a
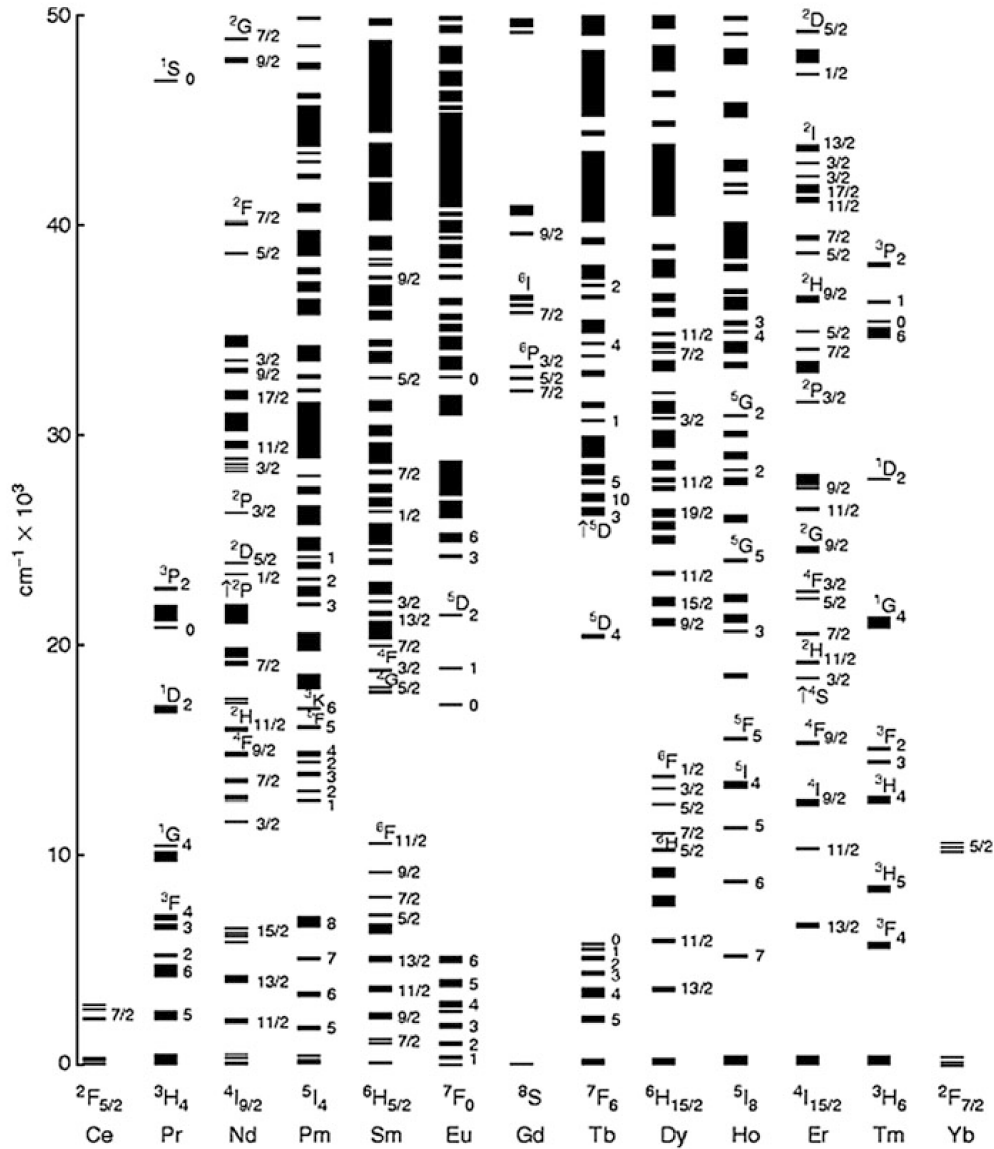
FIGURE 4.2: Dieke diagram (Dieke et al. 1968) showing the energy levels of the trivalent rare earth Re^{3+} ions arising from their $4f^n$ electron configurations (taken from Withnall et al. 2014)
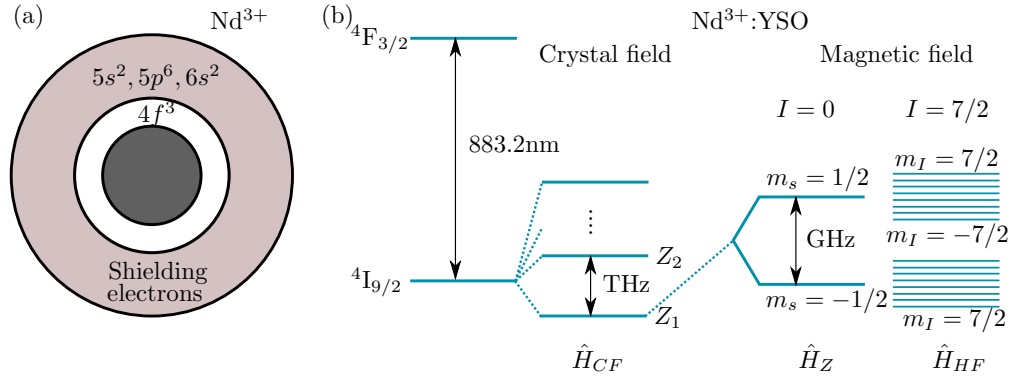
FIGURE 4.3: Rare-earth ion doped crystals. (a) Electronic structure of a tripositive Nd^{3+} rare earth ion: the 4f shell is shielded by the closed $5s$, $5p$ and $6s$ shells. (b) Level structure of Nd^{3+} doped into Y_2SiO_5 and under magnetic field.

very general interaction Hamiltonian (Reid 2013)

$$\hat{H}_{CF} = \sum_{kq} B_q^k C_q^{(k)}, \tag{4.3}$$

where the B_q^k parameters define the one-electron crystal-field interaction and the $C_q^{(k)}$ are spherical tensor operators for the $4f$ configuration.

In general, such a Hamiltonian mixes states of different J and M so that a crystal-field eigenfunction can be decomposed as $\sum_{JM} a_{JM} |\Psi_{nIJ}\rangle$. Neither J nor M constitute good quantum numbers for a crystal-field level. However, as long as the energy separation of the multiplets is much greater than the resulting crystal-field splitting, J mixing usually remains negligible (Liu 2005).

So far, the most reliable results for crystal-field parameters have been obtained by fitting them to experimentally observed spectra using a large number of observed transitions from near-infrared, optical to the UV domain (Liu 2005). Crystal-field interactions commonly amount to splittings on the order of ≈ 1 THz. See Fig. 4.3(b) for a comprehensive illustration of the energy splittings.

4.1.2 Zeeman interaction

Depending on the number of $4f$ electrons, even or odd, the rare earth ions form what are referred to as the non-Kramers or Kramers ions, respectively (Kramers 1930). For Kramers ions (neodymium (Nd), erbium (Er), ytterbium (Yb)), due to the unpaired electron, the state levels form a Kramers doublet with a magnetic moment of the order of the Bohr magneton. For non-Kramers ions, with even numbers of electrons, the levels are electronic singlets and the angular momentum is said to be "quenched" by the crystal field, having zero angular momentum (praseodymium (Pr), europium (Eu), thulium (Tm)). An important exception to this is if the ions are located at sites with axial or higher symmetry, in which case non-Kramers doublets

can occur, due to the non-zero angular momentum around the symmetry axis. These types of ions experience large first order Zeeman and hyperfine interactions with short dephasing times.

The interaction of the electronic spin with external magnetic filed lifts the degeneracy in magnetic quantum number m_s. The Hamiltonian for general case can be written as

$$\hat{H}_Z = \mu_B \vec{B} \cdot \tilde{g} \cdot \hat{S}, \tag{4.4}$$

where $\tilde{g}$-tensor characterizes the interaction strength with external magnetic field $\vec{B}$ applied in certain direction, $\hat{S}$ represents the electronic spin of the ion.

Due to the unquenched electronic spin for Kramers ions this term is significantly bigger. The sensitivity to the external magnetic field in this case can reach $\approx$100 GHz/T for Er^{3+} ion doped materials. Whereas for non-Kramers ions it is of the order of nuclear magneton and 1000 times smaller.

Optical and electronic spin transitions of Kramers ions are therefore much more sensitive to magnetic field fluctuations of the environment (Sun 2005). Large magnetic moment also increases the interaction between dopant ions, which is usually decreased by lower doping concentration.

4.1.3 Hyperfine splitting

Just as in atoms, the total spin J of the $4f$ electrons may interact with the Re^{3+} nuclear spin I by magnetic field coupling. This will give rise to magnetic hyperfine splittings, which can be described by the effective spin Hamiltonian in the case of the axial symmetry of the crystal site

$$\hat{H}_{HF} = A_{\parallel} \hat{J}_z \hat{I}_z + A_{\perp}(\hat{J}_x \hat{I}_x + \hat{J}_y \hat{I}_y), \tag{4.5}$$

where $\hat{J}_{x,y,z}$ and $\hat{I}_{x,y,z}$ are the electronic and nuclear spin operators in the respective crystal directions, and $A_{\parallel}$ and $A_{\perp}$ give the interaction coefficient along and perpendicular to the z direction, respectively. Usually, $A_{\parallel}$ and $A_{\perp}$ are specified in a reference frame where z coincides with the crystal axis denoted by c. The typical values for hyperfine splittings for the Kramers ions vary between 100 MHz and 1 GHz.

At crystal sites with a low symmetry, the diagonal elements of $\hat{H}_{HF}$ vanish for non-Kramers ions, i. e. there is no first-order magnetic hyperfine interaction. In this case, the contributions to hyperfine splitting are solely due to off-diagonal matrices between different multiplets J and J'. The leading component is of second order and can be described by a Hamiltonian that takes the same form as the Hamiltonian for electric quadrupolar interactions.

4.2 Optical properties

The intra-shell optical electric-dipole transitions of $4f$ electrons of Re^{3+} free ions are forbidden, since they can only connect states with opposite parities. However, the parity $(-1)^L$ ($L = \sum_i l_i$ is the total angular momentum
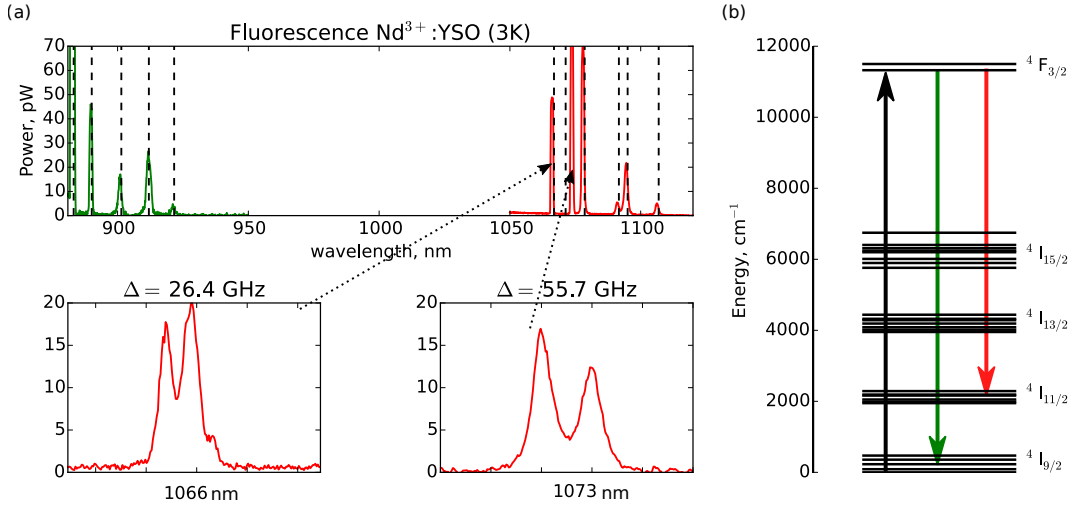
FIGURE 4.4: Fluorescence measurement. (a) Fluorescence spectra of the cryogenically cooled Nd^{3+}:Y_2SiO_5 crystal pumped with 883.2 nm wavelength at $^4I_{9/2} \rightarrow ^4F_{3/2}$. (b) Energy structure of Nd^{3+} ions doped in Y_2SiO_5 crystal.

of electronic system) is the same for all states within the $4f$ manifold. The crystal-field Hamiltonian (Eq. (4.3)) may mix states of opposite parity into the crystal-field levels and thus enable electric dipole transitions between them. The crystal-field components connecting the initial $|i\rangle$ and final states $|f\rangle$ can be written as

$$B_q^k = A_{kq} \langle f | r^k | i \rangle, \tag{4.6}$$

where A_{kq} are the structural coefficients parametrizing the crystal field and r^k is the radial part of spherical tensor operator. Due to the symmetry reasons B_q^k with odd k will enable electric dipole transitions within the $4f$ manifold. They are generated by a non-centrosymmetric crystal field around the Re^{3+}. For this reasons most of the selection rules do not hold and can be violated.

The relatively low intensities of the transitions within the $4f$ manifold correspond to small oscillator strengths of the optical transitions. Typical oscillator strengths are on the order of 10^{-7}. The rare-earth ion with the highest oscillator strength is Nd^{3+} doped in YVO_4 host media with value of 10^{-6}. This makes the single-ion detection extremely hard task (Petersen 2011; Kolesov et al. 2012) comparing with detection of the single dye molecules where oscillator strength can reach unity.

The typical values of radiative lifetimes T_1 vary from 100 µs to 10 ms. Such long T_1 lifetime means that to reach high optical depth one needs to use high density of ions which is possible in solid-state materials. The respective peak absorption cross-sections may thus still be largely comparable. This also means that the optical coherence lifetimes T_2 can reach impressive values which are four to five orders of magnitude larger compared to organic molecules.

4.2.1 Inhomogeneous broadening

Re^{3+} ions that are embedded in a crystalline host matrix experience individual shifts of their transition frequencies. These shifts are usually explained by the fact that the crystalline lattice has strain and exhibits defects, something that is ultimately dictated by thermodynamics. Therefore, each ion finds itself in a different local environment and experiences different local electric and magnetic fields, which will accordingly shift its transition frequency. The resulting distribution of frequencies gives rise to an inhomogeneously broadened line, where the term inhomogeneous suggests that the broadening is due to shifts that are not equal for all the Re^{3+}.

In many cases one can relate the inhomogeneous linewidth to the ionic size of the lattice ion which is replaced and the ionic size of the Re^{3+} ions. For example, for YSO crystal Y^{3+} ion is replaced by dopant. Eu^{3+} and Er^{3+} dopants have similar sizes as Y^{3+}, and good Er/Eu^{3+}:YSO crystals have sub-GHz inhomogeneous linewidths, with a strong dependence on the concentration. For Pr^{3+} and Nd^{3+} dopants, which have similar but larger ionic sizes, the inhomogeneous linewidths are much larger 5-10 GHz, and are not very concentration dependent (Liu 2005).

The biggest value for inhomogeneous linewidth reaches few THz (Thiel et al. 2011), where it is attributed to the natural defects of the media. The lower end of this scale is marked by Nd^{3+}:YLiF$_4$ which has been shown to broaden by 10 MHz at very low doping levels (Macfarlane et al. 1998).

The work toward growing rare-earth stoichiometric crystals with reduced inhomogeneous broadening is ongoing and have great potential for implementing quantum information protocols in these materials (Ahlefeldt et al. 2016).

4.2.2 Homogeneous broadening

Dynamical processes taking place on the microscopic level of the embedded Re^{3+} emitters will give rise to homogeneous broadening. Homogeneous in this context refers to the fact that the transition line of every single emitter underlies the same broadening effects.

In order to make clear how different effects contribute to the homogeneous linewidth Γ_h, we introduce its decomposition as

$$\Gamma_h = \frac{1}{2\pi T_1} + \frac{1}{2\pi T_1^*} + \Gamma_{deph} = \frac{1}{\pi T_2} \tag{4.7}$$

where T_1 denotes the population decay time associated with the undisturbed radiative transition, T_1^* characterizes nonradiative decay channels, and γ_{deph} is the relaxation rate arising from pure dephasing processes. An undisturbed system with $T_2 = 2T_1$ is called lifetime-limited. Alternatively, the homogeneous linewidth may be associated with an overall dephasing time T_2 that incorporates both population decay and pure dephasing processes.
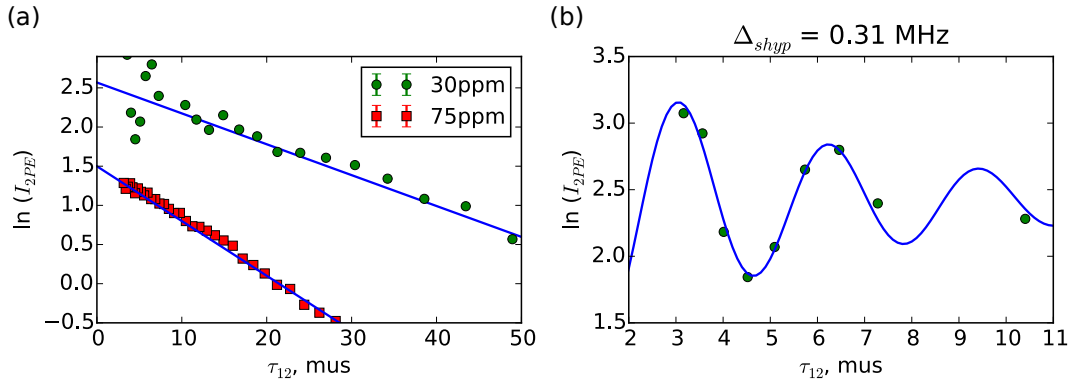
(a)

(b)

FIGURE 4.5: Homogeneous linewidth. (a) Homogeneous linewidth measured using two-pulse photon echo (2PPE) in Nd^{3+}:Y_2SiO_5 crystals with different concentrations (30 and 75 ppm) at magnetic field of 300 mT. The coherence lifetimes T_2=57μs for 75 ppm and T_2=102μs for 30 ppm crystal were measured. (b) The modulation of the 2PPE signal caused by the superhyperfine splitting due to Y atoms corresponding to the 2.1 MHz/T. Magnetic field of 150 mT was used for this measurement.

4.2.3   Homogeneous linewidth limitations

Lifetime-limited homogeneous linewidth is rarely observed due to the contribution to the dephasing processes from the environment. The optical transition of Re^{3+} can be modulated by the environment causing spectral diffusion. It has different sources including ion-phonon, ion-ion, ion-nuclear and spin interactions. The contributions strongly depend on the environment and Re^{3+} ion type (Sun et al. 2002; Thiel et al. 2011). Ion-phonon interactions usually can be neglected at cryogenic temperatures < 4 K (Abragam et al. 1970).

- **Ion-ion interactions**. Mutual electronic spin-flip interactions between the Re^{3+} emitters will instantaneously shift their optical transition frequencies, the average of which results in a broadening of the observed line. As one would expect, this effect is more severe for Kramers ions, which all carry a a large electronic magnetic moment. Although it is possible to suppress these spin flips in strong magnetic fields of several teslas, lifetime-limited linewidths are much more easily observed in non-Kramers ions (that do not carry any electronic magnetic moment).

- **Ion-nuclear spin interactions**. The Re^{3+} electronic spin of Kramers ions may moreover interact with nuclear spins of the surrounding crystal ligands to give rise to instantaneous frequency shifts caused by nuclear spin flips. Nearest neighbour interactions cause shifts on the order of 100 kHz, comparable to the contribution of electron spin-spin interactions. In analogy to the case of electronic spin-spin interactions, the broadening due to interactions with surrounding nuclear spins is more important for Kramers ions.

- **Superhyperfine interaction.** A process that will also affect the linewidth of non-Kramers ions is mutual nuclear spin flips of the Re^{3+} optical center and nearest-neighbours. This is even true for optical centers with vanishing nuclear magnetic moments since their quadrupole moments can still couple to surrounding nuclei. For non-Kramers ions, these effects usually impose a lower limit to the homogeneous linewidth since they cannot be easily suppressed (except at ultra-low temperatures and very strong magnetic fields) (Fig. 4.5(b)).

- **Spectral diffusion.** Both interactions with electronic and nuclear spins may, however, shift the transition frequencies of surrounding nuclei also on longer timescales. Most commonly, spectral diffusion will cause a narrow spectral feature to broaden over time.

- **Instantaneous spectral diffusion.** At higher excitation intensities, so-called excitation-induced frequency shifts or instantaneous spectral diffusion may contribute significantly to homogeneous broadening. In this case, the difference in the permanent electronic dipole moments of the ground and excited states of an ion causes a shift in the transition frequency of its neighbours.

In order to suppress all these contributions and decrease homogeneous line broadening usually the best choice is: non-Kramers ions, low dopant concentrations and low nuclear spin hosts. Each will reduce the possible dynamics which cause dephasing.

However, the coherence time for Kramers-ions can be also maximized along a preferred magnetic field orientation that minimize the effects of ion-ion, ion-nuclear interactions, and spectral diffusion. The narrowest homogeneous linewidth measured in the solid-state is 73 Hz and has been demonstrated in Er^{3+}:Y_2SiO_5 (Böttger et al. 2009). For non-Kramers ions the best homogeneous linewidth was observed for Eu^{3+} ions inserted into YSO crystal of 122 Hz for the $^7F \longleftrightarrow {}^5D$ transition (Equall et al. 1994).

For certain Re^{3+} hyperfine transitions, it is possible to entirely cancel the susceptibility to local field changes if the differential first-order Zeeman shifts of both the upper and lower hyperfine levels vanish (Fraval et al. 2004). This technique together with the dynamical decoupling on the nuclear transition was used to demonstrate six-hour coherence time of the optically addressable nuclear spins in $^{151}Eu^{3+}$:Y_2SiO_5 (Zhong et al. 2015a).

4.3   Optical pumping

An inhomogeneous absorption profile can be shaped via a process called spectral hole burning technique (Macfarlane et al. 1987b). In rare-earth ion-doped crystals, the large ratio of the hyperfine state lifetime to the optical state lifetime for non-Kramers ions (10^6 or more) and non-zero matrix elements of most optical transitions allow the optical pumping with narrowband laser fields. In particular, a laser applied somewhere in the inhomogeneous profile will pump ions out of states resonant at the laser frequency

into ground states that are not resonant (Fig. 2.2). This opens up a transparent spectral region, or hole, that persists for the ground state lifetime of the system. In general, the absorption spectrum in the region around the hole burning laser frequency will exhibit a set of side holes and anti-holes, regions of lower and higher absorption respectively, whose positions and depths depend on the hyperfine splittings and transition matrix elements of the particular system.

The absorption profile can be shaped arbitrarily via spectral hole-burning by appropriately modulating the frequency and amplitude of the hole-burning laser field (with limits on maximum and minimum hole width set by the hyperfine splitting).

The population trapping for Kramers ions is possible using the two Zeeman levels of the ground state and was first observed in Nd^{3+}:LaF_3 (Macfarlane et al. 1987a). In order to maximize the efficiency of the optical pumping the orientation of the crystal and magnetic field amplitude has to be tuned to maximize the lifetime of the spectral hole (Hastings-Simon et al. 2008a; Hastings-Simon et al. 2008b). In general this lifetime depends strongly on the spin-lattice relaxation and/or spin cross relaxation (flip-flop) processes. Due to the second contribution, the optimization strongly depends on the type and the concentration of the rare-earth ions (Lauritzen et al. 2008; Afzelius et al. 2010a). Spectral hole lifetimes up to few hundreds millisecond were observed for Zeeman level trapping.

The optical pumping on hyperfine levels of Kramers-ions is intensively studied in different material including isotopes of neodymium (^{143}Nd, ^{145}Nd), erbium (^{167}Er), and ytterbium (^{171}Yb,^{173}Yb). Long hyperfine lifetimes can be observed up to few seconds. This opens some new possibilities to realize different quantum memory protocols. In the beginning of this thesis this was unknown, which is why all optical pumping was done using the two Zeeman levels of naturally doped yttrium orthosilicate Nd^{3+}:Y_2SiO_5 crystal.

4.4 Neodymium-doped yttrium orthosilicate

In this section we will give some basic properties of the specific Nd^{3+}:Y_2SiO_5 samples that were used for all quantum memory experiments presented in this thesis.

Y_2SiO_5 crystallizes in a monoclinic cell of C_{2h}^6 symmetry. Its lattice constants are $a = 1.041$ nm, $b = 0.6726$ nm, $c = 1.249$ nm, where the a and c directions enclose an angle of $\beta = 102.65°$. Monoclinic crystals are birefringent in general. Thus, the principal axes of the optical indicatrix do not coincide with the a, b and c crystal axes. However, the b crystal axis is also a principal axis for symmetry reasons. The other two principal axes are commonly labelled D_1 and D_2 and thus lies in the $a - c$ plane (Li et al. 1992).

A rare-earth dopant Nd^{3+} in Y_2SiO_5 substitutes one of the two yttrium ions Y^{3+}, where each occupy a crystal site with distinct C_1 symmetry. The occupation distribution between two symmetry sites in general depends on the rare earth element. Different crystal fields for each site allows one to optically distinguish between them, the optical transition usually differs more

than 1 nm. For each site two magnetically inequivalent classes are distinct by C_2 symmetry around b axis. In $D_1 - D_2$ plane or along b axis the two classes are magnetically equivalent.

To implement two-level atomic frequency comb quantum memory protocol we used yttrium orthosilicate (Y_2SiO_5) crystal up to 1 cm length. The Nd^{3+} ions were doped in the crystal with concentrations up to 75 ppm. Trivalent neodymium Nd^{3+} has 3 electrons in its $4f$ shell, the corresponding terms are depicted on the energy level diagram (Fig. 4.3). The relevant transition, shown in Fig. 4.3, connects the $^4I_{9/2}$ ground state to the $^4F_{3/2}$ excited state at a wavelength of 883.2 nm. The crystal is mounted between two permanent magnets which create a magnetic field up to 400 mT at an angle of $30°$ to the crystal D_2-axis. This configuration was shown to be optimal to increase the lifetime of the spectral holes and improve optical pumping in this crystal between two Zeeman states of the ground level (Zambrini et al. 2016).

All previous storage experiments (Clausen et al. 2010; Usmani et al. 2012; Clausen et al. 2012) were performed using 30 ppm concentration crystals. The lifetimes up to 160 ms were measured for this concentration (Fig. 4.6) which enabled to realize optical pumping between two Zeeman states. To make system more compact and to reduce the size of the system the crystals with higher 75 ppm concentration have been grown in Paris group of Prof. P. Goldner using Czochralski method. These samples were used to perform all the experiments presented in this thesis. The study of the relaxation dynamics of the ground state showed that the higher concentration leads to the reduced lifetime of the Zeeman state (Fig. 4.6(b)) which is possibly caused by the increased ion-ion interactions. The maximum achieved lifetime (60 ms) in this case is lower and inversely proportional to the concentration. Thus, the gain due to higher absorption coefficient is negated by less efficient optical pumping that can be achieved for higher concentration. This problem can be potentially solved using cavity approach (Afzelius et al. 2010b) to reach high optical depth.

The maximum lifetime was measured in the presence of the magnetic field which leads to a splitting of the ground and excited states of approximately 14 GHz and 2.5 GHz for 400 mT, respectively. The crystal is placed in a cryo-cooler and cooled down to 2.7 K to suppress the spin lattice relaxation due to the phonons (Fig. 4.6). The ground state splitting is bigger than the inhomogeneous broadening (6 GHz for this crystal) which allows one to distinguish between two ground Zeeman levels (Fig. 4.3). The excited state lifetime is 300 µs and is much lower than the spectral hole lifetime which enables us to perform optical pumping between two Zeeman states. The homogeneous linewidth of up to 3 kHz was measured using two pulse photon echo technique (Fig. 4.5).

4.5   AFC preparation

The comb structure in the absorption profile is created by frequency-selective optical pumping of the population out of one of the Zeeman ground
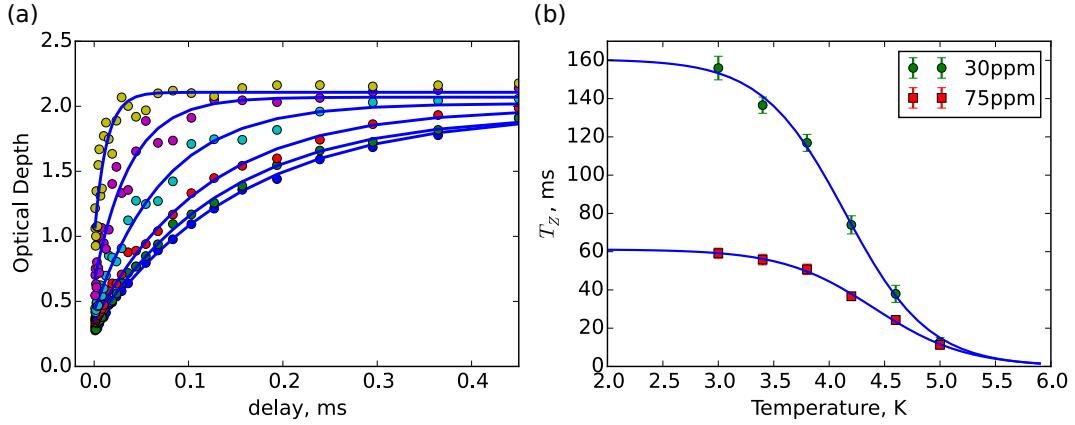
FIGURE 4.6: Spectral hole lifetime. (a) The decay of the spectrally burned hole in $Nd^{3+}:Y_2SiO_5$ crystal with 30 ppm doping concentration measured at different temperatures. The lowest temperature 3 K gives the slowest relaxation time which decreases when the temperature goes up to 5 K with 0.4 K step for each curve. (b) Higher temperature causes bigger contribution to the decay from the Raman spin-lattice relaxation (Kurkin et al. 1980) at the ground state which scales as T^7. For the low temperatures lower doping concentration gives bigger lifetimes due to the lower contribution to the relaxation from the flip-flop process between dopant ions.

states. In our case this is done by working directly in the frequency domain. However, time-domain techniques can be used as well (Usmani et al. 2010).

The preparation of the atomic frequency comb was done using a diode laser in resonance with the $|g\rangle \longleftrightarrow |e\rangle$ transition which is linearly swept over a frequency range up to 120 MHz using an acousto-optical modulator (AOM) in double-pass configuration. During the sweep the intensity was modulated to create absorption and transmission peaks. By repeating this many times during the time which is much longer than the lifetime of the excited state, the population can accumulated in the other Zeeman ground state $|aux\rangle$, creating comb structure on $|g\rangle \longleftrightarrow |e\rangle$ transition (Fig. 2.2). The arbitrary comb shape can be obtained by varying the parameters of the sweep and the number of repetitions.

The bandwidth of the AFC is extended using the phase modulator by applying the modulation signal with frequency 120 MHz. This leads to the creation of the sidebands with the period of 120 MHz, where each sideband is still scanned by the AOM. We were able to achieve the bandwidth of the AFC up to 600 MHz. It is limited by the intensity variation of the sidebands which reduces the efficiency of the optical pumping. The maximum bandwidth of the quantum memory for this configuration is limited by the excited state Zeeman splitting which reaches 2.5 GHz for 400 mT magnetic field.

5 Solid-state quantum light-matter interface

This chapter is partly based on the results published in

F. Bussières, C. Clausen, A. Tiranov, B. Korzh, V. B. Verma, S. W. Nam, F. Marsili, A. Ferrier, P. Goldner, H. Herrmann, C. Silberhorn, W. Sohler, M. Afzelius & N. Gisin, **"Quantum teleportation from a telecom-wavelength photon to a solid-state quantum memory"** Nature Photonics 8, 775-778 (2014) (pages 127-143)

In this chapter we first characterize the quantum storage of the single photons by combining the entangled photon pair source and quantum memory introduced in previous chapters. After, we discuss our experiment demonstrating the quantum teleportation of the polarization qubit into the solid-state quantum memory over 25 km of fibre.

5.1 Quantum storage

To test our light-matter quantum interface we first performed quantum storage experiments using the SPDC source (Chapter 3) producing single photons which are compatible with the quantum memory implemented in the Nd^{3+}:Y_2SiO_5 crystal (Chapter 4). For this, atomic frequency comb (AFC) is prepared using optical pumping techniques between Zeeman states as described in the previous chapter.

Storage delays up to 400 μs was performed using our method which requires the use of 2.5 MHz AFC period Δ (Fig. 5.1)(a). The efficiency decreases rather rapidly for long storage times, as it quickly becomes difficult to prepare an optimal AFC structure with small period Δ (Fig. 5.1(a)). The preparation in this case starts to be limited by the super-hyperfine interaction between the electronic spin of the neodymium ions with the nuclear spin of the nearby yttrium ions (Fig. 4.5). At magnetic fields up to 400 mT this sets a lower limit of 1 MHz to 2 MHz on the resolution of the spectral hole burning (Staudt et al. 2006).

To extend storage times lower magnetic field have to be used to be able to burn a narrower hole structure. However, due to the fast relaxation in the ground state at low magnetic fields the optical pumping efficiency is strongly reduced. The reason for this can be attributed to flip-flop interaction between Nd^{3+} ions which can be suppressed by lower doping concentrations (Zambrini et al. 2016). One order of magnitude longer Zeeman lifetime can be achieved at extremely low concentrations, but then the decreased absorption will reduce the storage efficiency. One would need to implement cavity-enhanced quantum memory to overcome this problem (Afzelius et al. 2010b).
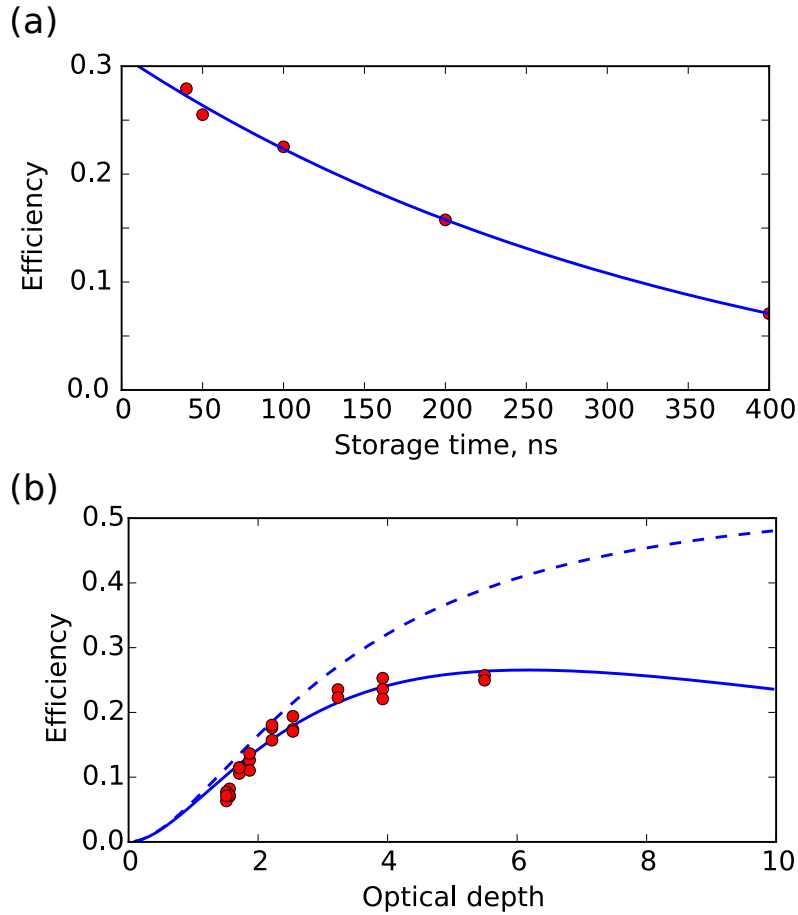
FIGURE 5.1: Efficiency of the memory based on AFC. (a) Efficiency measured as a function of storage time. The reduction is attributed to the lower resolution of the AFC structure which is caused by the superhyperfine interaction and preparation method. (b) Efficiency as a function of the optical depth (points). Imperfect optical pumping leads to the background absorption which reduces maximum efficiency (solid curve) comparing with the perfect optical pumping (dashed curve) (Eq. (2.5))
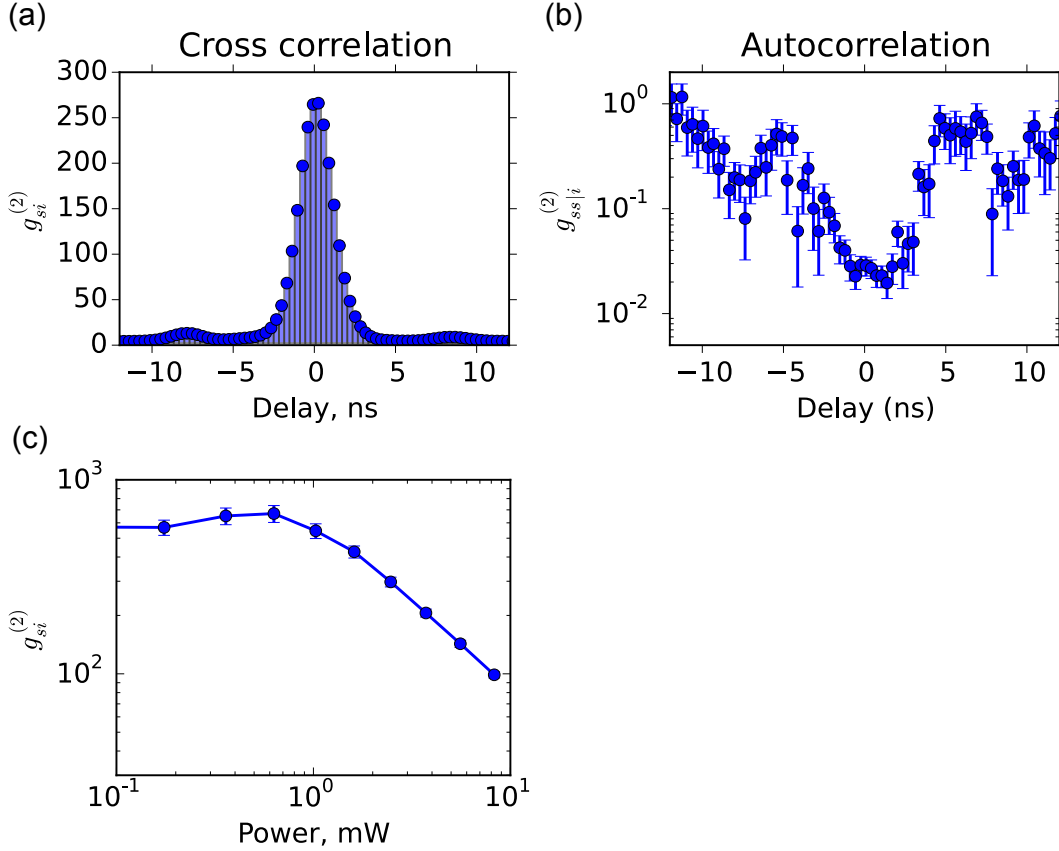
FIGURE 5.2: Second order correlation functions of the stored signal mode from the SPDC source. (a) Cross-correlation function $g_{si}^{(2)}$ between idler photon and signal photon reemitted from the quantum memory. (b) Auto-correlation function of the heralded single photon in the signal mode $g_{ss|i}^{(2)}$ stored in the quantum memory. (c) Cross-correlation $g_{si}^{(2)}$ measured as a function of the pump power. For the lowest pump power values the cross correlation is limited by the noise of the detection system.

Using classical light the efficiency of up to 25% was measured for short storage times which is limited by the quality of the optical pumping (Fig. 5.1(a)). This imperfection leads to the residual background absorption which doesn't contribute to the reemission. For this reason, optical depth of the absorption peaks has to be optimized in order to maximize the efficiency of the quantum memory (Fig. 5.1(b)).

The period of the AFC of 20 MHz prepared over 600 MHz bandwidth corresponding to the predetermined storage time of 50 ns was used for most of the experiments described in this thesis. The maximum efficiency for heralded single photons of 15% was obtained. The decrease is attributed to the preparation imperfections of the broadband AFC (as described in previous chapter) compared to classical storage.

To prove the single photon character of the reemission after the storage second order correlation functions were measured (Fig. 5.2). Ideally their values should be the same as for the input single photon state that was characterized previously (Fig. 3.1). In this case the fidelity of the quantum storage process can reach unity. However, due to the use of continuous wave pumping of the SPDC source the cross-correlation function $g^{(2)}$ is limited by the ratio between transmission probability of the quantum memory η_{trans} and total efficiency of the memory η (Fig. 5.1) such that (Usmani et al. 2012)

$$g_{si}^{(2)} = 1 + \frac{1}{p(1 + \eta_{trans}/\eta)}. \tag{5.1}$$

This means that if the absorption of the quantum memory is not perfect the transmitted part from the SPDC source emitted in the temporal mode of the reemission will reduce the cross-correlation $g_{si}^{(2)}$ value. Same arguments are applied for the autocorrelation function of the heralded and stored single photon $g_{ss|i}^{(2)}$ such that

$$g_{ss|i}^{(2)} \approx 4p(1 + \eta_{trans}/\eta), \text{(for } p \ll 1). \tag{5.2}$$

These values can be improved by increasing the absorption probability $(1 - \eta_{trans})$ of the quantum memory by use of higher optical depth. Another way is to turn off the pump laser each time the reemission from the quantum memory is expected (Bussières et al. 2014). For the predetermined storage time (for all the experiments in this thesis it was the case) the simple modulation of the pump power with the duty cycle less than 50% should eliminate this problem. For this an acousto-optic modulator (AOM) was used to modulate the pump power at the input of the SPDC source. However, due to the finite extinction ratio of the AOM and slightly multimode character of the SPDC source (Chapter 3) the effect of the memory was still observed (Fig. 5.2) as a reduction of the cross correlation and an increase of the autocorrelation function.

However, we argue that this reduction is due to the way we used the photon pair source but not the limitation of the storage process of the quantum memory itself. This could be verified by measuring the fidelity between

input and output quantum states of a single photon.

5.2 Quantum teleportation to a solid-state quantum memory

To demonstrate the capability of our approach for future long-distance quantum communication we performed quantum teleportation of a polarization qubit into a solid-state quantum memory. The qubit was encoded using weak coherent state at telecommunication wavelength and was distributed over 25 km of standard optical fibre.

5.2.1 Polarization preserving quantum memory

In order to able to store store polarization entangled single photon (Eq. (3.15)) and to perform quantum teleportation using our Nd^{3+}:Y_2SiO_5 crystal one has to compensate for the anisotropic absorption of the crystal along its principal axes D_1 and D_2. For this the configuration of two crystals with the half-waveplate between them was used. It has been shown that this configuration is compatible with storage of the heralded polarization qubits with the fidelities up to 99% (Clausen et al. 2012; Zhou et al. 2012b). We note that polarization based interferometer can also be used for this purpose (Gündoğan et al. 2012).

The two crystals are placed around a 2 mm-thick half wave plate and the whole arrangement is 14 mm-long. Two permanent 15 mm-long magnets placed above and below the crystals create a magnetic field up to 400 mT which splits the ground state in two Zeeman levels separated by $\approx$14 GHz. All surfaces, including the windows of the cryostat, are coated with anti-reflective coatings such that the transmission outside of the 6 GHz-wide absorption spectra is higher than 95%, which greatly reduces the parasitic optical loss compared to previous experiments within the group (Clausen et al. 2012).

5.2.2 Experiment

To perform quantum teleportation a pair of polarization-entangled photons was used and one photon from the pair is stored in a nearby rare-earth-ion doped crystal. The other telecom-wavelength entangled photon is sent to a Bell-state analyzer where it is jointly measured with a photon that is carrying the polarization qubit state to be teleported. The state of the photon retrieved from the quantum memory is analyzed with quantum state tomography, and the fidelity of several teleported states are measured to outperform the classical benchmark.

The entangled photons are generated yielding a state that is very close to maximally entangled state $\frac{1}{\sqrt{2}}(|HH\rangle + e^{i\varphi}|VV\rangle)$. The spectra of the photon pairs are filtered to 200 MHz, with a corresponding coherence time of 2 ns (Chapter 3). The large spectral width of the photons considerably increases the intrinsic repetition rate of our experiment over previous experiments
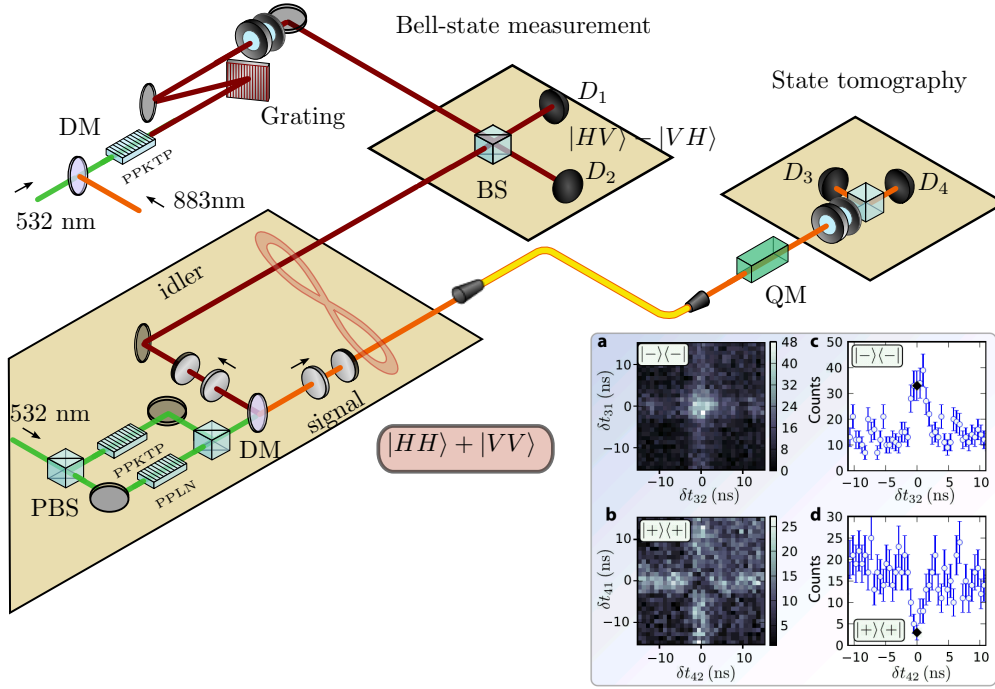
FIGURE 5.3: Quantum teleportation into a solid-state quantum memory. The signal photon is sent to a neodymium-based polarization-preserving quantum memory that was previously prepared as an atomic frequency comb using 883 nm light. The weak coherent state (WCS) at 1338 nm is created by means of difference-frequency generation from 532 and 883 nm light. The WCS is then selected using a grating. The input state to be teleported is prepared using wave plates and sent towards a 50/50 beamsplitter where it is mixed with the idler photon to perform the Bell-state measurement (BSM). The output modes of the beamsplitter are polarization-filtered and sent towards two high-efficiency detectors. A coincidence detection at D_1 and D_2 heralds a successful BSM. The signal photon retrieved from the quantum memory is sent to a polarization-state analyser where it is detected on D_3 or D_4. The idler and WCS photons are each transmitted either over a short distance or over 12.4 km of single-mode optical fibre. **Inset**: Results of the teleportation of input state $|-\rangle$. **a,** Two-dimensional histogram showing the number of threefold coincidences between detectors D_1, D_2 and D_3 as a function of delays δ_{31} and δ_{32} between detections at D_3 and D_1 and D_2. **b,** As in a, with D_4 instead of D_3. Each histogram indicates onto which polarization state the retrieved photon was projected ($|-\rangle\langle-|$ for a and $|+\rangle\langle+|$ for **b**). Each pixel corresponds to a square time window with sides of 486 ps. **c,d,** Horizontal slices of **a** and **b** (centered on $\delta_{31} = 0$ and $\delta_{41} = 0$, respectively), showing the peak and dip, respectively, in number of detections at the center.

with the same type of quantum memory (Clausen et al. 2010; Usmani et al. 2012). Following the creation of a pair, the signal photon is directly sent to a quantum memory consisting of two inline neodymium-doped yttrium orthosillicate crystals Nd^{3+}:Y_2SiO_5 described previously.

The qubit state to teleport is encoded in the polarization of a photon from a weak coherent state (WCS) at 1338 nm that is created through difference-frequency generation in a separate nonlinear waveguide. This automatically yields the same central wavelength for the WCS and idler photons. The mean number of photon is actively stabilized to $\mu \approx 10^{-2}$ in a 486 ps window. The Bell state measurement (BSM) between the idler photon and the input state is done by sending them through a 50/50 beamsplitter (Żukowski et al. 1993), projecting their joint state on $|\Psi^-\rangle = \frac{1}{\sqrt{2}}[|HV\rangle - |VH\rangle]$ when they are detected in different output modes.

Two polarizers respectively selecting horizontal and vertical polarizations on those output modes remove accidental coincidences of photons with identical polarizations. The photons are then coupled in single mode optical fibres and detected using tungsten-silicide superconducting nanowire single-photon detectors (Marsili et al. 2013), shown as D_1 and D_2 on Fig. 5.3. These detectors were specifically designed to operate at 2.5 K, which is higher than the previous demonstration (Marsili et al. 2013) (around 1 K or less), which means they could, for the first time, be operated in a simple two-stage closed-cycle cryocooler. Their efficiency reached 80% with a temporal resolution (jitter) of ~ 500 ps.

The jitter of the detectors is smaller than the coherence time of the photons, thus coincidences between D_1 and D_2 for which the WCS and idler photons temporally overlap can be temporally resolved and post-selected. The teleportation is completed by sending the signal photon retrieved from the quantum memory in a polarization analyzer where it is detected by single-photon detectors D_3 or D_4. The qubit state of the retrieved photon requires a unitary correction (Bennett et al. 1993) that is included in the polarization analyzer.

5.2.3 Results

In a first series of measurements, the WCS photon and the idler photon both travelled a few meters before the BSM (see Fig. 5.3), and their detection occurred while the signal photon was stored in the quantum memory. To post-select the threefold detections with the correct timing, we plot the temporal distribution of the measured threefold coincidences as function of the delays δt_{j1} and δt_{j2} between a detection at D_j ($j = 3$ or 4) and detections at D_1 and D_2. The results for the teleportation of the $|-\rangle = \frac{1}{\sqrt{2}}(|H\rangle - |V\rangle)$ state are shown as two-dimensional histograms on Fig. 5.3.

Events at the center of the histograms corresponds to the actual teleportation. One of the figures shows an increased number of counts at the center, whereas the other one has a dip, which is expected if the retrieved state is close to the input state $|-\rangle$.

The fidelity of the retrieved state ρ with respect to the input state $|\psi\rangle$ is $F = \langle\psi|\rho|\psi\rangle$. It corresponds to the probability of observing $|\psi\rangle$ when the signal photon is measured in the basis containing $|\psi\rangle$ (the probability is conditional to the detection of the photon). For the teleportation of the $|-\rangle$ discussed above, F can readily be estimated from the number of events observed at the maximum and minimum for zero delays, after a bias due to the different coupling and detection efficiencies of D_3 and D_4 is removed.

The measured fidelity is $92 \pm 4\%$. To obtain complete information about the state ρ, we performed quantum state tomography (Altepeter et al. 2006) by measuring in the $\{|R\rangle,|L\rangle\}$ and $\{|H\rangle,|V\rangle\}$ bases as well. With this information, we can also calculate the purity $P = \text{Tr}(\rho^2)$ of the retrieved state. Since the input state is close to pure, P is related to the depolarization caused by the teleportation. Here, the main cause of this depolarization is noise coming from multi-pair emission from the source and of multiple photons in the WCS. The measured purity with the input state $|-\rangle$ is $94 \pm 7\%$. This value allows us to find an upper bound $F_{\max} = \frac{1}{2}(1 + \sqrt{2P-1}) = 97 \pm 4\%$ on the observable fidelity.

Input state	Fidelity (%)	Purity (%)	$F_{\max}(\%)$
$|H\rangle$	94 ± 3	93 ± 3	96 ± 3
$|-\rangle = \frac{1}{\sqrt{2}}(|H\rangle - |V\rangle)$	92 ± 4	94 ± 7	97 ± 4
$|R\rangle = \frac{1}{\sqrt{2}}(|H\rangle + i|V\rangle)$	84 ± 4	73 ± 5	84 ± 4
$|+\rangle = \frac{1}{\sqrt{2}}(|H\rangle + |V\rangle)$	82 ± 4	83 ± 9	91 ± 6
$|+\rangle$ (12.4 km)	81 ± 4	—	—

TABLE 5.1: Measured fidelities and purities for all input states. The uncertainties are obtained from Monte Carlo simulations assuming a Poisson distribution of the number of threefold events. Also shown is the upper bound on the fidelity $F_{\max}$ that is obtained from the measured purity.

The fidelity and the purity of the retrieved state was evaluated with other input states, and the results are listed in Table 5.1. The expected fidelity of an arbitrary state is $\bar{F} = \frac{2}{3}\bar{F}_e + \frac{1}{3}\bar{F}_p$, where $\bar{F}_e$ and $\bar{F}_p$ are the average fidelities measured on the equator and the pole, respectively. We find $\bar{F} = 89 \pm 4\%$, which is larger than the maximum fidelity of 66.7% achievable with a prepare-and-measure strategy that does not use entanglement (Massar et al. 1995). The fidelities for states on the equator of the Bloch sphere ($|+\rangle,|-\rangle,|R\rangle$) are all smaller than for $|H\rangle$ which is consistent with the fact teleportation of the latter is unaffected by fluctuations in the phase φ of the entanglement, or by the finite jitter of the detectors. The fidelity of the $|-\rangle$ is

the largest among the remaining input states. The differences stem mostly from the non-uniform amount of noise (from varying pair creation probabilities) that those teleportations have been subjected to, which is apparent from variations in the measured purities.

We also performed a teleportation of the $|+\rangle$ state in a configuration where the weak coherent state and the idler photon each travelled through 12.4 km of standard single mode optical fibres before the BSM, yielding a combined distance nearly reaching 25 km with a loss of 4.5 dB per spool of fibre. This distance is much greater than the previous record of 6 km (Riedmatten et al. 2004a) for a fibre-based quantum teleportation, which did not include a quantum memory at the receiving end. It is also worth emphasizing that single mode fibre at shorter wavelengths is much lossier and would have precluded a long-distance experiment (25 km of standard single mode fibre at 880 nm has a total loss of the order of 75 dB).

5.3 Conclusion

We demonstrated the first quantum teleportation from a telecom-wavelength photon to a quantum memory (Fig. 5.3). We also demonstrated the unique long-distance capability of our approach by successfully teleporting a state in a configuration where the length of the telecom-wavelength channel (separating the initial location of the state to be teleported and the quantum memory) reaches 24.8 km of optical fibre.

Our teleportation experiment was based on the detection of three photons. The rate of the experiment can be increased with simple solutions. One is improving the memory efficiency. Another one is to add two more detectors to perform the Bell-state measurement, which would give improvement by a factor of 8, together with the single photon detectors which have high detection efficiencies (using superconducting single photon detectors one can reach efficiencies up to almost 90% (Verma et al. 2015)).

To use this scheme for real applications one has significantly improve the performance of the quantum memory. This should include the storage time which have to be increased up to millisecond scale. On demand storage also have to be realized for an efficient synchronization between different elementary links of a quantum repeater. To decrease the distribution time one has to significantly increase the efficiency of the quantum memory as well.

In a broader context, our experiment could be useful to transfer quantum information between quantum network nodes with built-in nonlinear processing capabilities. In particular, coupling between the spin levels of rare-earth crystals and superconducting microwave resonators was recently observed (Staudt et al. 2012; Probst et al. 2013). Combined with our work, this could lead to the long-distance transfer of optical quantum states to superconducting qubits performing two-qubit gate operations (Steffen et al. 2013).

6   Photon multiplexing

Progress towards practical entanglement distribution requires the use of quantum memories compatible with various multiplexing schemes in order to realize efficient quantum communication. Multiplexing can be performed by using various photonic degrees of freedom (DOF). Entanglement can be distributed using a photon pair entangled in many DOFs at the same time (hyperentangled photon pair). At the same time the progress towards practical entanglement distribution requires the use of quantum memories with strong multimode capacity in order to realize efficient quantum repeater. Both the possibility to store hyperentanglement and the temporal multimode capacity are an important resource in optical quantum information processing.

In this chapter we discuss two experiments involving solid-state quantum memory described in Chapter 5. First we performed quantum storage of the hyperentangled state using DOFs compatible with long distance quantum communication. While the second experiment is devoted to the simultaneous storage of two entangled photon pairs in a solid-state quantum memory. Also we present a theoretical method to certify entanglement which can also be used as Schmidt number witness without any assumptions on the quantum states. It allowed us to experimentally certify the presence of more than one entangled photon pair retrieved from the quantum memory with a reduced number of resources.

6.1   Hyperentanglement storage

Complete quantum interconnectivity between remote nodes requires the efficient distribution and storage of quantum entanglement, which is achieved by exchanging entangled photons and storing them in quantum memories. In this context, hyperentanglement is known to be a very useful resource for the task of entanglement purification, which can be used to increase the rate at which entanglement is distributed (Simon et al. 2002).
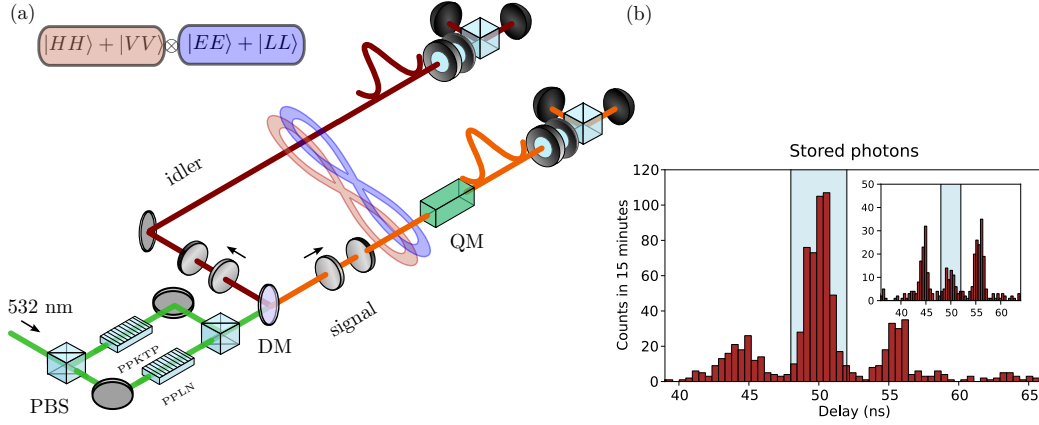
FIGURE 6.1: Hyperentanglement storage. (a) A pair of photons entangled in polarization (Eq. (3.15)) and energy-time (Eq. (3.13)) are generated from SPDC. The signal photon is stored inside a quantum memory (QM) and released after a predetermined time of τ_M =50 ns. The hyperentanglement (Eq. (6.1)) is revealed using time-bin analyzers having short (E) and long (L) arms and adjustable relative phases (ϕ_i and ϕ_s), followed by polarization analyzers. (b) Example of measurements used to violate CHSH inequality for time-bin degree of freedom for stored signal photon. The coincidence histograms between show three peaks corresponding to different path combinations . The figure represents a histogram from one measurement outcome of a correlator in the Bell–CHSH inequality (Eq. (1.9)). The insets correspond to histograms with an additional π phase shift between the two interferometers. Varying the angles of the polarization analyzers leads to variations of the intensity of all three peaks simultaneously.

Also it can be used for complete and deterministic Bell-state analysis in one of the DOF of a hyperentangled pair (Kwiat et al. 1998; Walborn et al. 2003; Schuck et al. 2006) and to perform quantum teleportation (Boschi et al. 1998; Kim et al. 2001; Schmid et al. 2009) and superdense coding (Barreiro et al. 2008; Graham et al. 2015). .

However, this is possible only if the degrees of freedom in which the hyperentanglement is coded are suitable for long-distance transmission, e.g. in optical fibre. Previous demonstrations of entanglement purification where all based on polarization and spatial modes, but the latter is not adequate for long-distance transmission in fibre (Pan et al. 2003; Walther et al. 2005). Energy-time (or time-bin) and polarization hyperentanglement is much better suited for this. The requirements that then arise for quantum repeaters is to have quantum memories that can efficiently store both DOF, combined with the possibility of efficiently distributing entanglement over long distances in optical fibre.

6.1.1   Experiment

To realize hyperentanglement storage we used the SPDC source of the photon pairs (Chapter 3) entangled in energy-time and polarization simultaneously (Fig. 6.1). The polarization preserving quantum memory based

on two-crystal configurations (Clausen et al. 2012) was used to store polarization degree of freedom, while AFC technique has been shown to be compatible to store energy-time entanglement (Clausen et al. 2010). By combining both these approaches the photonic state entangled simultaneously in polarization and energy-time was used for storage

$$\left|\Phi_\tau^+\right\rangle \otimes \left|\Phi_\pi^+\right\rangle = \frac{1}{2}(|EE\rangle + |LL\rangle) \otimes (|HH\rangle + |VV\rangle). \qquad (6.1)$$

The polarization entanglement is generated by sending this pump light onto a polarization interferometer containing two nonlinear waveguides in its arms, while the energy-time entanglement is obtained by pumping the waveguides with a continuous-wave laser (Chapter 3).

Two analyze stored hyperentangled pair both degrees of freedom has to be manipulated independently, and the measurement of the entanglement in one degree of freedom should not depend on the basis in which the other is measured. In our setup, this was achieved by compensating polarization rotations, due to birefringence, in both arms of the unbalanced interferometers used to analyze energy-time entanglement (Fig. 6.1(a)).

Both unbalanced interferometers are locked using reference lasers and both phases ϕ_s and ϕ_i can be varied. To lock the phase of the idler's time-bin analyzer, we use highly coherent light at 1338 nm obtained from difference-frequency generation from 532 and 883 nm light combined in the PPLN waveguide. The phase of the interferometer is controlled by coiling the fiber of the long arm around a cylindrical piezo transducer, and the interferometer is locked using a side-of-fringe technique. The phase of the signal photon's time-bin analyzer is controlled using a piezo-mounted mirror placed in the long arm. The phase is probed using part of the CW laser at 883 nm that is used to prepare the quantum memory. The light is frequency shifted using an acousto-optic modulator (AOM) and then sent trough the interferometer in a spatial mode that has no overlap with the signal photon. The phase ϕ_s in this case can be changed by changing the modulation frequency of the AOM.

After the interferometers, the polarization of each photon is analyzed. Each output of the polarization beamsplitter is coupled into a singlemode fiber and sent to single-photon detectors. The results of the measurements made at different analyzers are compared in order to reveal the nonlocal correlations in both degrees of freedom. Single photon detectors with 30% (Si avalanche photodiode) and 75% (WSi superconducting nanowire (Verma et al. 2014)) efficiencies are used to detect signal at 883 nm and idler at 1338 nm, respectively.

6.1.2 Results

A quantum state is hyperentangled if one can certify entanglement for each entangled DOF. Therefore, it is enough to violate a Bell inequality in both polarization and time independently to demonstrate hyperentanglement. Here we use the CHSH inequality to witness polarization S_π and

	S (transmitted)		S (stored)	
	π	τ	π	τ
$\pi_1 : \{\lvert H\rangle, \lvert V\rangle\}$	-	2.555(13)	-	2.60(7)
$\pi_2 : \{\lvert +\rangle, \lvert -\rangle\}$	-	2.571(11)	-	2.49(4)
$\tau_1 : \phi_{si} = 0$	2.716(11)	-	2.59(4)	-
$\tau_2 : \phi_{si} = \frac{\pi}{4}$	2.733(12)	-	2.64(4)	-

TABLE 6.1: Summary of all CHSH inequality violations. Measured S parameters (Eq. (1.9)) obtained with transmitted or stored signal photons are shown. For each case, the tests on energy-time (τ) degree of freedom were done with either the polarization basis $\pi_1 = \{\lvert H\rangle, \lvert V\rangle\}$ or $\pi_2 = \{\lvert +\rangle, \lvert -\rangle\}$, and tests on the polarization (π) degree of freedom was done with $\Delta\phi_s + \Delta\phi_i = \phi_{si} = 0$ (τ_1) or $\frac{\pi}{4}$ (τ_2). These results show clear violations of Bell-CHSH inequality and demonstrate entanglement in all degrees of freedom studied.

energy-time S_τ entanglement (Chapter 1). To illustrate the independence between the two degree of freedom, each polarization measurement was performed using two different projection bases for the energy-time degree of freedom, and vice versa. Specifically, the test on the energy-time entanglement was done with using either the polarization basis $\pi_1 = \{\lvert H\rangle, \lvert V\rangle\}$ for both photons, or $\pi_2 = \{\lvert +\rangle, \lvert -\rangle\}$. The test on the polarization entanglement was done with either $\Delta\phi_s + \Delta\phi_i = \phi_{si} = 0$ (denoted by τ_1) or $\phi_{si} = \frac{\pi}{4}$ (denoted by τ_2). The results of the CHSH inequality violations are summarized in the Table 6.1.

The corresponding CHSH parameters are $S_\pi^{(\tau_1)} = 2.59(4)$ and $S_\pi^{(\tau_2)} = 2.64(4)$ for polarization entanglement, and $S_\tau^{(\pi_1)} = 2.49(4)$ and $S_\tau^{(\pi_2)} = 2.60(7)$ for the energy-time. The violations exceed the local bound by more then 8 standard deviations. To see the effect of the storage process the quality of the hyperentanglement, we performed the same analysis using the transmitted signal photons The values for S_π and S_τ are very similar in all cases, showing that the quantum memory has little or not effect on the quality of the hyperentanglement.

In conclusion, we certified the storage of hyperentangled photonic state in the state solid-state quantum memory. For this we performed the violation of the CHSH inequality for both degrees of freedom, demonstrating the independence of the polarization and energy-time entanglement after storing it in the quantum memory.

6.2   Multiphoton Storage

Temporal multiplexing is a promising solution for long-distance quantum communication based on quantum repeaters. Solid-state quantum memories offer great potential in this direction thanks to significant temporal

multimode capacity allowing to perform efficient temporal multiplexing. Quantum memories based on ensembles of atoms provide such a resource, where different degrees of freedom can be used to achieve multimode storage, such as spatial (Lan et al. 2009; Zhou et al. 2015; Parigi et al. 2015), spectral (Sinclair et al. 2014) or temporal modes (Nunn et al. 2008).

Here we focus on temporal multimode storage in a single spatial mode. This type of multimode storage is compatible with optical fiber technologies and therefore attractive for long-distance quantum networks. Earlier studies showed, however, that most ensemble-based storage techniques require very high optical depths for high temporal multimode capacity (Nunn et al. 2008). Using atomic frequency comb approach (Afzelius et al. 2009) one can achieve multimode storage for much lower optical depths (Chapter 2).

Previous studies have demonstrated temporal multimode storage using the AFC scheme, but these experiments have employed either strong (Bonarota et al. 2011; Gündoğan et al. 2013; Jobez et al. 2016) or attenuated laser pulses (Usmani et al. 2010; Jobez et al. 2015; Gündoğan et al. 2015), and more rarely true single-photon pulses (Tang et al. 2015; Saglamyurek et al. 2016). Progress towards a practical quantum repeater requires going beyond these initial steps.

6.2.1 Experiment

The goal of this experiment was to demonstrate simultaneous storage of two polarisation-entangled photons in a solid-state quantum memory. As illustrated in Fig. 6.2, two independent pairs of entangled signal and idler photons are generated via spontaneous parametric down conversion (SPDC) (Chapter 3) within a time window shorter than the memory time. The idler photons are at the telecommunication wavelength of 1338 nm, while the signal photons are at 883 nm. The two signal photons are stored in the rare-earth ion doped crystal in the same spatial mode, but in two independent temporal modes that differ by up to ten times their coherence time. After a pre-determined storage time of 50 ns, the two photons are re-emitted from the memory and detected by the single-photon detectors (and similarly for the idler photons).

First, we demonstrate the capability to generate two independent entangled photon pairs for further quantum storage. For this we generate polarization-entangled photon pairs from SPDC inside two nonlinear waveguides. The continuous pump laser has a central wavelength of 532 nm and is modulated in intensity to obtain a 10 MHz train of 50 ns square pulses (Fig. 6.2). This modulation defines a temporal window, corresponding to the storage time, inside which two pairs can be generated. The configuration of the nonlinear waveguides, shown in Fig. 6.2(a), is such that photons are created in a coherent superposition of $|HH\rangle$, from the first waveguide, or $|VV\rangle$, from the second. We approximate each pair by the state

$$|\phi(t)\rangle = \frac{1}{\sqrt{2}} \left(|H_s, H_i\rangle_t + |V_s, V_i\rangle_t \right), \tag{6.2}$$
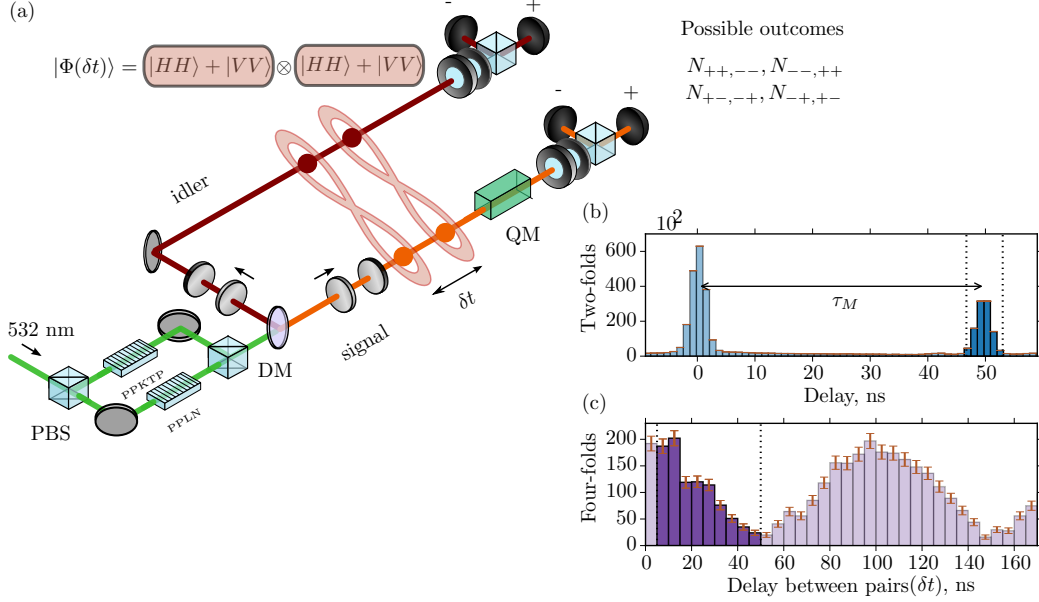
FIGURE 6.2: Temporal multimode storage of entangled photon pairs. (a) Creation of polarization-entangled photon pairs using two waveguides inside a polarization interferometer. Two different temporal modes are populated by the two independent photon pairs $\Phi(\delta t) = \Phi_t \otimes \Phi_{t+\delta t}$ (Eq. (6.3)). Temporally multiplexed photon pairs are stored in a multimode quantum memory (QM) and released after a predetermined time $\tau_M = 50$ ns. To certify entanglement after absorption and remission by the QM we analyze the correlations in polarization of the four-photon state using polarization projection for each photon type. (b) The two-fold coincidences between detections of the signal and idler photons as a function of the delay between two detection events. The first peak at 0 ns stems from the signal photons not absorbed by the QM while the second peak at 50 ns corresponds to the signal photons absorbed by the QM and released after the storage time. Such an histogram is accumulated for each pair of detectors between signal and idler photons. (c) The total four-fold coincidences collected during the experiment is plotted as a function of the delay δt between photon pairs. Events inside the storage time of the QM are delimited by dotted vertical lines from 5 to 50 ns. Only events corresponding to the state (6.3) are considered, for this reason events within the first 5 ns are excluded (Riedmatten et al. 2004b). There are 9 distinguishable time divisions, demonstrating storage of as many temporal modes with two single excitations. For longer delay (> 50 ns), two photons do not overlap at any time in the QM. Error bars represent one standard deviation assuming Poisson noise for the count

where t is the photon pair creation time within the square pump window, s and i subscripts label signal and idler modes, while $|H\rangle$ and $|V\rangle$ designate horizontal and vertical polarization states of a single photon, respectively.

Two independent polarization-entangled pairs can be generated from the same pulse, in condition that the delay between the pairs, δt, is sufficiently larger than the coherence time of one pair (Riedmatten et al. 2004b). In this case, the four-photon polarization entangled state can be described as

$$\left|\Phi_t^+\right\rangle \otimes \left|\Phi_{t+\delta t}^+\right\rangle = \frac{1}{2}(|HH\rangle + |VV\rangle)_t \otimes (|HH\rangle + |VV\rangle)_{t+\delta t}, \qquad (6.3)$$

where each photon pair was created at time t and $t + \delta t$ with a temporal separation δt bigger than the coherence time of he photon pair.

The signal mode of each pair is coupled to the quantum memory. The latter consists of two $Nd^{3+}:Y_2SiO_5$ crystals mounted around a half-wave plate, together enabling high-fidelity polarization storage (Clausen et al. 2012; Zhou et al. 2012b). The absorption profile of the broad resonant frequency transition of the atomic ensemble is tailored in a frequency comb using optical pumping techniques. The prepared AFC fixes the storage time to $\tau_M = 50$ ns and the measured total memory efficiency of the single photon is $\eta = 7(1)\%$.

To analyze the correlations between the released signal and idler photons, we use a combination of quarter-wave, half-wave plates, polarization beamsplitter and two detectors on each side of the experiment (Fig. 6.2). To detect the stored signal and the idler photons from each pair we put two single-photon detectors (SPDs) at the output ports of the PBS on each side (denoted as "+" and "−" in Fig. 6.2(a)). We use superconducting nanowire SPDs ($D_\pm^{(i)}$) with 75% efficiency, 100 ns dead time and 300 ps jitter (WSi superconducting nanowire Verma et al. 2014) for the idler photons. The signal photons are detected with two free-space free-running silicon avalanche photodiode ($D_\pm^{(s)}$) with 40% efficiency, 1 μs dead time and 400 ps jitter.

Figure 6.2(b) shows two-fold coincidences as a function of the delay between the detections of a signal and an idler photons. The temporally resolved peak structure corresponds to the transmitted (0 ns) and stored signal photon in the QM (50 ns) from a single photon pair (Eq. (6.2)). However, to detect and analyze the four-photon state (Eq. (6.3)) one has to look at coincidences between all four detectors (four-folds).

The use of only two detectors on each side limits the number of possible projections which can be applied to the four-photon state (6.3) to analyze entanglement. Another limitation is the number of possible outcomes from the measurement which is restricted by the deadtime of the detectors which is bigger than the storage time of the quantum memory. The deadtime prevented the two photons to be detected in the same output port of the polarization analyser which limits the number of possible outcomes, such that both photons were analyzed in the same basis.

All this together required to implement new entanglement witness technique to still prove entanglement preservation of the both photons stored in the quantum memory.
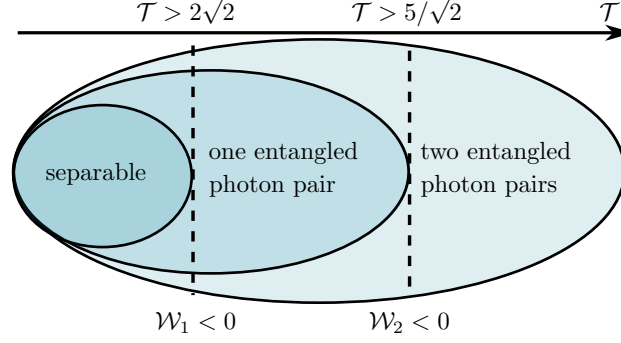
FIGURE 6.3: Indirect entanglement witness. From the measured four-fold correlations we can compute our central figure of merit $\mathcal{T}$ (Eq. (6.4)). A value of $\mathcal{T}$ implies that the operator $\mathcal{W}_k(\mathcal{T})$ has expectation value exactly zero. For a sufficiently large value of $\mathcal{T}$ this implies that the expectation value of $\mathcal{W}_1(\mathcal{T})$ (or $\mathcal{W}_2(\mathcal{T})$) is negative. Since we can prove that $\mathcal{W}_1$ is an entanglement witness and $\mathcal{W}_2$ a Schmidt number witness, we can thus conclude one/two entangled pairs.

6.2.2   Indirect entanglement witness

The full characterization of the state (6.3) of both photon pairs is complicated by the fact that their creation time is much smaller than the dead time of the detectors. This is typical of current single-photon detectors and it can complicate the analysis of temporally multiplexed quantum memories storing short (broadband) single photons. One obvious solution is to double the number of analyzers (and detectors), or use complex multiplexing schemes in space or frequency (Collins et al. 2013; Donohue et al. 2014). Here, instead, we want to use a pair of detectors on each side and apply the same projective measurement needed to analyze a single pair. This leads to a limited set of measurements and outcomes.

Here we give the details of the derivation of the entanglement witness used to certify two entangled photon pairs stored in the quantum memory. Although we expect the final state to be a product of two highly entangled states (6.3), we obviously do not want to make this assumption in the derivation of its entanglement certification. For that purpose we treat the underlying events as originating from a 4×4 dimensional Hilbert space without any assumption in its internal structure. In the ideal case that state should correspond to a tensor product of two Bell states and thus have a Schmidt number of 4. If only one of the pairs could retain its entanglement through the storage in the quantum memory its Schmidt number would be at most 2. If, on the other hand all the entanglement had been destroyed, the resulting state would be completely separable (i.e. Schmidt number 1).

Due to the technical limitation the acquisition of complete counts in any basis was prohibited (Fig. 6.2). For this reason it is impossible to perform full quantum state tomography of obtaining density matrix elements through local projective measurements (Sanpera et al. 2001). Even though there was no access to all the projective measurements we can construct the expression

that contains only the fraction of corresponding density matrix elements.

$$\mathcal{T} = \frac{\sum_{\{a,b\}\in X}\langle a,b|\rho|a,b\rangle}{\sum_{\{a,b\}\in Y}\langle a,b|\rho|a,b\rangle}. \tag{6.4}$$

Through the linearity of the trace we can conclude that the operator

$$\mathcal{W}(\mathcal{T}) = \sum_{\{a,b\}\in X}|a,b\rangle\langle a,b| - \mathcal{T}\sum_{\{a,b\}\in Y}|a,b\rangle\langle a,b|, \tag{6.5}$$

has expectation value zero, i.e. $\mathrm{Tr}(\mathcal{W}(\mathcal{T})\rho) = 0$ in analogy with classical entanglement witness described in Chapter 1. Different optimization algorithms (for example semi-definite programming (SDP)) can be used to find the lower bound on the expectation values $\mathcal{T}$ to prove the presence of entanglement or to address it's dimensionality using entanglement witness $\mathcal{W}$.

Now applying the above formalism to the two-photon pair experiment we can use

$$\mathcal{T} = \frac{1}{N}(C_{00} + C_{01} + C_{10} - C_{11}) \tag{6.6}$$

where we have defined correlation functions

$$C_{xy} = \sum_{a,b=\pm 1} ab\, N_{ab,\bar{a}\bar{b}|xy} \tag{6.7}$$

and a normalization factor

$$N = \frac{1}{4}\sum_{x,y=0,1}\sum_{a,b=\pm 1} N_{ab,\bar{a}\bar{b}|xy}. \tag{6.8}$$

In the case ρ contains one entangled pair (or less), the expression $\mathcal{T}$ is upper-bounded by

$$\mathcal{T} \leq \frac{5}{\sqrt{2}} \simeq 3.5355. \tag{6.9}$$

The optimization based on SDP programming gave Schmidt number witness for the state containing one entangled photon pair is $\mathcal{T} \approx 3.535$ (Fig. 6.3), thus showing that the indirect entanglement witnesses $\mathcal{W}(\mathcal{T})$ indeed proves that more than one entangled pair is required to explain the observed correlations.

With the increased number of modes in different multiplexing schemes the complexity of the quantum experiments grows dramatically and requires more and more resources for analysis. In this context, our approach is important for quantum communication community and for entanglement certification in general.

6.2.3 Results

We now use the recorded four-fold events and the entanglement witness to show that the two pairs used to probe the multimode properties of the

$\mathcal{C}_{00}$	$\mathcal{C}_{01}$	$\mathcal{C}_{10}$	$\mathcal{C}_{11}$	$\mathcal{T}$	$\tilde{\mathcal{T}}$
0.96(2)	0.91(3)	0.90(3)	-0.89(3)	3.67(6)	3.64(2)

TABLE 6.2: Experimental certification of two entangled pairs after storage. Each correlator $\mathcal{C}_{xy}$ is measured as described in the main text and used to compute the parameter $\mathcal{T}$ of Eq. (6.6). $\tilde{\mathcal{T}}$ is a model-based estimation of the expected $\mathcal{T}$ value in our experiment (see text). There is a good agreement between the two. These results above the bound (6.9) of 3.535 certify entanglement for each photon pair released from the QM. The uncertainties represent one standard deviation assuming Poisson statistics for the counts.

memory are polarization entangled. Each correlator of Eq. (6.6) is measured for 900 seconds and the sequence is repeated many times (see Table 6.2). The experimental value of the entanglement witness is $\mathcal{T} = 3.67 \pm 0.06$, two standard deviations above the upper bound (6.9) of 3.535 attainable when only one pair is entangled while the other is separable.

To understand what limits our measured value of $\mathcal{T}$, we developed a simple model to predict it using only the measurement of the Bell–CHSH parameter S for a single entangled pair. For this we assume that we are measuring two independent pairs and a total quantum state of the form $\rho(\mathcal{V}) = \rho_W(\mathcal{V}) \otimes \rho_W(\mathcal{V})$, where $\rho_W(\mathcal{V}) = \mathcal{V} |\phi_+\rangle \langle\phi_+| + (1 - \mathcal{V})\mathbb{1}/4$ is a two-qubit Werner state with visibility $\mathcal{V}$. We should measure the value $S = 2\sqrt{2}\mathcal{V}$ for a single entangled pair in the state $\rho_W(\mathcal{V})$, and we can use this to calculate the expected value of $\tilde{\mathcal{T}}$. With the photons retrieved from the QM, we found $S = 2.58 \pm 0.02$ which corresponds to a visibility of $\mathcal{V} = 0.912 \pm 0.007$, which leads to an expected value of $\tilde{\mathcal{T}} = 3.64 \pm 0.02$, in agreement with experimentally measured value of $\mathcal{T}$. We note that in this model, a minimum visibility of $\mathcal{V} \simeq 0.85$ (for each identical pair) is required to certify more than one entangled pair, which is more stringent than the case where all measurement outcomes are accessible.

In conclusion, we certified the storage of two entangled photon pairs in a temporal multimode solid-state quantum memory. For this, we developed an entanglement certification method that can also be used as Schmidt number witness, does not require any assumptions on the quantum states and works even with a limited set of projective measurements. Our results demonstrate the temporal multimode capacity directly probed by two quantum excitations.

6.3   Conclusion

We demonstrated the capability of our solid-state quantum memory to realize different multiplexing schemes for future quantum networks. The

ability to store various photonic degrees of freedom using solid-state material has been shown by performing hyperentanglement storage encoded in polarization and energy-time degrees of freedom. This is the first demonstration of hyperentanglement storage compatible for long-distance quantum communication. In this context hyperentangled states can be further used to implement the quantum purification schemes to increase the fidelity of the transferred quantum information. Such experiment involving quantum storage and retrieval of the purified quantum state should become one of the building blocks for future quantum communication applications. For this, for example energy-time degree of freedom can be used to purify the polarization state of the stored photonic excitation. One of the ways requires the implementation of the parity measurement for given degree of freedom in order to increase the fidelity of the state for other one (Simon et al. 2002).

The temporal multimode capacity of the atomic frequency comb quantum memory protocol is the main advantage of using it to realize quantum repeater. In this chapter we demonstrated it using solid-state quantum memory and two entangled photon pairs as a probe. The main limitation to increase the number of photons simultaneously stored in the memory is the probabilistic nature of the photon pair generation, its storage and detection. Each step has finite efficiency and is not ideal. Present experiment was possible thanks to the increased efficiency of the detection step by use of the superconducting single photon detectors (Verma et al. 2014) and the optimized overall transmission of the experimental setup. Further improvement should focus on increasing the efficiency of the quantum memory by optimizing the preparation of the AFC structure. The use of high-quality deterministic single photon sources (for example quantum dots) will allow one to dramatically increase the rate of the entangled photon generation and thus will help to increase the number of stored excitations,.

Both, the demonstration of the hyperentanglement storage and the temporal multimode storage of entangled photon pairs are necessary requirements to realize efficient quantum networks using solid-state quantum memories.

7 Multi-dimensional entanglement storage

This chapter is partly based on the results published in

Entanglement is the main resource for various applications in quantum information processing and quantum communication. Increasing entanglement structure complexity paves the way for both deeper fundamental tests of nature and new methods for quantum information tasks. Of particular interest is the possibility of using multi-dimensional entangled states, which are proven to outperform standard two-qubit entangled states for a wide range of applications. In particular, high-dimensional entanglement can enhance key rate and resilience to errors in quantum key distribution (Cerf et al. 2002; Sheridan et al. 2010). Moreover, it is also relevant for the implementation of device-independent quantum communication protocols (Acín et al. 2007), allowing for more robust Bell tests (Vértesi et al. 2010) and enhanced security (Huber et al. 2013b).

In this chapter we certify and quantify multi-dimensional energy-time entanglement stored in a quantum memory. The certified number of *e*bits exceeds all the previous experimental realizations involving quantum storage. To achieve this we implemented a novel entanglement certification scheme which gives a lower bound on the entanglement of formation based on the incomplete data provided by the measurements. This method can be generalized since it is based on basic properties of the density matrix and on the limited set of projective measurements.

7.1 Quantification of multi-dimensional energy-time entanglement

While these works open promising perspectives, the use of multi-dimensional entanglement for practical and efficient quantum communications still faces important challenges. Unavoidable losses in optical fibers require the use of quantum repeater schemes featuring quantum memories in order to reach long distances (Sangouard et al. 2011). First steps were taken in realizing

quantum memories beyond qubits. Notably experiments demonstrated the storage of three-dimensional entanglement of orbital angular momentum (Zhou et al. 2015; Ding et al. 2016b), as well as the implementation of a temporal multimode quantum memory capable of storing multiple entangled two-qubit pairs Chapter 6, a key step for achieving efficient entanglement distribution (Simon et al. 2007). A quantum memory which is capable of storing high-dimensional entanglement is an essential tool to go in this direction since it allows one to use the increased quantum information capacity for long-distance quantum communication.
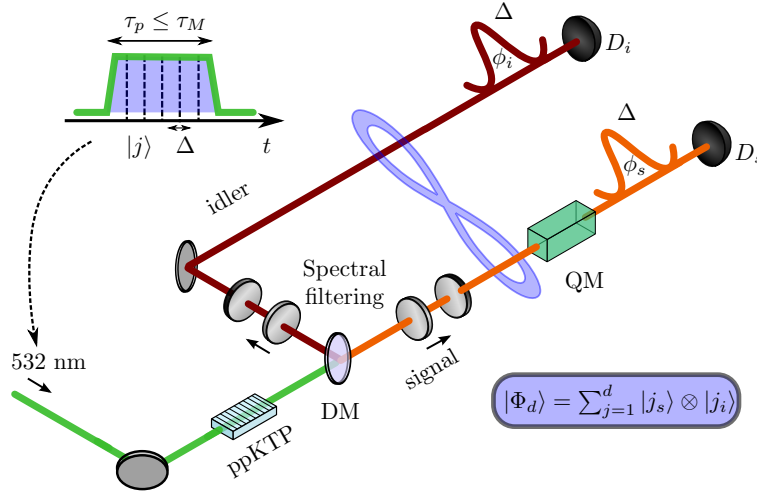
FIGURE 7.1: Experimental setup. Spontaneous parametric down-conversion (SPDC) in a periodically poled KTP waveguide (ppKTP) was used to create a pair of photons (signal and idler) entangled in energy-time. For this, we used a 532 nm wavelength monochromatic laser for pumping and spectral filtering based on optical cavities on both photons. The signal photon was sent to a quantum memory (QM) based on Nd^{3+}:Y_2SiO_5 crystal and stored for τ_M=50 ns. The laser intensity was modulated using an acousto-optic modulator to generate a square pulse with duration τ_p smaller than the storage time of the QM. Since the coherence time of the photon pair is much smaller than the coherence time of the pump laser, this leads to the generation of a multi-dimensional photonic state entangled in energy-time $|\Phi_d\rangle$. To reveal this type of entanglement we used Franson interferometry based on two interferometers with controllable phases ϕ_s and ϕ_i and identical path difference in time Δ equal to 5.5 ns. To analyse two-photon interference between idler and stored signal photons two single photon detectors (D_s and D_i) were used.

7.1.1 Experiment

We start from the generation of the energy-time entanglement between two single photons at different wavelengths using spontaneous parametric down conversion (SPDC). For this, a monochromatic continuous wave 532 nm laser pumps a nonlinear optical waveguide (periodically poled potassium titanyl phosphate (ppKTP) waveguide) to generate the signal and idler

photons at 883 nm and 1338 nm, respectively (Fig. 7.1). Two photons are cre-
ated simultaneously and are well correlated in energy. However, the use of
a monochromatic pump laser leads to an uncertainty on the photon pair cre-
ation time. This uncertainty is defined by the coherence time of the pump
laser and is approximately 1 µs in our case.

A d-dimensional two-photon state can be, in general, written as

$$|\Phi_d\rangle = \frac{1}{\sqrt{d}} \sum_{j=1}^{d} |j_i, j_s\rangle \ . \tag{7.1}$$

The entangled photon pair is filtered down to 200 MHz which corre-
sponds to a coherence time $\tau_c = 2.0$ ns (Chapter 3). This coherence time is
much smaller than the coherence time of the pump laser which leads to a
high number of temporal modes coherently populating the multi-dimensional
entangled two-photon state (Eq. (7.1)).

The signal photon from the photon pair is coupled to the quantum mem-
ory based on the Atomic Frequency Comb (AFC) protocol. The storage time
was predetermined and was equal to 50 ns with an overall efficiency of 15%.

The standard way to reveal energy-time entanglement is the use of Fran-
son interferometry (Franson 1989). In our case the signal photon retrieved
from the quantum memory is sent to an unbalanced interferometer (Fig. 7.1)
and the same operation is applied to the idler photon. The travel-time dif-
ference Δ between the short and long arms of the interferometers is bigger
than the coherence time of the photon pair and is equal to 5.5 ns for each.
In this case, the situation in which both photons passed through the short
arms is indistinguishable from one where both photons travelling through
the long arms, leading to quantum interference in the coincidence rate.

In practice, two Michelson interferometers (one bulk and one fiber based)
with controllable phases (ϕ_s and ϕ_i on Fig. 7.1) and identical travel-time dif-
ferences $\Delta_s = \Delta_i = \Delta$ were implemented on each side of the experiment
(for signal and idler photon, respectively). A mechanical switch inside the
signal interferometer was used to analyze the diagonal elements of the den-
sity matrix.

In order to analyze energy-time entangled photonic qu$d$its various in-
terferometric techniques could be used. The use of d interferometers is re-
quired in order to fully characterize $d \times d$ dimensional two-photon state
(Thew et al. 2004). This leads to technical difficulties which do not allow,
in practice, to reach high-dimensional energy-time entangled states. How-
ever, in order to quantify entanglement such a set of measurements can be
seen as overcomplete. In our experiment we show that with only a pair of
interferometers, one on each side of the experimental setup, it is possible
to give a lower bound on the amount of entanglement shared between two
photons.

7.1.2   Entanglement certification with incomplete data

Our goal now is to characterize the multi-dimensional entanglement at the output of the quantum memory. To do so, we reconstruct part of the $d^2 \times d^2$ density matrix ρ, with elements $\langle j, k| \rho |j', k'\rangle = \text{Tr}[\rho(|j\rangle_i \langle j'|_i \otimes |k\rangle_s \langle k'|_s)]$. Note however, that the measurement information at our disposal is very limited, due to the simplicity of our measurement setup. Hence we can obtain only very few elements of ρ. Specifically, we can measure

1. the diagonal of the density matrix, i.e. terms $\langle j, k| \rho |j, k\rangle$, via the time-coincide measurement;

2. ithe coherence between two neighboring temporal modes, i.e. terms $\langle j, j| \rho |j + 1, j + 1\rangle$, via the interference measurements. Note that a full state reconstruction of ρ would require the use of d different interferometers, and is extremely cumbersome and unpractical.

Nevertheless we will see that the limited information at our disposal is already enough to partly characterize the state, in particular leading to strong lower bounds on the entanglement of formation of ρ, E_{oF}. The latter is an operationally meaningful measure of entanglement, quantifying how much pure entanglement (counted in $e$bits, i.e. number of maximally entangled two-qubit pairs) is required in order to prepare ρ via an arbitrary LOCC procedure. Following Ref. Huber et al. 2013a, we have that

$$E_{oF} \geq -\log_2(1 - \frac{B^2}{2}) \,, \tag{7.2}$$

where we have defined the quantity B as

$$\frac{2}{\sqrt{|C|}} \left(\sum_{\substack{(j,k)\in C \\ j<k}} |\langle j, j| \rho |k, k\rangle| - \sqrt{\langle j, k| \rho |j, k\rangle \langle k, j| \rho |k, j\rangle} \right) . \tag{7.3}$$

Note that the indices (j, k) are taken from a set C that can be chosen at will. The quantity B lower bounds the concurrence of ρ. For a $d \times d$ maximally entangled state $|\Phi_d\rangle$ one has $B = \sqrt{2(d-1)/d}$, leading to the tight bound $E_{oF} = \log_2(d)$.

Note that the evaluation of B requires only $O(d^2)$ elements of the density matrix, comparing to the total number of $d^4 - 1$. While the diagonal elements, i.e. $\langle j, k| \rho |j, k\rangle$, can be estimated in the experiment (see below), measuring all coherence terms $\langle j, j| \rho |k, k\rangle$ is challenging and unpractical, as it requires many interferometers (with time delays $n\Delta$ with $n = 2, ..., d$) with controllable phases. Nevertheless we will see now that all unknown coherence terms (e.g. $\langle j, j| \rho |k, k\rangle$ with $|k - j| \geq 2$) can in fact be efficiently lower bounded based only on accessible data.

These bounds simply follow from the requirement of the density matrix ρ to be positive semi-definite, i.e. representing a valid quantum state. We first notice that if a matrix is semi-definite positive, then it is also the case

for its real part and all its sub-matrices. Hence, the following sub-matrix of ρ is semi-definite positive

$$\begin{pmatrix} r_{1,1} & r_{1,2} & \cdots & & r_{1,d} \\ r_{1,2} & r_{2,2} & \ddots & & \vdots \\ \vdots & \ddots & \ddots & & r_{d-1,d} \\ r_{1,d} & \cdots & r_{d-1,d} & & r_{d,d} \end{pmatrix} \tag{7.4}$$

where $r_{j,k} = r_{k,j} = \mathrm{Re}(\langle j, j | \rho | k, k \rangle)$. From Sylvester's criterion it follows that every sub-determinant of a semi-definite positive matrix should be non-negative. In particular, the following determinant of any 3×3 sub-matrix of (7.4) is non-negative, i.e.

$$\begin{vmatrix} r_{j,j} & r_{j,k} & r_{j,l} \\ r_{j,k} & r_{k,k} & r_{k,l} \\ r_{j,l} & r_{k,l} & r_{l,l} \end{vmatrix} \geq 0 , \tag{7.5}$$

for all $j < k < l$. We thus get the lower bound:

$$r_{j,l} \geq \frac{r_{j,k} r_{l,k} - \sqrt{(r_{j,j} r_{k,k} - r_{j,k}^2)(r_{k,k} r_{l,l} - r_{k,l}^2)}}{d_{k,k}} . \tag{7.6}$$

Notice that the square root in the above equation is real since its arguments are 2×2 sub-determinants of (7.5) and therefore non-negative. Moreover, even if we do not know the exact value of $r_{j,k}$ or $r_{k,l}$, but only a non-negative lower bound on them, the formula (7.6) remains valid. This property allows us to iteratively compute a lower bound on every element of the matrix (7.4), based only on its diagonal and its first off-diagonal. Finally, we can lower bound B and eventually the entanglement of formation E_{oF} via inequality (7.2).

Let us now focus on the situation of our experiment, for which we expect the following form of the density matrix (omitting normalization): $r_{j,j} = 1$ for $j = 1, ..., d$ and $r_{j+1,j} = \mathcal{V}$ for $j = 1, ..., d - 1$. The bounds on the first unknown off-diagonal elements read:

$$r_{j+2,j} \geq 2\mathcal{V}^2 - 1 \quad , \quad r_{j+3,j} \geq \mathcal{V}(4\mathcal{V}^2 - 3) . \tag{7.7}$$

Hence the matrix (7.4), containing initially many unknown elements, can be filled iteratively, as illustrated in Fig. 7.2. Finally, by computing parameter B, we get a lower bound on the entanglement of formation depending on the visibility, see Fig. 7.5(b). In particular, for a perfect visibility $\mathcal{V} = 1$, the only compatible state is the maximally entangled one (7.1), and the bound becomes tight, i.e. $E_{oF} = \log_2(d)$.

Notice that the bounds become worse when one moves away from the diagonal. In fact, depending on the value of $\mathcal{V}$, the bound (7.6) becomes negative at some point, and thus the corresponding (and following) off-diagonal elements cannot be lower bounded anymore. Nevertheless, until that point, the bounds computed are useful and it can be verified that the
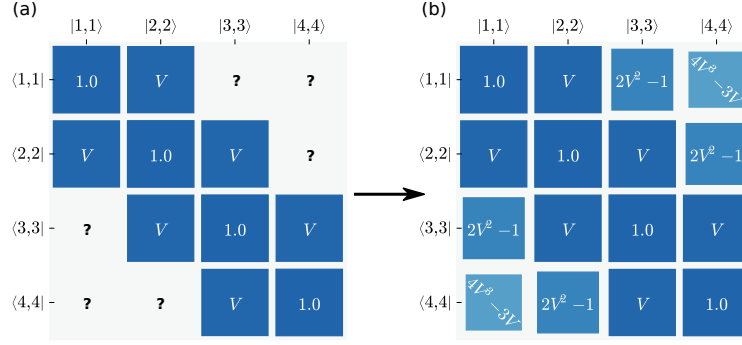
FIGURE 7.2: Illustration of the method. Given a sub matrix where only the diagonal and first off diagonal are known (a), the method allows us to complete the matrix (b), giving lower bounds on all unknown elements based on positivity constraints. Finally this construction leads to a lower bound on the entanglement of formation via relation (7.2).
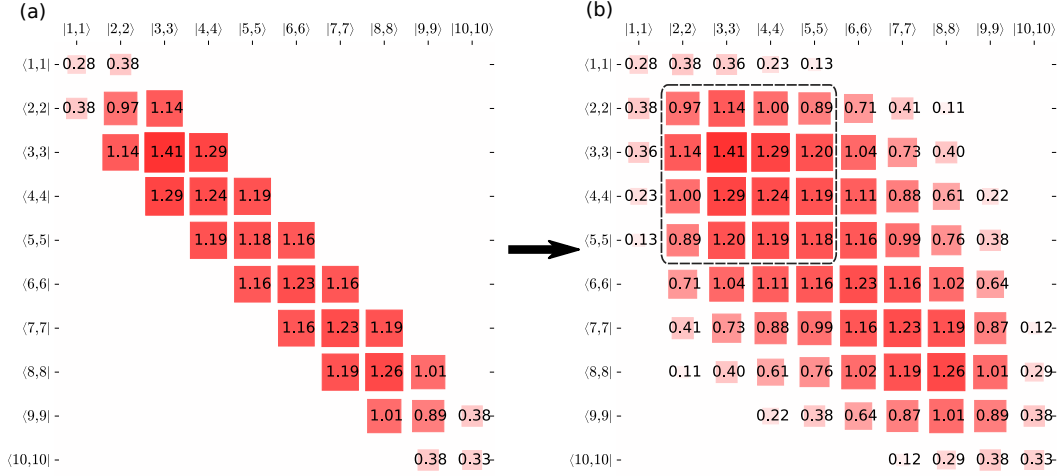

FIGURE 7.3: Illustration of the sub matrix reconstruction for experimental data of one run. The values were normalized with respect to the maximum dimension (10 in this case).

corresponding matrix is semi-definite positive. Hence the bound on the entanglement of formation we obtain is optimal. Notice also that we can play with the subset C in Eq. (7.3) to improve the final bound on E_{oF}. This comes from the fact that, while taking a larger set C makes the sum in Eq. (7.3) larger, the denominator $\sqrt{|C|}$ also grows. We find that in certain cases, better bounds on E_{oF} are obtained when considering small sets C.

7.1.3 Results

We now apply the above method to our experiment. We start by measuring the coherence between neighboring temporal modes, giving access to $r_{j,j+1}$. In order to do this, we use the two interferometers (Fig. 7.1) to extract coherences between temporal modes $|j\rangle$ and $|j+1\rangle$. The phase of
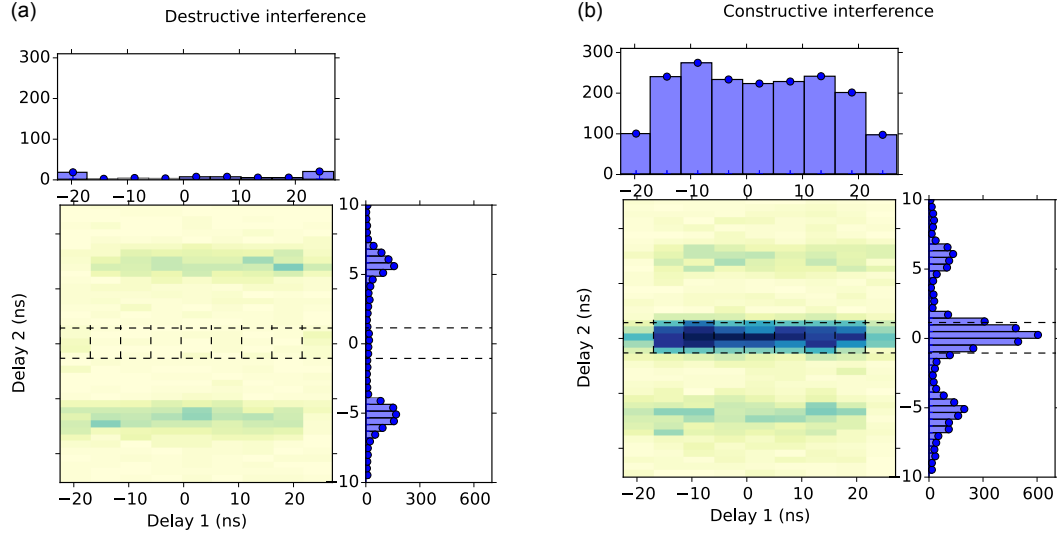
FIGURE 7.4: Example of the interference measurement corresponding to destructive and constructive interference between neighbouring temporal modes. From this measurement we extract the visibilities corresponding to different pairs of neighbouring temporal modes.

the idler interferometer ϕ_i is fixed while the phase of the signal interferometer ϕ_s is scanned over the interval $[0, 2\pi]$. For each time-bin the phase scan is done by measuring 15 points with 2 minutes per point. The coincidence rates are recorded, which correspond to local projections onto $e^{\phi_s + \phi_i} |j, j\rangle + |j + 1, j + 1\rangle$ for all $j = 1, ..., d - 1$. The visibility values are extracted by comparing number of coincidences corresponding to constructive (maximum) and destructive (minimum) interference. Results are given in Fig. 7.5(a). Note that the visibilities for the first two and the last two temporal modes are lower due to a significant change of the intensity between the two neighboring modes. The average visibility for the central temporal modes is $\sim$97%, and is limited by the interferometric stability and the multi-pair contribution from the SPDC process.

Fig. 7.3 shows the sub-matrix before and after application of the theoretical method. Only elements from the first $r_{j,j}$ and second $r_{j,j+1}$ diagonals were measured experimentally using a pair of interferometers. Application of the method based on the positivity of the density matrix (described in the main text) gives a lower bound on the elements for all other diagonals ($r_{j+2,j}$, $r_{j+3,j}$ and so on). These elements are further used to give a lower bound on the entanglement of formation E_{oF} based on Eq. (7.2). The sub-matrix which gives maximum value of E_{oF} is indicated by a dashed line.

Fig. 7.4 illustrates 2D image representing the coincidence measurement for different temporal modes (Delay 1) as a function of delay between two detectors D_s and D_i (Delay 2). The coincidence histograms between detectors D_s and D_i shows three peaks corresponding to different path combinations for travelling idler and signal photon after storage. By varying the phase of the interferometer ϕ_s we observe the interference for central peak which represents post-selected time-bin entangled state (7.1).

The separation between peaks is equal to the travel-time difference between different arms of the interferometer is $\Delta = 5.5$ ns. The central peak is post-selected using 3 ns temporal window (Delay 2) illustrated by dashed line. We define different temporal modes by discretizing temporal pulse using period Δ (Delay 1 in Fig. 7.4).

We measure the visibility for each pair of neighbouring temporal modes by comparing number of coincidences corresponding to destructive (Fig. 7.4(a)) and constructive (Fig. 7.4(b)) interferences between different temporal modes. The visibility is reduced at the edges of the pulse which can be seen from increased number of coincidences for destructive interference for first and last histogram bin (Fig. 7.4). This is explained by fast intensity variation at the beginning and at the end of the pulse which reduces the maximum achievable visibility. To measure intensity of each temporal mode c_j we block one of the arms of the signal interferometer and repeat coincidence measurement described above.

We then measure correlations in the time basis, leading to the terms $r_{j,j}$ for $j = 1, ..., d$. For this, we block the short (or long) arm of the signal interferometer to project on states $|j, j\rangle$ (or $|j + 1, j + 1\rangle$) using a mechanical switch. The results for one of the measurements is depicted in Fig. 7.5(a).
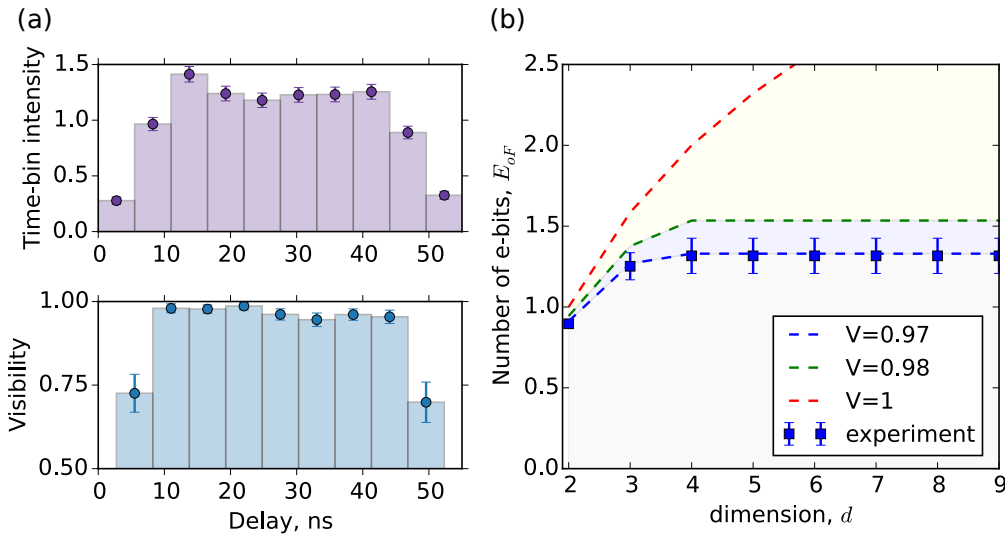
FIGURE 7.5: Results for one experimental run. (a) The measured intensities in the time-of-arrival basis (diagonal elements $r_{j,j}$) and visibilities (first off-diagonal $r_{j,j+1}$) for 10 temporal modes, separated by $\Delta = 5.5$ ns. (b) Lower bounds for the entanglement of formation (number of $e$bits) as a function of the number d of temporal modes taken into account when reconstructing the density matrix. Here the optimal value is $\sim$1.25(11) $e$bits. The data shows good agreement with our model considering the measured visibility of $\mathcal{V}$ of 97%. The case $\mathcal{V} = 1$, corresponding to the maximally entangled state (7.1), gives $\log_2(d)$ $e$bits.

Next we estimate the remaining terms of the diagonal of ρ, i.e. $\langle j, k| \, \rho \, |j, k\rangle$. Essentially the only contributions to these elements are the multipair emission of the SPDC and noise of the detectors. Since these processes are independent of the temporal mode we assume that all diagonal terms $\langle j, k| \, \rho \, |j, k\rangle$

are equal when $j \neq k$. Based on this assumption and using our interferometers we then measure contributions from neighbouring modes $\langle j, j+1 | \rho | j, j+1 \rangle$ and use these values for all other terms.

We now analyze the data via the method discussed above in order to estimate the entanglement of formation of the state. To do so, we first lower bound each element in the submatrix (7.4). We consider all possible submatrices of ρ (of different sizes) and keep the one leading to the best bound on E_{oF}, see Fig. 7.5. The maximum number of $e$bits corresponds to the cases where both the measured visibilities and intensities are largest and relatively constant. This is achieved by considering the central region of the pulse, excluding the edges where the intensity variation is limiting the visibility (Fig. 7.5(a)).

Finally we obtain a lower bound for the entanglement of formation $E_{oF} \geq 1.18(4)$ $e$bits, based on a dozen repetitions of the measurement procedure and analysis. Moreover, this result also certifies a genuinely 3×3 entangled state, as any two-qubit state contains at most one $e$bit. More generally, our approach can be used to place lower bounds on the entanglement dimensionality given by $\log_2(d) \geq E_{oF}$.

In the above analysis we certified a minimal degree of entanglement considering all possible quantum states (density matrices) compatible with our data. It is also relevant to estimate the entanglement based on a more physical model of our experiment. Indeed, this is expected to provide a much higher estimate of the entanglement, given that we consider here only quantum states of a specific form.

The visibility measured for bigger interferometric delays will monotonically decrease due to the finite linewidth of the pump laser. The phase noise of the pump laser can be approximated by gaussian distribution with standard deviation $\delta\phi$. In this case the visibility scales as $\mathcal{V} \sim e^{-\delta\phi^2/2}$ (Minář et al. 2008). In our case for different temporal modes separated by $n\Delta$ delay we can rewrite it as

$$\mathcal{V}_n = \mathcal{V}_1 e^{-2(\pi\delta\nu n\Delta)^2}, \tag{7.8}$$

where $\delta\nu$ is the spectral linewidth of the pump laser and $\mathcal{V}_1$ is the visibility between neighbouring modes.

Assuming the full-width half-maximum linewidth of the pump laser of 1 MHz and maximum delay between temporal modes of 50 ns, the expected visibility remains almost constant decreasing only by a factor 0.99. This verifies our approximation of coherent sum between all temporal modes generated and stored in the quantum memory. Hence we get that $r_{j,j+n} \approx \mathcal{V}$, where $\mathcal{V}$ is the measured visibility between two neighboring modes. This allows us to get a lower bound on the entanglement of formation of 2.6 $e$bits from our measurement data.

7.2 Conclusion

In conclusion, we characterized multi-dimensional energy-time entanglement between two photons where one photon was stored in a quantum

memory and the other photon is at telecom wavelength. In particular, we certified an entanglement of formation of 1.18(4) $e$bits.

To do so, we developed a general method for characterizing the a multidimensional entangled state based on very sparse measurement data. The generality of our method may find application in other physical platforms. Combined with the use of a quantum memory our approach offers promising perspectives for quantum communications based on multi-dimensional entanglement.

Our method also serves as tool for certifying the dimensionality of entanglement. While we could certify 3×3 entanglement, higher dimension could be reached by improving the state preparation and the measurement apparatus to achieve higher visibilities, or even use additional interferometers. Another possible direction would be perform device-independent tests of the degree of entanglement (Moroder et al. 2013) and its dimensionality (Brunner et al. 2008).

8 Large entanglement

Entanglement is the most striking feature of quantum mechanics which is usually attributed to microscopic objects. Recent theoretical and experimental progress in quantum physics is now opening new ways to observe quantum effects at macroscopic scale involving large number of photons or atoms.

The question whether macroscopic quantum effects can in principle be observed in macroscopic systems remains unsolved to date. The possibility to observe quantum effects using classical devices can lead to the creation of new quantum-enhanced metrological techniques since these effects are extremely sensitive to the losses and decoherence. While the violation of classical physics using macroscopic quantum systems is intriguing from the fundamental point of view to test macrorealism (Leggett et al. 1985).

In this chapter we discuss the key points of the performed experiments which demonstrate quantum correlations between a single photon and few tens of atomic excitations in the crystal. The potential to use such entangled state for the direct observation of the micro-macro quantum superpositions is discussed. For details we refer to the original publications that are presented in the Appendix.

8.1 Micro-macro entanglement

The definition of quantum macroscopicity is a source of many debates from which various theoretical approaches have been developed. Two main problems are the quantification of macroscopicity and the quantification of the macroscopic distinctness of the states in a quantum superpositions. Some approaches for definition of macroscopic distinctness can be found in (Leggett 2002; Dür et al. 2002; Fröwis et al. 2012) and especially for optical states (Sekatski et al. 2014a; Jeong et al. 2015; Laghaout et al. 2015).

There are many purely quantum effects which can be observed at macroscopic scale using classical devices: superfluidity and superconductivity are only some of them. However, these examples are based on quantum effects at microscopic scale which are coherently added together and the quantumness in their case does not involve macroscpoic degrees of freedom. The

observation of the macroscopic quantum superpositions is the main exper-
imental challenge in this direction (Leggett 1980; Martinis et al. 1987). The
non-classical effects have so far only been observed for microscopic objects
or microscopic properties of larger objects (Julsgaard et al. 2001; Martini et
al. 2008; Bruno et al. 2013; Lvovsky et al. 2013; Gerlich et al. 2011). While the
experimental generation of Schrödinger cat states so far was possible only
involving few of atoms or photons (Monroe et al. 1996; Ourjoumtsev et al.
2007).

The observation of macroscopically distinct states which are involved
to the quantum superpositions nowadays lies outside of the experimen-
tally feasible domain and requires measurements of macroscopically coarse-
grained observables. One of the potential realizations is based on the dis-
placement operation applied on one of the modes of the entangled single
photon state and further use of coarse grained measurement (Sekatski et al.
2014b). And potentially coupling to the optomechanical system (Ghobadi
et al. 2014).

8.1.1   Displacement of the entangled state

One of the ways to create micro-macro entangled state by use of dis-
placement operation on on eof the modes of entangled state. The displace-
ment operation can be performed by combining target state $|\psi\rangle$ with the
coherent state with amplitude α on a highly transmittive beamsplitter with
reflection amplitude r. The result will be displaced target state $\mathcal{D}(r\alpha)|\psi\rangle$
(Peres 1996).

First let's consider a polarization entangled photon pair

$$|\psi\rangle = \frac{1}{\sqrt{2}}(|1,0\rangle_s |1,0\rangle_i + |0,1\rangle_s |0,1\rangle_i), \tag{8.1}$$

where s and i subscripts are two modes corresponding to the generated
signal and *idler* single photon, while $|1,0\rangle_{s(i)} \equiv |H\rangle_{s(i)}$ and $|0,1\rangle_{s(i)} \equiv |V\rangle_{s(i)}$
correspond to the horizontal polarization state of the signal (idler) photon
and the vertical polarization state, respectively.

By displacing one of the photons in the certain polarization mode (hori-
zontal in this case) entangled state will become analogous to the recent ex-
periments (Lvovsky et al. 2013; Bruno et al. 2013):

$$|\Psi\rangle = \frac{1}{\sqrt{2}} \left[(\mathcal{D}_H^s(\alpha)|1,0\rangle)_s |1,0\rangle_i + |\alpha,1\rangle_s |0,1\rangle_i \right]. \tag{8.2}$$

This micro-macro entangled state (denoted with a capital Ψ for emphasis)
contains a displaced single-photon state of the form $\mathcal{D}(\alpha)|1\rangle$ in the first
term, and a coherent state $|\alpha\rangle = \mathcal{D}(\alpha)|0\rangle$ in the second. The idler photon
plays the role of the "micro" component of the entangled state. While two
states $\mathcal{D}(\alpha)|1\rangle$ and $\mathcal{D}(\alpha)|0\rangle$ are considered as macroscopically distinguish-
able.

The main argument is that they can be distinguished using coarse grained
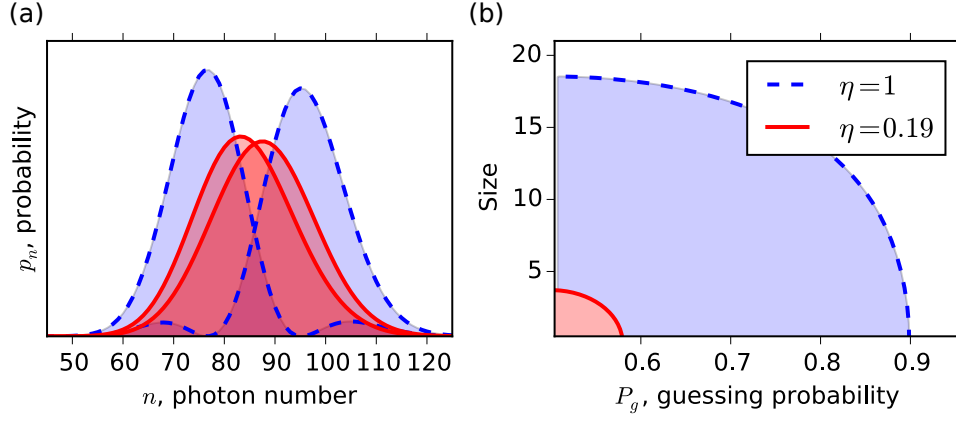
FIGURE 8.1: Theoretical model for the size of the superposition state. (a) Mean photon number distributions of the two macroscopic components of the state (8.2) written in the $\{|0\rangle + |1\rangle, |0\rangle - |1\rangle\}$ basis in the case of perfect transmission $\eta = 1$ (dashed blue line), or including experimental losses (solid red line). (b) Size of the superposition state (Sekatski et al. 2014b) prepared before the QM for the maximum mean photon number $|\alpha|^2 = 86(3)$ as a function of the guessing probability P_g to distinguish two macroscopic components of state (8.2) without (dash line, blue) and including (solid, red) the losses up to the first displacement.

detector with limited photon number resolution. For example the variance of a coherent state is $|\alpha|^2$, while the variance of the displaced single photon is three times bigger, $3|\alpha|^2$ (Oliveira et al. 1990). Using a classical threshold detector with the noise much smaller than the variance $|\alpha|^2$ one could distinguish the two states with a maximal probability of 74%.

By changing the measurement basis and considering the states $\mathcal{D}(|0\rangle + |1\rangle)$ and $\mathcal{D}(|0\rangle - |1\rangle)$ the probability can reach 91% due to the different mean energy of these two states (Fig. 8.1(a)). Indeed the state 8.2 can be written as

$$[\mathcal{D}_H^s(\alpha)(|0\rangle_{Hs} + |1\rangle_{Hs})] (|0\rangle_{Vs} |1, 0\rangle_i + |1\rangle_{Vs} |0, 1\rangle_i) -$$
$$- [\mathcal{D}_H^s(\alpha)(|0\rangle_{Hs} - |1\rangle_{Hs})] (|0\rangle_{Vs} |1, 0\rangle_i - |1\rangle_{Vs} |0, 1\rangle_i), \quad (8.3)$$

where the $\mathcal{D}_H^s(\alpha)(|0\rangle + |1\rangle)$ and $\mathcal{D}_H^s(\alpha)(|0\rangle - |1\rangle)$ components clearly appear in superposition, as part of the micro-macro entangled state. Hence, by projecting the idler photon on the diagonal or antidiagonal states and measuring the V-mode of the signal photon in the $(|0\rangle \pm |1\rangle)$ basis, one can obtain in the horizontal mode of the signal photon one of the these two states and possibly try to distinguish them with a coarse-grained detector.

Importantly, increasing $|\alpha|$ makes these two terms become more and more distinguishable when using a coarse-grained detector (Sekatski et al. 2014b).

8.1.2   Size of the macroscopic quantum states

To define the size of macroscopic quantum states in optics domain different approaches could be considered (Sekatski et al. 2014a; Jeong et al. 2015; Laghaout et al. 2015). One of the ideas (Sekatski et al. 2014a) is to characterize the size of the macroscopic correlations by the maximum coarse-graining $\sigma_{\max}$ that allows one to distinguish the two components of the quantum superposition with a given probability P_g, where P_g should be significantly above 50% to be meaningful for a single-shot measurement. Using this method, the effective size can be evaluated by comparing the results to an archetypical state involving the superposition of $|0\rangle$ and $|N\rangle$ Fock states, where N is the smallest value that allows distinguishing $|0\rangle$ from $|N\rangle$ with a probability P_g and a coarse graining $\sigma_{\max}$ (Fig. 8.1(b)).

All the losses in the signal mode before the beamsplitter used for the displacement, and before the detection has to eliminated in order to maximize the size of the directly observed macroscopic quantum states. The loss and finite efficiency of the detectors reduce the maximum probability to distinguish the two macroscopic states which makes direct observation of micro-macro entangled states technically challenging.

8.1.3   Experiment

Our experiment is conceptually represented on Fig. 8.2. First, a entangled photon pair is generated in the state (8.1) To displace one of the polarization modes of s, the signal photon is combined with an horizontally-polarized coherent state pulse on a highly transmittive beam splitter. This corresponds to the unitary displacement operation $\mathcal{D}_H^s(\alpha)$ of the horizontal mode of the signal photon. This leads to the generated photonic micro-macro state (8.2).

We then use a quantum memory protocol to map this all-optical state to a light-matter micro-macro entangled state. Specifically, the state of the signal mode is coherently mapped to the collective state of an ensemble of neodymium ions. To store light with an arbitrary polarization, we use a configuration consisting of two inline neodymium-doped yttrium orthosilicate crystals $Nd^{3+}:Y_2SiO_5$ separated by a half-wave plate (HWP). This configuration was previously used to faithfully store polarization qubits Clausen et al. 2012; Gündoğan et al. 2012; Zhou et al. 2012b. The bandwidth of the prepared AFC quantum memory is 600 MHz and stores photons for 50 ns with an overall efficiency of $\eta = 4.6(2)\%$.

The number of atoms part of the collective state is about 10 billions, and the number of excited atoms is as high as 35. After a pre-determined storage time τ_s of 50 ns, the stored state is mapped back to an optical mode with an efficiency η.

As part of the measurement, the retrieved state is superimposed with another displacement $\mathcal{D}_H^s(-\sqrt{\eta}\alpha)$ pulse, delayed by τ_s with respect to $\mathcal{D}_H^s(\alpha)$, whose role is to undo the initial displacement. This yields the original
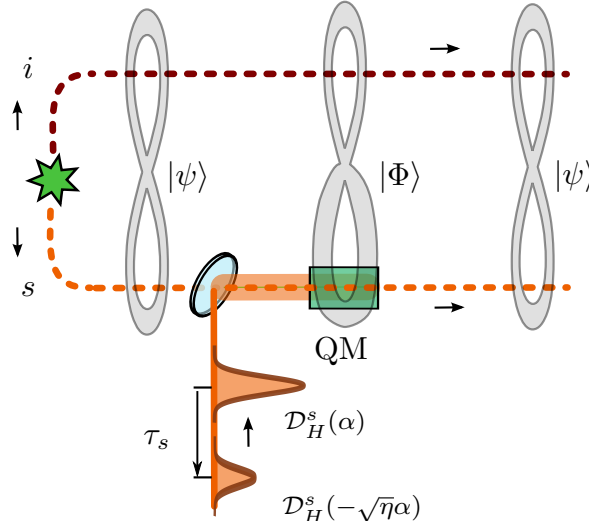
FIGURE 8.2: Experimental scheme. Conceptual scheme for generation, storage and analysis of the macroscopic quantum state (8.2). First, a displacement operation $\mathcal{D}_H^s(\alpha)$ is applied on signal mode of the micro-micro polarization entangled state $|\psi\rangle$ using highly transmittive beam splitter (BS). The displaced signal photon of the micro-macro state is then mapped inside a solid-state quantum memory (QM) that has a storage and retrieval efficiency η. To characterize the state after storage, it is first displaced back to $|\psi\rangle$ (in the ideal case) when it it retrieved from the memory using $\mathcal{D}_H^s(-\sqrt{\eta}\alpha)$, and is then analyzed using various entanglement witnesses.

micro-micro entangled state which can then be analyzed using various entanglement witnesses. The two displacement operations are performed locally and they cannot increase the entanglement of the state. This means that the amount of entanglement found in the final micro-micro entangled state is a lower bound for the entanglement of the light-matter micro-macro state. In practice, the second displacement is not perfect, which gradually decreases the amount of entanglement left in the micro-micro state as the size of the first displacement increases. This constitutes the ultimate limit on the size of the macro part of our state.

In practice, the quantum memory itself was used to implement second displacement operation. Light incident on the QM is either unabsorbed and transmitted with probability $T \approx 55\%$, or it can be absorbed with probability $\eta_{\text{abs}} \approx 45\%$ and retrieved from the QM after τ_s (with an overall probability η), or absorbed and kept inside the QM after τ_s. This was used to prepare the displacement pulses and to store the micro-macro entangled state.

8.1.4 Results and conclusion

In our experiment, with the maximum mean number of atomic excitations of ≈ 47 it was possible to demonstrate the presence of entanglement in the system. This corresponds to initial displacement operation containing $|\alpha^2| = 86$ photons in average. The CHSH inequality violations and the quantum state tomography of the polarization entangled state (Eq. (8.1))
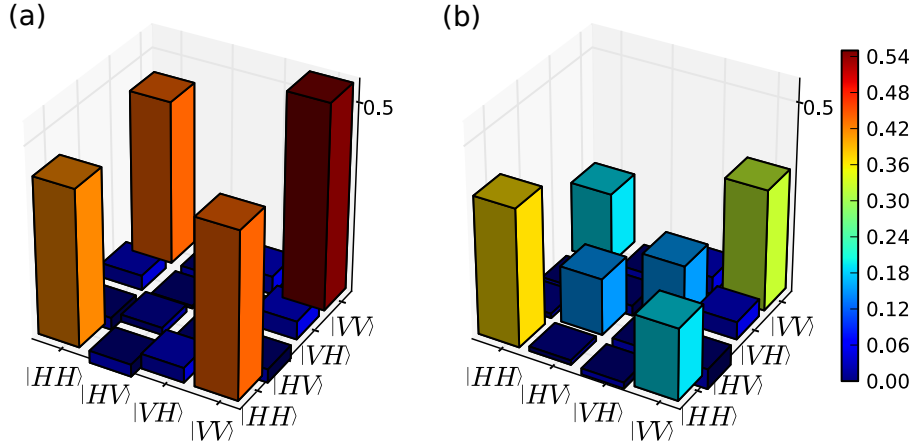
FIGURE 8.3: Example of quantum state tomography results. (a) Real part of the reconstructed density matrix of the micro-micro state with no displacement, after storage in the quantum memory. The fidelity with the target state $|\Psi\rangle$ of Eq. (8.1) is 96(2)%. (b) One instance of the real part of the reconstructed density matrix of a micro-micro entangled state after both displacements and storage in the QM. The size of the displacement was $|\alpha^2| = 72(3)$ before the QM. The corresponding values of the PPT test is -0.059(10) and of the concurrence is 0.131(22). The values of the imaginary parts are all below 0.05.

were applied (Fig. 8.3) to reconstruct the state and verify the presence of entanglement for different size of the initial displacement operation (Fig. 8.4).

In ideal case, the displacement back operation should remain the initial state (8.1) unchanged. However, the resulting state always contains some noise pollution due interferometric instability between two displacement operations. And when the displacement is getting larger, it becomes increasingly difficult to demonstrate that the entanglement is still present in the optical state that is obtained after re-emission by the memory. Observing this behaviour further supports that our quantum state has physically interesting quantum macroscopic properties. In previous publications, it has been shown that this is a feature inherent to micro-macro quantum states produced with displacements (Bruno et al. 2013; Lvovsky et al. 2013). The main difference of our approach comparing with previous experiments is the demonstration of light-matter micro-macro entangled state and the use of a CHSH inequality violation to probe entanglement.

Hence, in our experiment we could have displaced the single photon with more light (and created more atomic excitations), but we would have been unable to show that we had entanglement, due to the increased sensitivity of the entanglement measurement procedure with respect to the fluctuating experimental conditions.

To summarize, we created a state that involves the superposition of two components that are more and more easy to distinguish with a classical detector as the size grows, but at the same time this makes it increasingly difficult to reveal its quantum properties (entanglement). This captures the
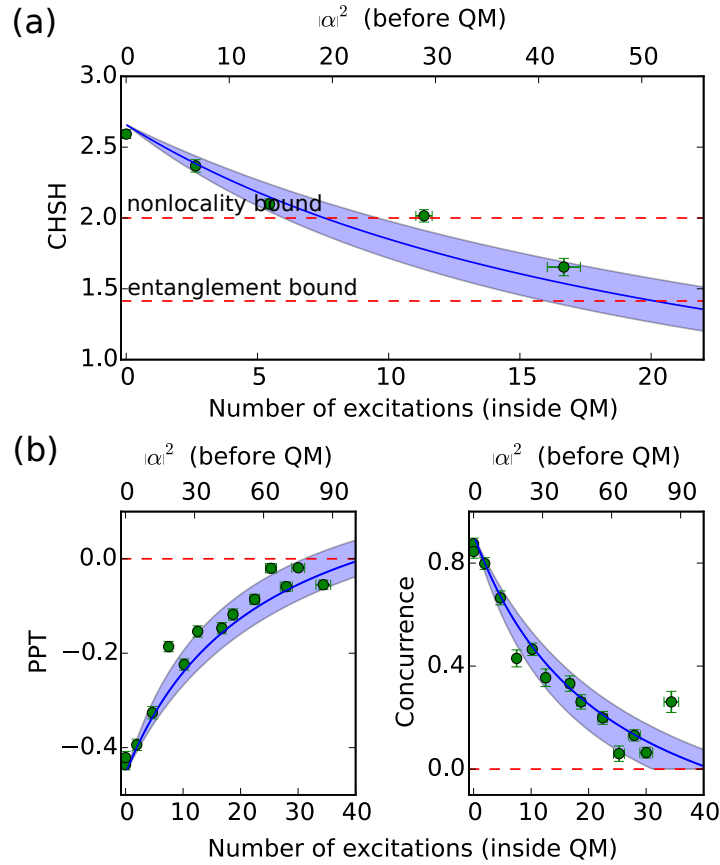
FIGURE 8.4: Results. (a) Measured values of the S parameter of the CHSH Bell inequality (dots) as a function of the size of the displacement before the QM (top x-axis) or as a function of the average number of atomic excitations inside the QM (bottom x-axis). CHSH violation values are above the local bound with up to $5.4(1)$ excitations on average, and above the entanglement bound with up to $16.7(6)$ excitations. The error bars are estimated assuming Poisson statistics for the counts. (b) PPT and concurrence values (obtained from quantum state tomography) as a function of the size of the displacement before the QM (top x-axis) or as a function of the average number of atomic excitations inside the QM (bottom x-axis). The solid line is a theoretical model The error bars are estimated from the Monte-Carlo simulation. The PPT criteria remains negative and the concurrence value remains positive with up to $34(2)$ excitations on average. The solid lines in all graphs are obtained from a theoretical model based on the independently measured parameters, and the shaded areas stem from the uncertainty on these parameters.

essence of why it is very difficult to observe quantum effects such as quantum superpositions in macroscopic systems (Fig. 8.1). From our results, which are well reproduced by our theoretical model based on independent measurements, we can confidently give an estimate of the size of the light-matter state from which the entanglement is measured. For $P_g = 2/3$, the state is analogous to the state $|\uparrow\rangle |0\rangle + |\downarrow\rangle |N\rangle$ with $N \approx 13$, where $|\uparrow\rangle$ and $|\downarrow\rangle$ represent microscopic orthonormal states.

In particular, by storing our optical states in quantum memories we do not only harness entanglement between a single photon and a "macroscopic" light pulse, but also store the later in matter. We also emphasize that our experiment is, to the best of our knowledge, the first one to implement this macroscopic part of entangled state in matter.

9   Conclusion and Outlook

In this chapter we summarize all the results presented in this thesis and published articles. We also discuss possible improvements and further developments in the context of quantum communications and quantum information.

Conclusions

We have experimentally demonstrated that the atomic frequency comb quantum memory protocol implemented in the rare-earth ion-doped crystals is suitable for future applications in quantum communication and quantum information processing. For this, the series of experiments involving storage of quantum light entangled in different degrees of freedom have been realized. First, we have demonstrated quantum teleportation of a photonic polarization qubit at telecommunication wavelength onto the state of a solid-state quantum memory - one of the building blocks of the quantum repeater scheme. Furthermore, the storage of the hyperentangled photonic states suitable for long-distance quantum communication and potentially useful for quantum purification has been implemented. The temporal multimode capacity - one of the basic features of solid-state quantum memories based on the atomic frequency protocol - has been demonstrated using entangled photon pairs. All together, these results demonstrate the core requirements to realize quantum repeaters and pave the way towards long-distance quantum communication based on solid-state technologies.

By increasing the size of the quantum states one can probe the limits of the quantum physics by trying to observe quantum effects (entanglement and superposition) on macroscopic scales. While the definition of "macroscopic" quantum states is still a source of numerous debates, this question triggered many experimental efforts to investigate this regime using purely photonic or atomic systems. In one of the experiments using our quantum memory, we have implemented a direct interface between a family of micro-macro entangled photonic states and an atomic ensemble in our crystal. Due to the limited storage efficiency of this interface, direct observation of macroscopic quantum effects was not possible. However, using indirect methods we were able to observe quantum correlations between the single photon and the atomic ensemble containing up to 40 atomic excitations. Further improvements of the single photon source with higher heralding

efficiencies and the development of quantum memories with storage efficiencies close to the unity will open a way to observe macroscopic quantum effects involving different types of systems, including light and matter.

Outlook

Solid-state quantum memories for quantum networks

The creation of a highly efficient light-matter interface capable of reversibly mapping various quantum states of light into matter is one of the most prominent goals in the field of long-distance quantum communication. The necessity to create quantum memories with near perfect quantum efficiency, long storage time and high multimode capacity was initially motivated mostly from the practical aspects of quantum communication. It should allow one to extend current quantum technologies (like quantum key distribution) towards longer distances. While most of the main components for long-distance quantum communication separately have been demonstrated, their combination and direct implementation for practical use remains unfulfilled. All these require both the creation of the fast and pure source of entangled photons and ideal quantum memories capable to efficiently store them and read out on-demand. This is a challenging task for which research and the development of new materials, compatible with certain quantum memory protocols, are necessary.

In this context, rare-earth ion-doped crystals have many advantages in terms of practical implementations and flexibility in the choice of wavelength and crystal host. The rich energy level structure offers a great number of possibilities to implement quantum memory protocols, but at the same time makes the preparation of the atomic states very challenging. The presence of a Λ-system in the energy structure is one of the requirements for most of the quantum memory protocols. So far, non-Kramers ions, in particular Pr^{3+} and Eu^{3+}, offered great possibility to perform efficient optical pumping on the hyperfine levels together with the spin state manipulation by means of dynamical decoupling. One of the drawbacks is inconvenient visible wavelengths which are not compatible for long distance communication. A lot of efforts are needed to perform high fidelity down-conversion to telecommunication wavelengths in this case.

For this reason Kramers ions, especially Er^{3+}, have more practical spectral properties. However, the search for a Λ-system in Kramers ions is complicated by the strong relaxation mechanisms between magnetic levels. For this reason, optical pumping in these materials is much less efficient and requires the use of particular configurations of the magnetic fields. The efforts to find compatible Λ-system include highly doped samples where pairs of ions (Nd^{3+}-Nd^{3+}) can be spectrally separated (Laplane et al. 2016a) or isotopically pure crystals doped with $^{143}Nd^{3+}$, $^{145}Nd^{3+}$ or $^{167}Er^{3+}$ ions with non-zero nuclear magnetic moments.

Up to now, it has been shown that the optical pumping can be improved for isotopically pure materials. However, big nuclear magnetic moments

($I = 7/2$) of these isotopes lead to an overloaded energy structure which will require new and complicated preparation schemes. This can potentially be overcome in the systems where inhomogeneous broadening is smaller than the hyperfine splitting (for example in Nd^{3+}:$YLiF_4$ (Macfarlane et al. 1998)). Simpler energy level structure can be found in crystals doped with $^{171}Yb^{3+}$ which has low nuclear spin ($I = 1/2$). These materials, particularly $^{171}Yb^{3+}$:Y_2SiO_5, are very promising to realize optical and microwave quantum memories (Welinski et al. 2016).

The main advantage is that the level-splittings for Kramers ions are much larger than for non-Kramers which permits easier spectral separation of the control fields and potentially bigger spectral bandwidth together with the number of temporal modes.

Another advantage of Kramers ions is the possibility to realize the storage of microwave excitations (Wolfowicz et al. 2015). In future, this could be used to implement hybrid quantum networks (Sørensen et al. 2004) to couple stationary superconducting qubits and photonic qubits which are used for communication . For this purpose Er^{3+} doped materials have good potential (Staudt et al. 2012; Probst et al. 2013).

Engineering multimode quantum memories directly combined with a source of entangled photon pairs will greatly simplify the practical implementation of the quantum repeater. It will help to overcome complicated filtering components required to match the operating bandwidth of quantum memories. During this thesis the probability to have a photon before our quantum memory was only 20% due to the losses during the filtering step, while for DLCZ-type scheme this value reaches unity. Research in this direction includes the realization of RASE protocol in Pr^{3+}:Y_2SiO_5 and an AFC-DLCZ quantum memories in Eu^{3+}:Y_2SiO_5 and Pr^{3+}:Y_2SiO_5 crystals. The main problem in this case is the maximum spectral bandwidth which is limited by the hyperfine energy structure.

Another exciting direction of research is the miniaturization of the quantum memories for scalability purposes. The use of integrated waveguide architectures to realize quantum memories includes different materials: Tm^{3+}:$LiNbO_3$ (Saglamyurek et al. 2011), Er^{3+}:LiNbO3 (Staudt et al. 2007) and Pr^{3+}:Y_2SiO_5 (Corrielli et al. 2016). On-chip cavities have been used to enhance light-matter interactions with rare-earth ions using Nd^{3+}:Y_2SiO_5 (Zhong et al. 2015b), Er^{3+}:Y_2SiO_5 (Miyazono et al. 2016), Yb^{3+}:Si_3N_4 (Ding et al. 2016a) and Nd^{3+}:YVO_4 (Zhong et al. 2016).

This cavity approach has been shown to increase the quantum memory efficiency of the AFC protocol up to 56% in Pr^{3+}:Y_2SiO_5 (Sabooni et al. 2013) and in Eu^{3+}:Y_2SiO_5 (Jobez et al. 2014). This technique should lead to quantum efficiencies close to unity even with very low absorbing materials (Afzelius et al. 2010b).

All these techniques combined together should finally allow one to realize elementary links of the quantum repeater based on the rare-earth solid-state technologies involving entanglement between two distant quantum memories. This will be an important step towards practical implementation of the quantum communication.

The search for new materials is another branch for deep research. For example, recently coherence time up to 39 min have been measured for the nuclear spins of ionized donors in enriched ^{28}Si materials (Saeedi et al. 2013). These unique nuclear properties of ^{28}Si, and their application to silicon-based solid-state quantum information research could be also very promising.

"Complex" entanglement

Quantum entanglement is a widespread resource in the field of quantum information and quantum communication. An impressively large number of experiments have been performed in this direction (Pan et al. 2012). The growing complexity of the investigated systems was achieved by increasing the number of particles or using d-level quantum bits (*qudits*). Mutipartite or multidimensional entanglement is a resource for fundamental tests of quantum mechanics as well as a key element for new capacity-increased quantum communication protocols.

Photonic multidimensional entanglement has been implemented using photonic qu*d*it states entangled in different degrees of freedom. For this, orbital angular momentum (Dada et al. 2011; Krenn et al. 2014), frequency (Olislager et al. 2010; Xing et al. 2014; Jin et al. 2016), spatial entanglement (Edgar et al. 2012; Fickler et al. 2014; Schaeff et al. 2015), time-bins (Riedmatten et al. 2002; Stucki et al. 2005; Ikuta et al. 2016) and energy-time (Thew et al. 2004; Richart et al. 2012) were efficiently used. The last two degrees of freedom are the most important for quantum communication since they are well suited for optical fiber technologies (Marcikic et al. 2002).

The ability to store high-dimensional quantum entanglement offers great potential for quantum information applications (Zhou et al. 2015; Ding et al. 2015; Ding et al. 2016b). It would allow one to use the large information capacity of high-dimensional entangled states (Dixon et al. 2012) for quantum communications. In cryptography, for example, it should allow one to maintain the security of the information in realistic situations, in the presence of noise and decoherence (Nunn et al. 2013).

Generating high-dimensional states often is easier than their certification. It is a complex problem usually requiring a large number of resources (high number of projective measurements and access to all the outcomes in the ideal case). During this thesis an entanglement witness was developed to be able to characterize entanglement under the experimental conditions of limited number measurement settings and restricted access to all the measurement outcomes. Such approaches are especially important for physical quantum systems living in multi-dimensional Hilbert spaces or containing large number of quantum particles. In this direction a great number of experiments have been performed (Shalm et al. 2012; Hamel et al. 2014; Hiesmayr et al. 2016; Malik et al. 2016; Reimer et al. 2016) demonstrating the importance of improving entanglement certification procedures for future quantum technologies.

Entanglement in large quantum systems (containing a large number of

particles) is much less established, despite the strong interest motivated by open questions on genuine quantum phenomena on large scales. On the theoretical side, the complexity of entanglement classification just explodes as the number of particles increases. It is therefore desirable to have some key identifiers that allow one to describe and to compare different states and system sizes. In addition, the precise role of entanglement in certain situations is not always entirely clear (e.g., in quantum computation). On the other hand, experimental challenges call for feasible entanglement verification in multipartite quantum systems. For example, access to single particles is often not possible and also collective measurements are typically restricted to certain types and finite resolution. One obvious example is the state of the atomic ensemble used in the storage of a single photon realized in present thesis.

Characterization of this multipartite entanglement involving a very large number of atoms (10^{10} was estimated using fluorescence measurement) without a direct access is extremely challenging. For this, the concept of *entanglement depth* (Sørensen et al. 2001) has to be applied. Entanglement depth is defined as the smallest number of mutually entangled particles that is compatible with the measured data. This simple definition can allow one to witness subgroups of mutually entangled particles in a state-independent and scale-invariant way. This framework has been applied to ensembles of two-level atoms. For example, comparison of first and second moments of collective excitation measurements in different bases give rise to powerful bounds on the entanglement depth (Sørensen et al. 2001; Lücke et al. 2014). Consequently, a large entanglement depth has been measured for so-called squeezed and oversqueezed states (Riedel et al. 2010; Gross et al. 2010; Lücke et al. 2014); recently up to 680 (Hosten et al. 2016). A promising alternative to squeezed states are W states, which are coherent superpositions of a single excitation shared by many atoms. This state is quite robust against particle loss, dephasing and admixture of the ground states. An entanglement depth of around 2900 was measured (Mcconnell et al. 2015).

All these approaches are based on sophisticated experimental techniques and are very specific to the systems under study. The search for observables offering a lower bound on the entanglement depth grounded in general assumptions and using simple experimental apparatus is very important for many-body quantum physics.

Our recent progress in developing solid-state quantum memories based on rare-earth-ion doped crystals for quantum repeaters also offers some ways to transfer optical macroscopic entanglement to solid objects, into which the state of single photons are mapped to the collective state of billions of atoms. This opens new possibilities to study entanglement that is macroscopic in terms of the number of stored modes, bits of entanglement (*e*bits), dimensionality of the quantum states and the number of crystals used for storage.

Bibliography

ABRAGAM, A. and B. Bleaney (1970). *Electron Paramagnetic Resonance of Transition Ions*. 1st. Clarendon Press (cited on p. 47).

ACÍN, A., N. Brunner, N. Gisin, S. Massar, S. Pironio, and V. Scarani (2007). "Device-Independent Security of Quantum Cryptography against Collective Attacks". *Phys. Rev. Lett.* **98** (23), 230501. DOI: 10.1103/PhysRevLett.98.230501 (cited on p. 75).

AFZELIUS, M., C. Simon, H. de Riedmatten, and N. Gisin (2009). "Multi-mode quantum memory based on atomic frequency combs". *Phys. Rev. A* **79** (5), 052329. DOI: 10.1103/PhysRevA.79.052329 (cited on pp. xi, 10, 20, 67).

AFZELIUS, M., I. Usmani, A. Amari, B. Lauritzen, A. Walther, C. Simon, N. Sangouard, J. Minář, H. de Riedmatten, N. Gisin, and S. Kröll (2010a). "Demonstration of Atomic Frequency Comb Memory for Light with Spin-Wave Storage". *Phys. Rev. Lett.* **104** (4), 040503. DOI: 10.1103/PhysRevLett.104.040503 (cited on pp. 22, 49).

AFZELIUS, M. and C. Simon (2010b). "Impedance-matched cavity quantum memory". *Phys. Rev. A* **82**.2, 022310. DOI: 10.1103/PhysRevA.82.022310 (cited on pp. 50, 53, 95).

AHLEFELDT, R. L., M. R. Hush, and M. J. Sellars (2016). "Ultra-narrow optical inhomogeneous linewidth in a stoichiometric rare earth crystal". *arXiv:1601.05013*. eprint: http://arxiv.org/abs/1601.05013 (cited on p. 46).

ALBRECHT, B., P. Farrera, X. Fernandez-Gonzalvo, M. Cristiani, and H. de Riedmatten (2014). "A waveguide frequency converter connecting rubidium-based quantum memories to the telecom C-band". *Nature Comm* **5**, 3376. DOI: 10.1038/ncomms4376 (cited on p. 15).

ALBRECHT, B., P. Farrera, G. Heinze, M. Cristiani, and H. de Riedmatten (2015). "Controlled Rephasing of Single Collective Spin Excitations in a Cold Atomic Quantum Memory". *Phys. Rev. Lett.* **115** (16), 160501. DOI: 10.1103/PhysRevLett.115.160501 (cited on p. 23).

ALEXANDER, A. L., J. J. Longdell, M. J. Sellars, and N. B. Manson (2006). "Photon Echoes Produced by Switching Electric Fields". *Phys. Rev. Lett.* **96** (4), 043602. DOI: 10.1103/PhysRevLett.96.043602 (cited on p. 19).

ALJUNID, S. A., G. Maslennikov, Y. Wang, H. L. Dao, V. Scarani, and C. Kurtsiefer (2013). "Excitation of a Single Atom with Exponentially

Rising Light Pulses". *Phys. Rev. Lett.* **111** (10), 103001. DOI: 10.1103/PhysRevLett.111.103001 (cited on p. 31).

ALTEPETER, J. B., E. R. Jeffrey, and P. G. Kwiat (2006). "Photonic state tomography". *Advances in Atomic, Molecular and Optical Physics*. Elsevier, New York. Chap. 3 (cited on p. 60).

ASPECT, A., J. Dalibard, and G. Roger (1982). "Experimental Test of Bell's Inequalities Using Time- Varying Analyzers". *Phys. Rev. Lett.* **49**.25, 1804–1807. DOI: 10.1103/PhysRevLett.49.1804 (cited on p. ix).

ASPELMEYER, M., T. Jennewein, M. Pfennigbauer, W. R. Leeb, and A. Zeilinger (2003). "Long-distance quantum communication with entangled photons using satellites". *IEEE Journal of Selected Topics in Quantum Electronics* **9**.6, 1541–1551. DOI: 10.1109/JSTQE.2003.820918 (cited on p. 7).

BAO, X.-H., A. Reingruber, P. Dietrich, J. Rui, A. Duck, T. Strassel, L. Li, N.-L. Liu, B. Zhao, and J.-W. Pan (2012). "Efficient and long-lived quantum memory with cold atoms inside a ring cavity". *Nat Phys* **8**.7, 517–521. DOI: 10.1038/nphys2324 (cited on pp. 16, 23).

BARREIRO, J. T., T.-C. Wei, and P. G. Kwiat (2008). "Beating the channel capacity limit for linear photonic superdense coding". *Nat Phys* **4**.4, 282–286. DOI: 10.1038/nphys919 (cited on p. 64).

BEAVAN, S. E., M. P. Hedges, and M. J. Sellars (2012). "Demonstration of Photon-Echo Rephasing of Spontaneous Emission". *Phys. Rev. Lett.* **109** (9), 093603. DOI: 10.1103/PhysRevLett.109.093603 (cited on p. 25).

BELL, J. (1964). "On the Einstein-Podolsky-Rosen paradox". *Physics* **1**, 195 (cited on pp. ix, 3, 5).

BENNETT, C. H. and G. Brassard (1984). "Quantum Key Distribution and coin tossing". *Proceedings of the IEEE International Conference on Computers, Systems, and Signal Processing*. 175–179. DOI: 10.1016/j.tcs.2014.05.025 (cited on p. ix).

BENNETT, C. H., G. Brassard, C. Crépeau, R. Jozsa, A. Peres, and W. K. Wootters (1993). "Teleporting an unknown quantum state via dual classical and Einstein-Podolsky-Rosen channels". *Phys. Rev. Lett.* **70** (13), 1895–1899. DOI: 10.1103/PhysRevLett.70.1895 (cited on pp. x, 7, 9, 59).

BENNETT, C. H., H. J. Bernstein, S. Popescu, and B. Schumacher (1996a). "Concentrating partial entanglement by local operations". *Phys. Rev. A* **53** (4), 2046–2052. DOI: 10.1103/PhysRevA.53.2046 (cited on p. 9).

BENNETT, C. H., G. Brassard, S. Popescu, B. Schumacher, J. A. Smolin, and W. K. Wootters (1996b). "Purification of Noisy Entanglement and Faithful Teleportation via Noisy Channels". *Phys. Rev. Lett.* **76**.5, 722–. DOI: 10.1103/PhysRevLett.76.722 (cited on p. 9).

BOLLER, K.-J., A. Imamoğlu, and S. E. Harris (1991). "Observation of electromagnetically induced transparency". *Phys. Rev. Lett.* **66** (20), 2593–2596. DOI: `10.1103/PhysRevLett.66.2593` (cited on p. 17).

BONAROTA, M., J. Ruggiero, J. L. L. Gouët, and T. Chanelière (2010). "Efficiency optimization for atomic frequency comb storage". *Phys. Rev. A* **81** (3), 033803. DOI: `10.1103/PhysRevA.81.033803` (cited on p. 20).

BONAROTA, M, J.-L. L. Gouët, and T Chanelière (2011). "Highly multimode storage in a crystal". *New Journal of Physics* **13**.1, 013013. DOI: `10.1088/1367-2630/13/1/013013` (cited on pp. 15, 22, 67).

BOSCHI, D., S. Branca, F. De Martini, L. Hardy, and S. Popescu (1998). "Experimental Realization of Teleporting an Unknown Pure Quantum State via Dual Classical and Einstein-Podolsky-Rosen Channels". *Phys. Rev. Lett.* **80** (6), 1121–1125. DOI: `10.1103/PhysRevLett.80.1121` (cited on p. 64).

BÖTTGER, T., C. W. Thiel, R. L. Cone, and Y. Sun (2009). "Effects of magnetic field orientation on optical decoherence in $Er^{3+} : Y_2SiO_5$". *Phys. Rev. B* **79** (11), 115104. DOI: `10.1103/PhysRevB.79.115104` (cited on p. 48).

BOUWMEESTER, D., J.-W. Pan, K. Mattle, M. Eibl, H. Weinfurter, and A. Zeilinger (1997). "Experimental quantum teleportation". *Nature* **390**.6660, 575–579. DOI: `10.1038/37539` (cited on p. x).

BRAUNSTEIN, S. L. and P. van Loock (2005). "Quantum information with continuous variables". *Rev. Mod. Phys.* **77** (2), 513–577. DOI: `10.1103/RevModPhys.77.513` (cited on p. 3).

BRIEGEL, H.-J., W. Dür, J. I. Cirac, and P. Zoller (1998). "Quantum Repeaters: The Role of Imperfect Local Operations in Quantum Communication". *Phys. Rev. Lett.* **81**.26, 5932–5935. DOI: `10.1103/PhysRevLett.81.5932` (cited on pp. x, 7).

BRUNNER, N., S. Pironio, A. Acin, N. Gisin, A. A. Méthot, and V. Scarani (2008). "Testing the Dimension of Hilbert Spaces". *Phys. Rev. Lett.* **100** (21), 210503. DOI: `10.1103/PhysRevLett.100.210503` (cited on p. 84).

BRUNO, N., A. Martin, P. Sekatski, N. Sangouard, R. T. Thew, and N. Gisin (2013). "Displacement of entanglement back and forth between the micro and macro domains". *Nat. Phys.* **9** (9), 545–548. DOI: `10.1038/nphys2681` (cited on pp. 86, 90).

BUSSIÈRES, F., N. Sangouard, M. Afzelius, H. de Riedmatten, C. Simon, and W. Tittel (2013). "Prospective applications of optical quantum memories". *Journal of Modern Optics* **60**.18, 1519–1537. DOI: `10.1080/09500340.2013.856482` (cited on pp. x, 11).

BUSSIÈRES, F., C. Clausen, A. Tiranov, B. Korzh, V. B. Verma, S. W. Nam, F. Marsili, A. Ferrier, P. Goldner, H. Herrmann, C. Silberhorn, W. Sohler, M. Afzelius, and N. Gisin (2014). "Quantum teleportation

from a telecom-wavelength photon to a solid-state quantum memory". *Nat. Photon.* **8**.10, 775–778 (cited on p. 56).

BUSTARD, P. J., R. Lausten, D. G. England, and B. J. Sussman (2013). "Toward Quantum Processing in Molecules: A THz-Bandwidth Coherent Memory for Light". *Phys. Rev. Lett.* **111** (8), 083901. DOI: 10.1103/PhysRevLett.111.083901 (cited on pp. 15, 23).

CERF, N. J., M. Bourennane, A. Karlsson, and N. Gisin (2002). "Security of Quantum Key Distribution Using *d*-Level Systems". *Phys. Rev. Lett.* **88** (12), 127902. DOI: 10.1103/PhysRevLett.88.127902 (cited on p. 75).

CHEN, Y.-H., M.-J. Lee, I.-C. Wang, S. Du, Y.-F. Chen, Y.-C. Chen, and I. A. Yu (2013). "Coherent Optical Memory with High Storage Efficiency and Large Fractional Delay". *Phys. Rev. Lett.* **110** (8), 083601. DOI: 10.1103/PhysRevLett.110.083601 (cited on p. 17).

CHO, Y.-W., G. T. Campbell, J. L. Everett, J. Bernu, D. B. Higginbottom, M. T. Cao, J. Geng, N. P. Robins, P. K. Lam, and B. C. Buchler (2016). "Highly efficient optical quantum memory with long coherence time in cold atoms". *Optica* **3**.1, 100–107. DOI: 10.1364/OPTICA.3.000100 (cited on pp. 14, 16).

CHOI, K. S., A. Goban, S. B. Papp, S. J. van Enk, and H. J. Kimble (2010). "Entanglement of spin waves among four quantum memories". *Nature* **468**.7322, 412–416. DOI: 10.1038/nature09568 (cited on p. 23).

CHRIST, A., K. Laiho, A. Eckstein, K. N. Cassemiro, and C. Silberhorn (2011). "Probing multimode squeezing with correlation functions". *New Journal of Physics* **13**.3, 033027. DOI: 10.1088/1367-2630/13/3/033027 (cited on p. 28).

CIRAC, J. I., P. Zoller, H. J. Kimble, and H. Mabuchi (1997). "Quantum State Transfer and Entanglement Distribution among Distant Nodes in a Quantum Network". *Phys. Rev. Lett.* **78** (16), 3221–3224. DOI: 10.1103/PhysRevLett.78.3221 (cited on p. 16).

CIREL'SON, B. S. (1980). "Quantum generalizations of Bell's inequality". *Letters in Mathematical Physics* **4**.2, 93–100. DOI: 10.1007/BF00417500 (cited on pp. 9, 14).

CLAUSEN, C. (2013). "Solid-state light-matter interfaces on the quantum test bench". PhD thesis. University of Geneva (cited on p. 29).

CLAUSEN, C., I. Usmani, F. Bussières, N. Sangouard, M. Afzelius, H. de Riedmatten, and N. Gisin (2010). "Quantum Storage of Photonic Entanglement in a Crystal". *Nature* **469**.7331, 508–511. DOI: 10.1038/nature09662 (cited on pp. xi, 22, 50, 59, 65).

CLAUSEN, C., F. Bussières, M. Afzelius, and N. Gisin (2012). "Quantum Storage of Heralded Polarization Qubits in Birefringent and Anisotropically Absorbing Materials". *Phys. Rev. Lett.* **108**.19, 190503. DOI: 10.1103/PhysRevLett.108.190503 (cited on pp. 22, 50, 57, 65, 69, 88).

CLAUSER, J. F., M. A. Horne, A. Shimony, and R. A. Holt (1969). "Proposed Experiment to Test Local Hidden-Variable Theories". *Phys. Rev. Lett.* **23** (15), 880–884. DOI: `10.1103/PhysRevLett.23.880` (cited on pp. ix, 5, 9, 36).

COLLINS, M. J., C. Xiong, I. H. Rey, T. D. Vo, J. He, S. Shahnia, C. Reardon, T. F. Krauss, M. J. Steel, A. S. Clark, and B. J. Eggleton (2013). "Integrated spatial multiplexing of heralded single-photon sources". *Nature Communications* **4**. DOI: `10.1038/ncomms3582` (cited on p. 70).

CORRIELLI, G., A. Seri, M. Mazzera, R. Osellame, and H. de Riedmatten (2016). "Integrated Optical Memory Based on Laser-Written Waveguides". *Phys. Rev. Applied* **5** (5), 054013. DOI: `10.1103/PhysRevApplied.5.054013` (cited on p. 95).

CURTZ, N., R. Thew, C. Simon, N. Gisin, and H. Zbinden (2010). "Coherent frequency-down-conversion interface for quantum repeaters". *Opt. Express* **18**.21, 22099–22104. DOI: `10.1364/OE.18.022099` (cited on p. 15).

DADA, A., J. Leach, G. Buller, M. Padgett, and E. Andersson (2011). "Experimental high-dimensional two-photon entanglement and violations of generalized Bell inequalities". *Nature Physics* **7**.9, 677–680. DOI: `10.1038/nphys1996` (cited on p. 96).

DEUTSCH, D. (1985). "Quantum Theory, the Church-Turing Principle and the Universal Quantum Computer". *Proceedings of the Royal Society of London A: Mathematical, Physical and Engineering Sciences* **400**.1818, 97–117. DOI: `10.1098/rspa.1985.0070` (cited on p. x).

DICKE, R. H. (1954). "Coherence in Spontaneous Radiation Processes". *Phys. Rev.* **93** (1), 99–110. DOI: `10.1103/PhysRev.93.99` (cited on p. 17).

DIEKE, G. H., H. M. Crosswhite, and C. Hannah (1968). *Spectra and energy levels of rare earth ions in crystals*. Interscience Publishers (cited on p. 42).

DIEKS, D. (1982). "Communication by EPR devices". *Physics Letters A* **92**.6, 271–272. DOI: `10.1016/0375-9601(82)90084-6` (cited on p. ix).

DING, D., L. M. C. Pereira, J. F. Bauters, M. J. R. Heck, G. Welker, A. Vantomme, J. E. Bowers, M. J. A. de Dood, and D. Bouwmeester (2016a). "Multidimensional Purcell effect in an ytterbium-doped ring resonator". *Nature Photonics* **10**, 385–388. DOI: `10.1038/nphoton.2016.72` (cited on p. 95).

DING, D. S., W. Zhang, Z. Y. Zhou, S. Shi, G. Y. Xiang, X. S. Wang, Y. K. Jiang, B. S. Shi, and G. C. Guo (2015). "Quantum storage of orbital angular momentum entanglement in an atomic ensemble". *Physical Review Letters* **114**.5, 1–5. DOI: `10.1103/PhysRevLett.114.050502` (cited on p. 96).

DING, D.-S., W. Zhang, S. Shi, Z.-Y. Zhou, Y. Li, B.-S. Shi, and G.-C. Guo (2016b). "High-dimensional entanglement between distant atomic

ensemble memories". *arXiv:* **1412.6188**, 1–15. eprint: `https://arxiv.org/abs/1412.6188` (cited on pp. 76, 96).

DIRAC, P. A. M. (1939). "A new notation for quantum mechanics". *Mathematical Proceedings of the Cambridge Philosophical Society* **35** (03), 416–418. DOI: `10.1017/S0305004100021162` (cited on p. 1).

DIXON, P. B., G. A. Howland, J. Schneeloch, and J. C. Howell (2012). "Quantum mutual information capacity for high-dimensional entangled states". *Physical Review Letters* **108**.14, 1–5. DOI: `10.1103/PhysRevLett.108.143603` (cited on p. 96).

DONOHUE, J. M., J. Lavoie, and K. J. Resch (2014). "Ultrafast Time-Division Demultiplexing of Polarization-Entangled Photons". *Physical Review Letters* **113**.16, 163602. DOI: `10.1103/PhysRevLett.113.163602` (cited on p. 70).

DUAN, L.-M., M. D. Lukin, J. I. Cirac, and P. Zoller (2001). "Long-distance quantum communication with atomic ensembles and linear optics". *Nature* **414**.6862, 413–418. DOI: `10.1038/35106500` (cited on pp. 13, 16, 23, 24).

DUAN, L.-M., G. Giedke, J. I. Cirac, and P. Zoller (2000). "Inseparability Criterion for Continuous Variable Systems". *Phys. Rev. Lett.* **84** (12), 2722–2725. DOI: `10.1103/PhysRevLett.84.2722` (cited on pp. 4, 25).

DÜR, W., C. Simon, and J. I. Cirac (2002). "Effective Size of Certain Macroscopic Quantum Superpositions". *Phys. Rev. Lett.* **89** (21), 210402. DOI: `10.1103/PhysRevLett.89.210402` (cited on p. 85).

EDGAR, M., D. Tasca, F. Izdebski, R. Warburton, J. Leach, M. Agnew, G. Buller, R. Boyd, and M. Padgett (2012). "Imaging high-dimensional spatial entanglement with a camera". *Nature Communications* **3**.May, 984–986. DOI: `10.1038/ncomms1988` (cited on p. 96).

EINSTEIN, A., B. Podolsky, and N. Rosen (1935). "Can Quantum-Mechanical Description of Physical Reality Be Considered Complete?" *Phys. Rev.* **47** (10), 777–780. DOI: `10.1103/PhysRev.47.777` (cited on pp. ix, 1).

EKERT, A. K. (1991). "Quantum cryptography based on Bell's theorem". *Phys. Rev. Lett.* **67** (6), 661–663. DOI: `10.1103/PhysRevLett.67.661` (cited on p. ix).

ENGLAND, D. G., P. J. Bustard, J. Nunn, R. Lausten, and B. J. Sussman (2013). "From Photons to Phonons and Back: A THz Optical Memory in Diamond". *Phys. Rev. Lett.* **111** (24), 243601. DOI: `10.1103/PhysRevLett.111.243601` (cited on p. 23).

EQUALL, R. W., Y. Sun, R. L. Cone, and R. M. Macfarlane (1994). "Ultraslow optical dephasing in $Eu^{3+}:Y_2SiO_5$". *Phys. Rev. Lett.* **72** (14), 2179–2182. DOI: `10.1103/PhysRevLett.72.2179` (cited on p. 48).

FERGUSON, K. R., S. E. Beavan, J. J. Longdell, and M. J. Sellars (2016). "Generation of Light with Multimode Time-Delayed Entanglement Using Storage in a Solid-State Spin-Wave Quantum Memory". *Phys. Rev.*

Lett. **117** (2), 020501. DOI: `10.1103/PhysRevLett.117.020501` (cited on p. 25).

FICKLER, R., R. Lapkiewicz, M. Huber, M. P. Lavery, M. J. Padgett, and A. Zeilinger (2014). "Interface between path and orbital angular momentum entanglement for high-dimensional photonic quantum information". *Nature Communications* **5**, 5. DOI: `10.1038/ncomms5502` (cited on p. 96).

FLEISCHHAUER, M. and M. D. Lukin (2000). "Dark-State Polaritons in Electromagnetically Induced Transparency". *Phys. Rev. Lett.* **84** (22), 5094–5097. DOI: `10.1103/PhysRevLett.84.5094` (cited on p. 17).

FRANSON, J. D. (1989). "Bell inequality for position and time". *Phys. Rev. Lett.* **62** (19), 2205–2208. DOI: `10.1103/PhysRevLett.62.2205` (cited on pp. 32, 77).

FRAVAL, E., M. J. Sellars, and J. J. Longdell (2004). "Method of Extending Hyperfine Coherence Times in $Pr^{3+} : Y_2SiO_5$". *Phys. Rev. Lett.* **92** (7), 077601. DOI: `10.1103/PhysRevLett.92.077601` (cited on p. 48).

FREEDMAN, S. J. and J. F. Clauser (1972). "Experimental Test of Local Hidden-Variable Theories". *Phys. Rev. Lett.* **28** (14), 938–941. DOI: `10.1103/PhysRevLett.28.938` (cited on p. ix).

FRÖWIS, F. and W. Dür (2012). "Measures of macroscopicity for quantum spin systems". *New Journal of Physics* **14**.9, 093039. DOI: `10.1088/1367-2630/14/9/093039` (cited on p. 85).

FURUSAWA, A., J. L. Sørensen, S. L. Braunstein, C. A. Fuchs, H. J. Kimble, and E. S. Polzik (1998). "Unconditional Quantum Teleportation". *Science* **282**.5389, 706–709. DOI: `10.1126/science.282.5389.706` (cited on p. x).

GAO, W. B., P. Fallahi, E. Togan, J. Miguel-Sanchez, and A. Imamoglu (2012). "Observation of entanglement between a quantum dot spin and a single photon". *Nature* **491**.7424, 426–430. DOI: `10.1038/nature11573` (cited on p. 16).

GERLICH, S., S. Eibenberger, M. Tomandl, S. Nimmrichter, K. Hornberger, P. J. Fagan, J. Tüxen, M. Mayor, and M. Arndt (2011). "Quantum interference of large organic molecules". *Nature Communications* **2**, 263. DOI: `10.1038/ncomms1263` (cited on p. 86).

GHOBADI, R., S. Kumar, B. Pepper, D. Bouwmeester, A. I. Lvovsky, and C. Simon (2014). "Optomechanical Micro-Macro Entanglement". *Phys. Rev. Lett.* **112** (8), 080503. DOI: `10.1103/PhysRevLett.112.080503` (cited on p. 86).

GIUSTINA, M. et al. (2015). "Significant-Loophole-Free Test of Bell's Theorem with Entangled Photons". *Phys. Rev. Lett.* **115** (25), 250401. DOI: `10.1103/PhysRevLett.115.250401` (cited on p. ix).

GORSHKOV, A. V., A. André, M. Fleischhauer, A. S. Sørensen, and M. D. Lukin (2007). "Universal Approach to Optimal Photon Storage in Atomic

Media". *Phys. Rev. Lett.* **98** (12), 123601. DOI: `10.1103/PhysRevLett.98.123601` (cited on p. 31).

GRAHAM, T. M., H. J. Bernstein, T.-C. Wei, M. Junge, and P. G. Kwiat (2015). "Superdense teleportation using hyperentangled photons". *Nature Communications* **6**.7185, 1–9. DOI: `10.1038/ncomms8185` (cited on p. 64).

GROSS, C., T. Zibold, E. Nicklas, J. Estève, and M. K. Oberthaler (2010). "Nonlinear atom interferometer surpasses classical precision limit". *Nature* **464**.7292, 1165–1169. DOI: `10.1038/nature08919` (cited on p. 97).

GÜHNE, O. and G. Tóth (2009). "Entanglement detection". *Physics Reports* **474**.1-6, 1–75. DOI: `10.1016/j.physrep.2009.02.004` (cited on p. 6).

GÜNDOĞAN, M., M. Mazzera, P. M. Ledingham, M. Cristiani, and H. de Riedmatten (2013). "Coherent Storage of Temporally Multimode Light Using a Spin-Wave Atomic Frequency Comb Memory". *New Journal of Physics* **15**, 045012. DOI: `10.1088/1367-2630/15/4/045012` (cited on p. 67).

GÜNDOĞAN, M., P. M. Ledingham, A. Almasi, M. Cristiani, and H. de Riedmatten (2012). "Quantum Storage of a Photonic Polarization Qubit in a Solid". *Phys. Rev. Lett.* **108** (19), 190504. DOI: `10.1103/PhysRevLett.108.190504` (cited on pp. 57, 88).

GÜNDOĞAN, M., P. M. Ledingham, K. Kutluer, M. Mazzera, and H. de Riedmatten (2015). "Solid State Spin-Wave Quantum Memory for Time-Bin Qubits". *Phys. Rev. Lett.* **114** (23), 230501. DOI: `10.1103/PhysRevLett.114.230501` (cited on pp. 22, 67).

HAMEL, D. R., L. K. Shalm, H. Hübel, A. J. Miller, F. Marsili, V. B. Verma, R. P. Mirin, S. W. Nam, K. J. Resch, and T. Jennewein (2014). "Direct generation of three-photon polarization entanglement". *Nature Photonics* **8**.10, 801–807. DOI: `10.1038/nphoton.2014.218` (cited on p. 96).

HAMMERER, K., M. M. Wolf, E. S. Polzik, and J. I. Cirac (2005). "Quantum Benchmark for Storage and Transmission of Coherent States". *Phys. Rev. Lett.* **94** (15), 150503. DOI: `10.1103/PhysRevLett.94.150503` (cited on p. 3).

HAMMERER, K., A. S. Sørensen, and E. S. Polzik (2010). "Quantum interface between light and atomic ensembles". *Rev. Mod. Phys.* **82**.2, 1041–1093. DOI: `10.1103/RevModPhys.82.1041` (cited on p. x).

HASTINGS-SIMON, S. R., M. Afzelius, M. U. Staudt, B. Lauritzen, H. de Riedmatten, N. Gisin, A. Amari, A. Walther, S. Kröll, E. Cavalli, and M. Bettinelli (2008a). "Spectral hole-burning spectroscopy in $Nd^{3+} : YVO_4$". *Phys. Rev. B* **77** (12), 125111. DOI: `10.1103/PhysRevB.77.125111` (cited on p. 49).

HASTINGS-SIMON, S. R., B. Lauritzen, M. U. Staudt, J. L. M. van Mechelen, C. Simon, H. de Riedmatten, M. Afzelius, and N. Gisin (2008b).

"Zeeman-level lifetimes in Er^{3+} : Y_2SiO_5". *Phys. Rev. B* **78** (8), 085410. DOI: `10.1103/PhysRevB.78.085410` (cited on p. 49).

HAU, L. V., S. E. Harris, Z. Dutton, and C. H. Behroozi (1999). "Light speed reduction to 17 metres per second in an ultracold atomic gas". *Nature* **397**.6720, 594–598. DOI: `10.1038/17561` (cited on p. 17).

HEDGES, M. P., J. J. Longdell, Y. Li, and M. J. Sellars (2010). "Efficient quantum memory for light". *Nature* **465**.7301, 1052–1056. DOI: `10.1038/nature09081` (cited on p. 19).

HEINZE, G., C. Hubrich, and T. Halfmann (2013). "Stopped Light and Image Storage by Electromagnetically Induced Transparency up to the Regime of One Minute". *Phys. Rev. Lett.* **111** (3), 033601. DOI: `10.1103/PhysRevLett.111.033601` (cited on p. 14).

HENSEN, B. et al. (2015). "Loophole-free Bell inequality violation using electron spins separated by 1.3 kilometres". *Nature* **526**.7575, 682–686. DOI: `10.1038/nature15759` (cited on p. ix).

HENTSCHEL, M., H. Hübel, A. Poppe, and A. Zeilinger (2009). "Three-color Sagnac source of polarization-entangled photon pairs". *Opt. Express* **17**.25, 23153–23159. DOI: `10.1364/OE.17.023153` (cited on p. 33).

HÉTET, G., J. J. Longdell, A. L. Alexander, P. K. Lam, and M. J. Sellars (2008). "Electro-Optic Quantum Memory for Light Using Two-Level Atoms". *Phys. Rev. Lett.* **100** (2), 023601. DOI: `10.1103/PhysRevLett.100.023601` (cited on p. 19).

HIESMAYR, B. C., M. J. A. de Dood, and W. Löffler (2016). "Observation of Four-Photon Orbital Angular Momentum Entanglement". *Physical Review Letters* **116**.7, 073601. DOI: `10.1103/PhysRevLett.116.073601` (cited on p. 96).

HOFMANN, J., M. Krug, N. Ortegel, L. Gérard, M. Weber, W. Rosenfeld, and H. Weinfurter (2012). "Heralded Entanglement Between Widely Separated Atoms". *Science* **337**.6090, 72–75. DOI: `10.1126/science.1221856` (cited on p. 16).

HONG, C. K., Z. Y. Ou, and L. Mandel (1987). "Measurement of sub-picosecond time intervals between two photons by interference". *Phys. Rev. Lett.* **59** (18), 2044–2046. DOI: `10.1103/PhysRevLett.59.2044` (cited on p. 37).

HORODECKI, M., P. Horodecki, and R. Horodecki (1996). "Separability of mixed states: necessary and sufficient conditions". *Physics Letters A* **223**.1, 1–8. DOI: `10.1016/S0375-9601(96)00706-2` (cited on p. 6).

HOSSEINI, M., B. Sparkes, G. Campbell, P. Lam, and B. Buchler (2011a). "High efficiency coherent optical memory with warm rubidium vapour". *Nat Commun* **2**, 174. DOI: `10.1038/ncomms1175` (cited on pp. 14, 23).

HOSSEINI, M., G. Campbell, B. M. Sparkes, P. K. Lam, and B. C. Buchler (2011b). "Unconditional room-temperature quantum memory". *Nature Physics* **7**.10, 794–798. DOI: `10.1038/nphys2021` (cited on p. 23).

HOSSEINI, M, B. M. Sparkes, G. T. Campbell, P. K. Lam, and B. C. Buchler (2012). "Storage and manipulation of light using a Raman gradient-echo process". *Journal of Physics B: Atomic, Molecular and Optical Physics* **45**.12, 124004. DOI: `10.1088/0953-4075/45/12/124004` (cited on p. 23).

HOSSEINI, M., B. M. Sparkes, G. Hetet, J. J. Longdell, P. K. Lam, and B. C. Buchler (2009). "Coherent optical pulse sequencer for quantum applications". *Nature* **461**.7261, 241–245. DOI: `10.1038/nature08325` (cited on p. 23).

HOSTEN, O., N. J. Engelsen, R. Krishnakumar, and M. A. Kasevich (2016). "Measurement noise 100 times lower than the quantum-projection limit using entangled atoms". *Nature* **529**.7587, 505–508. DOI: `10.1038/nature16176` (cited on p. 97).

HSIAO, Y.-F., P.-J. Tsai, H.-S. Chen, S.-X. Lin, C.-C. Hung, C.-H. Lee, Y.-H. Chen, Y.-F. Chen, I. A. Yu, and Y.-C. Chen (2016). "EIT-based photonic memory with near-unity storage efficiency". *arXiv* **1605.08519**. eprint: `http://arxiv.org/abs/1605.08519` (cited on p. 17).

HSU, M. T. L., G. Hétet, O. Glöckl, J. J. Longdell, B. C. Buchler, H.-A. Bachor, and P. K. Lam (2006). "Quantum Study of Information Delay in Electromagnetically Induced Transparency". *Phys. Rev. Lett.* **97** (18), 183601. DOI: `10.1103/PhysRevLett.97.183601` (cited on p. 17).

HUBER, M. and J. I. de Vicente (2013a). "Structure of Multidimensional Entanglement in Multipartite Systems". *Physical Review Letters* **110**.3, 030501. DOI: `10.1103/PhysRevLett.110.030501` (cited on p. 78).

HUBER, M. and M. Pawłowski (2013b). "Weak randomness in device-independent quantum key distribution and the advantage of using high-dimensional entanglement". *Phys. Rev. A* **88** (3), 032309. DOI: `10.1103/PhysRevA.88.032309` (cited on p. 75).

IKUTA, T. and H. Takesue (2016). "Enhanced violation of the Collins-Gisin-Linden-Massar-Popescu inequality with optimized time-bin-entangled ququarts". *Phys. Rev. A* **93**, 022307. DOI: `10.1103/PhysRevA.93.022307` (cited on pp. 33, 96).

JAMES, D. F. V., P. G. Kwiat, W. J. Munro, and A. G. White (2001). "Measurement of qubits". *Phys. Rev. A* **64** (5), 052312. DOI: `10.1103/PhysRevA.64.052312` (cited on p. 7).

JEONG, H., M. Kang, and H. Kwon (2015). "Characterizations and quantifications of macroscopic quantumness and its implementations using optical fields". *Optics Communications* **337**, 12 –21. DOI: `10.1016/j.optcom.2014.07.012` (cited on pp. 85, 88).

JIN, R.-B., R. Shimizu, M. Fujiwara, M. Takeoka, R. Wakabayashi, T. Yamashita, S. Miki, H. Terai, T. Gerrits, and M. Sasaki (2016). "Generation and distribution of high-dimensional frequency-entangled qudits". *arXiv* **1603.07887**, 1–5. eprint: `http://arxiv.org/abs/1603.07887` (cited on p. 96).

JOBEZ, P, I Usmani, N Timoney, C Laplane, N Gisin, and M Afzelius (2014). "Cavity-enhanced storage in an optical spin-wave memory". *New Journal of Physics* **16**.8, 083005. DOI: `doi:10.1088/1367-2630/16/8/083005` (cited on pp. 14, 22, 95).

JOBEZ, P., C. Laplane, N. Timoney, N. Gisin, A. Ferrier, P. Goldner, and M. Afzelius (2015). "Coherent Spin Control at the Quantum Level in an Ensemble-Based Optical Memory". *Phys. Rev. Lett.* **114** (23), 230502. DOI: `10.1103/PhysRevLett.114.230502` (cited on p. 67).

JOBEZ, P., N. Timoney, C. Laplane, J. Etesse, A. Ferrier, P. Goldner, N. Gisin, and M. Afzelius (2016). "Towards highly multimode optical quantum memory for quantum repeaters". *Phys. Rev. A* **93** (3), 032327. DOI: `10.1103/PhysRevA.93.032327` (cited on pp. 15, 22, 67).

JULSGAARD, B., A. Kozhekin, and E. S. Polzik (2001). "Experimental long-lived entanglement of two macroscopic objects". *Nature* **413**.6854, 400–403. DOI: `10.1038/35096524` (cited on p. 86).

KALB, N., A. Reiserer, S. Ritter, and G. Rempe (2015). "Heralded Storage of a Photonic Quantum Bit in a Single Atom". *Phys. Rev. Lett.* **114** (22), 220501. DOI: `10.1103/PhysRevLett.114.220501` (cited on p. 16).

KIM, T., M. Fiorentino, and F. N. C. Wong (2006). "Phase-stable source of polarization-entangled photons using a polarization Sagnac interferometer". *Phys. Rev. A* **73** (1), 012316. DOI: `10.1103/PhysRevA.73.012316` (cited on p. 33).

KIM, Y.-H., S. P. Kulik, and Y. Shih (2001). "Bell-state preparation using pulsed nondegenerate two-photon entanglement". *Phys. Rev. A* **63** (6), 060301. DOI: `10.1103/PhysRevA.63.060301` (cited on pp. 33, 64).

KIMBLE, H. J. (2008). "The quantum internet". *Nature* **453**.7198, 1023–1030. DOI: `10.1038/nature07127` (cited on p. 1).

KNILL, E., R. Laflamme, and G. J. Milburn (2001). "A scheme for efficient quantum computation with linear optics". *Nature* **409**.6816, 46–52. DOI: `10.1038/35051009` (cited on p. 36).

KOLESOV, R., K. Xia, R. Reuter, R. Stöhr, A. Zappe, J. Meijer, P. Hemmer, and J. Wrachtrup (2012). "Optical detection of a single rare-earth ion in a crystal". *Nature Commun.* **3**, 1029. DOI: `10.1038/ncomms2034` (cited on p. 45).

KRAMERS, H. A. (1930). "Théorie générale de la rotation paramagnétique dans les cristaux". *Proceedings Koninklijke Akademie van Wetenschappen* **33**, 959–972 (cited on p. 43).

KRENN, M., M. Huber, R. Fickler, R. Lapkiewicz, S. Ramelow, and A. Zeilinger (2014). "Generation and confirmation of a (100×100)-dimensional entangled quantum system". *Proceedings of the National Academy of Sciences* **111**.17, 6243–6247. DOI: `10.1073/pnas.1402365111` (cited on p. 96).

KURKIN, I. and K. Chernov (1980). "EPR and spin-lattice relaxation of rare-earth activated centres in Y_2SiO_5 single crystals". *Physica B+C* **101**, 233. DOI: `10.1016/0378-4363(80)90107-2` (cited on p. 51).

KUZMICH, A., W. P. Bowen, A. D. Boozer, A. Boca, C. W. Chou, L.-M. Duan, and H. J. Kimble (2003). "Generation of nonclassical photon pairs for scalable quantum communication with atomic ensembles". *Nature* **423**.6941, 731–734. DOI: `10.1038/nature01714` (cited on p. 29).

KWIAT, P. G., P. H. Eberhard, A. M. Steinberg, and R. Y. Chiao (1994). "Proposal for a loophole-free Bell inequality experiment". *Phys. Rev. A* **49** (5), 3209–3220. DOI: `10.1103/PhysRevA.49.3209` (cited on p. 33).

KWIAT, P. G., K. Mattle, H. Weinfurter, A. Zeilinger, A. V. Sergienko, and Y. Shih (1995). "New High-Intensity Source of Polarization-Entangled Photon Pairs". *Phys. Rev. Lett.* **75** (24), 4337–4341. DOI: `10.1103/PhysRevLett.75.4337` (cited on p. 33).

KWIAT, P. G. and H. Weinfurter (1998). "Embedded Bell-state analysis". *Phys. Rev. A* **58** (4), R2623–R2626. DOI: `10.1103/PhysRevA.58.R2623` (cited on p. 64).

KWIAT, P. G., E. Waks, A. G. White, I. Appelbaum, and P. H. Eberhard (1999). "Ultrabright source of polarization-entangled photons". *Phys. Rev. A* **60** (2), R773–R776. DOI: `10.1103/PhysRevA.60.R773` (cited on p. 33).

LAGHAOUT, A., J. S. Neergaard-Nielsen, and U. L. Andersen (2015). "Assessments of macroscopicity for quantum optical states". *Optics Communications* **337**, 96 –101. DOI: `10.1016/j.optcom.2014.07.046` (cited on pp. 85, 88).

LAMEHI-RACHTI, M. and W. Mittig (1976). "Quantum mechanics and hidden variables: A test of Bell's inequality by the measurement of the spin correlation in low-energy proton-proton scattering". *Phys. Rev. D* **14** (10), 2543–2555. DOI: `10.1103/PhysRevD.14.2543` (cited on p. ix).

LAN, S.-Y., A. G. Radnaev, O. A. Collins, D. N. Matsukevich, T. A. Kennedy, and A. Kuzmich (2009). "A multiplexed quantum memory". *Opt. Express* **17**.16, 13639–13645. DOI: `10.1364/OE.17.013639` (cited on p. 67).

LAPLANE, C., E. Zambrini Cruzeiro, F. Fröwis, P. Goldner, and M. Afzelius (2016a). "High-Precision Measurement of the Dzyaloshinsky-Moriya Interaction between Two Rare-Earth Ions in a Solid". *Phys. Rev. Lett.* **117** (3), 037203. DOI: `10.1103/PhysRevLett.117.037203` (cited on p. 94).

LAPLANE, C., P. Jobez, J. Etesse, N. Timoney, N. Gisin, and M. Afzelius (2016b). "Multiplexed on-demand storage of polarization qubits in a crystal". *New Journal of Physics* **18**.1, 013006. DOI: `10.1088/1367-2630/18/1/013006` (cited on p. 22).

LAURITZEN, B., S. R. Hastings-Simon, H. de Riedmatten, M. Afzelius, and N. Gisin (2008). "State preparation by optical pumping in erbium-doped solids using stimulated emission and spin mixing". *Phys. Rev. A* **78** (4), 043402. DOI: `10.1103/PhysRevA.78.043402` (cited on p. 49).

LAURITZEN, B., J. Minář, H. de Riedmatten, M. Afzelius, N. Sangouard, C. Simon, and N. Gisin (2010). "Telecommunication-Wavelength Solid-State Memory at the Single Photon Level". *Phys. Rev. Lett.* **104**.8, 080502. DOI: `10.1103/PhysRevLett.104.080502` (cited on p. 19).

LEDINGHAM, P. M., W. R. Naylor, J. J. Longdell, S. E. Beavan, and M. J. Sellars (2010). "Nonclassical photon streams using rephased amplified spontaneous emission". *Phys. Rev. A* **81** (1), 012301. DOI: `10.1103/PhysRevA.81.012301` (cited on p. 25).

LEDINGHAM, P. M., W. R. Naylor, and J. J. Longdell (2012). "Experimental Realization of Light with Time-Separated Correlations by Rephasing Amplified Spontaneous Emission". *Phys. Rev. Lett.* **109** (9), 093602. DOI: `10.1103/PhysRevLett.109.093602` (cited on p. 25).

LEE, K. C., B. J. Sussman, M. R. Sprague, P. Michelberger, K. F. Reim, J. Nunn, N. K. Langford, P. J. Bustard, D. Jaksch, and I. A. Walmsley (2011). "Macroscopic non-classical states and terahertz quantum processing in room-temperature diamond". *Nat Photon* **6**, 41–44. DOI: `10.1038/nphoton.2011.296` (cited on pp. 15, 23).

LEGGETT, A. J. (1980). "Macroscopic Quantum Systems and the Quantum Theory of Measurement". *Prog. Theor. Phys. Supplement* **69**, 80–100. DOI: `10.1143/PTPS.69.80` (cited on p. 86).

LEGGETT, A. J. (2002). "Testing the limits of quantum mechanics: motivation, state of play, prospects". *Journal of Physics: Condensed Matter* **14**.15, R415. DOI: `10.1088/0953-8984/14/15/201` (cited on p. 85).

LEGGETT, A. J. and A. Garg (1985). "Quantum mechanics versus macroscopic realism: Is the flux there when nobody looks?" *Phys. Rev. Lett.* **54** (9), 857–860. DOI: `10.1103/PhysRevLett.54.857` (cited on p. 85).

LEONG, V., M. A. Seidler, M. Steiner, A. Cerè, and C. Kurtsiefer (2016). "Time-resolved Scattering of a Single Photon by a Single Atom". *arXiv:1604.08020*. eprint: `http://arxiv.org/abs/1604.08020` (cited on p. 31).

LI, C., C. Wyon, and R. Moncorge (1992). "Spectroscopic properties and fluorescence dynamics of Er^{3+} and Yb^{3+} in Y_2SiO_5". *IEEE Journal of Quantum Electronics* **28**.4. DOI: `10.1109/3.135248` (cited on p. 49).

LI, T., G.-J. Yang, and F.-G. Deng (2014). "Entanglement distillation for quantum communication network with atomic-ensemble memories". *Opt.*

(2013). "Detecting single infrared photons with 93% system efficiency". *Nat Photon* **7**.3, 210–214. DOI: `10.1038/nphoton.2013.13` (cited on p. 59).

MARTINI, d. F., F. Sciarrino, and C. Vitelli (2008). "Entanglement Test on a Microscopic-Macroscopic System". *Phys. Rev. Lett.* **100** (25), 253601. DOI: `10.1103/PhysRevLett.100.253601` (cited on p. 86).

MARTINIS, J. M., M. H. Devoret, and J. Clarke (1987). "Experimental tests for the quantum behavior of a macroscopic degree of freedom: The phase difference across a Josephson junction". *Phys. Rev. B* **35** (10), 4682–4698. DOI: `10.1103/PhysRevB.35.4682` (cited on p. 86).

MASSAR, S. and S. Popescu (1995). "Optimal Extraction of Information from Finite Quantum Ensembles". *Phys. Rev. Lett.* **74** (8), 1259–1263. DOI: `10.1103/PhysRevLett.74.1259` (cited on pp. 3, 14, 60).

MCCONNELL, R., H. Zhang, J. Hu, S. Cuk, and V. Vuletic (2015). "Entanglement with negative Wigner function of almost 3,000 atoms heralded by one photon". *Nature* **519**, 439. DOI: `10.1038/nature14293` (cited on p. 97).

MINÁŘ, J., H. de Riedmatten, C. Simon, H. Zbinden, and N. Gisin (2008). "Phase-noise measurements in long-fiber interferometers for quantum-repeater applications". *Phys. Rev. A* **77** (5), 052325. DOI: `10.1103/PhysRevA.77.052325` (cited on p. 83).

MIYAZONO, E., T. Zhong, I. Craiciu, J. M. Kindem, and A. Faraon (2016). "Coupling of erbium dopants to yttrium orthosilicate photonic crystal cavities for on-chip optical quantum memories". *Applied Physics Letters* **108**.1, 011111. DOI: `http://dx.doi.org/10.1063/1.4939651` (cited on p. 95).

MOISEEV, S. A. and S. Kröll (2001). "Complete Reconstruction of the Quantum State of a Single-Photon Wave Packet Absorbed by a Doppler-Broadened Transition". *Phys. Rev. Lett.* **87** (17), 173601. DOI: `10.1103/PhysRevLett.87.173601` (cited on p. 19).

MONROE, C., D. M. Meekhof, B. E. King, and D. J. Wineland (1996). "A "Schrödinger Cat" Superposition State of an Atom". *Science* **272**.5265, 1131–1136. DOI: `10.1126/science.272.5265.1131` (cited on p. 86).

MORODER, T., J.-D. Bancal, Y.-C. Liang, M. Hofmann, and O. Gühne (2013). "Device-Independent Entanglement Quantification and Related Applications". *Phys. Rev. Lett.* **111** (3), 030501. DOI: `10.1103/PhysRevLett.111.030501` (cited on p. 84).

MUNRO, W. J., K. A. Harrison, A. M. Stephens, S. J. Devitt, and K. Nemoto (2010). "From quantum multiplexing to high-performance quantum networking". *Nat Photon* **4**.11, 792–796. DOI: `10.1038/nphoton.2010.213` (cited on p. 14).

NIELSEN, M. A. and I. L. Chuang (2000). *Quantum Computation and Quantum Information (Cambridge Series on Information and the Natural Sciences)*. 1st ed. (cited on p. 3).

NILSSON, M. and S. Kröll (2005). "Solid state quantum memory using complete absorption and re-emission of photons by tailored and externally controlled inhomogeneous absorption profiles". *Optics Communications* **247**.4–6, 393–403. DOI: `10.1016/j.optcom.2004.11.077` (cited on p. 19).

NUNN, J., K. Reim, K. C. Lee, V. O. Lorenz, B. J. Sussman, I. A. Walmsley, and D. Jaksch (2008). "Multimode Memories in Atomic Ensembles". *Phys. Rev. Lett.* **101** (26), 260502. DOI: `10.1103/PhysRevLett.101.260502` (cited on p. 67).

NUNN, J., L. J. Wright, C. Söller, L. Zhang, I. A. Walmsley, and B. J. Smith (2013). "Large-alphabet time-frequency entangled quantum key distribution by means of time-to-frequency conversion". *Opt. Express* **21**.13, 15959–15973. DOI: `10.1364/OE.21.015959` (cited on p. 96).

OLISLAGER, L., J. Cussey, A. T. Nguyen, P. Emplit, S. Massar, J.-M. Merolla, and K. P. Huy (2010). "Frequency-bin entangled photons". *Phys. Rev. A* **82** (1), 013804. DOI: `10.1103/PhysRevA.82.013804` (cited on p. 96).

OLIVEIRA, F. A. M. de, M. S. Kim, P. L. Knight, and V. Buek (1990). "Properties of displaced number states". *Phys. Rev. A* **41** (5), 2645–2652. DOI: `10.1103/PhysRevA.41.2645` (cited on p. 87).

OLMSCHENK, S., D. N. Matsukevich, P. Maunz, D. Hayes, L.-M. Duan, and C. Monroe (2009). "Quantum Teleportation Between Distant Matter Qubits". *Science* **323**.5913, 486–489. DOI: `10.1126/science.1167209` (cited on p. 16).

OU, Z. Y. and L. Mandel (1988). "Violation of Bell's Inequality and Classical Probability in a Two-Photon Correlation Experiment". *Phys. Rev. Lett.* **61** (1), 50–53. DOI: `10.1103/PhysRevLett.61.50` (cited on p. ix).

OURJOUMTSEV, A., H. Jeong, R. Tualle-Brouri, and P. Grangier (2007). "Generation of optical 'Schrödinger cats' from photon number states." *Nature* **448**.7155, 784–6. DOI: `10.1038/nature06054` (cited on p. 86).

PAN, J.-W., D. Bouwmeester, H. Weinfurter, and A. Zeilinger (1998). "Experimental Entanglement Swapping: Entangling Photons That Never Interacted". *Phys. Rev. Lett.* **80** (18), 3891–3894. DOI: `10.1103/PhysRevLett.80.3891` (cited on p. 36).

PAN, J.-W., C. Simon, C. Brukner, and A. Zeilinger (2001). "Entanglement purification for quantum communication". *Nature* **410**.6832, 1067–1070. DOI: `10.1038/35074041` (cited on p. 9).

PAN, J.-W., S. Gasparoni, R. Ursin, G. Weihs, and A. Zeilinger (2003). "Experimental entanglement purification of arbitrary unknown states".

Nature **423**.6938, 417–422. DOI: `10.1038/nature01623` (cited on pp. 9, 64).

PAN, J.-W., Z.-B. Chen, C.-Y. Lu, H. Weinfurter, A. Zeilinger (2012). "Multiphoton entanglement and interferometry". *Rev. Mod. Phys.* **84** (2), 777–838. DOI: `10.1103/RevModPhys.84.777` (cited on p. 96).

PARIGI, V., V. D'Ambrosio, C. Arnold, L. Marrucci, F. Sciarrino, and J. Laurat (2015). "Storage and retrieval of vector beams of light in a multiple-degree-of-freedom quantum memory". *Nature Communications* **6**, 7706. DOI: `10.1038/ncomms8706` (cited on p. 67).

PERES, A. (1996). "Separability Criterion for Density Matrices". *Phys. Rev. Lett.* **77** (8), 1413–1415. DOI: `10.1103/PhysRevLett.77.1413` (cited on pp. 36, 86).

PETERSEN, L. (2011). "High-resolution spectroscopy of praseodymium ions in a solid matrix: towards single-ion detection sensitivity". PhD thesis. ETH Zurich (cited on p. 45).

PHILLIPS, D. F., A. Fleischhauer, A. Mair, R. L. Walsworth, and M. D. Lukin (2001). "Storage of Light in Atomic Vapor". *Phys. Rev. Lett.* **86** (5), 783–786. DOI: `10.1103/PhysRevLett.86.783` (cited on p. 17).

PROBST, S., H. Rotzinger, S. Wünsch, P. Jung, M. Jerger, M. Siegel, A. V. Ustinov, and P. A. Bushev (2013). "Anisotropic Rare-Earth Spin Ensemble Strongly Coupled to a Superconducting Resonator". *Phys. Rev. Lett.* **110** (15), 157001. DOI: `10.1103/PhysRevLett.110.157001` (cited on pp. 61, 95).

RADNAEV, A. G., Y. O. Dudin, R. Zhao, H. H. Jen, S. D. Jenkins, A. Kuzmich, and T. A. B. Kennedy (2010). "A quantum memory with telecom-wavelength conversion". *Nature Physics* **6**, 894–899. DOI: `10.1038/nphys1773` (cited on pp. 14, 15, 23).

REID, M. F. (2013). *Electronic Structure and Transition Intensities in Rare-Earth Materials*. University of Canterbury (cited on p. 43).

REIM, K. F., J. Nunn, V. O. Lorenz, B. J. Sussman, K. C. Lee, N. K. Langford, D. Jaksch, and I. A. Walmsley (2010). "Towards high-speed optical quantum memories". English. *Nature Photonics* **4**.4, 218–221. DOI: `10.1038/NPHOTON.2010.30` (cited on pp. 15, 23).

REIMER, C., M. Kues, P. Roztocki, B. Wetzel, F. Grazioso, B. E. Little, S. T. Chu, T. Johnston, Y. Bromberg, L. Caspani, et al. (2016). "Generation of multiphoton entangled quantum states by means of integrated frequency combs". *Science* **351**.6278, 1176–1180. DOI: `10.1126/science.aad8532` (cited on p. 96).

REISERER, A., N. Kalb, G. Rempe, and S. Ritter (2014). "A quantum gate between a flying optical photon and a single trapped atom". *Nature* **508**.7495, 237–240. DOI: `10.1038/nature13177` (cited on p. 16).

REISERER, A. and G. Rempe (2015). "Cavity-based quantum networks with single atoms and optical photons". *Rev. Mod. Phys.* **87** (4), 1379–1418. DOI: `10.1103/RevModPhys.87.1379` (cited on p. 16).

RICHART, D., Y. Fischer, and H. Weinfurter (2012). "Experimental implementation of higher dimensional time–energy entanglement". *Applied Physics B* **106**.3, 543–550. DOI: `10.1007/s00340-011-4854-z` (cited on p. 96).

RIEDEL, M. F., P. Böhi, Y. Li, T. W. Hänsch, A. Sinatra, and P. Treutlein (2010). "Atom-chip-based generation of entanglement for quantum metrology". *Nature* **464**.7292, 1170–1173. DOI: `10.1038/nature08988` (cited on p. 97).

RIEDMATTEN, H. de, I. Marcikic, W. Tittel, H. Zbinden, D. Collins, and N. Gisin (2004a). "Long Distance Quantum Teleportation in a Quantum Relay Configuration". *Phys. Rev. Lett.* **92** (4), 047904. DOI: `10.1103/PhysRevLett.92.047904` (cited on p. 61).

RIEDMATTEN, H. de, V. Scarani, I. Marcikic, A. Acín, W. Tittel, H. Zbinden, and N. Gisin (2004b). "Two independent photon pairs versus four-photon entangled states in parametric down conversion". *Journal of Modern Optics* **51**, 1637–1649. DOI: `10.1080/09500340408232478` (cited on pp. 68, 69).

RIEDMATTEN, H. de, I. Marcikic, H. Zbinden, and N. Gisin (2002). "Creating high dimensional time-bin entanglement using mode-locked lasers". *Quant. Inf. Comp.* **2**, 425–433 (cited on p. 96).

RIEDMATTEN, H. de, M. Afzelius, M. U. Staudt, C. Simon, and N. Gisin (2008). "A solid-state light-matter interface at the single-photon level". *Nature* **456**.7223, 773–777. DOI: `10.1038/nature07607` (cited on p. 22).

RIELANDER, D., K. Kutluer, P. M. Ledingham, M. Gundogan, J. Fekete, M. Mazzera, and H. de Riedmatten (2014). "Quantum Storage of Heralded Single Photons in a Praseodymium-Doped Crystal". *Phys. Rev. Lett.* **112**.4, 040504–. DOI: `10.1103/PhysRevLett.112.040504` (cited on p. 22).

RITTER, S., C. Nolleke, C. Hahn, A. Reiserer, A. Neuzner, M. Uphoff, M. Mucke, E. Figueroa, J. Bochmann, and G. Rempe (2012). "An elementary quantum network of single atoms in optical cavities". *Nature* **484**.7393, 195–200. DOI: `10.1038/nature11023` (cited on p. 16).

RIVEST, R., A. Shamir, and L. Adleman (1978). "A Method for Obtaining Digital Signatures and Public-Key Cryptosystems". *Communications of the ACM* **21**, 120–126. DOI: `10.1145/359340.359342` (cited on p. ix).

ROY, S. M. (2005). "MultipartiteSeparability Inequalities Exponentially Stronger than Local Reality Inequalities". *Phys. Rev. Lett.* **94** (1), 010402. DOI: `10.1103/PhysRevLett.94.010402` (cited on p. 6).

SABOONI, M., Q. Li, S. Kröll, and L. Rippe (2013). "Efficient Quantum Memory Using a Weakly Absorbing Sample". *Phys. Rev. Lett.* **110** (13),

133604. DOI: `10.1103/PhysRevLett.110.133604` (cited on pp. 14, 22, 95).

SAEEDI, K., S. Simmons, J. Z. Salvail, P. Dluhy, H. Riemann, N. V. Abrosimov, P. Becker, H.-J. Pohl, J. J. L. Morton, and M. L. W. Thewalt (2013). "Room-Temperature Quantum Bit Storage Exceeding 39 Minutes Using Ionized Donors in Silicon-28". *Science* **342**.6160, 830–833. DOI: `10.1126/science.1239584` (cited on p. 96).

SAGLAMYUREK, E, N Sinclair, J. A. Slater, K Heshami, D Oblak, and W Tittel (2014). "An integrated processor for photonic quantum states using a broadband light–matter interface". *New Journal of Physics* **16**.6, 065019. DOI: `10.1088/1367-2630/16/6/065019` (cited on p. 15).

SAGLAMYUREK, E., N. Sinclair, J. Jin, J. A. Slater, D. Oblak, F. Bussières, M. George, R. Ricken, W. Sohler, and W. Tittel (2011). "Broadband waveguide quantum memory for entangled photons". *Nature* **469**.7331, 512–515. DOI: `10.1038/nature09719` (cited on pp. 15, 95).

— (2012). "Conditional Detection of Pure Quantum States of Light after Storage in a Tm-Doped Waveguide". *Phys. Rev. Lett.* **108**.8, 083602. DOI: `10.1103/PhysRevLett.108.083602` (cited on p. 15).

SAGLAMYUREK, E., T. Lutz, L. Veissier, M. P. Hedges, C. W. Thiel, R. L. Cone, and W. Tittel (2015a). "Efficient and long-lived Zeeman-sublevel atomic population storage in an erbium-doped glass fiber". *Phys. Rev. B* **92** (24), 241111. DOI: `10.1103/PhysRevB.92.241111` (cited on p. 15).

SAGLAMYUREK, E., J. Jin, V. B. Verma, M. D. Shaw, F. Marsili, S. W. Nam, D. Oblak, and W. Tittel (2015b). "Quantum storage of entangled telecom-wavelength photons in an erbium-doped optical fibre". *Nature Photonics* **9**, 83–87. DOI: `10.1038/nphoton.2014.311` (cited on p. 15).

SAGLAMYUREK, E., M. Grimau Puigibert, Q. Zhou, L. Giner, F. Marsili, V. B. Verma, S. Woo Nam, L. Oesterling, D. Nippa, D. Oblak, and W. Tittel (2016). "A multiplexed light-matter interface for fibre-based quantum networks". *Nat Commun* **7**, 11202. DOI: `10.1038/ncomms11202` (cited on p. 67).

SANGOUARD, N., C. Simon, H. de Riedmatten, and N. Gisin (2011). "Quantum repeaters based on atomic ensembles and linear optics". *Rev. Mod. Phys.* **83**.1, 33–80. DOI: `10.1103/RevModPhys.83.33` (cited on pp. xi, 10, 13, 14, 75).

SANPERA, A., D. Bruß, and M. Lewenstein (2001). "Schmidt-number witnesses and bound entanglement". *Phys. Rev. A* **63** (5), 050301. DOI: `10.1103/PhysRevA.63.050301` (cited on pp. 6, 70).

SCHAEFF, C., R. Polster, M. Huber, S. Ramelow, and A. Zeilinger (2015). "Experimental access to higher-dimensional entangled quantum systems using integrated optics". *Optica* **2**.6, 7. DOI: `10.1364/OPTICA.2.000523` (cited on p. 96).

SCHMID, C., N. Kiesel, U. K. Weber, R. Ursin, A. Zeilinger, and H. Weinfurter (2009). "Quantum teleportation and entanglement swapping with linear optics logic gates". *New Journal of Physics* **11**.3, 033008. DOI: 10.1088/0031-8949/11/3/033008 (cited on p. 64).

SCHRAFT, D., M. Hain, N. Lorenz, and T. Halfmann (2016). "Stopped Light at High Storage Efficiency in a $Pr^{3+} : Y_2SiO_5$ Crystal". *Phys. Rev. Lett.* **116** (7), 073602. DOI: 10.1103/PhysRevLett.116.073602 (cited on pp. 14, 17).

SCHRÖDINGER, E. (1935). "Discussion of Probability Relations between Separated Systems". *Mathematical Proceedings of the Cambridge Philosophical Society* **31** (04), 555–563. DOI: 10.1017/S0305004100013554 (cited on p. 3).

SCHUCK, C., G. Huber, C. Kurtsiefer, and H. Weinfurter (2006). "Complete Deterministic Linear Optics Bell State Analysis". *Phys. Rev. Lett.* **96** (19), 190501. DOI: 10.1103/PhysRevLett.96.190501 (cited on p. 64).

SCHUMACHER, B. (1995). "Quantum coding". *Phys. Rev. A* **51** (4), 2738–2747. DOI: 10.1103/PhysRevA.51.2738 (cited on p. 1).

SEKATSKI, P., N. Sangouard, N. Gisin, H. de Riedmatten, and M. Afzelius (2011). "Photon-pair source with controllable delay based on shaped inhomogeneous broadening of rare-earth-metal-doped solids". *Phys. Rev. A* **83** (5), 053840. DOI: 10.1103/PhysRevA.83.053840 (cited on pp. 13, 25).

SEKATSKI, P., N. Gisin, and N. Sangouard (2014a). "How Difficult Is It to Prove the Quantumness of Macroscropic States?" *Phys. Rev. Lett.* **113** (9), 090403. DOI: 10.1103/PhysRevLett.113.090403 (cited on pp. 85, 88).

SEKATSKI, P., N. Sangouard, and N. Gisin (2014b). "Size of quantum superpositions as measured with classical detectors". *Phys. Rev. A* **89** (1), 012116. DOI: 10.1103/PhysRevA.89.012116 (cited on pp. 86, 87).

SHALM, L. K., D. R. Hamel, Z. Yan, C. Simon, K. J. Resch, and T. Jennewein (2012). "Three-photon energy-time entanglement". *Nature Physics* **9**.1, 19–22. DOI: 10.1038/nphys2492 (cited on p. 96).

SHALM, L. K. et al. (2015). "Strong Loophole-Free Test of Local Realism". *Phys. Rev. Lett.* **115** (25), 250402. DOI: 10.1103/PhysRevLett.115.250402 (cited on p. ix).

SHERIDAN, L. and V. Scarani (2010). "Security proof for quantum key distribution using qudit systems". *Phys. Rev. A* **82** (3), 030301. DOI: 10.1103/PhysRevA.82.030301 (cited on p. 75).

SHOR, P. W. (1994). "Algorithms for quantum computation: discrete logarithms and factoring". *Foundations of Computer Science, 1994 Proceedings., 35th Annual Symposium on*, 124–134. DOI: 10.1109/SFCS.1994.365700 (cited on p. x).

SIMON, C. et al. (2010). "Quantum memories". *The European Physical Journal D - Atomic, Molecular, Optical and Plasma Physics* **58**.1, 1–22. DOI: `10.1140/epjd/e2010-00103-y` (cited on p. x).

SIMON, C. and J.-W. Pan (2002). "Polarization Entanglement Purification using Spatial Entanglement". *Phys. Rev. Lett.* **89** (25), 257901. DOI: `10.1103/PhysRevLett.89.257901` (cited on pp. 9, 10, 63, 73).

SIMON, C., H. de Riedmatten, M. Afzelius, N. Sangouard, H. Zbinden, and N. Gisin (2007). "Quantum Repeaters with Photon Pair Sources and Multimode Memories". *Phys. Rev. Lett.* **98** (19), 190503. DOI: `10.1103/PhysRevLett.98.190503` (cited on pp. 11, 15, 76).

SIMON, R. (2000). "Peres-Horodecki Separability Criterion for Continuous Variable Systems". *Phys. Rev. Lett.* **84** (12), 2726–2729. DOI: `10.1103/PhysRevLett.84.2726` (cited on p. 4).

SINCLAIR, N., E. Saglamyurek, H. Mallahzadeh, J. A. Slater, M. George, R. Ricken, M. P. Hedges, D. Oblak, C. Simon, W. Sohler, and W. Tittel (2014). "Spectral Multiplexing for Scalable Quantum Photonics using an Atomic Frequency Comb Quantum Memory and Feed-Forward Control". *Phys. Rev. Lett.* **113** (5), 053603. DOI: `10.1103/PhysRevLett.113.053603` (cited on pp. 15, 67).

SIPAHIGIL, A., M. L. Goldman, E. Togan, Y. Chu, M. Markham, D. J. Twitchen, A. S. Zibrov, A. Kubanek, and M. D. Lukin (2012). "Quantum Interference of Single Photons from Remote Nitrogen-Vacancy Centers in Diamond". *Phys. Rev. Lett.* **108** (14), 143601. DOI: `10.1103/PhysRevLett.108.143601` (cited on p. 16).

SØRENSEN, A., L.-M. Duan, J. I. Cirac, and P. Zoller (2001). "Many-particle entanglement with Bose–Einstein condensates". *Nature* **409**.6816, 63–66. DOI: `10.1038/35051038` (cited on p. 97).

SØRENSEN, A. S., C. H. van der Wal, L. I. Childress, and M. D. Lukin (2004). "Capacitive Coupling of Atomic Systems to Mesoscopic Conductors". *Phys. Rev. Lett.* **92** (6), 063601. DOI: `10.1103/PhysRevLett.92.063601` (cited on p. 95).

SPECHT, H. P., C. Nolleke, A. Reiserer, M. Uphoff, E. Figueroa, S. Ritter, and G. Rempe (2011). "A single-atom quantum memory". *Nature* **473**.7346, 190–193. DOI: `10.1038/nature09997` (cited on p. 16).

SRIVATHSAN, B., G. K. Gulati, A. Cerè, B. Chng, and C. Kurtsiefer (2014). "Reversing the Temporal Envelope of a Heralded Single Photon using a Cavity". *Phys. Rev. Lett.* **113** (16), 163601. DOI: `10.1103/PhysRevLett.113.163601` (cited on p. 31).

STAUDT, M. U., M. Afzelius, H. de Riedmatten, S. R. Hastings-Simon, C. Simon, R. Ricken, H. Suche, W. Sohler, and N. Gisin (2007). "Interference of Multimode Photon Echoes Generated in Spatially Separated Solid-State Atomic Ensembles". *Phys. Rev. Lett.* **99** (17), 173602. DOI: `10.1103/PhysRevLett.99.173602` (cited on p. 95).

STAUDT, M. U., S. R. Hastings-Simon, M. Afzelius, D. Jaccard, W. Tittel, and N. Gisin (2006). "Investigations of optical coherence properties in an erbium-doped silicate fiber for quantum state storage". *Opt. Comm.* **266**.2, 720–726 (cited on p. 53).

STAUDT, M. U., I.-C. Hoi, P. Krantz, M. Sandberg, M. Simoen, P. Bushev, N. Sangouard, M. Afzelius, V. S. Shumeiko, G. Johansson, P. Delsing, and C. M. Wilson (2012). "Coupling of an erbium spin ensemble to a superconducting resonator". *Journal of Physics B: Atomic, Molecular and Optical Physics* **45**.12, 124019. DOI: `10.1088/0953-4075/45/12/124019` (cited on pp. 61, 95).

STEFFEN, L., Y. Salathe, M. Oppliger, P. Kurpiers, M. Baur, C. Lang, C. Eichler, G. Puebla-Hellmann, A. Fedorov, and A. Wallraff (2013). "Deterministic quantum teleportation with feed-forward in a solid state system". *Nature* **500**.7462, 319–322. DOI: `10.1038/nature12422` (cited on p. 61).

STUCKI, D., H. Zbinden, and N. Gisin (2005). "A Fabry-Perot-like two-photon interferometer for high-dimensional time-bin entanglement". *Journal of Modern Optics* **52**.18, 2637–2648. DOI: `10.1080/09500340500283821` (cited on p. 96).

SUN, Y. (2005). "Spectroscopic Properties of Rare Earths in Optical Materials". Ed. by G. **LIU** and B. Jacquier. Springer-Verlag. Chap. Rare Earth Materials in Optical Storage and Data Processing Applications (cited on pp. 41, 44).

SUN, Y., C. W. Thiel, R. L. Cone, R. W. Equall, and R. L. Hutcheson (2002). "Recent progress in developing new rare earth materials for hole burning and coherent transient applications". *J. Lumin.* **98**.1-4, 281–287. DOI: `10.1016/S0022-2313(02)00281-8` (cited on p. 47).

TANG, J.-S. et al. (2015). "Storage of multiple single-photon pulses emitted from a quantum dot in a solid-state quantum memory". *Nat. Commun.* **6**, 9652. DOI: `10.1038/ncomms9652` (cited on p. 67).

TERHAL, B. M. and P. Horodecki (2000). "Schmidt number for density matrices". *Phys. Rev. A* **61** (4), 040301. DOI: `10.1103/PhysRevA.61.040301` (cited on pp. 4, 6).

THEW, R. T., A. Acín, H. Zbinden, and N. Gisin (2004). "Bell-Type Test of Energy-Time Entangled Qutrits". *Phys. Rev. Lett.* **93** (1), 010503. DOI: `10.1103/PhysRevLett.93.010503` (cited on pp. 32, 77, 96).

THIEL, C., T. Böttger, and R. Cone (2011). "Rare-earth-doped materials for applications in quantum information storage and signal processing". *Journal of Luminescence* **131**, 353 –361. DOI: `10.1016/j.jlumin.2010.12.015` (cited on pp. 46, 47).

TIMONEY, N., I. Usmani, P. Jobez, M. Afzelius, and N. Gisin (2013). "Single-photon-level optical storage in a solid-state spin-wave memory".

Phys. Rev. A **88**.2, 022324. DOI: `10.1103/PhysRevA.88.022324` (cited on p. 22).

TOGAN, E., Y. Chu, A. S. Trifonov, L. Jiang, J. Maze, L. Childress, M. V. G. Dutt, A. S. Sorensen, P. R. Hemmer, A. S. Zibrov, and M. D. Lukin (2010). "Quantum entanglement between an optical photon and a solid-state spin qubit". *Nature* **466**.7307, 730–734. DOI: `10.1038/nature09256` (cited on p. 16).

TROJEK, P. and H. Weinfurter (2008). "Collinear source of polarization-entangled photon pairs at nondegenerate wavelengths". *Applied Physics Letters* **92**.21, 211103. DOI: `10.1063/1.2924280` (cited on p. 33).

USMANI, I., M. Afzelius, H. de Riedmatten, and N. Gisin (2010). "Mapping multiple photonic qubits into and out of one solid-state atomic ensemble". *Nat Commun* **1**, 12. DOI: `10.1038/ncomms1010` (cited on pp. 15, 22, 51, 67).

USMANI, I., C. Clausen, F. Bussières, N. Sangouard, M. Afzelius, and N. Gisin (2012). "Heralded quantum entanglement between two crystals". *Nature Photonics* **6**, 234–237. DOI: `10.1038/nphoton.2012.34` (cited on pp. 22, 50, 56, 59).

VEDRAL, V. (1999). "On bound entanglement assisted distillation". *Physics Letters A* **262**.2-3, 121 –124. DOI: `10.1016/S0375-9601(99)00686-6` (cited on p. 9).

VERMA, V. B., B. Korzh, F. Bussières, R. D. Horansky, A. E. Lita, F. Marsili, M. D. Shaw, H. Zbinden, R. P. Mirin, and S. W. Nam (2014). "High-efficiency WSi superconducting nanowire single-photon detectors operating at 2.5K". *Applied Physics Letters* **105**.12, 122601. DOI: `10.1063/1.4896045` (cited on pp. 65, 69, 73).

VERMA, V. B., B. Korzh, F. Bussières, R. D. Horansky, S. D. Dyer, A. E. Lita, I. Vayshenker, F. Marsili, M. D. Shaw, H. Zbinden, R. P. Mirin, and S. W. Nam (2015). "High-efficiency superconducting nanowire single-photon detectors fabricated from MoSi thin-films". *Opt. Express* **23**.26, 33792–33801. DOI: `10.1364/OE.23.033792` (cited on p. 61).

VÉRTESI, T., S. Pironio, and N. Brunner (2010). "Closing the Detection Loophole in Bell Experiments Using Qudits". *Phys. Rev. Lett.* **104** (6), 060401. DOI: `10.1103/PhysRevLett.104.060401` (cited on p. 75).

VLECK, J. H. V. (1937). "The Puzzle of Rare-earth Spectra in Solids." *The Journal of Physical Chemistry* **41**.1, 67–80. DOI: `10.1021/j150379a006` (cited on p. 39).

WALBORN, S. P., S. Pádua, and C. H. Monken (2003). "Hyperentanglement-assisted Bell-state analysis". *Phys. Rev. A* **68** (4), 042313. DOI: `10.1103/PhysRevA.68.042313` (cited on p. 64).

WALTHER, P., K. J. Resch, i. c. v. Brukner, A. M. Steinberg, J.-W. Pan, and A. Zeilinger (2005). "Quantum Nonlocality Obtained from Local

States by Entanglement Purification". *Phys. Rev. Lett.* **94** (4), 040504. DOI: `10.1103/PhysRevLett.94.040504` (cited on p. 64).

WELINSKI, S., A. Ferrier, M. Afzelius, and P. Goldner (2016). "High-resolution optical spectroscopy and magnetic properties of Yb^{3+} in Y_2SiO_5". *Phys. Rev. B* **94** (15), 155116. DOI: `10.1103/PhysRevB.94.155116` (cited on p. 95).

WERNER, R. F. (1989). "Quantum states with Einstein-Podolsky-Rosen correlations admitting a hidden-variable model". *Phys. Rev. A* **40** (8), 4277–4281. DOI: `10.1103/PhysRevA.40.4277` (cited on p. 9).

WITHNALL, R. and J. Silver (2014). "Physics of Light Emission from Rare Earth-Doped Phosphors". *Handbook of Visual Display Technology*. Ed. by J. **CHEN**, W. Cranton, and M. Fihn. Berlin, Heidelberg: Springer Berlin Heidelberg, 1–8. DOI: `10.1007/978-3-642-35947-7_68-2` (cited on p. 42).

WOLFOWICZ, G., H. Maier-Flaig, R. Marino, A. Ferrier, H. Vezin, J. J. L. Morton, and P. Goldner (2015). "Coherent Storage of Microwave Excitations in Rare-Earth Nuclear Spins". *Phys. Rev. Lett.* **114** (17), 170503. DOI: `10.1103/PhysRevLett.114.170503` (cited on p. 95).

WOOTTERS, W. K. and W. H. Zurek (1982). "A single quantum cannot be cloned". *Nature* **299**.5886, 802–803. DOI: `10.1038/299802a0` (cited on pp. ix, 7).

XIANG, Z.-L., S. Ashhab, J. Q. You, and F. Nori (2013). "Hybrid quantum circuits: Superconducting circuits interacting with other quantum systems". *Rev. Mod. Phys.* **85** (2), 623–653. DOI: `10.1103/RevModPhys.85.623` (cited on p. 2).

XING, X., A. Feizpour, A. Hayat, and A. M. Steinberg (2014). "Experimental demonstration of a flexible time-domain quantum channel." *Optics express* **22**.21, 25128–25136. DOI: `10.1364/OE.22.025128` (cited on p. 96).

YANG, S.-J., X.-J. Wang, X.-H. Bao, and J.-W. Pan (2016). "An efficient quantum light-matter interface with sub-second lifetime". *Nature Photonics* **10**.6, 381–384. DOI: `10.1038/nphoton.2016.51` (cited on p. 23).

YOSHIKAWA, J.-i., K. Makino, S. Kurata, P. van Loock, and A. Furusawa (2013). "Creation, Storage, and On-Demand Release of Optical Quantum States with a Negative Wigner Function". *Phys. Rev. X* **3** (4), 041028. DOI: `10.1103/PhysRevX.3.041028` (cited on p. 13).

ZAMBRINI, C. E., A. Tiranov, I. Usmani, C. Laplane, J. Lavoie, A. Ferriere, P. Goldner, N. Gisin, and M. Afzelius (2016). "Spectral hole lifetimes and spin population relaxation dynamics in Neodymium-doped yttrium orthosilicate". *arXiv:1611.05444*. eprint: `https://arxiv.org/abs/1611.05444` (cited on pp. 50, 53).

ZASKE, S., A. Lenhard, C. A. Keßler, J. Kettler, C. Hepp, C. Arend, R. Albrecht, W.-M. Schulz, M. Jetter, P. Michler, and C. Becher (2012).

"Visible-to-Telecom Quantum Frequency Conversion of Light from a Single Quantum Emitter". *Phys. Rev. Lett.* **109** (14), 147404. DOI: `10.1103/PhysRevLett.109.147404` (cited on p. 15).

ZHONG, M., M. P. Hedges, R. L. Ahlefeldt, J. G. Bartholomew, S. E. Beavan, S. M. Wittig, J. J. Longdell, and M. J. Sellars (2015a). "Optically addressable nuclear spins in a solid with a six-hour coherence time". *Nature* **517**.7533, 177–180. DOI: `10.1038/nature14025` (cited on p. 48).

ZHONG, T., J. M. Kindem, E. Miyazono, and A. Faraon (2015b). "Nanophotonic coherent light-matter interfaces based on rare-earth-doped crystals". *Nature Comm.* **6**, 8206. DOI: `10.1038/ncomms9206` (cited on p. 95).

ZHONG, T., J. M. Kindem, J. Rochman, and A. Faraon (2016). "On-chip storage of broadband photonic qubits in a cavity-protected rare-earth ensemble". *arXiv:1604.00143*. eprint: `http://arxiv.org/abs/1604.00143` (cited on p. 95).

ZHOU, S., S. Zhang, C. Liu, J. F. Chen, J. Wen, M. M. T. Loy, G. K. L. Wong, and S. Du (2012a). "Optimal storage and retrieval of single-photon waveforms". *Opt. Express* **20**.22, 24124–24131. DOI: `10.1364/OE.20.024124` (cited on p. 17).

ZHOU, Z.-Q., W.-B. Lin, M. Yang, C.-F. Li, and G.-C. Guo (2012b). "Realization of Reliable Solid-State Quantum Memory for Photonic Polarization Qubit". *Phys. Rev. Lett.* **108** (19), 190505. DOI: `10.1103/PhysRevLett.108.190505` (cited on pp. 14, 57, 69, 88).

ZHOU, Z.-Q., Y.-L. Hua, X. Liu, G. Chen, J.-S. Xu, Y.-J. Han, C.-F. Li, and G.-C. Guo (2015). "Quantum Storage of Three-Dimensional Orbital-Angular-Momentum Entanglement in a Crystal". *Phys. Rev. Lett.* **115** (7), 070502. DOI: `10.1103/PhysRevLett.115.070502` (cited on pp. 15, 67, 76, 96).

ŻUKOWSKI, M., A. Zeilinger, M. A. Horne, and A. K. Ekert (1993). ""Event-ready-detectors" Bell experiment via entanglement swapping". *Phys. Rev. Lett.* **71** (26), 4287–4290. DOI: `10.1103/PhysRevLett.71.4287` (cited on pp. 7, 59).

Published articles

The articles that have been published during this thesis are listed in chronological order.

A F. Bussières, C. Clausen, A. Tiranov, B. Korzh, V. B. Verma, S. W. Nam, F. Marsili, A. Ferrier, P. Goldner, H. Herrmann, C. Silberhorn, W. Sohler, M. Afzelius & N. Gisin, **"Quantum teleportation from a telecom-wavelength photon to a solid-state quantum memory"** Nature Photonics 8, 775-778 (2014) (pages 127-143)

B C. Clausen, F. Bussières, A. Tiranov, H. Herrmann, C. Silberhorn, W. Sohler, M. Afzelius & N. Gisin, **"A source of polarization-entangled photon pairs interfacing quantum memories with telecom photons"**, New Journal of Physics 16, 093058 (2014) (pages 143-172)

C A. Tiranov, J. Lavoie, A. Ferrier, P. Goldner, V. B. Verma, S. W. Nam, R. P. Mirin, A. E. Lita, F. Marsili, H. Herrmann, C. Silberhorn, N. Gisin, M. Afzelius & F. Bussières, **"Storage of hyperentanglement in a solid-state quantum memory"**, Optica 2(4), 279-287 (2015) (pages 173-183)

D A. Tiranov, J. Lavoie, P. C. Strassmann, N. Sangouard, M. Afzelius, F. Bussières & N. Gisin ,**"Demonstration of light-matter micro-macro quantum correlations"**, Phys. Rev. Lett. 116, 190502 (2016) (pages 183-197)

E A. Tiranov, P. C. Strassmann, J. Lavoie, N. Brunner, M. Huber, V. B. Verma, S. W. Nam, R. P. Mirin, A. E. Lita, F. Marsili, M. Afzelius, F. Bussières & N. Gisin, **"Temporal multimode storage of entangled photon pairs"**, arXiv:1606.07774 (2016) (To be published in Phys. Rev. Lett.) (pages 197-209)

F A. Tiranov, S. Designolle, E. Zambrini Cruzeiro, J. Lavoie, N. Brunner, M. Afzelius, M. Huber & N. Gisin, **"Quantification of multi-dimensional photonic entanglement stored in a quantum memory based on sparse data"**, arXiv:1609.05033 (2016) (pages 209-219)

G E. Zambrini Cruzeiro, A. Tiranov, I. Usmani, C. Laplane, J. Lavoie, A. Ferrier, P. Goldner, N. Gisin & M. Afzelius, **"Spectral hole lifetimes and spin population relaxation dynamics in neodymium-doped yttrium orthosilicate"**, arXiv:1611.05444 (2016) (pages 219-232)

"Quantum teleportation from a telecom-wavelength photon to a solid-state quantum memory"

F. Bussières, C. Clausen, A. Tiranov, B. Korzh, V. B. Verma, S. W. Nam, F. Marsili, A. Ferrier, P. Goldner, H. Herrmann, C. Silberhorn, W. Sohler, M. Afzelius & N. Gisin, Nature Photonics 8, 775-778 (2014)

Quantum teleportation from a telecom-wavelength photon to a solid-state quantum memory

Félix Bussières[1‡]*, Christoph Clausen[1†‡], Alexey Tiranov[1], Boris Korzh[1], Varun B. Verma[2],
Sae Woo Nam[2], Francesco Marsili[3], Alban Ferrier[4,5], Philippe Goldner[4], Harald Herrmann[6],
Christine Silberhorn[6], Wolfgang Sohler[6], Mikael Afzelius[1] and Nicolas Gisin[1]

Quantum teleportation[1] is a cornerstone of quantum information science due to its essential role in important tasks such as the long-distance transmission of quantum information using quantum repeaters[2,3]. This requires the efficient distribution of entanglement between remote nodes of a network[4]. Here, we demonstrate quantum teleportation of the polarization state of a telecom-wavelength photon onto the state of a solid-state quantum memory. Entanglement is established between a rare-earth-ion-doped crystal storing a single photon that is polarization-entangled with a flying telecom-wavelength photon[5,6]. The latter is jointly measured with another flying polarization qubit to be teleported, which heralds the teleportation. The fidelity of the qubit retrieved from the memory is shown to be greater than the maximum fidelity achievable without entanglement, even when the combined distances travelled by the two flying qubits is 25 km of standard optical fibre. Our results demonstrate the possibility of long-distance quantum networks with solid-state resources.

Quantum teleportation[1] allows the transfer of a quantum state between remote physical systems through the use of quantum entanglement and classical communication. The combination of quantum teleportation with quantum memories can provide scalable schemes for quantum computation[7], quantum repeaters[2,3] and quantum networks[4]. Light-to-matter quantum teleportation has been demonstrated using quantum memories based on warm[8,9] or cold[10,11] atomic ensembles, single atoms[12,13] or a quantum dot spin qubit[14]. In these demonstrations, the memory emits a photonic qubit, with which it is entangled, and the photon is used to distribute the entanglement necessary to perform teleportation.

To achieve long-distance light-to-matter quantum teleportation, and more generally to exchange quantum information between distant nodes of a quantum network, we require an efficient method to distribute entanglement[3]. Optical fibre is naturally suited to entanglement distribution, but it requires the flying qubits to have a suitable telecom wavelength. Satisfying this requirement using emissive quantum memories is difficult, because the relevant atomic transition is typically far away from the low-loss region of standard optical fibre. An approach based on practical sources of photon pairs combined with multimode quantum memories can overcome this limitation[15]. The essential idea is that spontaneous parametric down-conversion (SPDC) sources create pairs comprised of one photon stored in a nearby quantum memory,

while the other telecom-wavelength photon is used to distribute the entanglement to a remote nodes. For quantum repeaters, multimode storage with selective recall is essential to achieve practical rates. A promising candidate for the multimode quantum memories of this proposal are rare-earth-ion doped crystals[16], which offer a technologically simple way of trapping an atomic ensemble using a solid-state host. In recent years they have been used to demonstrate key properties such as high-efficiency storage[17,18], coherence times as long as one minute[19,20], multimode storage[21], on-demand readout at the single-photon level[22], gigahertz-wide storage bandwidth[6] and storage of photonic entanglement[5,6]. Here, we demonstrate quantum teleportation of the polarization state of a telecom-wavelength photon onto the state of a single collective excitation stored in a rare-earth-ion doped crystal. To achieve this, a pair of polarization-entangled photons is first generated from SPDC in nonlinear waveguides. One photon from the pair is then stored in a nearby rare-earth-ion doped crystal for a pre-determined storage time. The other telecom-wavelength photon from the entangled pair is sent to a Bell-state analyser, where it is jointly measured with a photon that is carrying the polarization qubit state to be teleported. The polarization state of the photon retrieved from the quantum memory is then analysed with quantum state tomography and the fidelity is shown to outperform the classical benchmark. We also performed teleportation in a configuration where the combined distance travelled by both telecom-wavelength photons was 25 km in standard optical fibre, demonstrating the long-distance capability of the approach.

The experiment set-up is presented in Fig. 1. A pair of entangled photons at 883 nm (the 'signal' photon) and 1,338 nm (the 'idler' photon) is created from SPDC. To achieve this, 532 nm light coherently pumps two nonlinear waveguides such that the photon pair is in a superposition of being created in a first waveguide (with horizontal polarizations $|HH\rangle$) and in a second waveguide (with vertical polarizations $|VV\rangle$). Recombining the output modes of the waveguides on two polarizing beamsplitters (PBSs) yields two optical modes containing the signal and idler photons, respectively, prepared in an entangled state that is very close to $\frac{1}{\sqrt{2}}(|HH\rangle + e^{i\varphi}|VV\rangle)$. The spectra of the idler photon (and consequently of the frequency-correlated signal photon of the pair) are subsequently filtered to a spectral width of ~240 MHz, corresponding to a coherence time of $\tau = 1.4$ ns. This spectral width is more than five times larger than in our previous experiments with the

[1]Group of Applied Physics, University of Geneva, CH-1211 Geneva 4, Switzerland, [2]National Institute of Standards and Technology, Boulder, Colorado 80305, USA, [3]Jet Propulsion Laboratory, California Institute of Technology, 4800 Oak Grove Drive, Pasadena, California 91109, USA, [4]PSL Research University, Chimie ParisTech – CNRS, Institut de Recherche de Chimie Paris, 75005 Paris, France, [5]Sorbonne Universités, UPMC Univ Paris 06, Paris 75005, France, [6]Applied Physics/Integrated Optics Group, University of Paderborn, 33095 Paderborn, Germany; [†]Present address: Vienna Center for Quantum Science and Technology, TU Wien—Atominstitut, Stadionallee 2, 1020 Vienna, Austria. [‡]These authors contributed equally to this work.
*e-mail: felix.bussieres@unige.ch
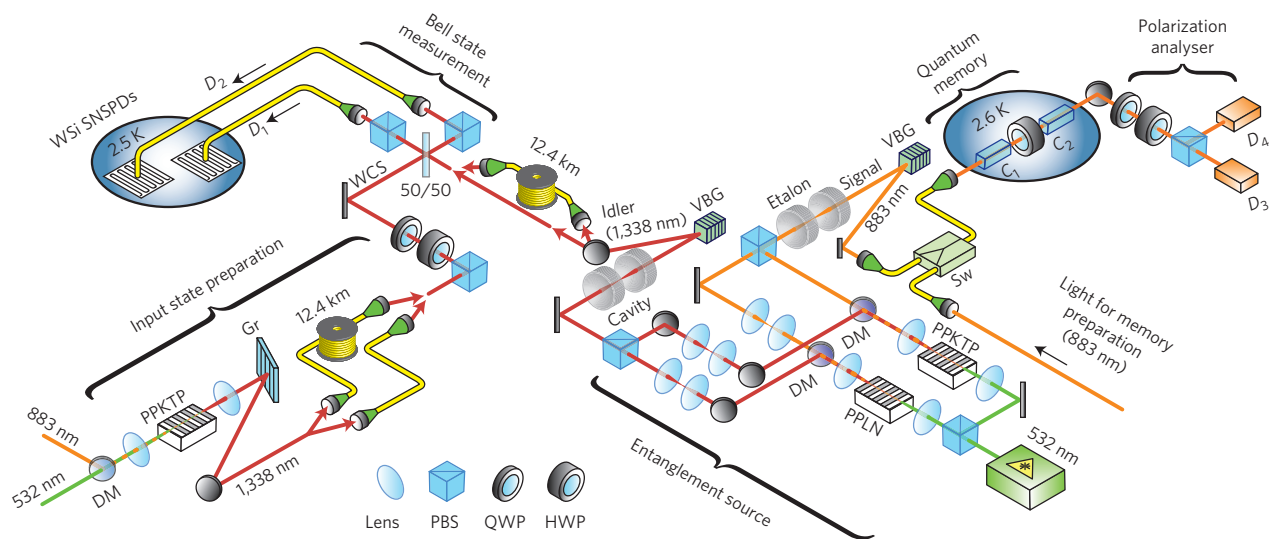
Figure 1 | Experimental set-up. The system includes a source of polarization-entangled photons at 883 nm (the signal) and 1,338 nm (the idler) using filtered spontaneous parametric down-conversion from two nonlinear waveguides (PPLN and PPKTP) coherently pumped with 532 nm light. After the waveguides, the signal and idler modes are separated using dichroic mirrors (DM) and are then individually manipulated to obtain good overlap after recombination at two polarization beam splitters (PBSs), as well as high transmission through the filtering cavity and etalon. A single pair of energy-correlated spectral modes of the signal and idler photons are selected using volume Bragg gratings (VBG). The signal photon is sent to a neodymium-based polarization-preserving quantum memory that was previously prepared as an atomic frequency comb using 883 nm light (see Methods). A switch (Sw) selects either the preparation light or the signal photons. The weak coherent state (WCS) at 1,338 nm is created by means of difference-frequency generation from 532 and 883 nm light. The WCS is then selected using a grating (Gr) and coupled in an optical fibre. The input state to be teleported is prepared using wave plates and sent towards a 50/50 beamsplitter where it is mixed with the idler photon to perform the Bell-state measurement (BSM). The output modes of the beamsplitter are polarization-filtered and sent towards two high-efficiency detectors based on WSi superconducting nanowires (D_1 and D_2) operated at 2.5 K in a closed-cycle cryocooler 10 m away from the quantum memory. A coincidence detection at D_1 and D_2 heralds a successful BSM. The signal photon retrieved from the quantum memory is sent to a polarization-state analyser where it is detected on D_3 or D_4. The idler and WCS photons are each transmitted either over a short distance or over 12.4 km of single-mode optical fibre. See Supplementary Information for details.

same type of quantum memory[5], and therefore increases the intrinsic repetition rate of our experiment by the same factor.

Following the creation of a pair, the signal photon is directly sent to a 14-mm-long quantum memory consisting of two inline neodymium-doped yttrium orthosilicate crystals interspaced with a half-wave plate. This configuration compensates for the polarization-dependent absorption of a single crystal[23–25]. The absorption bandwidth of the quantum memory is 600 MHz and stores photons for 50 ns with an overall efficiency of 5% using the atomic frequency comb (AFC) storage protocol[16]. The qubit state to teleport, hereon termed the 'input state', is encoded in the polarization of a photon from a weak coherent state (WCS) at 1,338 nm, which is created by means of difference-frequency generation in a separate nonlinear waveguide. This automatically yields the same central wavelength for the WCS and idler photons. The Bell-state measurement (BSM) between the idler photon and the input state is performed by sending them through a 50/50 beamsplitter, projecting their joint state onto the Bell state $|\Psi^-\rangle = \frac{1}{\sqrt{2}}(|HV\rangle - |VH\rangle)$ when they are detected in different output modes. The photons are then coupled in single-mode optical fibres and detected using tungsten-silicide superconducting-nanowire single-photon detectors[26] (SNSPDs; D_1 and D_2 in Fig. 1), which are designed to operate at 2.5 K in a two-stage closed-cycle cryocooler. Their efficiency reaches 75% with a temporal resolution (jitter) of 500 ps and a dark count rate of 300 Hz (see Supplementary Information for full details). The resolution is smaller than the coherence time of the photons, meaning that coincidences on the SNSPDs for which the WCS and idler photons overlap can be temporally resolved. The teleportation is completed by retrieving the stored signal photon from the quantum memory and sending it into a polarization analyser,

where it is detected by single-photon detector D_3 or D_4. The qubit state of the retrieved photon (hereon termed the 'retrieved state') requires a unitary correction[1], which is included in the polarization analyser. The overall detection rate was approximately six threefold coincidences per hour when using a 500 ps coincidence window.

In the first series of measurements the WCS photon and the idler photon both travelled a few metres before the BSM (Fig. 1), and their detection occurred while the signal photon was stored in the quantum memory. To post-select the threefold detections with the correct timing, we plot the temporal distribution of the measured threefold coincidences as a function of the delays δt_{j1} and δt_{j2} between a detection at D_j ($j = 3$ or 4) and detections at D_1 and D_2. The results for the teleportation of the state $|-\rangle = \frac{1}{\sqrt{2}}(|H\rangle - |V\rangle)$ are shown as two-dimensional histograms in Fig. 2a (with D_3 projecting on $|-\rangle$) and Fig. 2b (with D_4 projecting on $|+\rangle$). Offsets on the detection times are chosen such that events in the vicinity of the centre of the histograms (that is, for $\delta t_{j1}, \delta t_{j2} < \tau = 1.4$ ns) correspond to the actual teleportation. Figure 2a shows an increased number of counts at the centre, whereas Fig. 2b has a dip, which is expected if the retrieved state is close to input state $|-\rangle$. This is more easily visualized in Fig. 2c (or Fig. 2d), which shows a horizontal slice of Fig. 2a (or Fig. 2b) centred on $\delta t_{31} = 0$ (or $\delta t_{41} = 0$).

The fidelity of the retrieved state ρ with respect to the input state $|\psi\rangle$ (which here is effectively pure) is $F = \langle\psi|\rho|\psi\rangle$. For teleportation of state $|-\rangle$, the fidelity of the retrieved state can be estimated from the number of events observed at the centre of Fig. 2c ($\delta t_{32} = 0$) and at the minimum of Fig. 2d ($\delta t_{42} = 0$). The measured fidelity is $92 \pm 4\%$. To obtain complete information about state ρ, we performed quantum state tomography. With this information, we can assess if the reduced fidelity is due to an undesired unitary rotation

Figure 2 | Experimental results. a–d, Results of the teleportation of input state |−⟩. **a,** Two-dimensional histogram showing the number of threefold coincidences between detectors D₁, D₂ and D₃ as a function of delays δt_{31} and δt_{32} between detections at D₃ and D₁ and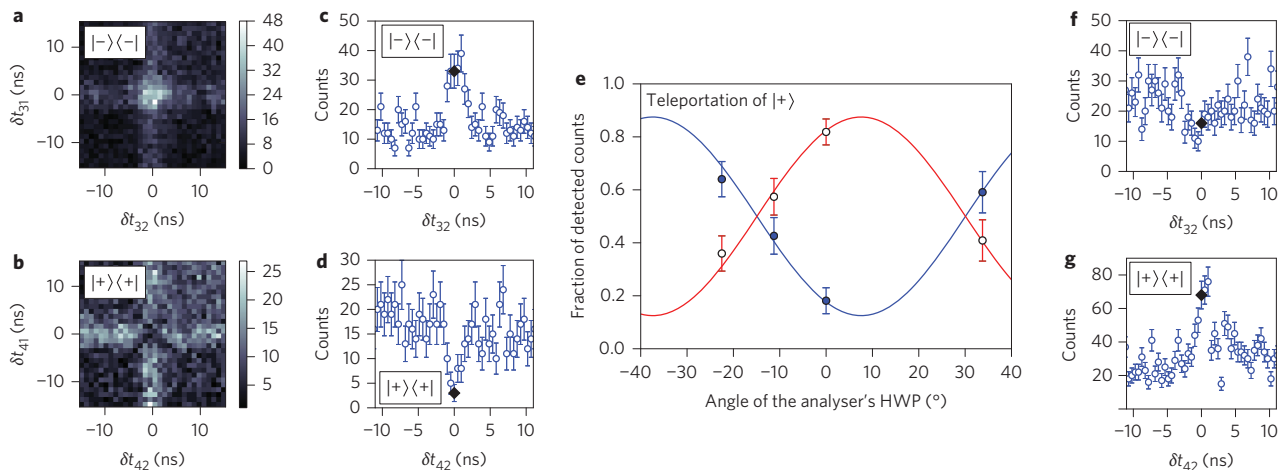 D₂. **b,** As in **a,** with D₄ instead of D₃. Each histogram indicates onto which polarization state the retrieved photon was projected (|−⟩⟨−| for **a** and |+⟩⟨+| for **b**). Each pixel corresponds to a square time window with sides of 486 ps. This is smaller than the coherence time of the photons, which is necessary to temporally resolve the detection events corresponding to a successful Bell-state measurement. **c,d,** Horizontal slices of **a** and **b** (centred on $\delta t_{31} = 0$ and $\delta t_{41} = 0$, respectively), showing the peak and dip, respectively, in number of detections at the centre. Black diamonds are the points used to estimate the fidelity of the teleportation. **e,** Detected fraction of counts on D₃ and D₄ of the analyser with input state |+⟩, when the retrieved state is measured in a basis that is rotated around the equator of the Bloch sphere. Solid lines show the values expected from quantum state tomography. **f,g,** Results of the teleportation of |+⟩ when the combined distance travelled by the idler and weak coherent state photons is 25 km of standard optical fibre. Uncertainties are obtained assuming a Poisson detection statistics.

on the Bloch sphere, or due to depolarization, which leads to a reduction in the purity $P = \text{Tr}(\rho^2)$ of the retrieved state. The undesired rotation can stem from drifts of the phase φ and/or of the amplitude of the |HH⟩ and |VV⟩ terms of the entangled state, while the main cause of the depolarization is noise arising from multi-pair emission of the source and/or of multiple photons in the WCS. The measured purity with input state |−⟩ is 94 ± 6%. This value allows us to find an upper bound $F_{\max} = \frac{1}{2}(1 + \sqrt{2P - 1}) = 97 \pm 3\%$ on the observable fidelity. See Supplementary Information for details.

The tomography was repeated for other input states, and the results are listed in Table 1. The expected fidelity of an arbitrary state is $\bar{F} = \frac{2}{3}\bar{F}_e + \frac{1}{3}\bar{F}_p$, where $\bar{F}_e$ and $\bar{F}_p$ are the average fidelities measured on the equator and the pole, respectively. We find $\bar{F} = 89 \pm 4\%$, which is larger than the maximum fidelity of 66.7% achievable with a prepare-and-measure strategy that does not use entanglement[27]. Most of the obtained fidelities are very close to $F_{\max}$ and are therefore limited by depolarization. For the teleportation of |+⟩, the measurements around the equator of the Bloch sphere shown in Fig. 2e reveal an additional rotation of the Bloch vector that further reduces the observed fidelity below the $F_{\max}$ upper bound (see Supplementary Information for details).

We also performed a teleportation of the |+⟩ state in a configuration where the WCS photon and the idler photon each travel

through 12.4 km of standard single-mode optical fibre before the BSM. This distance exceeds the previous record of 6 km for a fibre-based (and quantum memory-less) quantum teleportation[28]. The histograms show a dip (Fig. 2f) and a peak (Fig. 2g), which are indicative of the teleportation. The fidelity of this measurement is 81 ± 4%. We note that in this configuration, the signal photon was retrieved after 50 ns, that is, before the idler photon reached the BSM. The realization of a complete teleportation with feed-forward over this distance requires a storage time of at least 120 μs. A promising approach towards this goal is to combine spin-wave storage[22] with dynamical decoupling[19,20].

Our experiment demonstrates the feasibility of long-distance teleportation of single quanta of light onto a solid-state quantum memory. The fundamentals of our experiment could be used in future demonstrations of a small-scale network of remote quantum memories, or ultimately in a real-world quantum repeater based on an optical-fibre architecture. In a broader context, our experiment could be useful for transferring quantum information between remote quantum network nodes made of rare-earth crystals coupled to superconducting qubits[29], which could ultimately lead to the realization of deterministic Bell-state measurements on photonic qubits[30].

Methods

Source of polarization-entangled photons. Details about the source are provided in the Supplementary Information. In brief, it uses two periodically poled (PP) nonlinear waveguides (Fig. 1). One is a 1.3-cm-long waveguide embedded in potassium titanyl phosphate (PPKTP) and the other is a 6-cm-long titanium-indiffused waveguide based in lithium niobate (PPLN). Several procedures were implemented to monitor and stabilize the properties of the source. First, the pump light at 532 nm was continuously frequency-stabilized using a feedback mechanism based on difference-frequency generation of light at 1,338 nm from mixing the 532 and 883 nm preparation light in the PPLN waveguide. This ensures that the energy of a pump photon is correlated with the central frequency of the spectra of the signal and idler photons, which are determined by the filters. Second, the residual 532 nm light present in the unused output ports of the two PBSs located just before the cavity and the etalon was used to continuously lock the phase φ of the entangled state. To achieve this, an error signal was derived from the 532 nm light and feedback was applied on two piezo-mounted mirrors (one for the signal photon and one for the idler photon) located immediately after the dichroic mirrors. Fast

Table 1 | Measured fidelities and purities for all input states.

Input state	Fidelity (%)	Purity (%)	$F_{\max}$ (%)
|H⟩	94 ± 3	93 ± 3	96 ± 3
$\|-\rangle = \frac{1}{\sqrt{2}}(\|H\rangle - \|V\rangle)$	92 ± 4	94 ± 6	97 ± 3
$\|R\rangle = \frac{1}{\sqrt{2}}(\|H\rangle + i\|V\rangle)$	84 ± 4	73 ± 5	84 ± 4
$\|+\rangle = \frac{1}{\sqrt{2}}(\|H\rangle + \|V\rangle)$	82 ± 4	83 ± 9	91 ± 6
|+⟩ (24.8 km)	81 ± 4	–	–

The uncertainties are obtained from Monte Carlo simulations assuming a Poisson distribution of the number of threefold events. Also shown is the upper bound on the fidelity $F_{\max}$ that is obtained from the measured purity.

fluctuations were compensated for, but φ could still slowly drift by a few degrees per hour, at most. Third, a characterization of the properties of the source was performed every 30 min with a completely automatized procedure. For this, the teleportation was stopped for a few minutes by switching off the WCS. Then, by measuring twofold coincidences between the idler photon and the transmitted signal photon, the visibility of the source was measured, and the value of phase φ was extracted (see Supplementary Information). The measured average visibility was 93%. From these measurements, the second-order cross-correlation function between the idler and the signal photons was estimated and used to monitor the probability P of emitting a pair of photons in a time window of $\sim$500 ps. We measured $P \approx 10^{-2}$. The monitoring and stabilization yielded stability for periods as long as 24 h. We note that the 532 nm light was pulsed in 25-ns-long Gaussian pulses with 100 ns between successive pulses (which is twice the storage time) to improve the signal-to-noise ratio of the teleportation experiment (see Supplementary Information for details).

Polarization-preserving quantum memory. The compact, broadband and polarization-preserving quantum memory was achieved by placing two 5.8-mm-long Nd^{3+}:Y_2SiO_5 crystals around a 2-mm-thick half-wave plate, resulting in a total device length of 14 mm. Anti-reflective coatings were added on all surfaces (cryostat windows, crystals and half-wave plate). The resulting off-resonance transmission coefficient was 95%. To obtain short crystals with sufficient absorption we grew Nd^{3+}:Y_2SiO_5 crystals using the Czochralski process, with a neodymium concentration estimated to be 75 ppm. These crystals have an absorption coefficient of $\alpha = 3.7$ cm^{-1} (with an applied magnetic field of 300 mT, as in ref. 21). The resulting optical depth of the polarization-preserving memory device was $d = 2.3 \pm 0.1$. The AFC was prepared using an acousto-optic modulator (AOM), used in a double-pass configuration, which modulates the intensity and frequency of the light from an external cavity diode laser at 883 nm (centred on the absorption line of the $^4I_{9/2}$–$^4F_{3/2}$ transition) in order to pump some of the atoms to the other Zeeman level (see ref. 21). This was used to create a 120 MHz comb with a spacing of 20 MHz between peaks. To increase the memory bandwidth beyond 120 MHz, the light at the output of the AOM was sent into a phase modulator that creates first- and second-order sidebands separated by 120 MHz. In this way, the comb at the carrier frequency was copied twice on each side, yielding an overall comb width of 600 MHz. The overall efficiency of the polarization preserving memory was 5% with a 50 ns storage time.

References

1. Bennett, C. H. *et al.* Teleporting an unknown quantum state via dual classical and Einstein–Podolsky–Rosen channels. *Phys. Rev. Lett.* **70,** 1895–1899 (1993).
2. Briegel, H.-J., Dür, W., Cirac, J. I. & Zoller, P. Quantum repeaters: the role of imperfect local operations in quantum communication. *Phys. Rev. Lett.* **81,** 5932–5935 (1998).
3. Sangouard, N., Simon, C., de Riedmatten, H. & Gisin, N. Quantum repeaters based on atomic ensembles and linear optics. *Rev. Mod. Phys.* **83,** 33–80 (2011).
4. Kimble, H. J. The quantum internet. *Nature* **453,** 1023–1030 (2008).
5. Clausen, C. *et al.* Quantum storage of photonic entanglement in a crystal. *Nature* **469,** 508–511 (2011).
6. Saglamyurek, E. *et al.* Broadband waveguide quantum memory for entangled photons. *Nature* **469,** 512–515 (2011).
7. Kok, P. *et al.* Linear optical quantum computing with photonic qubits. *Rev. Mod. Phys.* **79,** 135–174 (2007).
8. Sherson, J. F. *et al.* Quantum teleportation between light and matter. *Nature* **443,** 557–560 (2006).
9. Krauter, H. *et al.* Deterministic quantum teleportation between distant atomic objects. *Nature Phys.* **9,** 400–404 (2013).
10. Chen, Y.-A. *et al.* Memory-built-in quantum teleportation with photonic and atomic qubits. *Nature Phys.* **4,** 103–107 (2008).
11. Bao, X.-H. *et al.* Quantum teleportation between remote atomic-ensemble quantum memories. *Proc. Natl Acad. Sci. USA* **109,** 20347–20351 (2012).
12. Olmschenk, S. *et al.* Quantum teleportation between distant matter qubits. *Science* **323,** 486–489 (2009).
13. Nölleke, C. *et al.* Efficient teleportation between remote single-atom quantum memories. *Phys. Rev. Lett.* **110,** 140403 (2013).
14. Gao, W. B. *et al.* Quantum teleportation from a propagating photon to a solid-state spin qubit. *Nature Commun.* **4,** 3744 (2013).
15. Simon, C. *et al.* Quantum repeaters with photon pair sources and multimode memories. *Phys. Rev. Lett.* **98,** 190503 (2007).
16. Afzelius, M., Simon, C., de Riedmatten, H. & Gisin, N. Multimode quantum memory based on atomic frequency combs. *Phys. Rev. A* **79,** 052329 (2009).
17. Hedges, M. P., Longdell, J. J., Li, Y. & Sellars, M. J. Efficient quantum memory for light. *Nature* **465,** 1052–1056 (2010).
18. Sabooni, M., Li, Q., Kröll, S. & Rippe, L. Efficient quantum memory using a weakly absorbing sample. *Phys. Rev. Lett.* **110,** 133604 (2013).
19. Longdell, J. J., Fraval, E., Sellars, M. J. & Manson, N. B. Stopped light with storage times greater than one second using electromagnetically induced transparency in a solid. *Phys. Rev. Lett.* **95,** 063601 (2005).
20. Heinze, G., Hubrich, C. & Halfmann, T. Stopped light and image storage by electromagnetically induced transparency up to the regime of one minute. *Phys. Rev. Lett.* **111,** 033601 (2013).
21. Usmani, I., Afzelius, M., de Riedmatten, H. & Gisin, N. Mapping multiple photonic qubits into and out of one solid-state atomic ensemble. *Nature Commun.* **1,** 12 (2010).
22. Timoney, N., Usmani, I., Jobez, P., Afzelius, M. & Gisin, N. Single-photon-level optical storage in a solid-state spin-wave memory. *Phys. Rev. A* **88,** 022324 (2013).
23. Clausen, C., Bussières, F., Afzelius, M. & Gisin, N. Quantum storage of heralded polarization qubits in birefringent and anisotropically absorbing materials. *Phys. Rev. Lett.* **108,** 190503 (2012).
24. Gündoğan, M., Ledingham, P. M., Almasi, A., Cristiani, M. & de Riedmatten, H. Quantum storage of a photonic polarization qubit in a solid. *Phys. Rev. Lett.* **108,** 190504 (2012).
25. Zhou, Z.-Q., Lin, W.-B., Yang, M., Li, C.-F. & Guo, G.-C. Realization of reliable solid-state quantum memory for photonic polarization qubit. *Phys. Rev. Lett.* **108,** 190505 (2012).
26. Marsili, F. *et al.* Detecting single infrared photons with 93% system efficiency. *Nature Photon.* **7,** 210–214 (2013).
27. Massar, S. & Popescu, S. Optimal extraction of information from finite quantum ensembles. *Phys. Rev. Lett.* **74,** 1259–1263 (1995).
28. de Riedmatten, H. *et al.* Long distance quantum teleportation in a quantum relay configuration. *Phys. Rev. Lett.* **92,** 047904 (2004).
29. Probst, S. *et al.* Anisotropic rare-earth spin ensmble strongly coupled to a superconducting resonator. *Phys. Rev. Lett.* **110,** 157001 (2013).
30. Steffen, L. *et al.* Deterministic quantum teleportation with feed-forward in a solid state system. *Nature* **500,** 319–322 (2013).

Author contributions

The experiment was conceived by F.B., C.C., M.A. and N.G. The superconducting detectors were fabricated by V.B.V., S.W.N. and F.M. and characterized by V.B.V., B.K. and F.B. The rare-earth-ion doped crystals were grown by A.F. and P.G. and characterized by A.T. and F.B. The lithium niobate waveguide was fabricated by H.H., C.S. and W.S. and characterized by C.C. The measurements and data analysis were done by C.C., A.T. and F.B. The manuscript was written by F.B., A.T. and C.C., with contributions from all authors.

Additional information

Supplementary information is available in the online version of the paper. Reprints and permissions information is available online at www.nature.com/reprints. Correspondence and requests for materials should be addressed to F.B.

Competing financial interests

The authors declare no competing financial interests.

Quantum teleportation from a telecom-wavelength photon to a solid-state quantum memory

Félix Bussières,[1] Christoph Clausen,[1] Alexey Tiranov,[1] Boris Korzh,[1] Varun Verma,[2]
Sae Woo Nam,[2] Francesco Marsili,[3] Alban Ferrier,[4] Philippe Goldner,[4] Harald
Herrmann,[5] Christine Silberhorn,[5] Wolfgang Sohler,[5] Mikael Afzelius,[1] and Nicolas Gisin[1]

[1]*Group of Applied Physics, University of Geneva, CH-1211 Geneva 4, Switzerland*
[2]*National Institute of Standards and Technology, Boulder, Colorado 80305, USA*
[3]*Jet Propulsion Laboratory, California Institute of Technology,*
4800 Oak Grove Drive, Pasadena, California 91109, USA
[4]*Chimie ParisTech, Laboratoire de Chimie de la Matière Condensée de Paris,*
CNRS-UMR 7574, UPMC Univ Paris 06, 75005 Paris, France
[5]*Applied Physics / Integrated Optics Group, University of Paderborn, 33095 Paderborn, Germany*
(Dated: July 15, 2014)

I. INTRODUCTION

In this Supplementary Information, we provide additional details on our experiment. Section II provides details on the fabrication of the WSi superconducting detector. Section III describes how the monitoring of the properties of the source of entangled photons and of the source of weak coherent state is done. Section IV presents a detailed description of the features of the two-dimensional histograms of the threefold coincidences from which the quantum state tomography results are derived. We also model the noise stemming from multiple photon pairs and multiple photons in the weak coherent. Section V provides details on the how the quantum state tomography is performed. The effect of the aforementioned noise on the fidelity and purity is discussed.

II. SUPERCONDUCTING NANOWIRE DETECTORS

The WSi detectors were fabricated to obtain maximum efficiency at a wavelength of 1340 nm and for operation at 2.5 K in a two-stage closed-cycled cryocooler. Their fabrication and characterization is detailed in Ref. [1]. A gold mirror was fabricated by depositing 80 nm of gold on top of Ti on a 3 inch Silicon wafer using electron-beam evaporation and photolithographically patterned using a lift-off process. A space layer between the gold mirror and WSi detector consisting of 195 nm of SiO_2 was then deposited by plasma-enhanced chemical vapour deposition (PECVD). A 4.5 nm-thick W_xSi_{1-x} layer ($x \approx 0.8$) was deposited by DC magnetron co-sputtering from separate W and Si targets at room temperature, and capped with 2 nm of amorphous Si to prevent oxidation. Electron-beam lithography and etching in an SF_6 plasma were used to define nanowire meanders with a width of 130 nm and pitch of 260 nm. An antireflection coating was deposited on the top surface consisting of 225 nm SiO2, 179 nm SiN_x, 231 nm SiO_2, and 179 nm SiN_x. A key-hole shape was etched through the Si wafer around each SNSPD, which could then be removed from the wafer

and self-aligned to a single mode optical fibre [2, 3]. The size of the SNSPD is $16 \times 16 \ \mu m^2$, larger than the 10 μm mode field diameter of a standard single mode fibre, to allow for slight misalignment. The optimal system detection efficiency reaches 75% with a dark count rate of the order of 300 counts per second. However, during the experiment, the temperature of the cryostat fluctuated and affected the performance, yielding in the worst case a detection efficiency of 60% with a dark count rate of a few kHz.

III. MONITORING OF THE SOURCE OF ENTANGLED PHOTONS AND SOURCE OF WEAK COHERENT STATE

Complete details on the source of entangled photons can be found in Ref. [4].

A. Characterization of the source of entangled photon pairs

The source of entangled photons was continuously monitored during the experiment. Here we provide details on how we monitored the relative phase φ of the entangled state $\frac{1}{\sqrt{2}}(|HH\rangle + \mathrm{e}^{i\varphi}|VV\rangle)$ that was produced, as well as the fluctuations of the number of photon pairs created in a given time window.

1. Entanglement visibility and phase drift compensation

Automatized monitoring of the source was performed a least once per hour by producing a visibility curve, which was accomplished as follows. First, the weak coherent state (WCS) was switched off (see Fig. A1, which is the same as Fig. 1 of the main text). Then, a half wave plate was inserted before the 50/50 beam splitter (BS) used for Bell state measurement, and its angle was set such that, when combined with the polarizers placed just after the beam splitter, a detection on D_1 would project on $|+\rangle$,
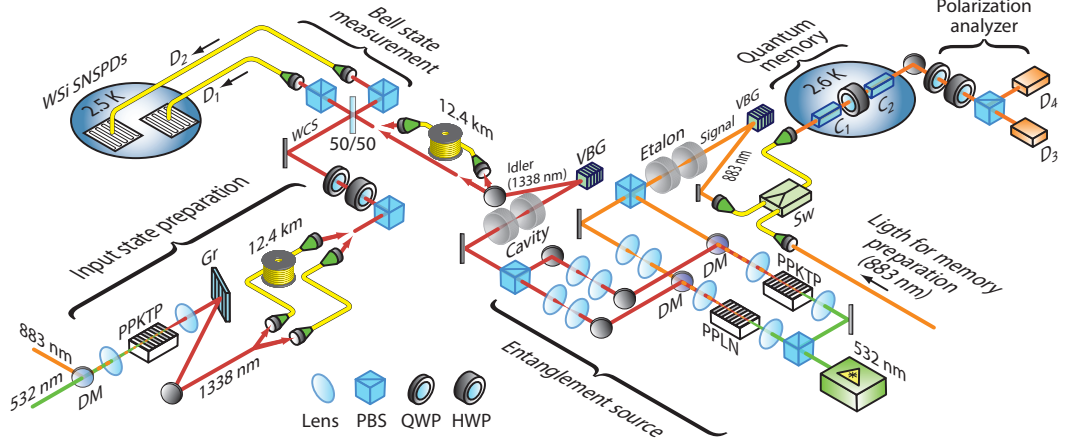
FIG. A1. Experimental setup. This figure is identical to Fig. 1 of the main text, and is shown here for convenience.

and D_2 would project on $|-\rangle$. The state of the corresponding signal photon, e.g. $\frac{1}{\sqrt{2}}(|H\rangle + e^{i\varphi}|V\rangle)$ when the detection occurred at D_1, was then analyzed by rotating the half wave plate (HWP) of the analyzer, projecting on states on the equator of the Bloch sphere. For this measurement we use only coincidences stemming from the *transmitted photons*, i.e. the signal photons that passed through the quantum memory without being absorbed.

The resulting visibility curves (see Fig. A2 for an example) show the number of coincidences on each detector of the analyzer (i.e. D_3 and D_4), as a function of the angle of the HWP. The phase φ is determined from the common horizontal offset of the four curves. The phase slowly drifted with time, typically by a few degrees per several hours. For the teleportation measurements, this phase was effectively cancelled by rotating the quarter wave plate of the analyzer to set the offset of the visibility curves to zero. By monitoring the overall variations of the amplitudes of the visibility curves, we could also monitor the balance between two waveguides, as well as the coincidence rate of the source. The visibility, averaged over all measurements, was 93%.

2. Cross-correlation of idler and signal modes

To monitor the magnitude and stability of the number of photon pairs created in a given time window, we measured the zero-time second-order cross-correlation function between the detected idler photon and the transmitted signal photon, g_{si}, defined as

$$g_{si} = \frac{\langle d_i^\dagger d_i d_s^\dagger d_s\rangle}{\langle d_i^\dagger d_i\rangle\langle d_s^\dagger d_s\rangle},$$

where d_i (or d_s) is the annihilation operator for the idler mode (or signal mode), and $d_i^\dagger$ (or $d_s^\dagger$) is the associated
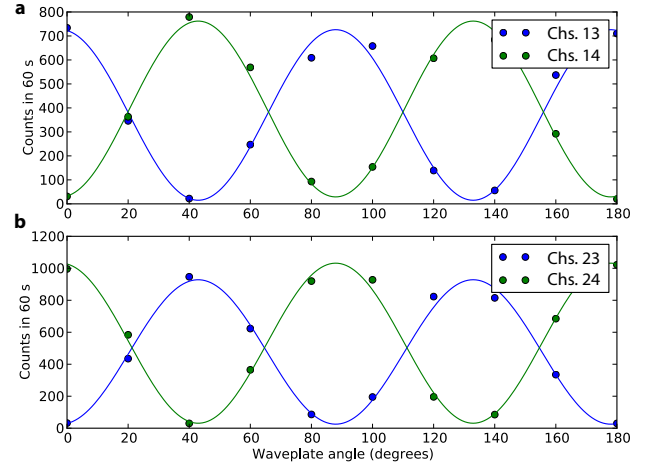
FIG. A2. Visibility curves for, **a**, detector pairs D_1-D_3 and D_1-D_4, and **b**, pairs D_2-D_3 and D_2-D_4, where D_1 and D_2 are the detectors for the idler photons, and D_3 and D_4 are the detectors of the analyzer of the signal photon.

creation operator [5]. With negligible dark counts and single-photon detectors having a timing resolution that is much smaller than the coherence time of the photons, one can show that $g_{si} = 1 + 1/p \approx p^{-1}$, where $p \ll 1$ is the probability to create a pair of photons in a given time window [6]. It is also equal to the ratio of the probability to detect a coincidence stemming from two photons of the same pair, over the probability to detect two photons from different pairs. Measuring a value $g_{si} > 2$ implies that the signal and idler fields are non-classically correlated [6]. Moreover, measuring a value $g_{si} \gg 1$ (which implies that $p \ll 1$) is a necessary condition to create close-to-maximally entangled states [5] and to show the non-classical nature of the heralded signal photon [7].
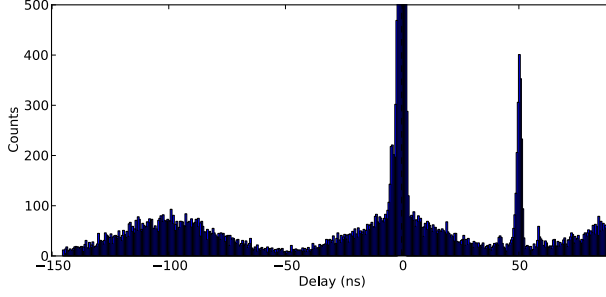
FIG. A3. Histogram of the number of coincidences as a function of the delay between the detection of a signal and an idler photon. Each bin is 162 ps wide. We see the peak corresponding to the detection of a transmitted signal photon (at 0 ns) and the peak of the stored and retrieved photon (50 ns). The transmitted peak is vertically clipped.

In practice, g_{si} was estimated using all the data accumulated for the visibility curves during one day. Using these data, we produced a histogram of the number of coincidences between the idler and signal modes as a function of the delay between them. Fig. A3-a shows one such histogram, on which we can see two main peaks over an oscillating background level. The peak at 0 ns is due to coincidences involving a transmitted signal photon, and the one at 50 ns is due to a stored signal photon, i.e. a signal photon that was stored and retrieved from the quantum memory. Note that the transmitted peak is clipped because we expanded the vertical scale so that we could see the effect of the pulsed pump laser, which gives rise to the wide and small bumps centred on -100, 0 and 100 ns, etc (we recall that the pump light at 25 ns was shaped into 25 ns-wide gaussian pulses separated by 100 ns). We see the reduction of the number of accidental coincidences between the bumps, which was the desired effect. The cross-correlation of the transmitted peak $g_{si}^{(t)}$ is estimated by dividing the number of coincidences in a narrow window centred on 0 ns by the number of coincidences in another window centred on a neighbouring bump that is 100 ns away. The average value of $g_{si}^{(t)}$ was 100, and varied from 80 to 150 for all the measurements. The cross-correlation of the stored photon $g_{si}^{(s)}$ is estimated by centering the first window on the stored photon peak, and the second one 100 ns away, which is falls on a minimum of the oscillating background. The measured value of $g_{si}^{(s)}$ varied from 6 to 20. All values were measured with 486 ps-wide coincidence windows. The measured values of $g_{si}^{(s)}$ fluctuate strongly, but they are nevertheless well above the classical upper bound of 2, which highlights the single-photon nature of the polarization state that is retrieved from the quantum memory [6–8].

B. Weak coherent state (WCS)

As explained in the main text, the source of entangled photons was designed such that central frequency of signal photons corresponds to the centre of the atomic frequency comb that is created using the 883 nm diode laser, and such that the frequency of the pump light at 532 nm create photon pairs that satisfy the energy-conservation imposed by the transmission wavelength of the Fabry-Perot cavity of the idler photon. Hence, mixing part of the 532 nm light and part of the 883 nm diode laser into a separate PPKTP waveguide automatically creates coherent pulses of light (through difference-frequency generation, DFG) having a frequency that matches the central frequency of the Fabry-Perot cavity, and thus of the idler photons (see Fig A1). This light therefore has suitable spectral properties to be indistinguishable from the idler photons, and therefore to encode the input state of the teleportation. The intensity of the WCS was monitored and stabilized by diverting a small portion towards a single-photon detector creating a feedback signal controlling a variable attenuator. We estimated that the mean number of photons contained in a 486 ps-wide window at the centre of one WCS was $\mu \approx 0.011 \pm 0.002$ for the teleportation of $|-\rangle$, and 0.016 for the teleportation of $|+\rangle$, $|R\rangle$ and $|H\rangle$.

C. Indistinguishability of the idler and the WCS

Projecting the input state and the idler photon on a Bell state (see Fig. 1) requires the ability to post-select events where the two photons temporally overlapped on the 50/50 beam splitter (see Fig. 1). This is possible only if the temporal resolution (i.e. the jitter) of the detectors is smaller than the coherence time of the idler photon (because the WCS is generated from DFG between two narrowband lasers, its coherence time is much longer than the 1.4 ns coherence time of the idler). The temporal resolution effectively defines temporal modes on which the photons are projected onto when they are detected. Therefore, we need to consider the indistinguishability in these modes, which was verified through the observation of a Hong-Ou-Mandel dip in an experiment performed before the quantum teleportation [9]. For this, continuous-wave (CW) light at 532 nm was used to pump the PPLN waveguide of the source while the PPKTP waveguide was blocked (see Fig. A1), and the filtered idler photons were mixed on the 50/50 beam splitter with the WCS. The signal photon was bypassing the quantum memory and used to herald an idler photon with an horizontal polarization, the same as the WCS. The idler photon was detected with a niobium nitride SNSPDs (7% efficiency) that had jitter of about 100 ps. The photon-pair creation probability $p \approx 1/g_{si}$ was ≈ 0.0025 in a 486-ps window, and the mean number of photon for the WCS was $\mu \approx 0.0035$. Fig. A4 shows the observed dip, with a visibility of 81%. From this, we conclude that the idler
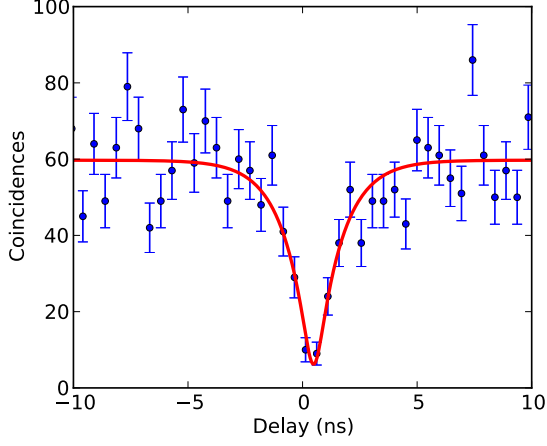
FIG. A4. Coincidence histogram showing a Hong-Ou-Mandel dip between an heralded signal photon and the weak coherent light. The visibility of the dip is 81%. The horizontal axis is the delay between the detection of the signal photon and one of the detectors behind the 50/50 beam splitter.

photons and the WCS are close to be completely indistinguishable. The visibility is partly reduced by the noise stemming from the accidental detection of two photon from the WCS or two idler photons coming from two pairs created simultaneously.

IV. THREEFOLD DETECTION HISTOGRAMS

A. Teleportation of $|-\rangle$, $|R\rangle$ and $|+\rangle$

Let us consider the conceptual setup of Fig. A5 representing the teleportation of the $|-\rangle$ state. We will use it to explain the main features of the two 2D histograms corresponding to teleportation of the $|-\rangle$ state towards the signal, when the analyzer is set to measure in the $\{|+\rangle, |-\rangle\}$ basis; see Fig. A6-a and Fig. A6-b (they are identical to Fig. 2-a and 2-b on the main text). For comparison, the histograms corresponding to the events where the detected signal photon was not absorbed by the memory (the transmitted photon) are shown on Fig. A7-a and A7-b. Each histogram shows either the number of threefold coincidences at D_1, D_2 and D_3, or at D_1, D_2 and D_4. Each bin (i.e. each pixel) corresponds to a window of fixed width and height, which is $(486 \text{ ps})^2$ here. For a histogram with a detection at D_j ($j = 3$ or 4), the y-axis corresponds to the delay δt_{j1} between the detections at D_j and D_1, and the x-axis to the delay δt_{j2} between the detections at D_j and D_2.

We first describe what we would expect in the vicinity of the central bin of the histogram, at $\delta t_{j1} = \delta t_{j2} = 0$, assuming ideal conditions (i.e perfect optical alignment; negligible contribution from multi-photons in the WCS,
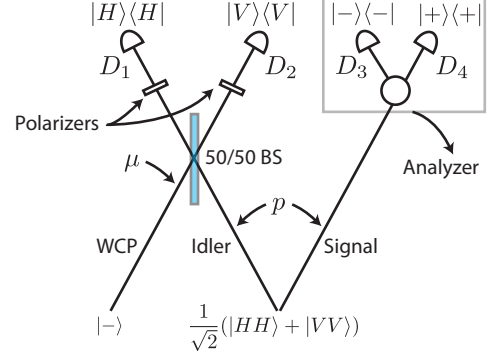
FIG. A5. Conceptual experimental setup for the teleportation of the $|-\rangle$ state. The polarization of a photon in the WCS is prepared in the the $|-\rangle$ state, and the probability to find a photon in a given time window is μ. The idler and signal modes are populated with a pair of polarization-entangled photons with a probability p. The WCS and the idler modes are mixed on a 50/50 beam splitter (BS). The output modes of the BS are filtered with polarizers, such that a detection at D_1 projects on $|H\rangle$, and a detection at D_2 projects on $|V\rangle$. The signal mode is sent towards a polarization qubit analyzer set such that a successful Bell state measurement should result in a detection of the signal photon in detector D_3 (we represent this by indicating that D_3 projects on $|-\rangle$, and D_4 on $|+\rangle$).

multi-pairs and dark counts; negligible detection jitter and dark counts). This centre region corresponds to the threefold coincidences where the idler photon and a photon from the WCS were temporally overlapping at the 50/50 beam splitter (which heralds a successful Bell state measurement), and the detected signal photon is the entangled companion of the detected idler photon. The area of the region is of the order of τ_i^2, where $\tau_i \approx 1.4$ ns coherence time of the idler photon. In this region, the probability to have a photon from the WCS just before the BS and to have an idler photon just before the BS, is given by $p\mu$ (we do not need to take into account the losses and detector efficiencies in the system because they all factor out in the final step of the calculation when we compare the probabilities for the different events). Given this, the probability that they split at the BS can be shown to be equal to 1/4, which corresponds to the probability of a successful projection on the $|\Psi^-\rangle = 2^{-1/2}(|HV\rangle - |VH\rangle)$ Bell state [10]. Because the two photons are indistinguishable, they must have orthogonal polarizations behind the BS (otherwise they would bunch), but there are two possibilities happening with equal probabilities, namely V in one mode and H in the other, or the opposite. Hence, the presence of the orthogonally oriented polarizers after the BS further reduces by a factor of 2 the probability to find one photon in each output arm after the polarizers. In practice, the polarizers were introduced to minimize the probability to detect two photons with the same polarization after

the BS, which can happen if the photon are not perfectly indistinguishable.

When a successful teleportation occurs, the polarization state of the signal photon is equal to the polarization state of the photon from the WCS, up to a constant unitary transformation that we include in the analyzer. We assume the analyzer is oriented such that a detection at D_3 corresponds to a projection on the input state. The total threefold coincidence probability is given by

$$P_{123}(\delta t_{31} = 0, \delta t_{32} = 0) = p\mu \cdot \frac{1}{4} \cdot \frac{1}{2} = \frac{1}{8}p\mu. \quad \text{(A1)}$$

Since D_4 projects on $|+\rangle$, the probability to register a threefold coincidence at D_1, D_2 and D_4 should be zero:

$$P_{124}(\delta t_{41} = 0, \delta t_{42} = 0) = 0. \quad \text{(A2)}$$

Let us now consider the case where the WCS photon is arriving later (by a time greater than τ_i) compared to the two entangled photons. A possible realization of this would be a threefold with $\delta t_{31} = 0$ and $\delta t_{32} > \tau_i$. In this specific case, the detection at D_2 must stem from the WCS, because its detection time is not correlated to the detection of the signal photon, contrary to the idler photon (this is true only if $\mu \gg p$, which is shown in section IV C to be a necessary condition to get a good signal-to-noise ratio). The probability for this threefold event is easily calculated to be

$$P_{123}(\delta t_{31} = 0, \delta t_{32} > \tau_i) = \frac{1}{32}p\mu, \quad \text{(A3)}$$

and we see that

$$\frac{P_{123}(\delta t_{31} = 0, \delta t_{32} = 0)}{P_{123}(\delta t_{31} = 0, \delta t_{32} > \tau_i)} = 4. \quad \text{(A4)}$$

The same result applies to all the threefold events where one delay is zero, and the absolute value of the other is greater that τ_i, i.e. for

$$P_{123}(\delta t_{31} = 0, |\delta t_{32}| > \tau_i),$$
$$P_{123}(|\delta t_{31}| > \tau_i, |\delta t_{32}| = 0),$$
$$P_{124}(|\delta t_{41}| > \tau_i, |\delta t_{42}| = 0),$$
$$P_{124}(\delta t_{41} = 0, |\delta t_{42}| > \tau_i).$$

Finally, event with $|\delta t_{j1}| > \tau_i$ and $|\delta t_{j2}| > \tau_i$ correspond to threefold detections involving the creation of two entangled photon pairs created at different times and the detection of a WCS photon at a another time that differs from the previous two. These events happen with a probability of order $p^2\mu/32$ and are thus much less frequent than all the other ones consider above.

This simple model explains the 2D histograms of Fig. A6-a-b with the stored photon, on which we see a cross-like structure centred on the origin, and either a peak or a dip at the centre. The one-dimensional histogram of Fig. A6-a corresponds to a horizontal slice of the 2D histogram with $\delta t_{31} = 0$. We see a peak whose height rises above 30 counts, while the average number

of counts away from the centre is approximately 12 per bin. The width of the peak is of the order of 2 ns, which is consistent with $\tau_i = 1.44$ ns. Similarly, we see a dip on the 1D histogram of Fig. A6-b that nearly reaches 0 counts. The same structure appears for the teleportation of the $|R\rangle$ state with the analyzer set to the $\{|R\rangle, |L\rangle\}$ basis (Fig. A6-i-j). Finally, we also see the structure on the histograms of the transmitted signal photon, Fig. A7-a-b-i-j. Since all histograms obtained with the transmitted photon have more counts, they should be considered as indicators of what the results with the stored photons should be with better statistics. We note that the results for the teleportation of $|+\rangle$ are not shown here, but the above observations also apply for this state.

We now follow the same reasoning as above to explain the structure of the teleportation of $|-\rangle$, but when the analyzer is set to project in the $\{|R\rangle, |L\rangle\}$ basis instead of $\{|+\rangle, |-\rangle\}$ (we recall that this measurement is used in the quantum state tomography of the state retrieved from the memory). For the events that are away from the centre of the histogram, the probabilities are easily found to be the same as the previous case. For the events at the centre, the probability to detect the signal photon at D_3 must be half of the probability $P_{123}(\delta t_{31} = 0, \delta t_{32} = 0)$ calculated above (eq. A2). This is because the retrieved state is in the $|-\rangle$ state and is analyzed in a maximally conjugated basis, which yields a 50% probability of detecting it in a given detector. Hence, the 2D histograms corresponding to a detection at D_3 or D_4 should both show a peak at the centre, but with a height that is twice higher than the value found away from the centre. Fig. A6-c-d show the relevant 2D histograms for the stored photon, on which the expected structure does not clearly appear, but the results are nevertheless conclusively different from the ones of Fig A6-a-b. The expected structure is more apparent for the teleportation of the $|R\rangle$ state, when measured in the $\{|+\rangle, |-\rangle\}$ basis (Fig. A6-g-h). Finally, the expected structure clearly appears for the transmitted photon (Fig. A7-c-d-g-h).

The structure of the teleportation of $|-\rangle$, $|R\rangle$ and $|+\rangle$ when measured in the $\{|H\rangle, |V\rangle\}$ basis is explained as follows. Let us assume the analyzer is set such that D_3 projects on $|H\rangle$. Due to the polarization entanglement between the signal and idler, a detection at D_3 remotely prepares the idler in the state $|H\rangle$. Therefore, the latter can only be detected at D_1 with a delay $\delta t_{31} = 0$, which means that the coherent state can only be detected at D_2 to create a threefold coincidence. The probability for this process is $p\mu/16$, and it does not depend on the time at which the coherent state is detected. Because D_1 and D_3 are both projecting on $|H\rangle$, the probability to observe a coincidence between these two events with a delay $|\delta t_{31}| > \tau_i$ can only stem from the creation of more than one pair of entangled photons, and a threefold in this case would scale as $p^2\mu$ and is much less probable. The structure of the 2D histogram should therefore consists in a peak centred on $\delta t_{31} = 0$ that is extending over all values of δt_{32}. Alternatively, the 2D histogram of D_4

should be a peak centred on δt_{32} that is extending over δt_{31}. That is indeed what we observe with the stored photon (Fig. A6-e-f-k-l), and with the transmitted photon (Fig. A7-e-f-k-l).

B.   Additional remarks

We note that the measurement time required to generate each of the histograms on Fig. A6 and A7 typically varied from 8 to 15 hours. These variations partly explain why the number of counts in the crosses is not always the same. The other contribution is the different collection and detection efficiencies of D_3 and D_4.

The time required to produce each histogram could have been reduced by a factor of 4 by using two more detectors placed on the unused ports of the polarizing beam splitters, which are after the BS (see Fig. 1 of the main text). This would allow the projection of the idler and the WCS photon on the $|\Psi^+\rangle = 2^{-1/2}(|HV\rangle + |VH\rangle)$ Bell state with a probability of 1/4 (in the ideal case), and thus doubling the probability to herald a Bell state measurement [10].

C.   Multiphoton emission

The setup described on Fig. A5 is also useful to estimate the contribution of the emission of more than one photon in the WCS, or the creation of more than one photon pair, to the noise.

For the teleportation of $|-\rangle$ considered above, we can calculate the probability $P(2,0)$ of getting a threefold coincidence stemming from two photons in the WCS, while the idler photon is lost and the signal photon is detected (the calculation applies to the other states as well). This probability is given by the probability $\mu^2/2$ to have two WCS photons; the probability p to create a pair; the probability $(1-\eta_i)$ to loose the idler photon on the path from the source to the BS; the probability 1/8 for both WCS photons to split at the BS and to pass through the polarization filters; the probability $1/2 \cdot \eta_s$ to detect the signal photon in a given detector of the analyzer with a transmission η_s. This amounts to

$$P(2,0) = p\mu^2(1-\eta_i)\eta_s/32. \qquad (A5)$$

We can also calculate the probability $P(0,2)$ of a threefold stemming from the detection of two idler photons, while the WCS photon is lost. For this, we need to evaluate the probability to create two pairs of photons and that the two idlers have orthogonal polarizations. The Hamiltonian H of spontaneous parametric downconversion process with polarization entanglement is proportional to $H \sim \frac{1}{\sqrt{2}}(\hat{a}_H^\dagger \hat{b}_H^\dagger + \hat{a}_V^\dagger \hat{b}_V^\dagger)$, where $\hat{a}_H^\dagger$ (or $\hat{b}_H^\dagger$) creates a photon in the idler mode (or the signal mode) with horizontal polarization, etc. The state we get when two

pairs of photons are created is proportional to $\frac{1}{2}pH^2|00\rangle$, i.e.

$$\frac{p}{4}\left[(\hat{a}_H^\dagger \hat{b}_H^\dagger)^2 + (\hat{a}_V^\dagger \hat{b}_V^\dagger)^2 + 2\hat{a}_H^\dagger \hat{a}_V^\dagger \hat{b}_H^\dagger \hat{b}_V^\dagger\right]|00\rangle. \qquad (A6)$$

The probability to get two idler photons with orthogonal polarizations, and the same for the two signal photons $(\hat{a}_H^\dagger \hat{a}_V^\dagger \hat{b}_H^\dagger \hat{b}_V^\dagger)$ is therefore $p^2/4$, and the probability that they split at the BS and get transmitted through the polarizer is 1/4. When this is the case, the probability for one of the two signal photons to be detected in a given detector of the analyzer is $\eta_s/2$, which we multiply by two because we have two photons. Overall, the probability of this threefold is

$$P(0,2) \approx \left(1 - \mu - \frac{\mu^2}{2}\right) \cdot \frac{1}{32} \cdot p^2\eta_i^2 \cdot 2\eta_s \approx \frac{1}{16} \cdot p^2\eta_i^2\eta_s. \qquad (A7)$$

Using similar arguments, we can calculate the probability of other processes contributing to the noise, and show that only the ones given above are significant. Let $P(1,1) = p\mu\eta_i/8$ be the probability to register a threefold corresponding to an actual teleportation (see eq. A1). In order to maximize the signal-to-noise ratio, we must satisfy $P(1,1) \gg P(2,0)$ and $P(1,1) \gg P(0,2)$, which translates to

$$\eta_i \gg \frac{\mu}{4+\mu} \approx \frac{\mu}{4},$$
$$\mu \gg \frac{1}{2} \cdot p\eta_i.$$

By combining the two inequalities we get

$$\eta_i \gg \frac{\mu}{4} \gg \frac{p\eta_i}{8}. \qquad (A8)$$

The measured values are $\eta_i \approx 0.13$, $\eta_s \approx 6.3 \times 10^{-3}$, $p \approx 10^{-2}$ and $\mu \approx 0.011$, which satisfy the inequality. The value of p given here is taken as $1/g_{si}^{(t)} \approx 1/100$.

V.   QUANTUM STATE TOMOGRAPHY

We performed quantum state tomography to obtain complete information about the state retrieved from the memory. Quantum state tomography can be performed by measuring the photon in the three usual bases ($\{|H\rangle, |V\rangle\}$, $\{|+\rangle, |-\rangle\}$ and $\{|R\rangle, |L\rangle\}$), from which the x,y and z components of the Bloch vector are extracted [11]. Measurements with the different bases was performed in an alternating fashion, i.e. we would measure in each basis for one hour, and then cycle through. Quantum state tomography requires a suitable normalization of the observed number of counts to compensate for the uneven detection efficiencies of D_3 and D_4. The method used is based on the following reasoning. Since the state of the signal photon sent to the polarization analyzer after the quantum memory is from a close-to-maximally entangled pair, its polarization is in the completely mixed state (when we trace out the idler photon).

The probability to observe it in D_3 or D_4 is therefore be same, provided their collection and detection efficiencies are identical. Any observed deviation can therefore be used to normalized the number counts observed in a given period of time. To measure this deviation, we used the 2D histograms discussed in section IV, but with delays extending from -100 to 100 ns instead of -15 to 15 ns. Any threefold coincidence for which the delays are not equal to each other (i.e. away from the diagonal) heralds a signal photon in a completely mixed state. Hence, counting the total number of such events for the histogram with a detection at D_3, and comparing it to the number extracted from the equivalent histogram for D_4, directly gives the information about the detection efficiency mismatch. It can then be used to normalize the number of counts. This method is reliable since the wide area covered in the histogram yields a statistically significant number of counts, from which a good estimate of the mismatch is obtained. This method works only if the source is well balanced (that is the probability to find the pair in $|HH\rangle$ is essentially the same as finding it in $|VV\rangle$). This condition was satisfied in our experiment, and was automatically checked every hour.

The above method does not work for the teleportation of $|H\rangle$, because here the state of the signal photon is, ideally, in a pure polarization state and the aforementioned argument does not work. The efficiency mismatch was instead extracted from the maxima of the fitted visibility curves that are measured every hour.

The delays δt_{ij} ($i = 3, 4$ and $j = 1, 2$) of Fig. A6 and A7 have all been adjusted to position the events corresponding to an actual teleportation at the centre of the histograms. To determine the offsets that needs to be applied, we used the data accumulated for the visibility curves and from which we produced histograms of the twofold coincidences between the four detection combinations (1-3, 1-4, 2-3 and 2-4). For each histogram, the stored photon peak was fit with a gaussian, and the position of the maxima was used to adjust the offsets of the histograms.

A. Fidelity and purity

The fidelity F of a mixed state ρ with respect to a pure target state $|\psi\rangle$ is defined as $F = \langle\psi|\rho|\psi\rangle$. It corresponds to the probability obtaining the result $|\psi\rangle$ when subjecting ρ to a projective measurement in the orthonormal basis $\{|\psi\rangle, |\psi^\perp\rangle\}$, where $\langle\psi|\psi^\perp\rangle = 0$. In practice, the effect of loss in the channel is post-selected out by keeping only the events where the signal photon is detected. For our experiment, the input states were always contained in one of the measurement bases used for the quantum state tomography of the retrieved state. Hence, the measurement in that basis can readily be used to estimate the fidelity. Let N_3 (or N_4) be the number of threefold coincidences observed at D_3 (or D_4), properly normalized to compensate for its efficiency mismatch (see section V). If

D_3 is the detector projecting on the target state, then the fidelity is directly given by $N_3/(N_3 + N_4)$. It can also be written as $F = (1+V)/2$, where $V = (N_3-N_4)/(N_3+N_4)$ is called the visibility of the state.

The previous measurement is combined with the measurements in the other two bases to construct the Bloch vector $\mathbf{r} = r_x\hat{\mathbf{x}} + r_y\hat{\mathbf{y}} + r_z\hat{\mathbf{z}}$ of the retrieved state, which is used to parametrize the state ρ as $\rho = (1+\mathbf{r}\cdot\boldsymbol{\sigma})/2$, where $\boldsymbol{\sigma} = \sigma_x\hat{\mathbf{x}} + \sigma_y\hat{\mathbf{y}} + \sigma_z\hat{\mathbf{z}}$ is the vector of Pauli matrices. It can also be used to estimate the purity P of the state, defined as $P = \text{Tr}(\rho^2)$. It is related to the length of the Bloch vector through

$$P = \frac{1}{2}(1 + |\mathbf{r}|^2). \qquad (A9)$$

The purity should be equal to 1 if the experimental noise is negligible, and $1/2$ if we measure unbiased noise only. Hence, the purity is an indicator of the signal-to-noise ratio of the teleportation itself.

The fidelity decreases with the purity and with any unwanted rotation around the Bloch sphere, that could be due to, e.g. optical misalignment. We could therefore get some indication about whether the less-than-unity fidelities we observed are mostly due to the purity reduction (assuming the input state is pure) or to a rotation. Specifically, let us assume there is no such rotation, and that the effect of the teleportation is to recreate the target state $|\psi\rangle$ with a probability V, mixed with white noise with a probability $1 - V$:

$$\rho = V|\psi\rangle\langle\psi| + (1 - V)\frac{\mathbb{I}}{2} \qquad (A10)$$

where $\mathbb{I}$ is the 2×2 identity matrix. In this model, the probability V corresponds to the visibility of the state defined above. Using $F = (1 + V)/2$, we have

$$\rho = F|\psi\rangle\langle\psi| + (1 - F)|\psi^\perp\rangle\langle\psi^\perp|. \qquad (A11)$$

In this case, the purity can be written as a function of the fidelity:

$$P(F) = \text{Tr}(\rho^2) = 2F^2 - 2F + 1. \qquad (A12)$$

We can also write the fidelity as a function of the measured purity,

$$F_{\text{max}} = \frac{1}{2}(1 + \sqrt{2P - 1}). \qquad (A13)$$

Inserting the measured value of the purity in the previous equation effectively yields an upper bound to our measured value of the fidelity. If the measured value of the fidelity is close to this upper bound, than we can say that it is mostly noise-limited.

Our experimental results for the teleportation to the stored photon are presented in Table A1. The uncertainties are evaluated using Monte Carlo simulations assuming that the number of counts measured follows a Poisson distribution. We notice that the purity varies from

TABLE A1. Measured values of the fidelity and the purity for different input states, with either the stored or the transmitted signal photon. The purity-limited fidelity $F_{\max}$ is also given for the stored photon, for comparison with the measured fidelity.

	Stored photon			Transmitted photon		
State	Purity (%)	Fidelity (%)	$F_{\max}$	Purity (%)	Fidelity (%)	$F_{\max}$
$|H\rangle$	93 ± 5	94 ± 3	96 ± 3	94 ± 1	95 ± 1	97 ± 1
$|-\rangle$	94 ± 6	92 ± 4	97 ± 3	77 ± 2	86 ± 1	87 ± 1
$|R\rangle$	73 ± 5	82 ± 4	84 ± 4	69 ± 1	79 ± 1	81 ± 1
$|+\rangle$	83 ± 9	82 ± 4	91 ± 6	68 ± 2	80 ± 1	80 ± 2
$|+\rangle$ (12.4 km)	—	81 ± 4	—	—	80 ± 1	—

state to state, which is an indication that the experimental parameters that affected the signal-to-noise ratio (see section III A) also varied during the measurements. We also notice that the measured fidelity is very close to the noise-limited upper bound $F_{\max}$, except for $|+\rangle$.

The results of the teleportation with the transmitted photon are shown on Table. A1. The fidelities are all close to the results obtained with the stored photon. Close inspection however reveals that all the fidelities are slightly lower than their stored photon counterparts, and the difference is more important for the purities. The most likely explanation for this is related to the fact that storage acts as a temporal filter which selects only the stored light [12] and effectively removes other spurious sources light.

We can compare these values to what is expected from the model described in section IV C (assuming there is no additional rotation of the Bloch vector). Specifically, the fidelity can be estimated from the expressions $P(1,1)$, $P(2,0)$ and $P(0,2)$ given above:

$$ F = \frac{P(1,1) + P(2,0) + P(0,2)}{P(1,1) + 2[P(2,0) + P(0,2)]}, \qquad (A14) $$

from which the purity can also be calculated using eq. A12. With the experimental parameters $\eta_i \approx 0.13$, $\eta_s \approx 6.3 \times 10^{-3}$, $p \approx 10^{-2}$ and $\mu \approx 0.011$, we find $F \approx 0.93$ and $P \approx 0.88$, which is close to what we measured. This gives an indication that multi-pairs and

multi-photons are the main factors affecting the fidelities and purities that we measured.

We note here that we assumed $p \approx 1/g_{si}^{(t)} = 1/100$, which would be correct if the transmission spectra of the idler and the signal filters had the same widths, but this was not the case. Hence, using that relation actually slightly overestimates the value of p.

We also note that the measured values of $p \sim 1/g_{si}^{(t)}$ varied during our measurements, by approximately a factor of two at most (see section III A 2). This contributed to the fluctuations of the fidelity and purity.

B. Fidelity of the teleportation with the 12.4 km fibre spools

We also performed a teleportation of the $|+\rangle$ state in a configuration where the WCS and the idler photon each travelled through 12.4 km of standard single mode optical fibres before the BSM; see Fig. 1 of the main text. The measured fidelity obtained from the measurement in the $\{|+\rangle, |-\rangle\}$ basis is $81 \pm 4\%$. It is of the same order as the one measured without the fibres, which is consistent with the fact that the loss introduced by the fibre spools is the same for the idler mode and the WCS. Specifically, the transmission η of the fibres changes μ and η_i to $\eta\mu$ and $\eta\eta_i$ in the inequality of Eq. A8, which satisfies it just as well as the one without η and leaves the expression of the fidelity of Eq. A14 unchanged (when neglecting other sources of noise such as dark counts).

[1] V. B. Verma, B. Korzh, F. Bussières, R. D. Horansky, A. E. Lita, F. Marsili, M. D. Shaw, H. Zbinden, R. P. Mirin, and S. W. Nam, "High-efficiency WSi superconducting nanowire single-photon detectors operating at 2.5 K," arXiv:1406.1810 [cond-mat.supr-con] (2014).

[2] F. Marsili, V. B. Verma, J. A. Stern, S. Harrington, A. E. Lita, T. Gerrits, I. Vayshenker, B. Baek, M. D. Shaw, R. P. Mirin, and S. W. Nam, Nature Photon **7**, 210 (2013).

[3] V. B. Verma, F. Marsili, S. Harrington, A. E. Lita, R. P. Mirin, and S. W. Nam, Appl. Phys. Lett. **101**, 251114 (2012).

[4] C. Clausen, F. Bussières, A. Tiranov, H. Herrmann, C. Silberhorn, W. Sohler, M. Afzelius, and N. Gisin, "A source of polarization-entangled photon pairs interfacing quantum memories with telecom photons," arXiv:1405.6486 [quant-ph] (2014).

[5] P. Sekatski, N. Sangouard, F. Bussières, C. Clausen, N. Gisin, and H. Zbinden, Journal of Physics B: Atomic, Molecular and Optical Physics **45**, 124016 (2012).

[6] A. Kuzmich, W. P. Bowen, A. D. Boozer, A. Boca, C. W. Chou, L.-M. Duan, and H. J. Kimble, Nature **423**, 731 (2003).

[7] C. Clausen, F. Bussières, M. Afzelius, and N. Gisin, Phys. Rev. Lett. **108**, 190503 (2012).

[8] I. Usmani, C. Clausen, F. Bussières, N. Sangouard, M. Afzelius, and N. Gisin, Nature Photon **6**, 234 (2012).

[9] C. K. Hong, Z. Y. Ou, and L. Mandel, Phys. Rev. Lett. **59**, 2044 (1987).

[10] M. Żukowski, A. Zeilinger, M. A. Horne, and A. K. Ekert, Phys. Rev. Lett. **71**, 4287 (1993).

[11] J. B. Altepeter, E. R. Jeffrey, and P. G. Kwiat, "Advances in Atomic, Molecular and Optical Physics," (Elsevier, New York, 2006) Chap. 3.

[12] D. L. McAuslan, L. R. Taylor, and J. J. Longdell, Applied Physics Letters **101**, 191112 (2012).
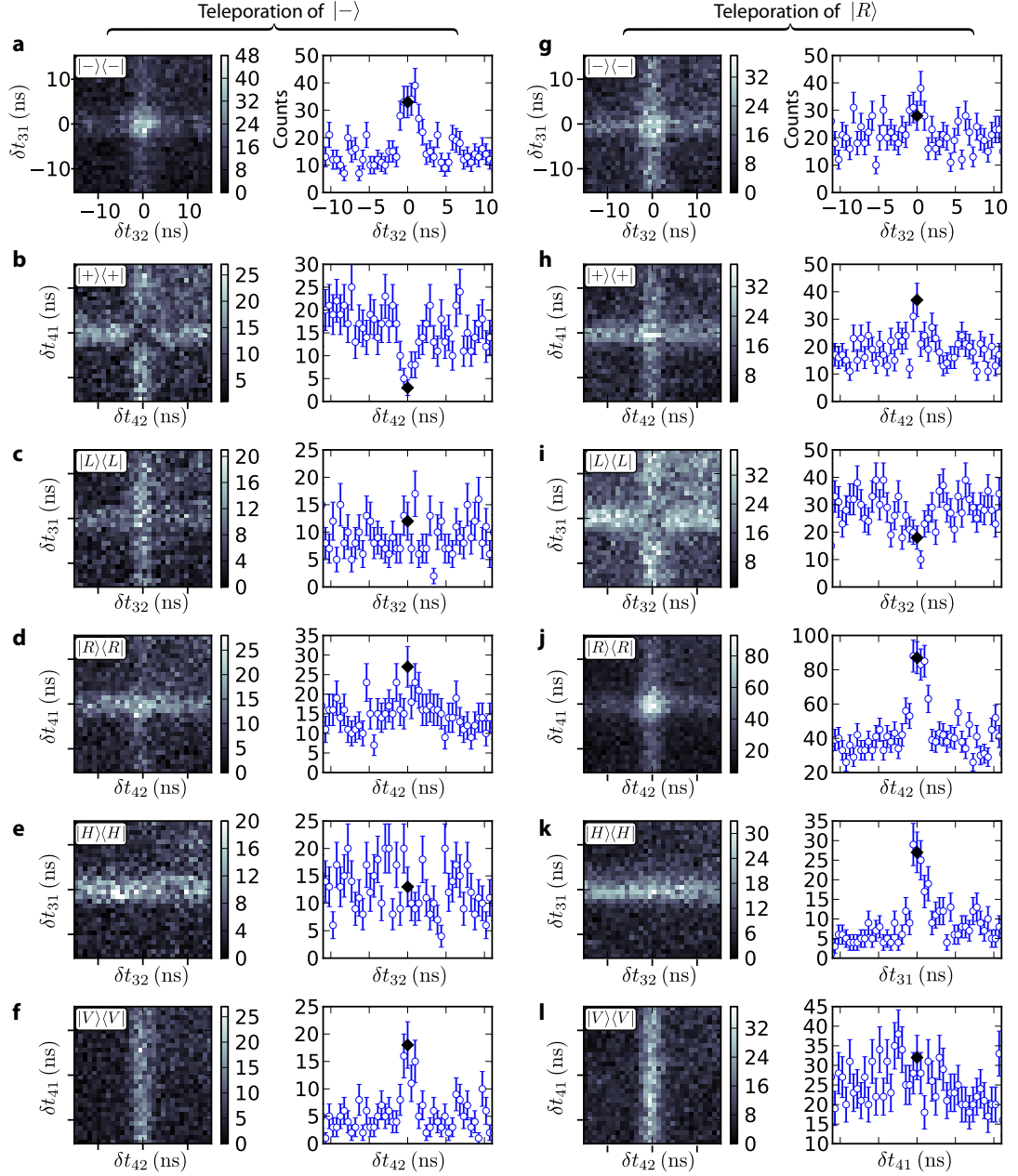
FIG. A6. Histograms of the number of threefold coincidences with the stored signal photon. They are shown as a function of delays δt_{ij} between detector D_i of the analyzer ($i = 3, 4$) and detector D_j ($j = 1, 2$), where D_j is one of the two SNSPDs used for the Bell state measurement. **a** and **b** show histograms corresponding to the teleportation of $|-\rangle$, when the analyzer was set to measure in the $\{|+\rangle, |-\rangle\}$ basis. For **a** (or **b**), the left histogram is a shows the number of threefold coincidences with D_1, D_2 and D_3 (D_1, D_2 and D_4) or as a function of δt_{31} and δt_{32} (or δt_{41} and δt_{42}). Each pixel corresponds corresponds to a $(486 \text{ ps})^2$ window. The one-dimensional histogram on the right side of **a** (or **b**) is a horizontal slice, centred on $\delta t_{31} = 0$ (or $\delta t_{41} = 0$), of the associated two-dimensional histogram. **c** and **d** (or **e** and **f**) are the histograms corresponding to the teleportation of $|-\rangle$, when the analyzer was set to measure in the $\{|R\rangle, |L\rangle\}$ basis ($\{|H\rangle, |V\rangle\}$ basis). **g** through **l** are the histograms corresponding to the teleportation of $|R\rangle$. The black diamonds shown on the one-dimensional histograms are the points that have been used for the quantum state tomography.

FIG. A7. Histograms of the number of threefold coincidences with the transmitted signal photon. They are shown as a function of delays δt_{ij} between detector D_i of the analyzer ($i = 3, 4$) and detector D_j ($j = 1, 2$), where D_j is one of the two SNSPDs used for the Bell state measurement. **a** and **b** show histograms corresponding to the teleportation of $|-\rangle$, when the analyzer was set to measure in the $\{|+\rangle, |-\rangle\}$ basis. For **a** (or **b**), the left histogram is a shows the number of threefold coincidences with D_1, D_2 and D_3 (D_1, D_2 and D_4) or as a function of δt_{31} and δt_{32} (or δt_{41} and δt_{42}). Each pixel corresponds corresponds to a $(486 \text{ ps})^2$ window. The one-dimensional histogram on the right side of **a** (or **b**) is a horizontal slice, centred on $\delta t_{31} = 0$ (or $\delta t_{41} = 0$), of the associated two-dimensional histogram. **c** and **d** (or **e** and **f**) are the histograms corresponding to the teleportation of $|-\rangle$, when the analyzer was set to measure in the $\{|R\rangle, |L\rangle\}$ basis ($\{|H\rangle, |V\rangle\}$ basis). **g** through **l** are the histograms corresponding to the teleportation of $|R\rangle$. The black diamonds shown on the one-dimensional histograms are the points that have been used for the quantum state tomography.

"A source of polarization-entangled photon pairs interfacing quantum memories with telecom photons"

C. Clausen, F. Bussières, A. Tiranov, H. Herrmann, C. Silberhorn, W. Sohler, M. Afzelius & N. Gisin,

A source of polarization-entangled photon pairs interfacing quantum memories with telecom photons

C Clausen[1,3]**, F Bussières**[1]**, A Tiranov**[1]**, H Herrmann**[2]**, C Silberhorn**[2]**,
W Sohler**[2]**, M Afzelius**[1] **and N Gisin**[1]

[1] Group of Applied Physics, University of Geneva, CH-1211 Geneva 4, Switzerland
[2] Applied Physics / Integrated Optics Group, University of Paderborn, D-33095 Paderborn, Germany
E-mail: christoph.clausen@ati.ac.at and felix.bussieres@unige.ch

Abstract

We present a source of polarization-entangled photon pairs suitable for the implementation of long-distance quantum communication protocols using quantum memories. Photon pairs with wavelengths 883 nm and 1338 nm are produced by coherently pumping two periodically poled nonlinear waveguides embedded in the arms of a polarization interferometer. Subsequent spectral filtering reduces the bandwidth of the photons to 240 MHz. The bandwidth is well-matched to a quantum memory based on an Nd:YSO crystal, to which, in addition, the center frequency of the 883 nm photons is actively stabilized. A theoretical model that includes the effect of the filtering is presented and accurately fits the measured correlation functions of the generated photons. The model can also be used as a way to properly assess the properties of the source. The quality of the entanglement is revealed by a visibility of $V = 96.1(9)\%$ in a Bell-type experiment and through the violation of a Bell inequality.

Keywords: parametric downconversion, entanglement, quantum communication, quantum memory, nonlinear waveguide

[3] Present address: Vienna Center for Quantum Science and Technology, TU Wien-Atominstitut, Stadionallee 2, A-1020 Vienna, Austria.

1. Introduction

Spontaneous parametric down-conversion (SPDC) is a simple and efficient technique for the generation of non-classical light and of photonic entanglement. Several important tasks of quantum communication require photonic entanglement, but also optical quantum memories to store this entanglement [1]. A prominent example is the quantum repeater [2, 3], which can extend the transmission distance of entanglement beyond the hard limit dictated by loss in optical fibre. In this context, the combination of photon pair sources and multimode quantum memories was proposed [4]. The essence of this proposal is that the sources create pairs comprised of one telecom-wavelength photon that is used to distribute entanglement between distant nodes, while the other photon is stored in a nearby quantum memory. This increases the probability of successfully heralding a stored photon when the telecom photon is detected. Multimode storage with selective recall then multiplies the entanglement distribution rate by the number of stored modes, and is essential to reach practical rates over distances of 500 km or more [3].

Creating photon pairs such that one photon exactly matches the absorption profile of the quantum memory, while the other is within a telecom wavelength window of standard optical fibre, is a challenging task in itself. Sources of photon pairs based on emissive atomic ensembles or single emitters [3] typically generate photons at wavelengths in the vicinity of 800 nm, where the loss in standard optical fibre is on the order $\sim$3 dB km^{-1}, i.e. at least ten times larger than in telecom fibres. Reaching telecom wavelengths with such sources therefore requires frequency conversion techniques, which has been demonstrated [5–10], but imposes an important technical overhead. SPDC offers much more flexibility, since the wavelengths of the pump can be easily chosen (and tuned) to directly generate the desired wavelengths. However, unfiltered SPDC photons have a bandwidth on the order of hundreds of GHz or more. Hence, they still need to be spectrally filtered to the memory absorption bandwidth, which typically ranges from a few MHz to a few GHz at most [1].

Different approaches for the filtering of SPDC photons were demonstrated. Direct filtering (using Fabry–Perot cavities) of frequency-degenerate photon pairs created in a lithium niobate waveguide was first demonstrated [11], and used for storage of an heralded photon on the D_1 line (795 nm) of cold rubidium atoms. The high conversion efficiency of the waveguide was here used to counterbalance the extreme filtering (down to 9 MHz), which effectively rejects almost all of the generated SPDC bandwidth. A similar source was also developed to demonstrate the heralded single-photon absorption by a single calcium atom at 854 nm [12]. Another approach is based on pumping a bulk crystal put inside a cavity, yielding a doubly resonant optical parametric oscillator (OPO) operated far below threshold. The cavity effectively enhances the length of the nonlinear medium, and is well-suited to generate narrowband photons. This was first demonstrated with frequency-degenerate photons resonant with the D_2 line of rubidium (780 nm) [13, 14], and later with photons resonant with the D_1 line (795 nm) [15]. It was also demonstrated with photon pairs generated at 1436 nm and 606 nm [16], and used for storage in a praseodymium-doped crystal [17]. One important technical difficulty in using an OPO is to fulfill the doubly resonant condition and simultaneously lock one photon's frequency on the quantum memory. Even though such sources can in principle emit the photons in a single longitudinal mode with the help of the clustering effect [18, 19], current state-of-the-art sources [16, 20, 21] do not yet achieve all the requirements, and in

practice some additional filtering outside of the cavity is still necessary to remove spurious longitudinal modes.

　　All the aforementioned experiments produced photons with linewidths $\Delta\nu$ ranging from 1 to 20 MHz, which is dictated by the absorption bandwidth of the respective quantum memory they were developed for. The coherence time $\tau_c \sim 1/\Delta\nu$ of the photons produced can therefore be as long as a microsecond, which impacts on the rate at which those photons can be distributed. It is therefore desirable for the quantum memory to absorb over a large bandwidth to increase the photon distribution rate.

　　In this article, we present a CW-pumped source of polarization-entangled photon pairs with 240 MHz linewidth using a direct filtering approach. This source was designed for experiments involving quantum memories based on the atomic frequency comb (AFC) protocol [22] in a Nd:YSO crystal. Earlier versions of this source produced energy-time entangled photons with a smaller linewidth, and was used to demonstrate the quantum storage of photonic entanglement in a crystal [23], heralded entanglement of two crystals [24] and the storage of heralded polarization qubits [25]. Recently, the source described in this paper was used to demonstrate the teleportation from a telecom-wavelength photon to a solid-state quantum memory [26]. We note that a similar source, based on a pulsed pump, was used for the storage of broadband time-bin entangled photons in a Tm : LiNbO$_3$ waveguide [27].

　　The paper is organized as follows. We give the requirements for the photon-pair source in section 2. The concept behind the implementation is given in section 3 with the details of the actual implementation following in section 4. In section 5 the spectral properties and the correlation functions of the filtered photons are presented and compared to the predictions of a model that includes the effect of the filtering. The efficiency and detection rate of the source is presented in section 6. Section 7 presents measurements showing the high degree of polarization entanglement of the photon pairs, as well as its nonlocal nature. The appendices contain all the details pertaining to the characterization of the source.

2. Requirements

The source was designed for experiments involving an AFC type of quantum memory in a Nd:YSO crystal, so the *signal* photon of a pair has to be in resonance with the transition from the $^4I_{9/2}$ ground state to the $^4F_{3/2}$ excited state of the Nd^{3+} ion at $\lambda_s = 883$ nm. Quantum communication over long distances in optical fibre requires the wavelength of the idler photon of a pair to be inside one of the so-called telecom windows, which span the region from 1300 nm to 1700 nm. The condition for the idler wavelength can be conveniently satisfied using a pump wavelength of $\lambda_p = 532$ nm, for which high-quality solid-state lasers are readily available. This places the idler wavelength at $\lambda_i = (\lambda_p^{-1} - \lambda_s^{-1})^{-1} = 1338$ nm.

　　The bandwidth of the generated photon pairs is dictated by the bandwidth of the quantum memory. In earlier experiments this bandwidth was 120 MHz [23, 24]. Recently it has been increased to about 600 MHz [26]. Although this is fairly large for a quantum memory, it is still three orders of magnitude narrower than the typical bandwidth of photons generated by SPDC, which is given by the phasematching condition and can be as large as 1 THz.

　　We also require quantum entanglement between the signal and idler photons. Entanglement can be established between various degrees of freedom. In particular energy-time entanglement is intrinsically present when using a highly coherent pump laser. In this
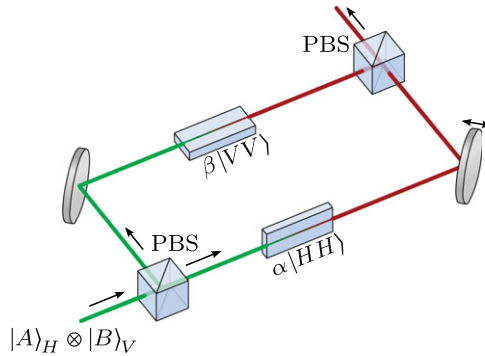
Figure 1. Creation of polarization-entangled photon pairs with the help of two waveguides inside a polarization interferometer. A PBS coherently splits the pump photons according to their polarization. Each polarization component has a certain probability to be converted into a photon pair with the same polarization. The two polarization components of the photon pair are then recombined into the same spatial mode by a second PBS. The relative phase can be adjusted by moving one of the mirrors.

work, however, we focus on polarization entanglement because of the experimental convenience in manipulating and measuring the polarization state of light.

3. Concept

Various schemes have been devised to generate polarization-entangled photon pairs through SPDC. These schemes include selective collection of photon pairs emitted at specific angles for non-collinear type-II phasematching [28], collinear SPDC in two orthogonally oriented crystals [29, 30], and SPDC in Sagnac interferometers [31, 32]. We wanted to extend our existing and well-functioning waveguide source [23], which is inherently collinear, to a configuration that can create polarization-entangled photon pairs. Putting two waveguides back to back is in principle possible, but as the cross-section of the waveguides is only a few micrometres and may vary from waveguide to waveguide, efficient and stable coupling from one to the other is experimentally extremely challenging. Using a waveguide in a Sagnac configuration is complicated by the need for achromatic optics for coupling into and out of the waveguide and for the necessary polarization rotation.

   To be able to efficiently employ our waveguides we follow the ideas of [33, 34] that suggest using a nonlinear crystal in each arm of a polarization interferometer, as sketched in figure 1. We consider the situation of type-I phasematching and that the two nonlinear crystals may have different down-conversion efficiencies. Let the photons from the pump laser be in a polarization state $|A\rangle_H \otimes |B\rangle_V$, where $|A\rangle_H$ corresponds to a horizontally polarized coherent state of complex amplitude A, and similarly for $|B\rangle_V$. A polarizing beam splitter (PBS) at the entrance of the interferometer splits the two coherent state components in two paths. In the horizontal path the photons can be converted into a photon pair $|HH\rangle$ with a probability amplitude $\alpha \propto A$ by a first nonlinear waveguide. A second waveguide rotated by $90°$ in the vertical path can produce a photon pair $|VV\rangle$ with probability amplitude $\beta \propto B$. Another PBS recombines the two paths, and the final single-pair state $|\psi_1\rangle$ is given by

Table 1. A selection of the parameters of the two waveguides for direct comparison.

	Waveguide	
	PPKTP	PPLN
Supplier	AdvR Inc.	University of Paderborn
Poling period	$8.2\,\mu$m	$6.45\,\mu$m
Length of poled region	13 mm	50 mm
Waveguide width	$\sim$4 μm	$\sim$6 μm
Waveguide height	$\sim$7 μm	$\sim$6 μm
Phase-matching temperature	$\sim$53 °C	$\sim$173 °C

$$|\psi_1\rangle \propto |\alpha||HH\rangle + \mathrm{e}^{\mathrm{i}\phi}\,|\beta||VV\rangle, \tag{1}$$

where the phase ϕ depends on the path-length difference of the interferometer, and on the relative phase between α and β. By choosing the pump polarization such that it compensates the efficiency difference, i.e. $|\alpha| = |\beta|$, and by slightly varying the position of one of the mirrors to obtain $\mathrm{e}^{\mathrm{i}\phi} = \pm 1$, the single-pair state becomes equivalent to one of the two Bell-states $|\Phi_\pm\rangle = (|HH\rangle \pm |VV\rangle)/\sqrt{2}$. However, one could equally well produce non-maximally entangled states by choosing the polarization of the pump laser accordingly.

4. Implementation

In the following we detail the actual implementation of the source of polarization-entangled photon pairs. We start by describing the two waveguides that have been used. We then discuss the problem of matching the spatial modes of the photons with the same wavelength from different waveguides. Next, we consider the relative phase ϕ in equation (1). Finally, we describe the measures taken to reduce the bandwidth of the photons.

4.1. The waveguides

Waveguides are used instead of bulk crystals because they yield a much higher conversion efficiency. This is necessary because the spectral filtering we apply is much narrower than the intrinsic spectral width of the down-conversion process, so only a small fraction of the pump power is used to create photons in the desired spectral range. Hence, the larger conversion efficiency essentially compensates the loss in power of the pump.

The photon pair source is based on two nonlinear waveguides made from different materials and with different parameters. The choice of using two different types of waveguides was made for practical reasons that are not important for the results presented in this paper. However, this choice allows for a direct comparison of the performance of the two waveguides. A selection of parameters for the two waveguides is shown in table 1.

The first waveguide was obtained from AdvR Inc. and has been fabricated in a chip of periodically poled potassium titanyl phosphate (PPKTP) by ion exchange. The chip contains a collection of identical waveguides of width and height approximately 4 μm and 7 μm, respectively. Each waveguide spans the entire 13 mm length of the chip. The poling period of 8.2 μm allows to achieve type-I phase matching for the signal and idler wavelengths of 883 nm and 1338 nm at a temperature of about 53 °C. The chip is heated to this temperature using a

custom oven based on a thermo-electric cooler. No dielectric coatings have been applied to the end faces of the chip. We previously used this waveguide, henceforth referred to as the PPKTP waveguide, for the generation of narrowband photon pairs in a series of experiments with solid-state quantum memories [23–25].

The second waveguide was custom designed at the University of Paderborn. It was fabricated by titanium indiffusion on a periodically poled lithium niobate (PPLN) chip. The chip is 62 mm long and contains 25 groups of 50 mm long regions with poling periods between 6.40μm–6.75μm. Within each group there are three waveguides of 5μm, 6μm and 7μm width, respectively. We achieved the best results with a waveguide of poling period 6.45μm and 6μm width, where the temperature for type-I phase matching at the desired wavelengths is about 173 °C. The chip is heated to this temperature with the help of an oven by Covesion Ltd, which has been slightly modified to accommodate the long chip. The elevated temperature is chosen to mitigate the deterioation of the phasematching by photorefraction.

The custom design of the second waveguide, from now on called the PPLN waveguide, allowed for the addition of a number of features which make it especially suitable for SPDC at the desired wavelengths. On the input side, a $\lambda/4$ SiO$_2$-layer has been applied to the input face to provide an anti-reflective coating for the pump laser at 532 nm. Additionally, the input side has a 12 mm long region without periodic poling where the waveguide width is linearly increased from 2μm to the final width. Such a taper should facilitate the coupling of the pump laser to the fundamental spatial mode of the waveguide. The output side of the chip has been coated with a 15-layer SiO$_2$/TiO$_2$ stack optimized for high reflection of the pump light and high transmission of the signal and idler photons. Measurements on a reference mirror that was coated simultaneously with the chip revealed reflectivities of 94%, 2.4% and 12% at 532 nm, 880 nm and 1345 nm, respectively.

4.2. Matching of the spatial modes

To obtain a high degree of entanglement between the photon pairs generated in the two waveguides, it is essential that the spatial mode of the photon does not reveal in which waveguide it has been created. A small mismatch can be corrected with a suitable spatial-mode filter, such as a single-mode optical fiber. If, however, the mismatch is large, the asymmetric losses introduced by the filter can significantly reduce the amount of entanglement.

In theory, the use of identical waveguides should ensure a perfect overlap of the spatial modes of the generated photons. In practice, however, the production process often introduces small variations between identically designed waveguides. In our case, the situation is complicated by the fact that the waveguides are made of different materials, have different dimensions and the signal and idler photons are at widely separated wavelengths. In short, these factors make a simple configuration with just a single interferometer, as depicted in figure 1, impossible for several reasons, in particular when only a single aspheric lens is used to collect the signal and idler photons at the output of the waveguides. Already for a single waveguide, the chromatic aberration of the lense does not allow for simultaneous collimation of the signal and idler beams. On top of that there is the more fundamental problem that the refractive index profiles of the waveguides depend on the chip and on the wavelength. The result is that the signal and idler spatial modes have different sizes and are not centered with respect to each other, even if generated in the same waveguide. For different waveguides, signal and idler beams can in general not be pairwise matched by even the most sophisticated lens system.
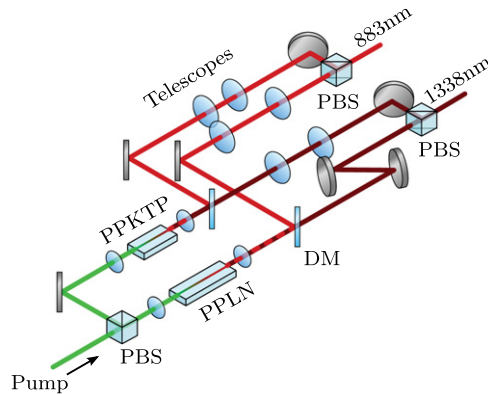
Figure 2. The spatial modes of the photons generated in different waveguides can be efficiently matched by using two interleaved interferometers with appropriate telescopes.

One way to properly match the spatial modes is to part ways with the idea of using a single interferometer and instead use two interleaved interferometers, as shown in figure 2. This gives control of all four spatial modes involved. A single uncoated achromatic lens (Thorlabs C220-TME) after each waveguide is positioned such that the idler beams are collimated. Right after that, dichroic mirrors separate signal and idler beams, leading to four individual beam paths. Telescopes in three of the paths adapt the spatial modes such that the signal and idler modes are separately matched to each other and to the single-mode fibers that will eventually receive the photons. Finally, the signal and idler modes are, respectively, recombined on two PBSs.

4.3. Relative phase

The relative phase from equation (1) has contributions from signal and idler photons, $\phi = \phi_s(\omega_s) + \phi_i(\omega_i)$, and depends, in general, on the frequencies ω_s and ω_i of the signal and idler photons, respectively. In turn, ϕ_s is the difference phase acquired between the horizontal and vertical paths of the respective interferometer, and similarly for the idler photon. To obtain a high degree of entanglement, it is important that ϕ is well-defined for all frequencies within the final bandwidth of the photons. Hence, the path length difference ΔL_x ($x = $ s, i) for the two interferometers should be much smaller than the coherence length of the photons after spectral filtering. For the estimation of ΔL_x one should not forget the dispersion inside the waveguides and that also the propagation of the pump light up to the waveguides is important.

In the experiment we actively stabilize ϕ. For this purpose, each interferometer contains a mirror mounted on a piezo-electric transducer. We use the pump light at 532 nm that is transmitted through the waveguides and leaks into all parts of the interferometer to continuously probe the phase. The PBSs at the input and outputs of the interferometers are not perfect at this wavelength, such that residual interference can be seen on the intensity variations picked up by two photodiodes. Note that, in general, the pump light transmitted through the horizontal and vertical paths of the interferometers will not have the same intensity. Additionally, the coating on the end face of the PPLN chip, the reliance on imperfections and the bad spatial mode-matching of the 532 nm light at the output result in peak-to-peak intensity variations as low as a few 10 nW. Using a lock-in technique, an error signal can nevertheless be extracted and used to stabilize the phases of the interferometers.

Using this technique, the stabilization works reliably for a typical duration of 5–10 h, a duration after which the thermal drift in the laboratory would typically exceed the compensation range of the piezos. However, the technique has two limitations to keep in mind. First, the absolute value of the phase can not be chosen at will and is more or less random for every activation of the lock. Second, since the 532 nm light follows a slightly different path than the signal and idler photons, and the temperature dependence of the refractive index inside the waveguides is wavelength dependent, differential phase shifts can appear. In practice, we observe residual phase drifts on the order of 1° per hour, as determined by repeatedly applying the measurement procedure described in section 7.

4.4. Spectral filtering

In experiments where one of the photons in a pair is coupled to a narrowband receiver, such as an atomic ensemble, spectral filtering is essential. In the typical scenario of SPDC with a narrowband pump laser, energy conservation ensures that a detection of, say, the idler photon after a suitable spectral filter guarantees that the signal photon is within the target spectral range. At first glance such one-sided filtering might seem entirely sufficient. In practice, however, and in particular in the case of strong filtering, multi-pair production can add a significant background of signal photons outside the desired bandwidth, which leads to a reduction of the signal-to-noise ratio of coincidence detections. Hence, also the signal photon needs to be filtered at least to some extent.

Efficiency, stability and ease of use are typical criteria for choosing suitable spectral filters. For a given bandwidth, one wants to use as few filtering elements as possible, as all of them are bound to introduce photon loss and have stabilization requirements. The case of polarization-entangled photon pairs adds the concern that both the spectrum and the efficiency of the filters need to be independent of polarization. This precludes the use of traditional techniques such as diffraction gratings, but also of some more recent developments such as phase-shifted fiber Bragg gratings and Fabry–Perot cavities based on coated lenses [35].

The spectra of the two waveguides were measured using custom-built spectrometers based on diffraction gratings and single-photon-sensitive CCD cameras; see figure 3. The spectrometers have an estimated resolution on the order of 200 GHz full width at half maximum (FWHM) at 883 nm and 100 GHz at 1338 nm. Gaussian fits to the respective signal and idler spectra serve to estimate the phasematching bandwidth. For the PPKTP waveguide the two fits approximately agree, yielding a FWHM of 791(28) GHz for the signal and 724(39) GHz for the idler. The signal photons generated in the PPLN waveguide are measured to be 443(12) GHz wide, and the idler photons 328(11) GHz. While both values may be resolution limited, the discrepancy is most likely due to the inferior resolution at 883 nm.

Assuming the sinc²-shaped spectrum of ideal SPDC and neglecting the dispersion caused by the refractive index profile of the waveguide, we can use Sellmeier equations for KTP [36] and LiNbO$_3$ [37] to find a theoretical estimate of the bandwidths (see appendix A). For the waveguide from AdvR the FWHM is estimated to 540 GHz, while for the guide from Paderborn we find 100 GHz. In both cases, the measured bandwidths are larger. Apart from the limited resolution of the spectrometer, we attribute this deviation to inhomogeneities of the waveguide structure over the interaction length, which also explains why the measured spectra do not exhibit a sinc² shape. Finally, propagation losses of the pump laser in the waveguide can lead to a reduced effective interaction length and hence a broadening of the spectra.
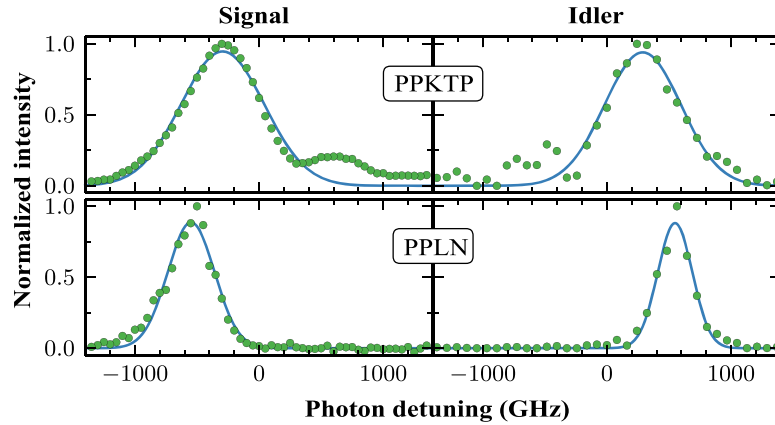
Figure 3. Non-filtered spectra of the photons generated by the two waveguides. Detunings are given with respect to a reference laser at 883.2 nm for the signal photon, and for the idler with respect to light from difference-frequency generation using the same laser. Gaussian fits (solid lines) give estimates of the spectral bandwidths (see text). For these plots, the temperature of the waveguides had not yet been properly adjusted.

We shall now describe the filtering system used to reduce the spectral width of the photon pairs to 240 MHz FWHM. We use two-sided filtering, that is, filters are applied to both the signal and idler photons. At first glance, it would seem that one-sided filtering is sufficient, because energy conservation dictates that the two photons in a pair created by a narrowband pump laser have the same bandwidth, if detected in coincidence. However, accidental coincidences stemming from different pairs do not have this restriction, such that the cross-correlations for one-sided filtering are strongly reduced. This reduction is typically much stronger than the increase in the pair detection rate (corrected for accidental coincidences) gained by one-sided filtering. A quantitative comparison between one-sided and two-sided filtering is given in appendix C.

The filtering for the signal and idler photons is very similar and is done in two steps. The signal photon is first sent onto a volume Bragg grating (VBG) made by Optigrate. The VBG has a nominal diffraction efficiency of 98.6%, although the value in the experiment is ≈90%. The spectral selectivity is specified to 54 GHz at FWHM. Grating parameters are such that the diffracted beam forms an angle of about 7° with the incoming beam. We have not seen any polarization dependence of significance in the performance of the VBG. The second filtering step is an air-spaced Fabry–Perot etalon made by SLS Optics Ltd. The etalon has a line width of $\Gamma_s/(2\pi) = 600$ MHz and a free spectral range (FSR) of 50 GHz, corresponding to a finesse of 83. The peak transmission of the etalon is about 80%.

For the idler photon, the first filter is a custom-made Fabry–Perot cavity with line width $\Gamma_i/(2\pi) = 240$ MHz and an FSR of 60 GHz, corresponding to a finesse of 250. By itself, we achieved peak transmissions through the cavity exceeding 80%. Integrated in the setup of the photon pair source, mode matching was slightly worse, giving a typical transmission around 60%. The cavity was followed by a VBG with a FWHM diffraction window of 27 GHz and nominal efficiency of 99.6%. In this case, experimental observations were compatible with specifications.

The idea behind the combination of Fabry–Perot filter and VBG is to select only a single longitudinal mode of the cavity or the etalon. In practice, however, a typical reflection spectrum of a VBG can have significant side lobes [38]. From the measured second-order auto-correlation functions (see section 5), we estimate that more than 70% of the transmitted signal photons and more than 95% of the idler photons belong to the desired longitudinal mode.

One issue with narrowband filters is the spectral stability. Long-term stability for the VBGs is easily achieved by using a stable mechanical mount, as they have practically no sensitivity to temperature fluctuations. The Fabry–Perot filters are stabilized in temperature, but exhibit residual drifts on the order of 100 MHz per hour. If the center frequencies of the signal and idler filters drift such that they no longer add up to the frequency of the pump laser, the coincidence rate will drop. We compensate this by using a reference laser at 883 nm, which may be stabilized to the etalon, for difference frequency generation (DFG) in the PPLN waveguide, effectively giving coherent light at the idler frequency. The frequency of the pump laser is then adjusted to optimize the transmission of the DFG light through the cavity. During experiments, we switch between DFG and SPDC every few tens of milliseconds, and the transmitted DFG light is detected with single-photon detectors and integrated over approximately 1 s. The stabilization was implemented in software for previous work [23–25], and reliably compensates the slow and weak thermal drifts. This technique also provides a means for active stabilization to the Nd:YSO quantum memory: tuning the 883 nm reference laser to the relevant transition ensures that the photon pairs are simultaneously in resonance with the idler cavity and the quantum memory.

An advantage of the direct filtering approach to generate narrowband photon pairs is the low sensitivity to fluctuations of the temperature of the waveguides themselves. Techniques based on OPO are much more sensitive [18, 20, 21]. In our case, temperature fluctuations shift the phase-matching spectrum as a whole. Since the frequency filters post-select a very small part of the whole spectrum, these variations can be tolerated as long as the shift is small compared to the phase-matching bandwidth, such that the pair-creation rate at the position of the filters remains approximately constant. We measured a temperature-dependent shift of the phase-matching spectrum of $280\,\mathrm{GHz\,K^{-1}}$ and $190\,\mathrm{GHz\,K^{-1}}$ for the PPLN and PPKTP waveguides, respectively. Requiring that the spectra shift less than, say, 5% of their width corresponds to a temperature stability below 0.05 K and 0.2 K, respectively, which is routinely achieved also in the long term.

5. Spectral characterization via correlation functions

Correlation functions are a useful tool for the characterization of light sources. We consider, in particular, the normalized second-order correlation functions, which are unaffected by photon loss or detector inefficiency. They are defined as

$$g_{jk}^{(2)}(\tau) \equiv \frac{\left\langle E_j^\dagger(t)E_k^\dagger(t+\tau)E_k(t+\tau)E_j(t)\right\rangle}{\left\langle E_j^\dagger(t)E_j(t)\right\rangle\left\langle E_k^\dagger(t+\tau)E_k(t+\tau)\right\rangle}, \tag{2}$$

where the indices $j, k \in \{\mathrm{s}, \mathrm{i}\}$ represent the signal or idler photon, respectively. A measurement of $g_{jk}^{(2)}(\tau)$ consists of first determining the rate of coincidence detections between modes j and k at a time delay τ. This is effectively a measurement of the non-normalized

second-order coherence function, which is the numerator in equation (2). The normalization is then performed with respect to the rate of coincidences between photons from uncorrelated pairs created at times differing by much more than the coherence time of the photons.

By itself, the second-order cross-correlation function $g_{\mathrm{si}}^{(2)}(\tau)$ gives a measure of the quality of a photon-pair source, because noise photons stemming from imperfect spectral filtering or fluorescence generated in the down-conversion crystal inevitably reduce the amount of correlations. The auto-correlation functions $g_{\mathrm{ss}}^{(2)}(\tau)$ and $g_{\mathrm{ii}}^{(2)}(\tau)$ give information about the multimode character of the photons and their spectra. Finally, the cross- and auto-correlation functions can be combined in a Cauchy–Schwarz inequality whose violation proves the quantum character of the photon-pair source [39].

In this section we look at the normalized auto- and cross-correlation functions of the signal and idler photons. We show that the shape of the correlation functions is exactly as one would expect from the spectral filtering, if the jitter of the detectors is taken properly into account. Additionally, we use the auto-correlation functions to deduce the probability that a detected signal (or idler) photon stems from the desired mode of the filtering etalon (or cavity).

5.1. Correlation functions

The spectral filtering reduces the uncertainty in energy of the signal and idler photons. The effect can be directly seen on the normalized second-order auto- and cross-correlation functions, for which simple analytical expressions can be derived for collinear, low-gain, SPDC with plane-wave fields. The detailed derivation is given in appendix B. In brief, it procedes as follows. First, expressions for the first-order field correlation functions without filtering can be obtained via the Bogoliubov transformation that describes the input–output relation of the SPDC process [40, 41]. Next, spectral filtering is included through the convolution of the correlation functions with the filter impulse response [42]. In the case where the bandwidth of the filters is much smaller than the bandwidth of the SPDC process, the temporal dependence of the correlation functions is entirely given by the spectral filtering. Finally, higher-order correlation functions are obtained by applying the quantum form of the Gaussian moment-factoring theorem [40]. We arrive at the following expressions for the normalized second-order cross- and auto-correlation functions for Lorentzian-shaped spectral filters

$$g_{\mathrm{si}}^{(2)}(\tau) = 1 + 4\frac{B}{R}\frac{\Gamma_{\mathrm{s}}\Gamma_{\mathrm{i}}}{\left(\Gamma_{\mathrm{s}} + \Gamma_{\mathrm{i}}\right)^2}f_{\mathrm{si}}(\tau),$$

$$g_{\mathrm{ss}}^{(2)}(\tau) = 1 + f_{\mathrm{ss}}(\tau),$$

$$g_{\mathrm{ii}}^{(2)}(\tau) = 1 + f_{\mathrm{ii}}(\tau), \tag{3}$$

where the temporal dependence is given by

$$f_{jk}(\tau) = \begin{cases} \mathrm{e}^{\Gamma_j\tau} & \text{for } \tau < 0 \\ \mathrm{e}^{-\Gamma_k\tau} & \text{for } \tau \geqslant 0 \end{cases}. \tag{4}$$

The cross-correlation function depends on the inverse of the ratio of the R/B. Here, B is the phase-matching bandwidth and R is the rate of photon pair creation. Hence, $1/B$ is seen as the duration of one temporal mode. The low-gain limit of the source is obtained with the probability to create a pair per temporal mode is much smaller than one, i.e. $R/B \ll 1$. In this regime, the
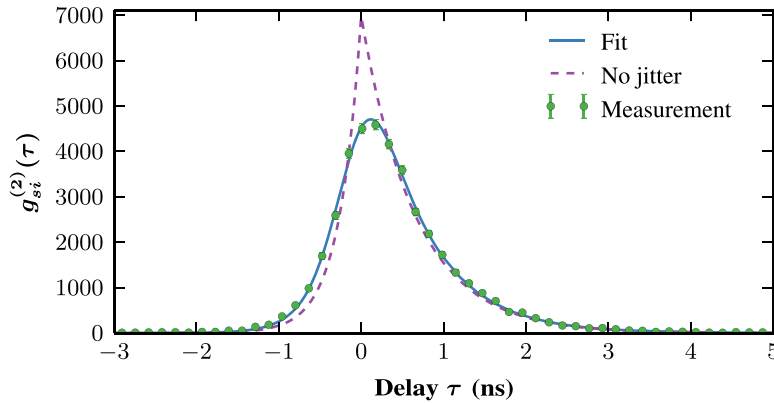
Figure 4. Example of a cross-correlation function measured for the PPKTP waveguide using a binning of 162 ps. The solid line is a fit to the theoretical line shape (equation (3)), corrected for detector jitter, where the only free parameters are the ratio R/B and a horizontal offset. The dashed line is the cross-correlation that we could have obtained with a jitter-free detection system.

rate R is proportional to the pump power. Additionally, the cross-correlation depends on the ratio of the filter bandwidths. For a given value of R/B, a larger mismatch makes it more likely that only one of the photons in a pair passes the filters, which leads to a reduction of the cross-correlation.

5.2. Detector jitter

Figure 4 shows an example of a measured cross-correlation function for the PPKTP waveguide. The combination of detectors, a Perkin–Elmer SPCM-AQRH-13 silicon avalanche photo diode and a super-conducting nanowire single-photon detector (SNSPD), had negligible dark count rates. To compare the measured temporal dependence with theory, the jitter of the detection system has to be taken into account. This can be done by convoluting the expression in equation (4) with the distribution function of the jitter. In our case the jitter is well modeled by a normal distribution, and the expression for the refined temporal dependence $\tilde{f}_{jk}(\tau)$ is given in the appendix. After this modification, we find excellent agreement between the measurement and a theoretical fit, where the only free parameters are a horizontal offset and the ratio R/B. Note that the jitter of $\sigma = 250$ ps for this combination of detectors reduces the maximum cross-correlation by a factor $\tilde{f}_{\mathrm{si}}(0) = 0.65$.

5.3. Multimode properties

Contrary to the cross-correlation function, the normalized auto-correlation functions do not depend on the spectral brightness. Instead, they reach a maximum value of $g_{jj}^{(2)}(0) = 2$, which reveals the thermal nature of the individual signal and idler fields.

A comparison between theory and experiment for the auto-correlation function of the idler photons generated in the PPKTP waveguide is plotted in figure 5. Detector jitter has been included as before by using $\tilde{f}_{\mathrm{ii}}(\tau)$ instead of $f_{\mathrm{ii}}(\tau)$. The detectors were a pair of SNSPDs with $\sigma = 125$ ps. The theoretical prediction is in excellent agreement with the measured data.
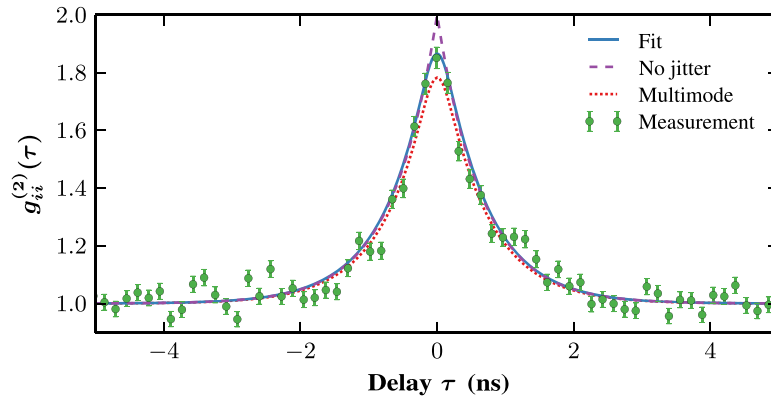
Figure 5. The second-order auto-correlation function of the idler photons generated in the PPKTP waveguide. Bins are 162 ps. The solid line is a fit to the theoretical line shape (equation (3) with jitter included), where the only free parameter is a horizontal offset. The dashed line is the auto-correlation that we could have obtained with a jitter-free detection system. The dotted line is a simulation corresponding to a 2.5% occupation of each nearest-neighbor longitudinal cavity mode.

A measurement of the second-order auto-correlation function allows, additionally, to characterize the presence of spurios spectral modes, that is, undesired modes of the Fabry–Perot filters, in the signal and idler fields. This has first been shown for pulsed and broadband SPDC in [43], where a set of orthogonal spectral modes is obtained via Schmidt decomposition of the joint-spectral amplitude of the signal and idler fields. By normalizing the occupation probabilities p_n of these modes such that $\sum p_n = 1$, the authors define an effective number of modes $K = 1\big/ \sum p_n^2$. This number, also known as the Schmidt number, quantifies the amount of spectral entanglement and is the reciprocal of the purity of the reduced states of the signal and idler modes [44]. Furthermore, it is shown in [43] that the inability to resolve these spectral modes results in a reduction of the auto-correlation functions, given by $g_{jj}^{(2)}(0) = 1 + 1/K$. Hence, a measurement of $g_{jj}^{(2)}(0)$ allows to directly determine K.

For continuous-wave SPDC subjected to narrow-band Fabry–Perot filters, the longitudinal modes of the filter form a suitable basis for the spectral decomposition. We define p_0 as the probability to find the photon in the desired longitudinal mode, and let p_n be the nth red-detuned (or blue-detuned) mode for $n > 0$ (or $n < 0$). We would like to determine a lower bound on p_0 via a measurement of the auto-correlation function. As in the case of pulsed SPDC, the presence of spurious longitudinal modes of the Fabry–Perot filter reduces the auto-correlation function. This is easily seen from the fact that $f_{jj}(\tau)$ is proportional to the absolute square of the Fourier transform of the power spectral density of the cavity transfer function (see also equations (B.6) and (B.8)). The presence of multiple longitudinal cavity modes will hence lead to oscillations of $g_{jj}^{(2)}(\tau)$ at a frequency corresponding to the FSR of the filter. If the detectors do not resolve these oscillations, they will be averaged out, leading to a reduction of $g_{jj}^{(2)}(\tau)$. However, in our case the detector jitter is sufficiently strong to give a reduction of the $g_{jj}^{(2)}(0)$ even for the single-mode case. To more clearly separate the contributions from detector jitter and spurious modes, we rewrite the auto-correlation function of equation (2) as
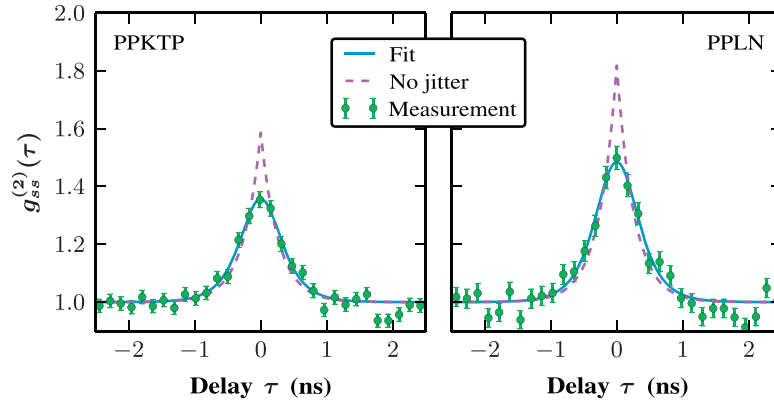
Figure 6. The second-order auto-correlation function of the signal photons generated in the PPKTP (left) and PPLN (right) waveguides. Spurious etalon modes prevent the peak from reaching a value of 2, even after the correction for detector jitter. Bins are 162 ps.

$$g_{jj}^{(2)}(\tau) = 1 + \frac{1}{K}\tilde{f}_{jj}(\tau), \tag{5}$$

where jitter has been taken into account explicitly via the use of $\tilde{f}_{jj}(\tau)$.

For the idler photon, the red dotted line in figure 5 shows the case of $p_0 = 0.95$ for the central cavity mode and $p_{\pm 1} = 0.025$ for the neighboring red- or blue-detuned modes, giving $K = 1.1$. The mismatch with the experimental data at zero delay is consistent with the selection of a single cavity mode by the filtering system.

The situation is different for the signal photon, for which auto-correlation measurements are shown in figure 6. Here, the bandwidth of the VBG is comparable to the FSR of the etalon, and contributions from spurious modes are to be expected. From a fit of equation (5) to the data, with K and σ as free parameters, we obtain $K = 1.71(8)$ for the PPKTP waveguide and $K = 1.22(6)$ for the PPLN waveguide. Assuming the worst case of only a total of two etalon modes with non-zero population, this corresponds to probabilities of $p_0 = 0.71(3)$ and $p_0 = 0.90(3)$, respectively, for the photon being in the desired etalon mode. We attribute the larger value of K for the PPKTP waveguide to the larger phase-matching bandwidth.

6. Efficiency characterization of the filtered photon sources

In this section we show a characterization of the individual performances of the two waveguides, including spectral filtering. The characterization aims at determining the spectral brightness and the collection and detection efficiencies of the photons. It consists of measuring as a function of the pump power the detection rates of signal and idler photons. Furthermore, we measured the photon-pair rate, that is, the signal-idler coincidence rate, corrected for accidental coincidences, for a coincidence window that is large compared to the coherence time. Finally, we also determined the power-dependence of the second-order cross-correlation function $g_{si}^{(2)}(\tau)$ at delay $\tau = 0$. The results are shown in figure 7.

For comparison to a theoretical model, we use the same derivation as for the correlation functions in the previous section. However, in the previous section the dark counts of the detectors were negligible. Dark counts add an offset to the signal and idler detection rates. Additionally, they give rise to accidental coincidences, which set an upper bound on the
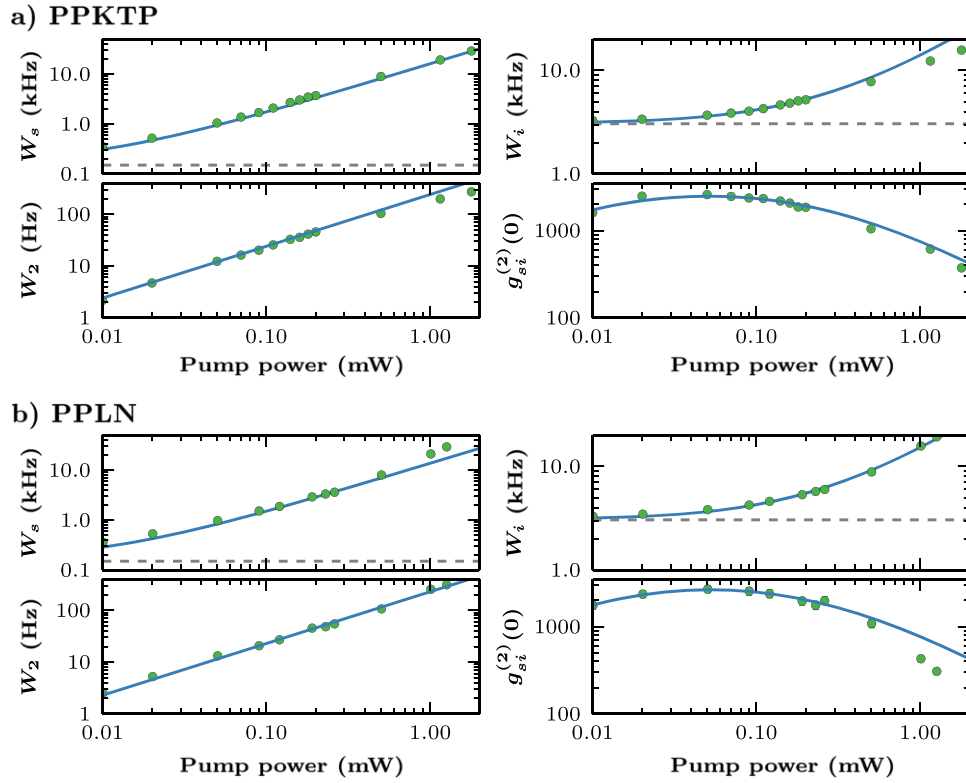
Figure 7. Characterization of (a) the PPKTP and (b) the PPLN waveguide. For each waveguide, the signal, idler and pair detection rates are plotted, as well as the value of the cross-correlation function at $\tau = 0$ delay. The dashed horizontal lines in the panels for the signal and idler rates indicate the detector noise level. For the measurement of the pair rate, a coincidence window of 6 ns was used, which is sufficiently large to encompass the entire coincidence peak (see figure 4). Additionally, accidental coincidences have been subtracted. The values of the cross-correlation function are based on a binning of 162 ps. A common fit (solid lines) to all four data sets for each waveguide was used to extract the spectral brightness and collection efficiencies (see also table 2).

normalized cross-correlation function at low pump powers. We included the dark count rate D_j in the model and also added finite detection efficiencies η_j to end up with the following set of equations (see also appendix B),

$$W_{\mathrm{s}} = \frac{1}{4}\frac{\eta_{\mathrm{s}}}{p_0}\frac{R}{B}\Gamma_{\mathrm{s}} + D_{\mathrm{s}},$$

$$W_{\mathrm{i}} = \frac{1}{4}\eta_{\mathrm{i}}\frac{R}{B}\Gamma_{\mathrm{i}} + D_{\mathrm{i}},$$

$$W_2 = \frac{1}{4}\eta_{\mathrm{s}}\eta_{\mathrm{i}}\frac{R}{B}\frac{\Gamma_{\mathrm{s}}\Gamma_{\mathrm{i}}}{\Gamma_{\mathrm{s}} + \Gamma_{\mathrm{i}}},$$

$$g_{\mathrm{si}}^{(2)}(0) = 1 + \frac{1}{4}\frac{\tilde{f}_{\mathrm{si}}(0)\eta_{\mathrm{s}}\eta_{\mathrm{i}}}{W_{\mathrm{s}}W_{\mathrm{i}}}\frac{R}{B}\left(\frac{\Gamma_{\mathrm{s}}\Gamma_{\mathrm{i}}}{\Gamma_{\mathrm{s}} + \Gamma_{\mathrm{i}}}\right)^2. \tag{6}$$

Table 2. Parameters as extracted from fitting the data in figure 7 to equations (6). $2\pi R/B$ is the spectral brightness, given in conventional units, for a pump power of 1 mW. η_s (or η_i) is the overall collection and detection efficiency for the signal (or idler) photon.

	Waveguide	
	PPKTP	PPLN
$2\pi R/B$	$2.45(6) \times 10^3$ (s MHz)$^{-1}$	$3.08(6) \times 10^3$ (s MHz)$^{-1}$
η_s	3.1(2)%	2.6(2)%
η_i	7.4(1)%	6.6(1)%

Here, the signal and idler rates W_s and W_i are essentially given by the spectral brightness of the waveguide times the respective bandwidth of the filtering system and attenuated by the detection efficiency. Since R is proportional to the pump power, so are W_s and W_i. W_s has also been corrected for the contribution of spurious etalon modes, which will increase the detection rate by a factor $1/p_0$. The behavior of the pair rate W_2 is similar, except that the photon pairs have an effective bandwidth of $\Gamma_s\Gamma_i/(\Gamma_s + \Gamma_i)$, which is smaller than the bandwidth of the signal and idler photons individually. Note that the measurement of W_2 includes correction for accidental coincidences, and no correction for dark counts needs to be applied to the theory. Finally, the expression for $g_{si}^{(2)}(0)$ is equivalent to the one given in equation (3), but the inclusion of dark counts prevents further simplification.

We used commercially available detectors for the measurements presented in figure 7. The signal detector by Perkin–Elmer has a dark-count rate of 150 Hz and a detection efficiency of about 30% at 880 nm. As detector for the idler photon served an ID220 by Id Quantique with 20% efficiency. To reduce the contribution of afterpulsing, the dead time of this detector was set to 20 μs, and we observed a dark-count rate of 3.0 kHz. The offset on the signal and idler count rates given by the dark counts is indicated by dashed lines in the top panels of figure 7.

A simultaneous fit to the equations (6) reproduces the measurements to a high extent. The free parameters in the fit are the spectral brightness R/B and the overall collection and detection efficiencies η_s and η_i. The results of the fit are shown in table 2. For the PPKTP waveguide the idler rate shows a negative deviation from the expected behavior at pump powers above 1 mW, where the detector starts being saturated. For the PPLN waveguide the saturation seems to be compensated by a higher pair-creation efficiency, indicated by a positive deviation of the signal rate and a significant drop in the cross-correlation.

In terms of the spectral brightness, the two waveguides perform on a similar level. We note however, that the specified pump power is measured in front of the waveguide. For both waveguides we estimate a coupling of the pump laser into the waveguide between 40–50%. Of this, only a fraction is coupled into the fundamental spatial mode, and hence contributing to SPDC. In principle, we would expect a higher brightness for the waveguide from Paderborn, since it is longer and PPLN has a larger nonlinear coefficient than PPKTP. The reason that we observe something different could be a non-optimal temperature of this waveguide in this measurement, which shifts the perfect phase matching slightly away from the filter transmission maximum. We also note that at pump powers above a few milliwatts, the operation of the PPLN waveguide is impaired by photorefraction, which leads to strong fluctuations of the spatial mode of the pump laser inside the waveguide.

In our experiments we are rarely constrained by the available pump laser power, and the spectral brightness is only of minor importance. More important are the achievable coincidence rates and the correlations between signal and idler photons. The coincidence rate is proportional to the product of the signal and idler collection and detection efficiencies, η_s and η_i. Also here we see similar values for the two waveguides, indicating a spatial mode-matching better than 80% for the signal photon and around 90% for the idler. The expected peak transmission for the signal path is $\eta_s \approx 3.6\%$ with contributions from a long-pass filter that removes the pump light (80%), the VBG (90%), the etalon (80%), fiber coupling (60%) and detector efficiency (30%). Additionally, the setup was already prepared for storage and retrieval in the quantum memory, adding losses due to a fiber-optical switch (70%), fiber connectors (70%) and another fiber coupling (70%). On the idler side, we expect $\eta_i \approx 8\%$, distributed over the cavity (60%), fiber coupling (70%) and detector efficiency (20%). The measured value for η_s and η_i, given in table 2, corresponds quite well to the expected values. We attribute the small differences to loss inside and at the end facets of the waveguides.

The measured cross-correlation function reaches for both waveguides a peak value of approximately 2600 at a pump power of $50\,\mu$W. At lower pump power correlations are reduced by dark counts, at higher pump powers by multi-pair emission.

7. Entanglement

The characterization of the two waveguides showed that a very high degree of mode-matching for the photons originating from the two waveguides has been obtained. Additionally, the spectral brightness is about the same. This means that it should be possible to achieve a high degree of entanglement by setting the pump polarization to an approximately equal superposition of horizontal and vertical, such that similar amounts of light arrive at the two waveguides. In practice, we neglect the small differences in coupling efficiencies and adjust the pump polarization such that the rate of coincidences from the two waveguides is about the same. It remains to be shown that the horizontally and vertically polarized photon pairs form a coherent superposition with a stable phase, which corresponds to an entangled state between the two photons.

Let us, for simplicity, assume that the photon pairs are produced in the maximally entangled state

$$\frac{1}{\sqrt{2}}\left(|HH\rangle + e^{i\phi}\,|VV\rangle\right). \tag{7}$$

A measurement that verifies the coherent nature of this state is illustrated in figure 8(a). First, the idler photon is measured in the basis $|\pm\rangle = (|H\rangle \pm |V\rangle)/\sqrt{2}$ using a half-wave plate and a PBS. If a photon is detected in the port of the beam splitter corresponding to, say, $|+\rangle$, the signal photon is projected onto the state $|\phi_+\rangle = (|H\rangle + e^{i\phi}\,|V\rangle)/\sqrt{2}$. Sending this through a quarter-wave plate and a half-wave plate whose fast axes are at angles of $\pi/4$ and θ to horizontal, respectively, transforms the signal photon into the linearly polarized state $|\beta\rangle = \sin\beta\,|H\rangle - \cos\beta\,|V\rangle$ with $\beta = 2\theta + \phi/2 + \pi/4$. We hence expect that the probability of detecting the signal photon after a PBS shows sinusoidal fringes as a function of θ with a period of $\pi/2$. The phase of the fringes depends on the phase ϕ of the initial entangled state (7), such that this kind of measurement can be used to determine ϕ. If, instead, the photon pairs are generated in a maximally mixed state $(|HH\rangle\langle HH| + |VV\rangle\langle VV|)/2$, the same measurement of
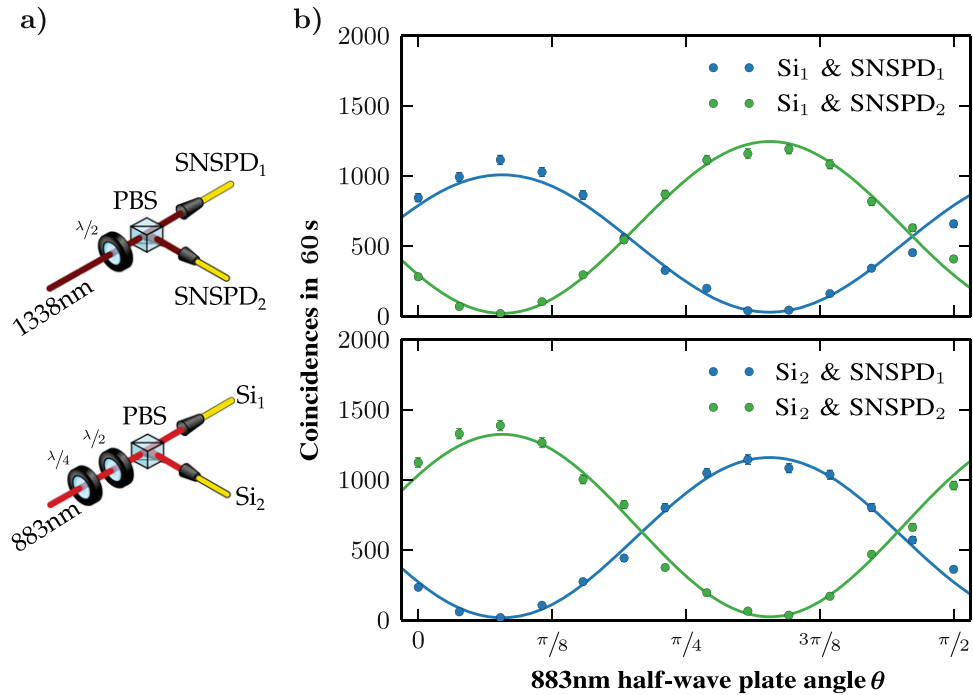
Figure 8. Characterization of the coherence of the pair source. (a) The idler photons are measured in the bases of diagonal polarization. This projects the signal photon onto a coherent superposition of $|H\rangle$ and $|V\rangle$ with unknown relative phase. A quarter-wave plate at fixed angle transforms this state into a linear polarization, which is analyzed with the help of a half-wave plate and a polarizing beam splitter. (b) Corresponding coincidence measurement for a coincidence window of 2 ns for the four detector combinations. Solid lines are sinusoidal fits with a fixed period and common phase. The fits yield an average visibility of $V = 96.1(9)\%$.

the coincidence rate will not show any dependence on θ. A fringe visibility larger than 33% is necessary to infer the presence of entanglement [45].

In figure 8(b) we show the outcome of the described measurement procedure. A pair of SNSPDs has been used for the idler photon, and Si avalanche photo diodes (Perkin–Elmer) for the signal photon. For each value of θ the number of coincidences in a 2 ns window have been integrated over a duration of 60 s for each of the four possibly detector combinations. The number of measured coincidences oscillates as a function of θ, as expected. A sinusoidal fit reveals an average visibility $V = 96.1(9)\%$, which indicates that the source generates photon pairs that are close to maximally entangled in polarization.

To unequivocally prove the presence of entanglement we performed a violation of the Clauser–Horne–Shimony–Holt (CHSH) inequality [46]. A quarter-wave plate was added to the polarization analysis of the idler photon, such that the setups for signal and idler photon of figure 8(a) were now identical. Additionally, the SNSPDs were replaced by ID220s for their higher detection efficiency. The wave plate allows to switch the measurement basis of the idler photon between $|\pm\rangle$ and the circular polarizations $(|H\rangle \pm \mathrm{i}\, |V\rangle)/\sqrt{2}$ by a rotation of the half-wave plate. These two basis sets were used for the measurement. Since we do not *a priori* know the relative phase ϕ of the photon pairs, we determine the optimal settings for the signal analyzer as follows. We set the idler analyzer to $|\pm\rangle$ and perform another measurement of the

type of figure 8 to determine the angle $\theta_{\max}$ of the half-wave plate of the signal analyzer that gives a maximum between detectors Si_1 and $ID220_1$. For the violation of the CHSH inequality we then use the angles $\theta_{\max} \pm \pi/16$. For an acquisition time of 5 min per setting we find a CHSH parameter of $S = 2.708(9)$, which is almost 80 standard deviations above the bound for separable states of $S \leqslant 2$.

8. Summary and outlook

We have presented a source of polarization-entangled photon pairs based on the nonlinear waveguides of different materials embedded in the arms of a polarization interferometer. We have shown that the source emits photon pairs with a high degree of entanglement and is compatible with the storage of one of the photons in a quantum memory. The wavelength of the other photon is in a telecom window, which permits the low-loss transmission over optical fiber. This combination makes the source particularly useful for quantum communication experiments.

Even though the photon-pair source is conceptually simple, a higher degree of integration would be desirable. Recent work along this direction includes the integrated spatial separation of signal and idler photons using an on-chip wavelength-division multiplexer [47] and the direct generation of 150 MHz broad photon pairs using a monolithic waveguide resonator [21]. Both of these techniques were demonstrated with similar wavelengths as used in this work. In particular the latter could greatly simplify the efficient generation of narrowband photon pairs, provided that the intrinsic resonator loss can be reduced. If this could further be combined with the on-chip generation of polarization-entangled photons using an interlaced bi-periodic structure [48], one would have the equivalent of the whole setup of figure 2 on a single chip, including spectral filtering. Together with the recent progress in solid-state quantum memories, these are promising perspectives for the development of compact and practical nodes for quantum communication.

Acknowledgments

Appendix A. Estimation of phase-matching bandwidth

The frequency dependence of SPDC is given by the joint spectral amplitude $f(\omega_s, \omega_i)$, which can be written as the product of two functions,

$$f(\omega_s, \omega_i) = \alpha(\omega_s + \omega_i)\Phi(\omega_s, \omega_i), \tag{A.1}$$

where ω_s (or ω_i) is the frequency of the signal (or idler) photon, $\alpha(\omega)$ represents the spectrum of the pump laser and $\Phi(\omega_s, \omega_i) = \mathrm{sinc}(\Delta k L/2)$ is the phase-matching function. The state of a single photon pair can be written in terms of the joint spectral amplitude as

$$|\Psi\rangle \propto \int_{-\infty}^{\infty} d\omega_s \int_{-\infty}^{\infty} d\omega_i \, f(\omega_s, \omega_i) a^{\dagger}(\omega_s) a^{\dagger}(\omega_i)|vac\rangle, \tag{A.2}$$

where $a^{\dagger}(\omega)$ is the photon creation operator at frequency ω. We recognize, that $f(\omega_s, \omega_i)$ is the spectral wavefunction of the photon pair. It follows that the spectral distribution, that is, the probability to find a photon in an infinitesimal interval at frequency ω, of the signal or idler photon is given by

$$S(\omega_s) \propto \left| \int_{-\infty}^{\infty} d\omega_i \, f(\omega_s, \omega_i) \right|^2$$

$$S(\omega_i) \propto \left| \int_{-\infty}^{\infty} d\omega_s \, f(\omega_s, \omega_i) \right|^2. \tag{A.3}$$

In the case of a highly coherent pump laser, $\alpha(\omega)$ can be approximated by a Dirac delta function, $\delta(\omega - \omega_p)$, and the spectra of the signal and idler photons is given by the phase matching, only, i.e.

$$S(\omega_j) \propto \mathrm{sinc}^2(\Delta k L/2). \tag{A.4}$$

The phase mismatch is given by

$$\Delta k = 2\pi \left(\frac{n_p(\lambda_p)}{\lambda_p} - \frac{n_s(\lambda_s)}{\lambda_s} - \frac{n_i(\lambda_i)}{\lambda_i} - \frac{1}{\Lambda} \right), \tag{A.5}$$

with n_x and λ_x ($x = $ p, s, i) the refractive index and wavelength of pump, signal and idler photons, respectively. Λ is the period of poling. Here, as a first approximation, we have neglected the effect of the waveguide. A more accurate expression would use the propagation constants of the pump, signal and idler modes for the given waveguide refractive index profile.

We want to estimate the FWHM bandwidth of the photons generated by SPDC. To this end, we first remember that $\lambda_i = (\lambda_p^{-1} - \lambda_s^{-1})^{-1}$ due to energy conservation, such that the phase mismatch becomes a function of the signal wavelength only. For phase-matching $\Delta k = 0$, and the bandwidth is determined by the dispersion, which to first order is given by

$$\Delta k(\lambda) \simeq \frac{d\Delta k(\lambda)}{d\nu}\Delta\nu = \frac{d\Delta k(\lambda)}{d\lambda}\frac{d\lambda}{d\nu}\Delta\nu$$

$$= \frac{d\Delta k(\lambda)}{d\lambda}\frac{-\lambda^2}{c}\Delta\nu$$

$$\equiv \Delta k' \Delta\nu. \tag{A.6}$$

Note that the contributions of the pump wavelength and the periodic poling to $\Delta k(\lambda)$ are constant, so they will not affect $\Delta k'$. Using equation (A.6), the argument of the sinc² function in equation (A.4) becomes $x = \Delta k' \Delta\nu L/2$. Knowing that the sinc squared reaches half its maximum value at $x_{1/2} = 1.39156$, the FWHM bandwidh is given by

$$\Delta\nu_{\mathrm{FWHM}} = \frac{4x_{1/2}}{|\Delta k'|\, L}. \tag{A.7}$$

Using the Sellmeier equations for KTP [36] and LiNbO$_3$ [37], we can calculate $\Delta k'$ and the resulting values for $\Delta\nu_{\mathrm{FWHM}}$. These are given in table A1.

Table A1. Values for the estimation of the FWHM bandwidth of the two waveguides. For the PPLN waveguide we assume a temperature of 180 °C.

Waveguide	$\Delta k'$ ((mm GHz)$^{-1}$)	L (mm)	$\Delta \nu_{\text{FWHM (GHz)}}$
PPKTP	-7.93×10^{-4}	13	539
PPLN	-1.14×10^{-3}	50	97

Appendix B. Analytical model for SPDC with spectral filtering

We shall here give a brief derivation of the expressions for the signal and idler rates, the coincidence rate and the second-order correlation function of the waveguides, including the application of spectral filtering. As a starting point we will take the treatment presented by Razavi *et al* [40] (see also [41]), assuming collinear SPDC with plane-wave fields. Furthermore, the depletion of the pump and group-velocity dispersion have been neglected.

   We start by giving expressions for the first-order correlation functions, from which one can calculate the event rates. With the help of the quantum form of the Gaussian moment-factoring theorem, all higher-order correlation functions can be derived [40].

B.1. First-order correlation functions

Defining scalar photon-units positive-frequency field operators

$$E_j(t) = \frac{1}{2\pi} \int_{-\infty}^{\infty} d\omega \, a(\omega) e^{-i\omega t}, \quad j = \text{s, i}, \tag{B.1}$$

where $a(\omega)$ is the photon annihilation operator in the frequency domain, Razavi *et al* use a Bogoliubov transformation to derive the following set of first-order correlation functions for the SPDC output state

$$\left\langle E_j^{\dagger}(t + \tau) E_j(t) \right\rangle = e^{i\omega_j \tau} \times C_{\text{auto}}(\tau),$$
$$\left\langle E_j(t + \tau) E_k(t) \right\rangle = \left(1 - \delta_{jk}\right) e^{-i\left(\omega_p t + \omega_j \tau\right)} \times C_{\text{cross}}(\tau), \tag{B.2}$$

where δ_{jk} is the Kronecker delta function and $j, k \in \{\text{s, i}\}$. In the low-gain regime of SPDC, the envelope functions $C_{\text{auto}}(\tau)$ and $C_{\text{cross}}(\tau)$ are given by

$$C_{\text{auto}}(\tau) = \begin{cases} R(1 - |\tau| B) & \text{for } |\tau| B \leqslant 1, \\ 0 & \text{otherwise} \end{cases},$$

$$C_{\text{cross}}(\tau) = \begin{cases} \sqrt{RB} & \text{for } |\tau| B \leqslant \frac{1}{2} \\ 0 & \text{otherwise} \end{cases}. \tag{B.3}$$

Here, R is the rate of photon pair creation and proportional to the pump power, and $B = 2\pi/(\Delta k' L)$ is proportional to the bandwidth. The ratio R/B is often termed the spectral brightness of the photon pair source.

   When adding spectral filtering, the envelope functions get convoluted with the impulse response functions $F_j(t)$ of the filters [42]. For the autocorrelation,

$$C_{\text{auto}}^{(j)}(\tau) = \int_{-\infty}^{\infty}dt' \int_{-\infty}^{\infty}dt''\ F_j^*(t+\tau-t')F_j(t-t'')\ C_{\text{auto}}(t'-t'')$$

$$\approx \alpha \int_{-\infty}^{\infty}dt'\ F_j^*(t+\tau-t')F_j(t-t'), \tag{B.4}$$

where we have taken $C_{\text{auto}}(t'-t'') \approx \alpha\, \delta(t'-t'')$, which is valid if the bandwidth of the filter is much smaller than B. The constant α is

$$\alpha = \int_{-\infty}^{\infty}dt'\, C_{\text{auto}}(t'-t'') = \frac{R}{B}. \tag{B.5}$$

We further consider a Lorentzian filter with FWHM Γ_j whose transfer and impulse response functions are given by

$$H_j(\omega) = \frac{\Gamma_j}{\Gamma_j - 2i\omega}, \tag{B.6}$$

$$F_j(\tau) = \frac{1}{2\pi}\int_{-\infty}^{\infty}d\omega\ H_j(\omega)e^{i\omega\tau}$$

$$= \frac{\Gamma_j}{2}\Theta(\tau)e^{-\Gamma_j\tau/2}, \tag{B.7}$$

where $\Theta(\tau)$ is the Heaviside step function. We then arrive at the final expression for the auto-correlation envelope

$$C_{\text{auto}}^{(j)}(\tau) = \frac{1}{4}\frac{R}{B}\Gamma_j e^{-\Gamma_j|\tau|/2}. \tag{B.8}$$

Performing a similar calculation for the cross-correlation envelope, we get

$$C_{\text{cross}}^{(jk)}(\tau) = \frac{1}{2}\sqrt{\frac{R}{B}}\frac{\Gamma_j\Gamma_k}{\Gamma_j+\Gamma_k} \times \begin{cases} e^{\Gamma_k\tau/2} & \text{for } \tau < 0 \\ e^{-\Gamma_j\tau/2} & \text{for } \tau \geqslant 0 \end{cases}. \tag{B.9}$$

Finally, let us introduce, for convenience, the signal and idler flux,

$$W_j \equiv C_{\text{auto}}^{(j)}(0) = \frac{1}{4}\frac{R}{B}\Gamma_j, \tag{B.10}$$

and the pair flux

$$W_2 \equiv \int_{-\infty}^{\infty}d\tau\ \left| C_{\text{cross}}^{(jk)}(\tau) \right|^2$$

$$= \frac{1}{4}\frac{R}{B}\frac{\Gamma_j\Gamma_k}{\Gamma_j+\Gamma_k}$$

$$= W_j \times \frac{\Gamma_k}{\Gamma_j+\Gamma_k}. \tag{B.11}$$

The last line of equation (B.11) says that the pair flux is equal to the flux if signal or idler rescaled by the probability that a photon that has already been projected onto the spectrum of one of the filters also passes the second filter. We note that this expression is valid only for perfectly correlated photon pairs and does not contain contributions from multi-pair emission. These will be included in the next section, where we consider second-order correlation functions.

B.2. Second-order correlation functions

The normalized second-order cross-correlation function is defined as

$$g_{si}^{(2)}(\tau) \equiv \frac{\left\langle E_s^\dagger(t) E_i^\dagger(t+\tau) E_i(t+\tau) E_s(t) \right\rangle}{\left\langle E_s^\dagger(t) E_s(t) \right\rangle \left\langle E_i^\dagger(t+\tau) E_i(t+\tau) \right\rangle}$$

$$= \frac{G_{si}^{(2)}(\tau)}{W_s W_i}, \tag{B.12}$$

where the numerator is the non-normalized second-order cross-correlation function. Applying the Gaussian moment-factoring theorem, it can be shown that

$$G_{si}^{(2)}(\tau) = W_s W_i + \left| C_{cross}^{(si)}(\tau) \right|^2, \tag{B.13}$$

where the first term is proportional to the coincidence rate that is expected for completely uncorrelated photons, often called accidental coincidences. Using equations (B.9) and (B.10), we find

$$g_{si}^{(2)}(\tau) = 1 + \frac{\left| C_{cross}^{(si)}(\tau) \right|^2}{W_s W_i}$$

$$= 1 + 4\frac{B}{R} \frac{\Gamma_s \Gamma_i}{(\Gamma_s + \Gamma_i)^2} \times f_{si}(\tau)$$

$$f_{jk}(\tau) = \begin{cases} e^{\Gamma_j \tau} & \text{for } \tau < 0 \\ e^{-\Gamma_k \tau} & \text{for } \tau \geqslant 0 \end{cases}. \tag{B.14}$$

The derivation of the second-order auto-correlation functions for the signal and idler photons proceeds along the same lines as that of the cross-correlation. The auto-correlation function is defined as

$$g_{jj}^{(2)}(\tau) \equiv \frac{\left\langle E_j^\dagger(t) E_j^\dagger(t+\tau) E_j(t+\tau) E_j(t) \right\rangle}{\left\langle E_j^\dagger(t) E_j(t) \right\rangle \left\langle E_j^\dagger(t+\tau) E_j(t+\tau) \right\rangle}. \tag{B.15}$$

Applying the same steps as before, this can be shown to be equal to

$$g_{jj}^{(2)}(\tau) = 1 + \frac{\left| C_{auto}^{(j)}(\tau) \right|^2}{W_j^2} = 1 + f_{jj}(\tau), \tag{B.16}$$

where we have reused the definition of $f_{jk}(\tau)$ from equation (B.14).

B.3. Inclusion of experimental imperfections

Before the expressions derived in the appendices B.1 and B.2 can be compared to the experimental data, they need to be slightly modified to take into account experimental imperfections in the shape of finite efficiencies, dark counts and electronic jitter.

Let us start by considering the jitter of our detection system, which is well modeled by a normal distribution

$$j(t) = \frac{1}{\sqrt{2\pi\sigma^2}} e^{-t^2/(2\sigma^2)}. \tag{B.17}$$

The effect on the measured cross- and auto-correlation functions can be calculated as the convolution of $f_{jk}(\tau)$ from equation (B.14) with $j(t)$, and one obtains

$$\tilde{f}_{jk}(\tau) = \frac{1}{2}\left[e^{\Gamma_j\left(\Gamma_j\sigma^2/2+t\right)} \operatorname{erfc}\left(\frac{\Gamma_j\,\sigma^2 + t}{\sqrt{2}\,\sigma}\right) + e^{\Gamma_k\left(\Gamma_k\sigma^2/2-t\right)} \operatorname{erfc}\left(\frac{\Gamma_k\,\sigma^2 - t}{\sqrt{2}\,\sigma}\right) \right]. \tag{B.18}$$

The spectral filters do not have unit peak transmission. Additionally, the detectors have a finite efficiency and there is loss on the surfaces of optical elements and when coupling into single-mode fiber. By gathering all the losses into a single coefficient, they can be taken into account by adding a prefactor of $\sqrt{\eta_j}$ to the transfer function (B.6). This leads to a reduction of the signal and idler flux (B.10) by a factor of η_j, and the pair flux (B.11) is correspondingly reduced by a factor $\eta_j\eta_k$.

Besides the finite efficiency of the filtering, the etalon or cavity may not be well-approximated by a single Lorentzian filter. This is the case if more than one longitudinal mode is excited. Spurious modes contribute the photon flux and increase it by a factor $1/p_0$ where p_0 is fraction of the photons that end up in the desired mode. However, spurious modes cannot contribute to the pair flux, since the FSR of etalon and cavity are incommensurate. As explained in the main text, the signal filtering suffers from such spurious modes, and a correction has been added to the signal flux.

Detector dark counts add an offset to the detected photon flux and will also contribute to the accidental coincidences. This effect can be added to the formalism by introducing a constant term D_j to equation (B.10) and using equations (B.12) and (B.13) for comparison with the measurements, instead of the simplified expression (B.14). Please note that the pair flux W_2 by definition does not contain contributions from accidental coincidences. In summary, the experimental data presented in figure 7 has been fitted to the expressions

$$W_s = \frac{1}{4}\frac{\eta_s}{p_0}\frac{R}{B}\Gamma_s + D_s,$$

$$W_i = \frac{1}{4}\eta_i\frac{R}{B}\Gamma_i + D_i,$$

$$W_2 = \frac{1}{4}\eta_s\eta_i\frac{R}{B}\frac{\Gamma_s\Gamma_i}{\Gamma_s + \Gamma_i},$$

$$g_{si}^{(2)}(0) = 1 + \frac{1}{4}\frac{\tilde{f}_{si}(0)\eta_s\eta_i}{W_s W_i}\frac{R}{B}\left(\frac{\Gamma_s\Gamma_i}{\Gamma_s + \Gamma_i}\right)^2 \tag{B.19}$$

with the free parameters η_s, η_i, R/B.

Appendix C. Comparison between one- and two-sided filtering

We can use our theoretical model to quantitatively compare the situations for one- and two-sided filtering. In particular, we show that the gain in pair rate obtained by removing the loss caused by the filters typically does not justify the strong reduction of the cross-correlation.

Suppose that only the idler photon is filtered. This can be introduced into the formulas of equation (B.19) by substituting Γ_s with $\Gamma_s{}' \gg \Gamma_i$, and η_s with $\eta_s{}' = \eta_s/\eta_{\text{filt}}$, where $\eta_{\text{filt}} = 0.72$ is the peak transmission of the combination of etalon and VBG. After this substition, the modified pair rate can be approximated by

$$W_2{}' \approx \frac{1}{4} \frac{\eta_s}{\eta_{\text{filt}}} \eta_i \frac{R}{B} \Gamma_i = W_2 \frac{1}{\eta_{\text{filt}}} \frac{\Gamma_s + \Gamma_i}{\Gamma_s}. \tag{C.1}$$

In our experiment, $\Gamma_s = 2.5\,\Gamma_i$, so switching to one-sided filtering would improve the pair rate by a factor of 2.

Neglecting, for simplicity, detector dark counts, the expression for the zero-delay cross-correlation function reduces to

$$g_{\text{si}}^{(2)}(0) = 1 + 4\tilde{f}_{\text{si}}(0) \frac{B}{R} \frac{\Gamma_s \Gamma_i}{(\Gamma_s + \Gamma_i)^2}, \tag{C.2}$$

which is independent of the filter transmission. Note that the highest cross-correlation is achieved for $\Gamma_s = \Gamma_i$. For $\Gamma_s{}' \gg \Gamma_i$, on the other hand, the modified cross-correlation is approximately

$$\left[g_{\text{si}}^{(2)}\right]'(0) \simeq 1 + 4\tilde{f}_{\text{si}}(0) \frac{B}{R} \frac{\Gamma_i}{\Gamma_s{}'}. \tag{C.3}$$

Without filtering of the signal photon $\Gamma_s{}'$ is on the order of the phase-matching bandwidth, which is three orders of magnitude larger than Γ_i, practically removing any correlations. This is because the pair rate becomes negligible compared to the accidental coincidences caused by the large amount of unfiltered signal photons.

The visibility of the sinusoidal fringes used to characterizate the entanglement in section 7 is related to the cross-correlation function via $V = (g_{\text{si}}^{(2)} - 1)/(g_{\text{si}}^{(2)} + 1)$. Hence, a reduction of the cross-correlation entails a lower-quality entanglement.

Appendix D. Details for the violation of the CHSH inequality

The violation of the CHSH inequality requires the joint measurement of the signal and idler photons in four combinations of bases. In our case, we chose the idler bases X_1 and X_2 to correspond to the Pauli matrices σ_x and σ_y, respectively. If the source would produce the Bell state $|\Phi^+\rangle$, i.e. equation (7) with $\phi = 0$, an optimal choice for the signal photon could be $Y_{1,2} = (\sigma_x \pm \sigma_y)/\sqrt{2}$. For non-zero ϕ, this can be generalized to $Y_{1,2} = \cos\theta_\pm \sigma_x + \sin\theta_\pm \sigma_y$ with $\theta_\pm = \phi \pm \pi/4$. In the experiment, we first determined ϕ by a separate measurement and then proceeded to the violation of the CHSH inequality, which consists of measuring the four correlators

$$E\left(X_i, Y_i\right) = \frac{N_{11} + N_{22} - N_{12} - N_{21}}{N_{11} + N_{22} + N_{12} + N_{21}}, \qquad (D.1)$$

where, e.g., N_{11} is the number of coincidences between detectors Si_1 and $ID220_1$. The CHSH parameter is then given by

$$S = \left| E\left(X_1, Y_1\right) + E\left(X_1, Y_2\right) + E\left(X_2, Y_1\right) - E\left(X_2, Y_2\right) \right|. \qquad (D.2)$$

We obtained the following values for the correlators

$$E\left(X_1, Y_1\right) = 0.638(5),$$
$$E\left(X_1, Y_2\right) = 0.702(5),$$
$$E\left(X_2, Y_1\right) = 0.700(5),$$
$$E\left(X_2, Y_2\right) = -0.669(5)$$

which gives $S = 2.708(9)$.

References

[1] Bussières F, Sangouard N, Afzelius M, de Riedmatten H, Simon C and Tittel W 2013 Prospective applications of optical quantum memories *J. Mod. Opt.* **60** 1519–37

[2] Briegel H-J, Dür W, Cirac J I and Zoller P 1998 Quantum repeaters: the role of imperfect local operations in quantum communication *Phys. Rev. Lett.* **81** 5932–5

[3] Sangouard N, Simon C, de Riedmatten H and Gisin N 2011 Quantum repeaters based on atomic ensembles and linear optics *Rev. Mod. Phys.* **83** 33–80

[4] Simon C, de Riedmatten H, Afzelius M, Sangouard N, Zbinden H and Gisin N 2007 Quantum repeaters with photon pair sources and multimode memories *Phys. Rev. Lett.* **98** 190503

[5] Radnaev A G, Dudin Y O, Zhao R, Jen H H, Jenkins S D, Kuzmich A and Kennedy T A B 2010 A quantum memory with telecom-wavelength conversion *Nat. Phys.* **6** 894–9

[6] Ikuta R, Kusaka Y, Kitano T, Kato H, Yamamoto T, Koashi M and Imoto N 2011 Wide-band quantum interface for visible-to-telecommunication wavelength conversion *Nat. Commun.* **2** 537

[7] Zaske S *et al* 2012 Visible-to-telecom quantum frequency conversion of light from a single quantum emitter *Phys. Rev. Lett.* **109** 147404

[8] de Greve K *et al* 2012 Quantum-dot spin-photon entanglement via frequency downconversion to telecom wavelength *Nature* **491** 421–5

[9] Pelc J S *et al* 2012 Downconversion quantum interface for a single quantum dot spin and 1550 nm single-photon channel *Opt. Express* **20** 27510–9

[10] Albrecht B, Farrera P, Fernandez-Gonzalvo X, Cristiani M and de Riedmatten H 2014 A waveguide frequency converter connecting rubidium-based quantum memories to the telecom c-band *Nat. Commun.* **5** 02

[11] Akiba K, Kashiwagi K, Arikawa M and Kozuma M 2009 Storage and retrieval of nonclassical photon pairs and conditional single photons generated by the parametric down-conversion process *New J. Phys.* **11** 013049

[12] Piro N, Rohde F, Schuck C, Almendros M, Huwer J, Ghosh J, Haase A, Hennrich M, Dubin F and Eschner J 2011 Heralded single-photon absorption by a single atom *Nat. Phys.* **7** 17–20

[13] Bao X-H, Qian Y, Yang J, Zhang H, Chen Z-B, Yang T and Pan J-W 2008 Generation of narrow-band polarization-entangled photon pairs for atomic quantum memories *Phys. Rev. Lett.* **101** 190501

[14] Zhang H *et al* 2011 Preparation and storage of frequency-uncorrelated entangled photons from cavity-enhanced spontaneous parametric downconversion *Nat. Photonics* **5** 628–32

[15] Scholz M, Koch L and Benson O 2009 Statistics of narrow-band single photons for quantum memories generated by ultrabright cavity-enhanced parametric down-conversion *Phys. Rev. Lett.* **102** 063603

[16] Fekete J, Rieländer D, Cristiani M and de Riedmatten H 2013 Ultranarrow-band photon-pair source compatible with solid state quantum memories and telecommunication networks *Phys. Rev. Lett.* **110** 220502

[17] Rieländer D, Kutluer K, Ledingham P M, Gündoğan M, Fekete J, Mazzera M and de Riedmatten H 2014 Quantum storage of heralded single photons in a praseodymium-doped crystal *Phys. Rev. Lett.* **112** 040504

[18] Pomarico E, Sanguinetti B, Gisin N, Thew R, Zbinden H, Schreiber G, Thomas A and Sohler W 2009 Waveguide-based OPO source of entangled photon pairs *New J. Phys.* **11** 113042

[19] Pomarico E, Sanguinetti B, Osorio C I, Herrmann H and Thew R T 2012 Engineering integrated pure narrow-band photon sources *New J. Phys.* **14** 033008

[20] Förtsch M, Fürst J U, Wittmann C, Strekalov D, Aiello A, Chekhova M V, Silberhorn C, Leuchs G and Marquardt C 2013 A versatile source of single photons for quantum information processing *Nat. Commun.* **4** 1818

[21] Luo K-H, Herrmann H, Krapick S, Ricken R, Quiring V, Suche H, Sohler W and Silberhorn C 2013 Two-color narrowband photon pair source with high brightness based on clustering in a monolithic waveguide resonator arXiv:1306.1756

[22] Afzelius M, Simon C, de Riedmatten H and Gisin N 2009 Multimode quantum memory based on atomic frequency combs *Phys. Rev.* A **79** 052329

[23] Clausen C, Usmani I, Bussières F, Sangouard N, Afzelius M, de Riedmatten H and Gisin N 2011 Quantum storage of photonic entanglement in a crystal *Nature* **469** 508

[24] Usmani I, Clausen C, Bussières F, Sangouard N, Afzelius M and Gisin N 2012 Heralded quantum entanglement between two crystals *Nat. Photonics* **6** 234–7

[25] Clausen C, Bussières F, Afzelius M and Gisin N 2012 Quantum storage of heralded polarization qubits in birefringent and anisotropically absorbing materials *Phys. Rev. Lett.* **108** 190503

[26] Bussières F *et al* 2014 Quantum teleportation from a telecom-wavelength photon to a solid-state quantum memory *Nat. Photonics* 215

[27] Saglamyurek E, Sinclair N, Jin J, Slater J A, Oblak D, Bussières F, George M, Ricken R, Sohler W and Tittel W 2011 Broadband waveguide quantum memory for entangled photons *Nature* **469** 512–5

[28] Kwiat P G, Mattle K, Weinfurter H, Zeilinger A, Sergienko A V and Shih Y 1995 New high-intensity source of polarization-entangled photon pairs *Phys. Rev. Lett.* **75** 4337–41

[29] Kwiat P G, Waks E, White A G, Appelbaum I and Eberhard P H 1999 Ultrabright source of polarization-entangled photons *Phys. Rev.* A **60** 773–6

[30] Trojek P and Weinfurter H 2008 Collinear source of polarization-entangled photon pairs at nondegenerate wavelengths *Appl. Phys. Lett.* **92** 211103

[31] Kim T, Fiorentino M and Wong F N C 2006 Phase-stable source of polarization-entangled photons using a polarization sagnac interferometer *Phys. Rev.* A **73** 012316

[32] Hentschel M, Hübel H, Poppe A and Zeilinger A 2009 Three-color sagnac source of polarization-entangled photon pairs *Opt. Express* **17** 23153–9

[33] Kwiat P G, Eberhard P H, Steinberg A M and Chiao R Y 1994 Proposal for a loophole-free bell inequality experiment *Phys. Rev.* A **49** 3209–20

[34] Kim Y-Ho, Kulik S P and Shih Y 2001 Bell-state preparation using pulsed nondegenerate two-photon entanglement *Phys. Rev.* A **63** 060301

[35] Palittapongarnpim P, MacRae A and Lvovsky A I 2012 Note: A monolithic filter cavity for experiments in quantum optics *Rev. Sci. Instrum.* **83** 066101

[36] Kato K and Takaoka E 2002 Sellmeier and thermo-optic dispersion formulas for KTP *Appl. Opt.* **41** 5040–4

[37] Jundt D H 1997 Temperature-dependent sellmeier equation for the index of refraction, n_e, in congruent lithium niobate *Opt. Lett.* **22** 1553–5

[38] Ciapurin I V, Drachenberg D R, Smirnov V I, Venus G B and Glebov L B 2012 Modeling of phase volume diffractive gratings, part 2: reflecting sinusoidal uniform gratings, bragg mirrors *Opt. Eng.* **51** 058001

[39] Kuzmich A, Bowen W P, Boozer A D, Boca A, Chou C W, Duan L-M and Kimble H J 2003 Generation of nonclassical photon pairs for scalable quantum communication with atomic ensembles *Nature* **423** 731–4

[40] Razavi M, Söllner I, Bocquillon E, Couteau C, Laflamme R and Weihs G 2009 Characterizing heralded single-photon sources with imperfect measurement devices *J. Phys. B: At. Mol. Opt. Phys.* **42** 114013

[41] Wong F N C, Shapiro J H and Kim T 2006 Efficient generation of polarization-entangled photons in a nonlinear crystal *Laser Phys.* **16** 1517–24

[42] Mitchell M W 2009 Parametric down-conversion from a wave-equation approach: geometry and absolute brightness *Phys. Rev.* A **79** 043835

[43] Christ A, Laiho K, Eckstein A, Cassemiro K N and Silberhorn C 2011 Probing multimode squeezing with correlation functions *New J. Phys.* **13** 033027

[44] Eberly J H 2006 Schmidt analysis of pure-state entanglement *Laser Phys.* **16** 921–6

[45] Peres A 1996 Separability criterion for density matrices *Phys. Rev. Lett.* **77** 1413–5

[46] Clauser J F, Horne M A, Shimony A and Holt R A 1969 Proposed experiment to test local hidden-variable theories *Phys. Rev. Lett.* **23** 880–4

[47] Krapick S, Herrmann H, Quiring V, Brecht B, Suche H and Silberhorn Ch 2013 An efficient integrated two-color source for heralded single photons *New J. Phys.* **15** 033010

[48] Herrmann H, Yang X, Thomas A, Poppe A, Sohler W and Silberhorn C 2013 Post-selection free, integrated optical source of non-degenerate, polarization entangled photon pairs *Opt. Express* **21** 27981–91

"Storage of hyperentanglement in a solid-state quantum memory"

A. Tiranov, J. Lavoie, A. Ferrier, P. Goldner, V. B. Verma, S. W. Nam,
R. P. Mirin, A. E. Lita, F. Marsili, H. Herrmann, C. Silberhorn,
N. Gisin, M. Afzelius & F. Bussières, Optica 2(4), 279-287 (2015)

optica

Storage of hyperentanglement in a solid-state quantum memory

Alexey Tiranov,[1,*] Jonathan Lavoie,[1] Alban Ferrier,[2,3] Philippe Goldner,[3]
Varun B. Verma,[4] Sae Woo Nam,[4] Richard P. Mirin,[4] Adriana E. Lita,[4]
Francesco Marsili,[5] Harald Herrmann,[6] Christine Silberhorn,[6] Nicolas Gisin,[1]
Mikael Afzelius,[1] and Félix Bussières[1]

[1]*Group of Applied Physics, University of Geneva, CH-1211 Geneva 4, Switzerland*

[2]*Sorbonne Universités, UPMC Université Paris 06, 75005 Paris, France*

[3]*PSL Research University, Chimie ParisTech—CNRS, Institut de Recherche de Chimie Paris, 75005 Paris, France*

[4]*National Institute of Standards and Technology, 325 Broadway, Boulder, Colorado 80305, USA*

[5]*Jet Propulsion Laboratory, California Institute of Technology, 4800 Oak Grove Dr., Pasadena, California 91109, USA*

[6]*Applied Physics/Integrated Optics Group, University of Paderborn, 33095 Paderborn, Germany*

Corresponding author: alexey.tiranov@unige.ch

Two photons can simultaneously share entanglement between several degrees of freedom such as polarization, energy-time, spatial mode, and orbital angular momentum. This resource is known as hyperentanglement, and it has been shown to be an important tool for optical quantum information processing. Here we demonstrate the quantum storage and retrieval of photonic hyperentanglement in a solid-state quantum memory. A pair of photons entangled in polarization and energy-time is generated such that one photon is stored in the quantum memory, while the other photon has a telecommunication wavelength suitable for transmission in optical fiber. We measured violations of a Clauser–Horne–Shimony–Holt Bell inequality for each degree of freedom, independently of the other one, which proves the successful storage and retrieval of the two bits of entanglement shared by the photons. Our scheme is compatible with long-distance quantum communication in optical fiber, and is in particular suitable for linear-optical entanglement purification for quantum repeaters.   © 2015 Optical Society of America

OCIS codes: (270.0270) Quantum optics; (270.5565) Quantum communications; (270.5585) Quantum information and processing; (160.5690) Rare-earth-doped materials.

http://dx.doi.org/10.1364/OPTICA.2.000279

---

1. INTRODUCTION

Quantum entanglement is an essential resource for quantum information processing, and in particular for quantum communication and for quantum computing. There are many ways in which quantum systems can be entangled. For example, two photons can be entangled in their polarization, or in their energy. They can also be entangled in more than one of their degrees of freedom (DOFs), i.e., hyperentangled [1–3].

Two photons can thus share more entanglement bits (ebits) than what a singly entangled pair allows.

Hyperentanglement is an important resource in optical quantum information processing [4]. For example, complete and deterministic Bell-state analysis in one of the DOFs of a hyperentangled pair is possible with linear optics [5–7]. This was used to perform quantum teleportation [8–10] and superdense coding [11]. Hyperentanglement also has applications in

optical tests of nonlocality [12], as well as linear-optical quantum computing [13,14] and the generation of multi-qubit entangled states using a smaller number of photons [15]. In this context, light–matter hyperentanglement was demonstrated using spatial and polarization DOFs, and was used in a demonstration of one-way quantum computing [16]. The optical implementation of entanglement purification can be simplified greatly using hyperentanglement [17]. This could play an important role in the context of long-distance quantum communication with quantum repeaters, where purification can be used to increase the rate at which entanglement is distributed [18,19]. However, this is possible only if the DOFs in which the hyperentanglement is coded are suitable for long-distance transmission, e.g., in optical fiber. Previous demonstrations of entanglement purification were all based on polarization and spatial modes [20,21], but the latter is not adequate for long-distance transmission in fiber. Energy-time (or time-bin) and polarization hyperentanglement is much better suited for this. The requirements that then arise for quantum repeaters is to have quantum memories that can efficiently store both DOFs, combined with the possibility of efficiently distributing entanglement over long distances in optical fiber.

Here we report on the quantum storage of hyperentanglement that is compatible for long-distance quantum communication in optical fiber. A source first generates photons hyperentangled in polarization and energy-time. One photon from the pair is then stored in a quantum memory based on rare-earth-ion doped crystals that is designed to store both DOFs. The other photon has a telecommunication wavelength and can be distributed over long distances.

The paper is organized as follows. In Section 2 we describe our experimental setup, including the source of hyperentangled photons. Details on the quantum memory are given in Section 3. Section 4 describes how the Clauser–Horne–Shimony–Holt (CHSH) Bell inequalities on each DOF are measured, and Section 5 presents the main results.

2. EXPERIMENTAL SETUP

A conceptual setup of our experiment is depicted in Fig. 1(a). It consists of a source of pairs of entangled photons (denoted as signal and idler photons) entangled in both polarization and energy-time, a solid-state quantum memory based on rare-earth-ion doped crystals, analyzers (denoted as τ) used to reveal the energy-time entanglement, followed by analyzers (denoted as π) used to reveal the polarization entanglement.

Figure 1(b) shows a detailed version of our setup. Photon pairs entangled in both DOFs (hyperentangled photon pairs), consisting of a signal photon at 883 nm and an idler photon at 1338 nm, are produced by spontaneous parametric downconversion (SPDC) in nonlinear waveguides. Energy-time entanglement is obtained by pumping the waveguides with a continuous-wave laser at 532 nm with an average power of 2.5 mW. Photons from a given pair are created simultaneously at a time that is uncertain within the coherence time of the pump, which creates the entanglement. The polarization entanglement is generated by sending diagonally polarized pump light onto a polarizing beam splitter (PBS) that transmits
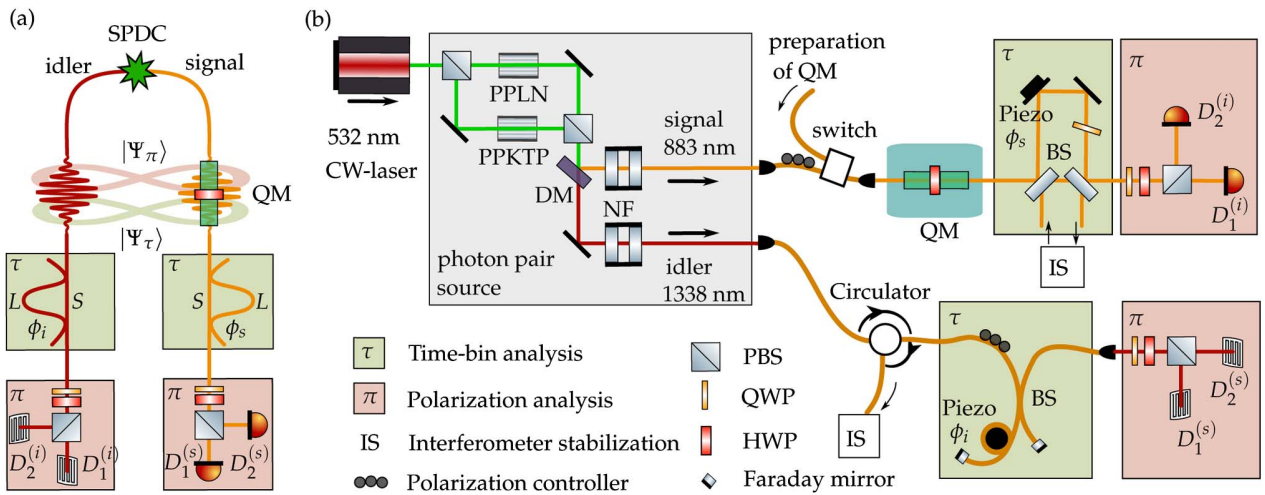
Fig. 1. Experimental setup. (a) Conceptual setup of hyperentanglement storage inside a solid-state quantum memory (QM). A pair of photons entangled in polarization ($|\Psi_\pi\rangle$) and energy-time ($|\Psi_\tau\rangle$) are generated from SPDC. The signal photon is stored inside a quantum memory and released after a predetermined time of 50 ns. The hyperentanglement is revealed using time-bin analyzers (τ) having short (S) and long (L) arms and adjustable relative phases (ϕ_i and ϕ_s), followed by polarization analyzers (π). (b) Experimental setup (see text for details). Polarization-entangled photon pairs are created by coherently pumping two nonlinear waveguides (PPLN and PPKTP) and recombining the optical paths. The pump is a CW laser at 532 nm, which inherently produces pairs that are also energy-time entangled. A dichroic mirror (DM) separates signal and idler photons. The appropriate linewidth for storage of the signal photon in the QM is obtained with narrow filtering (NF), which consists of a cavity and a volume Bragg grating for the signal (883 nm) and the idler (1338 nm). An optical switch is used to direct either the light necessary for the preparation of the QM, or the signal photons, to the QM. The time-bin analyzers of the signal and idler photons are made with free-space and fiber components, respectively, using 50/50 beam splitters (BSs), and are both actively locked. Piezo elements are used to control the phases ϕ_s and ϕ_i of the analyzers. They are followed by free-space polarization analyzers composed of quarter-wave and half-wave plates (QWPs and HWPs) followed by polarizing beam splitters (PBSs). $D_{1,2}^{(s)}$ are avalanche photodiodes, and $D_{1,2}^{(i)}$ are WSi superconducting nanowire single-photon detectors.

horizontal polarization and reflects vertical. The horizontal output of the PBS is followed by a periodically poled lithium niobate waveguide (PPLN) oriented to ensure nondegenerate, collinear type-0 phase matching generating horizontally polarized photons. Similarly, the vertical output is sent to a potassium titanyl phosphate waveguide (PPKTP) generating vertically polarized photons. After each waveguide, the signal and idler are separated by a dichroic mirror (DM), and the modes are recombined at a PBS. A photon pair is then in a coherent superposition of being emitted by the first ($|HH\rangle$) and second waveguides ($|VV\rangle$), yielding a state close to the maximally entangled Bell state

$$|\Psi_\pi\rangle = \frac{1}{\sqrt{2}}(|HH\rangle + e^{i\theta}|VV\rangle). \qquad \textbf{(1)}$$

Using the residual pump light collected at the unused output port of the PBS, we derive a feedback signal that is used to stabilize the phase θ. The polarization entanglement of this source was described in detail in Ref. [22].

Storage of the photon in an atomic ensemble requires reducing its spectral width from its initial ≈ 500 GHz linewidth down to a fraction of the storage bandwidth of the memory, which is ~ 600 MHz. The narrow filtering (NF) for the signal and idler photons is done in two steps: in each path, we combine a filtering cavity and a volume Bragg grating (VBG) to select only a single longitudinal mode of the cavity. The idler photon first passes through a Fabry–Perot cavity with linewidth of 240 MHz and free spectral range (FSR) of 60 GHz. It is then followed by a VBG with a FWHM diffraction window of 27 GHz. The signal photon is first sent onto a VBG with a spectral bandwidth of 54 GHz and then sent through an air-spaced Fabry–Perot etalon with a linewidth of 600 MHz and FSR of 50 GHz. Due to the strong energy correlation between both photons, the heralded signal photon's linewidth is effectively filtered to ≈ 170 MHz, corresponding to a coherence time $\tau_c \approx 1.9$ ns [22].

The signal photon is then sent for storage in a compact, polarization-preserving, and multimode solid-state quantum memory (QM), as described in Section 3. It is then retrieved from the QM after a predetermined 50 ns storage time with an efficiency of $\approx 5\%$.

To reveal energy-time entanglement of the photon retrieved from the memory, a Franson interferometer [23] is used. Specifically, each photon is then sent through unbalanced interferometers with controllable phases and identical travel-time differences between the short (S) and long (L) arms [these interferometers are shown as all-fiber Mach–Zehnder interferometers in Fig. 1(a)]. In practice [Fig. 1(b)], the idler is sent through an unbalanced all-fiber Michelson interferometer using Faraday mirrors, and the signal is sent through a free-space Mach–Zehnder interferometer. The travel-time difference between the short and long arms is 5.5 ns, which is greater than the coherence time of the photons τ_c and eliminates single-photon interference. However, due to the large uncertainty in the creation time, a coincidence stemming from both photons traveling the short arms is indistinguishable from one

in which both photons travel the long arms, leading to quantum interference in the coincidence rate.

Hence, interference fringes can be observed by varying the phase in each interferometer. These coincidences can be seen as stemming from a time-bin entangled state that is close to the maximally entangled Bell state

$$|\Psi_\tau\rangle = \frac{1}{\sqrt{2}}(|SS\rangle + |LL\rangle). \qquad \textbf{(2)}$$

Coincidences between photons traveling different arms are also observed, but they do not yield any kind of interference and are discarded when analyzing the energy-time DOF. They can, however, be kept when analyzing the polarization DOF.

When considering entanglement in both DOFs, the state of a single pair can be written as

$$|\Psi_\tau\rangle \otimes |\Psi_\pi\rangle. \qquad \textbf{(3)}$$

Both DOFs of a hyperentangled pair can in principle be manipulated independently, and the quality of the entanglement in one DOF should not depend on the basis in which the other is measured. In our setup, this is possible only if polarization rotations, due to birefringent optics, are the same in both arms of the unbalanced interferometers. For the idler photon, this is happening automatically, thanks to the Faraday mirrors reflecting the light with a polarization that is orthogonal to the one at the input of the 50/50 fiber beam splitter (BS). For the signal photon, this is more challenging because free-space mirrors affect the phase of the $|H\rangle$ and $|V\rangle$ polarizations in different ways. This effectively means that without any kind of compensation the measurement basis of the time-bin analyzer is not the same for an input $|H\rangle$ or an input $|V\rangle$ polarization state. To eliminate this problem, we insert a wave plate in the long arm. The fast axis is set to horizontal, and the plate is tilted with respect the beam (see Fig. 1). The tilt controls the relative phase between horizontal and vertical polarizations, and is adjusted to equalize the birefringence of both arms and therefore eliminate the polarization-dependent relative phase between the two arms.

To lock the phase of the idler's time-bin analyzer, we use highly coherent light at 1338 nm obtained from difference-frequency generation (DFG) from 532 and 883 nm light combined in the PPLN waveguide. A feedback mechanism locks this DFG light on the idler's cavity transmission peak [22]. The phase of the interferometer is controlled by coiling the fiber of the long arm around a cylindrical piezo transducer, and the interferometer is locked using a side-of-fringe technique. The phase of the signal photon's time-bin analyzer is controlled using a piezo-mounted mirror placed in the long arm. The phase is probed using part of the CW laser at 883 nm that is used to prepare the QM. The light is frequency shifted using an acousto-optic modulator (AOM) and then sent through the interferometer in a spatial mode that has no overlap with the signal photon. The phase of the interferometer is modulated with a sinusoidal signal oscillating at 18 kHz. This yields intensity fluctuations that can be demodulated using a lock-in technique and allows us to obtain the derivative of the

transmission of the interferometer. To scan the phase, we fix the locking point to a maxima of the transmission (i.e., a zero of its derivative) and sweep the frequency of the probe laser using the AOM. The time difference of 5.5 ns between the short and long arms yields a period that can be covered by scanning the frequency over ≈180 MHz. One advantage of this technique compared to a side-of-fringe lock is that it yields a locking point that is unaffected by fluctuations of the intensity of the laser that probes the phase.

After the interferometers, the polarization of each photon is analyzed. Each output of the PBS is coupled into a single-mode fiber and sent to single-photon detectors. The results of the measurements made at different analyzers are compared in order to reveal the nonlocal correlations in both DOFs. Single-photon detectors with 30% (Si avalanche photodiode) and 75% (WSi superconducting nanowire [24]) efficiencies are used to detect the signal at 883 nm and the idler at 1338 nm, respectively.

The heralding efficiency of signal photons up to the quantum memory is ≈20%, while the overall detection efficiency of idler photons is ≈10%. The average input pump power at 532 nm of 2.5 mW was used and corresponds to a photon pair creation probability of ≈0.015 for the time window of $\tau_c = 1.9$ ns [22]. The overall coincidence rates for the transmitted and stored photons were ≈20 and 2 Hz, respectively.

3. MULTIMODE AND POLARIZATION-PRESERVING BROADBAND QUANTUM MEMORY

In this section we describe our quantum memory and how it can store both DOFs. The storage is implemented using the atomic frequency comb (AFC) storage protocol in rare-earth-ion doped crystals [25]. To realize this, the inhomogeneously broadened absorption profile of the crystal is first shaped into a comb-like structure in frequency using optical pumping. When a photon is absorbed by the AFC, it creates an atomic excitation delocalized over all atoms inside the comb. The collective state then dephases and the excitation is stored. Thanks to the periodic profile of the AFC, the atoms then collectively interfere after a specific time, which can lead to reemission of the signal photon into the same spatial mode it was absorbed in. The storage time is predetermined and equal to $1/\Delta$, where Δ is the period of the frequency comb.

The temporal multimode capacity for this protocol is given by the ratio of the storage time over the duration of the temporal modes that are stored. For a given storage time, the multimode capacity therefore increases with the storage bandwidth. The large inhomogeneous broadening of rare-earth-ion doped crystals makes them an excellent material to realize multimode quantum memories at the single-photon level [26], and they are well suited for the storage of energy-time and time-bin entanglement, as demonstrated in [27,28].

We implement the AFC quantum memory protocol using rare-earth-ion doped $Nd^{3+}:Y_2SiO_5$ crystals with a dopant concentration of ≈75 ppm. Optical pumping is used to shape the absorption profile of the QM in an AFC. This requires splitting the ground state $^4I_{9/2}$ into two Zeeman levels [Fig. 2(a)] using a static magnetic field of 300 mT [26]. This is done to
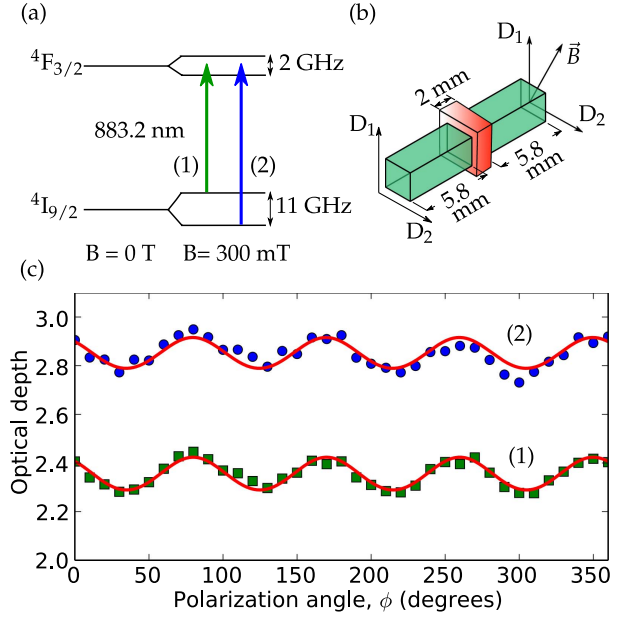
Fig. 2. Scheme for storage of polarization qubits. (a) Energy level structure of Nd^{3+} ions inside a Y_2SiO_5 crystal with and without applied external magnetic field $B = 300$ mT. External magnetic field lies in D_1–D_2 plane with 30° angle with respect to D_1 axis. (b) The compact configuration of the quantum memory is obtained by placing a HWP between two identical $Nd^{3+}:Y_2SiO_5$ crystals. The fast axis of the HWP is oriented at 45° with respect to the axes D_1 and D_2, which are the two of the principal axes of the dielectric tensor. The 14-mm-long arrangement is cooled to 2.7 K and placed in a static magnetic field to split the ground into two Zeeman levels. (c) The optical depth of the two-crystal configuration is shown as a function of the linear polarization angle of the input. The green squares and blue circles correspond to transitions [(1) and (2)] from each of the Zeeman-split ground states shown in (a). Lines are fits of the model described in [33].

spectrally resolve two optical transitions that are inhomogeneously broadened to 6 GHz and to perform optical pumping from one ground Zeeman state to another. The Zeeman splitting of the excited state is not spectrally resolved in this configuration. We measured a ground-state Zeeman lifetime of 43 ms using spectral hole burning measurements, which is much greater than the 300 μs radiative lifetime of the optical transition, as required for optical pumping. We note that this lifetime is, however, shorter than the ∼100 ms measured in 30-ppm-doped crystals [26], which unavoidably affects the quality of the AFC that we can prepare; see below.

The efficiency η of the AFC protocol [25] depends on the optical depth d through $\eta = \tilde{d}^2 e^{-\tilde{d}} e^{-d_0} \eta_{deph}$, where $\tilde{d} = \frac{d}{F}$ is the average optical depth of the comb, F is the finesse of the comb, d_0 the residual optical depth, and η_{deph} is the dephasing term, which is maximized for square peak shapes [29]. The storage of polarization qubits in rare-earth-ion doped crystals is therefore hindered by their polarization-dependent optical depth. It is, however, possible to mitigate this problem, as demonstrated in [30–32]. Specifically, consider a crystal cut such that its input face contains two principal axes of the dielectric tensor; see Fig. 2(a). Let D_1 and D_2 be those axes,

which we assume coincident with the polarizations for which the optical depth is minimum and maximum. This condition is satisfied for a yttrium orthosilicate crystal doped with neodymium ions [30], $Nd^{3+}:Y_2SiO_5$, the material we use here. Let d_1 and d_2 be the optical depth for light polarized along the D_1 and D_2 axes. By placing two identical crystals on each sides of a half-wave plate (HWP) oriented to rotate a D_1-polarized photon to D_2 and vice versa, an absorbed single photon with an arbitrary polarization will be in superposition of being stored in both crystals with an effective optical depth equal to $d_1 + d_2$, yielding a polarization-independent efficiency.

Here we realize this polarization-independent scheme in a compact manner using two 5.8-mm-long $Nd^{3+}:Y_2SiO_5$ crystals placed on each side of a 2-mm-thick HWP, resulting in a total length of about 14 mm [Fig. 2(b)]. This setup system is cooled to a temperature of 2.7 K using a closed-cycle cryocooler. The Nd^{3+} dopant concentration is higher than we used in a previous demonstration of polarization-independent storage of single photons [30]. The higher doping level allows us to use shorter crystals for a more compact setup. All faces of the crystals, HWP, and cryostat windows are coated with antireflective films, and the overall transmission through the system is higher than 95%, when factoring out the absorption of the crystals.

We achieve an average optical depth of 2.35 ± 0.10, averaged over all linear polarization states, for the optical transition starting from the higher-energy level of the Zeeman doublet. The variations are smaller than 5% [Fig. 2(c)]. They may be attributed to the imperfect alignment and retardation of the HWP, as well as an imperfect optical alignment of the beam with respect to the input face. The transition from the other Zeeman level yields 2.85 ± 0.11 [see Fig. 2(c), blue circles]. This difference is consistent with thermalized populations, which dictates that the ratio of the optical depths should be $\exp(-\Delta E/k_B T)$, where $\Delta E = h\Delta\nu$, $\Delta\nu = 11$ GHz, k_B is Boltzmann's constant, and T is the temperature. For our temperature of 2.7 K, the expected ratio is 0.82, which matches the observed ratio of $2.35/2.85 = 0.825$. For our storage of hyperentangled photons, we could only use the optical transition with the lowest optical depth due to the limited tuning range of the Fabry–Perot etalon of the source. Using the other optical transition could have led to a higher quantum memory efficiency.

The AFC is prepared with an AOM that modulates the intensity and frequency of the light from an external cavity diode laser centered on the absorption line of the $^4I_{9/2} \rightarrow {}^4F_{3/2}$ transition. In this way we create a 120 MHz absorption comb with a spacing of $\Delta = 20$ MHz between the peaks, which corresponds to $1/\Delta = 50$ ns storage time [25]. To extend the bandwidth of QM beyond the 120 MHz limit imposed by the double-pass in the AOM, the light from the AOM is coupled inside an electro-optical phase modulator that creates first- and second-order sidebands separated by 120 MHz from each other. This yields an overall comb width of 600 MHz, larger than the 170 MHz spectrum of the heralded signal photon, as shown in Fig. 3. The contrast of the absorption profile is reduced on the sides due to the smaller optical power available in the second-order sidebands. The fact that the
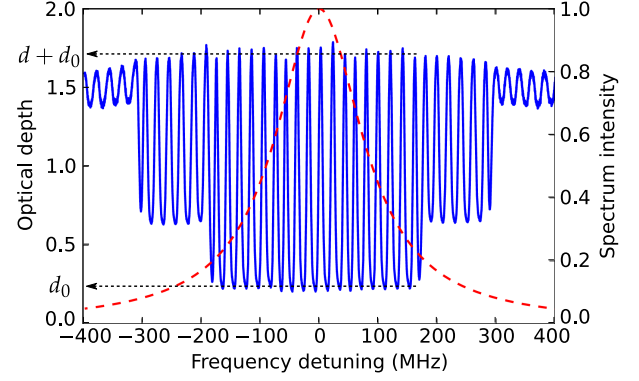

Fig. 3. Spectrum of the AFC prepared by optical pumping inside the absorption profile. The central 120-MHz-wide region is prepared by the carrier frequency of the laser diode that is modulated in intensity and frequency by an AOM. The subsequent 120-MHz-wide regions on both sides are prepared by generating first- and second-order sidebands separated by 120 and 240 MHz from the carrier frequency, respectively, using an electro-optic phase modulator placed after the AOM. The finesse of the comb is ≈ 2, and the width of the comb is ≈ 600 MHz. For comparison, the dashed red line shows the power spectra of a 170 MHz Lorentzian, which is close to the spectral width of the heralded signal photon. The values of d and d_0 used in equation of efficiency are shown for the central part.

maximum optical depth of the comb (1.8) is less than the one of the transition itself (2.35) can be attributed to power broadening, which can reduce the maximum optical depth between the peaks. The remaining absorption of $d_0 \geq 0.25$ also reduces the storage efficiency. The efficiency of the quantum memory with this comb is $\approx 5\%$ for a 50 ns storage time, while the total absorption and the transmission of the memory are both close to 50%. Imperfect rephasing and reabsorption processes inside the memory lead to the decrease of the QM efficiency [25]. The photons that were not absorbed could be used to analyze storage process and calibrate the analyzers for CHSH inequality violation.

4. BELL TESTS ON HYPERENTANGLEMENT

A quantum state is hyperentangled if one can certify entanglement for each entangled DOF. Therefore, it is enough to violate a Bell inequality in both polarization and time independently to demonstrate hyperentanglement. Here we use the inequality derived by Clauser *et al.* [34] (CHSH) to witness entanglement. The Bell–CHSH inequality for a single DOF reads

$$S = |E(\mathbf{X}, \mathbf{Y}) + E(\mathbf{X'}, \mathbf{Y}) + E(\mathbf{X}, \mathbf{Y'}) - E(\mathbf{X'}, \mathbf{Y'})| \leq 2, \quad (4)$$

where $\mathbf{X}$ and $\mathbf{X'}$ ($\mathbf{Y}$ and $\mathbf{Y'}$) are two observables that are measured on the signal (idler) side. E is the correlator corresponding to the expectation value of the correlation between measurement results obtained on both photons of an entangled pair. Those correlators are calculated from the number of coincidences between idler detector $D_k^{(i)}$ and signal detector $D_l^{(s)}$, denoted R_{kl}, where $k, l \in \{1, 2\}$ are the possible outcomes for each measurement. In terms of the coincidence rate, the correlation

function is written as $E = [R_{11} + R_{22} - R_{12} - R_{21}]/R_T$, where $R_T = \sum_{k,l} R_{kl}$ is the total rate of coincidences.

Let us first consider the polarization DOF only, and suppose for now that the time-bin analyzers in the setup of Fig. 1 are bypassed. Consider as well that the signal and idler photons are measured in the set of linear polarizations. This is done by setting the QWPs of the analyzers at 0° with respect to horizontal, and the HWPs at θ_s and θ_i for the signal and idler, respectively. Finally, let us assume the phase θ of state $|\Psi_\pi\rangle$ is equal to zero [Eq. (1)]. One can show that the coincidence rates should be $R_{11}^{(\pi)} = R_{22}^{(\pi)} \sim (1 + V_\pi \cos[4(\theta_s - \theta_i)])$ and $R_{12}^{(\pi)} = R_{21}^{(\pi)} \sim (1 - V_\pi \cos[4(\theta_s - \theta_i)])$. In these expressions we introduced the polarization entanglement visibility $0 \leq V_\pi \leq 1$ that arises by assuming the experimental imperfections can be described by replacing $|\Psi_\pi\rangle$ with a Werner state of visibility V_π [35].

Let us now consider the case in which the interferometers are inserted before the polarization analyzers, as in Fig. 1. This yields a Franson interferometer, and one can show that the observed coincidence rate between $D_k^{(s)}$ and $D_l^{(i)}$ (when considering the appropriate time difference between detections; see below) is given by

$$R_{kl}^{(\pi,\tau)} = R_{kl}^{(\pi)} \cdot R^{(\tau)}, \qquad (5)$$

where $R^{(\tau)} \sim (1 + V_\tau \cos[\Delta\phi_s + \Delta\phi_i])$, and $\Delta\phi_s$ (or $\Delta\phi_i$) is the relative phase between the long and short arms of the signal (or idler) interferometer. Like the polarization DOF, we assumed the measurement is performed on a Werner state of visibility V_τ instead of $|\Psi_\tau\rangle$. Note that in our setup, we use only one of the output ports of the interferometers. This translates into saying that $R^{(\tau)}$ corresponds to one of the four rates possible $R_{mn}^{(\tau)}$ ($m, n \in \{1, 2\}$) at a time. Which one is measured is decided by an appropriate choice of the relative phases $\Delta\phi_{s,i}$. This limitation can nevertheless be used to violate a Bell–CHSH inequality, assuming fair sampling of the outcomes.

When measuring the Bell–CHSH inequality on the polarization DOF only, $R_{kl}^{(\pi)}$ is obtained from a measurement of $R_{kl}^{(\pi,\tau)}$ by considering $R^{(\tau)}$ as a constant loss factor. Measurement of $R^{(\tau)}$ is obtained by summing all coincidences between either $D_1^{(s)}$ or $D_2^{(s)}$ and $D_1^{(i)}$ or $D_2^{(i)}$. Quantum mechanics predicts that $S_\pi \leq 2\sqrt{2} V_\pi$ (or $S_\tau \leq 2\sqrt{2} V_\tau$) for polarization (or energy-time), where the inequality is saturated with an optimal set of measurements. The local bound is $S_{\pi,\tau} = 2$.

5. RESULTS

Before characterizing quantum correlations, we first need to determine the phase θ of the polarization-entangled state $|\Psi_\pi\rangle$, as well as the sum $\Delta\phi_s + \Delta\phi_i$ of the phases of the interferometers. Once they are known, we consider them as phase offsets in $R_{kl}^{(\pi)}$ and $R^{(\tau)}$. For this, we use the signal photons that are transmitted by the quantum memory (i.e., not stored). We do so because the signal photons are more likely to be transmitted than stored and retrieved, and this allows a faster characterization of the phases. Figure 4(a) shows coincidence

(a) Transmitted photons

(b) Stored photons
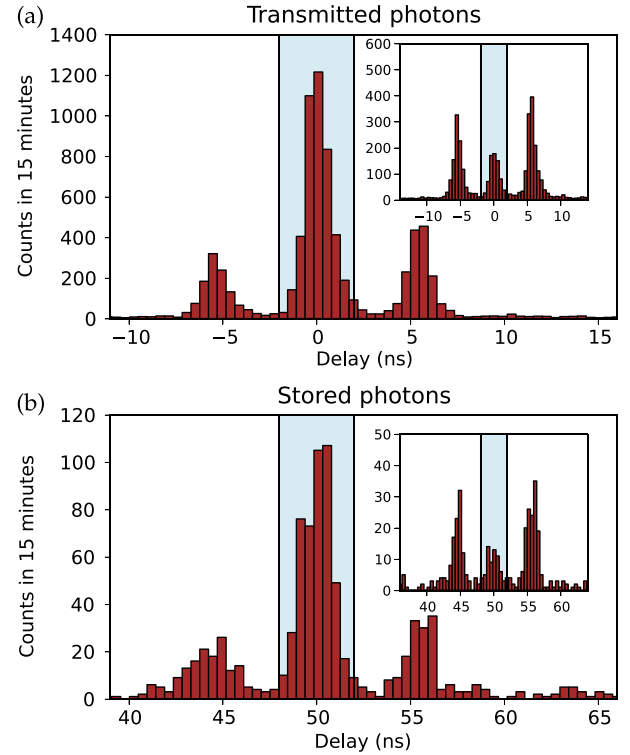
Fig. 4. Example of measurements used to violate CHSH inequality for time-bin qubits. The coincidence histograms between detectors $D_1^{(s)}$ and $D_1^{(i)}$ show three peaks corresponding to different path combinations for (a) transmitted signal photon, i.e., not absorbed by the QM, and (b) stored signal photon. Each figure represents a histogram from one measurement outcome, $R_{11}^{(\pi,\tau)}$, of a correlator in the Bell–CHSH inequality [Eq. (4)]. The insets correspond to histograms with an additional π phase shift between the two interferometers. Varying the angles of the polarization analyzers leads to variations of the intensity of all three peaks simultaneously.

histograms between the pair of detectors $D_1^{(s)}$ and $D_1^{(i)}$ (the other histograms are similar). The coincidences are resolved into two satellite peaks and a central peak. The rate estimated from the central peak corresponds to $R_{11}^{(\pi,\tau)}$. The rate in the satellite peaks is proportional to $R_{11}^{(\pi)}$ only since the timing between detections cannot lead to quantum interference due to the energy-time entanglement. Hence, the satellite peaks are included in the analysis of the polarization entanglement, but not in that of the energy-time.

To extract $\Delta\phi_s + \Delta\phi_i$, we scan the free-space interferometer as described in Section 2, while the polarization is measured in the basis $\{|H\rangle, |V\rangle\}$ on both sides. In this way, detectors $D_1^{(s)}$ and $D_1^{(i)}$ are revealing the energy-time entanglement of the $|HH\rangle$ component of $|\Psi_\pi\rangle$, while $D_2^{(s)}$ and $D_2^{(i)}$ are revealing that of the $|VV\rangle$ component. Figure 5(a) shows coincident events in the central peak as a function of $\Delta\phi_s$, while $\Delta\phi_i$ is kept constant. The rates $R_{11}^{(\pi,\tau)}$ (solid line) and $R_{22}^{(\pi,\tau)}$ (dashed line) overlap, as is required to measure both DOFs independently. The visibility is $V_\tau = 92(3)\%$. To extract the value of θ, we set $\Delta\phi_s + \Delta\phi_i = 0$ and

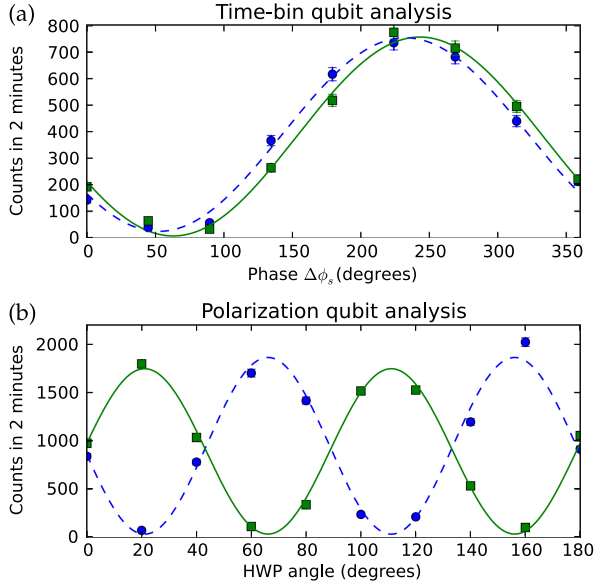**Fig. 5.** Calibration of the analyzers using transmitted signal photons. (a) Rates in the central coincidence peak of Fig. 4(a) are plotted as a function of the sum of the phases of each interferometer, for both output ports of the polarization analyzer. The small phase shift between the curves appears due to a residual phase difference between $|H\rangle$ and $|V\rangle$ components at the output of the interferometer on the signal side. (b) Rates in the central coincidence peak of Fig. 4(a) as a function of polarization analyzer's HWP angle of the signal photon (with the QWP at 45°), for two pairs of detectors, namely $D_1^{(s)}$ and $D_1^{(i)}$ (solid line) or $D_2^{(s)}$ and $D_2^{(i)}$ (dashed line). Each curve represents a fit to data points using a sinusoidal function, and the error bars are estimated assuming Poisson statistics for the counts. The average visibilities for polarization and energy-time entanglement are $V_\tau = 92(3)\%$ and $V_\pi = 96(2)\%$, respectively.
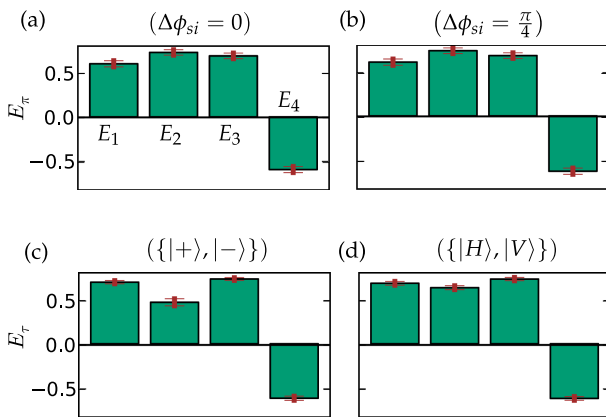

Fig. 6. Correlators for stored photons. The four panels are different sets of correlation measurements that violate the Bell–CHSH inequality of Eq. (4) reported in Table 1. The top row shows the values for polarization measurements with either (a) measurement on the energy-time entanglement such that $\Delta\phi_s + \Delta\phi_i = 0$ or (b) $\Delta\phi_s + \Delta\phi_i = \pi/4$. In the bottom row we show the values for energy-time measurements while projecting the polarization of both the signal and the idler in (c) the $\{|+\rangle, |-\rangle\}$ basis, or (d) the $\{|H\rangle, |V\rangle\}$ basis (right).

Table 1. Summary of all Bell–CHSH Violations[a]

	S (Transmitted)		S (Stored)	
	π	τ	π	τ
$\pi_1:\{|H\rangle, |V\rangle\}$	–	2.555(13)	–	2.60(7)
$\pi_2:\{|+\rangle, |-\rangle\}$	–	2.571(11)	–	2.49(4)
$\tau_1:\phi_{si} = 0$	2.716(11)	–	2.59(4)	–
$\tau_2:\phi_{si} = \frac{\pi}{4}$	2.733(12)	–	2.64(4)	–

[a]Measured S parameters obtained with transmitted or stored signal photons are shown. For each case, tests on the energy-time (τ) DOF were done with either the polarization basis $\pi_1 = \{|H\rangle, |V\rangle\}$ or $\pi_2 = \{|+\rangle, |-\rangle\}$, and tests on the polarization (π) DOF were done with $\Delta\phi_s + \Delta\phi_i = \phi_{si} = 0$ (τ_1) or $\frac{\pi}{4}$ (τ_2). These results show clear violations of Bell–CHSH inequality and demonstrate entanglement in all DOFs studied.

project the idler photon in the basis $\{|+\rangle, |-\rangle\}$, where $|\pm\rangle = \frac{1}{\sqrt{2}}(|H\rangle \pm |V\rangle)$. This prepares the signal photon in the state $\frac{1}{\sqrt{2}}(|H\rangle \pm e^{i\theta}|V\rangle)$. The QWP of the signal polarization analyzer is then set to transform that state into one with a linear polarization. Figure 5(b) shows the rates $R_{11}^{(\pi)}$ and $R_{22}^{(\pi)}$, as a function of the HWP angle, from which the phase of the polarization Bell state can be extracted from the horizontal offset. The visibility $V_\pi = 96(2)\%$.

Once the phases are estimated, we measure correlations that violate the Bell–CHSH inequality for each DOF using the photons that are stored and retrieved from the quantum memory. To illustrate the independence between the two DOFs, each polarization measurement was performed using two different projection bases for the energy-time DOF, and vice versa. Specifically, the test on the energy-time DOF was done using either the polarization basis $\pi_1 = \{|H\rangle, |V\rangle\}$ for both photons, or $\pi_2 = \{|+\rangle, |-\rangle\}$. The test on the polarization DOF was done with either $\Delta\phi_s + \Delta\phi_i = \phi_{si} = 0$ (denoted by τ_1) or $\phi_{si} = \frac{\pi}{4}$ (denoted by τ_2). The values of the measured correlators are shown on Fig. 6. The corresponding CHSH parameters are $S_\pi^{(\tau_1)} = 2.59(4)$ and $S_\pi^{(\tau_2)} = 2.64(4)$ for polarization entanglement, and $S_\tau^{(\pi_1)} = 2.60(7)$ and $S_\tau^{(\pi_2)} = 2.49(4)$ for the energy-time. The violations exceed the local bound by more than eight standard deviations. To see the effect of the storage process on the quality of the hyperentanglement, we performed the same analysis using the transmitted signal photons. Table 1 summarizes all the results.

The values for S_π and S_τ for stored photons are all lower than for transmitted photons except the S_τ value for the π_1 polarization basis (which we believe is higher due to a statistical fluctuation). The lower values are most likely caused by accidental coincidences between idler photon (from one photon pair) and signal photon (from another photon pair) generated within the time delay equal to the storage time of the memory. This effect was studied in detail in a previous publication [36]. It limits the maximally achievable visibility and reduces the CHSH inequality violation. The relative difference between the transmitted and the stored cases is at most 5%, and hence the storage in the QM has very little effect on the quality of the hyperentanglement.

6. CONCLUSIONS

We have shown the storage of energy-time and polarization hyperentanglement in a solid-state quantum memory. This choice of DOFs, combined with the fact that one of the photons of each pair is at a telecom wavelength, makes our source and memory very attractive for the implementation of linear-optical entanglement purification in quantum repeaters. This would ultimately require the use of a quantum memory that can retrieve photon on-demand using a complete AFC storage scheme [25,37]. Alternatively, a scheme based on spectral multiplexing [38] could be used. The storage of hyperentanglement demonstrated here is suitable with both of the approaches. Our experiment also shows that we can store two ebits in a single quantum memory. Expanding on this idea, our memory could be used to store other DOFs, and an even larger number of ebits, by using frequency, orbital angular momentum, and spatial modes. The multimode capacity of rare-earth-ion doped quantum memories goes beyond the temporal DOF, and this might prove a useful tool for optical quantum information processing.

REFERENCES

1. P. G. Kwiat, "Hyper-entangled states," J. Mod. Opt. **44**, 2173–2184 (1997).
2. J. T. Barreiro, N. K. Langford, N. A. Peters, and P. G. Kwiat, "Generation of hyperentangled photon pairs," Phys. Rev. Lett. **95**, 260501 (2005).
3. M. Barbieri, C. Cinelli, P. Mataloni, and F. De Martini, "Polarization-momentum hyperentangled states: realization and characterization," Phys. Rev. A **72**, 052110 (2005).
4. J.-W. Pan, Z.-B. Chen, C.-Y. Lu, H. Weinfurter, A. Zeilinger, and M. Z. Żukowski, "Multiphoton entanglement and interferometry," Rev. Mod. Phys. **84**, 777–838 (2012).
5. P. G. Kwiat and H. Weinfurter, "Embedded Bell-state analysis," Phys. Rev. A **58**, R2623–R2626 (1998).
6. S. P. Walborn, S. Pádua, and C. H. Monken, "Hyperentanglement-assisted Bell-state analysis," Phys. Rev. A **68**, 042313 (2003).
7. C. Schuck, G. Huber, C. Kurtsiefer, and H. Weinfurter, "Complete deterministic linear optics Bell state analysis," Phys. Rev. Lett. **96**, 190501 (2006).
8. D. Boschi, S. Branca, F. De Martini, L. Hardy, and S. Popescu, "Experimental realization of teleporting an unknown pure quantum state via dual classical and Einstein–Podolsky–Rosen channels," Phys. Rev. Lett. **80**, 1121–1125 (1998).
9. Y.-H. Kim, S. P. Kulik, and Y. Shih, "Quantum teleportation of a polarization state with a complete Bell state measurement," Phys. Rev. Lett. **86**, 1370–1373 (2001).
10. C. Schmid, N. Kiesel, U. K. Weber, R. Ursin, A. Zeilinger, and H. Weinfurter, "Quantum teleportation and entanglement swapping with linear optics logic gates," New J. Phys. **11**, 033008 (2009).
11. J. T. Barreiro, T.-C. Wei, and P. G. Kwiat, "Beating the channel capacity limit for linear photonic superdense coding," Nat. Phys. **4**, 282–286 (2008).
12. Z.-B. Chen, J.-W. Pan, Y.-D. Zhang, Č. Brukner, and A. Zeilinger, "All-versus-nothing violation of local realism for two entangled photons," Phys. Rev. Lett. **90**, 160408 (2003).
13. K. Chen, C.-M. Li, Q. Zhang, Y.-A. Chen, A. Goebel, S. Chen, A. Mair, and J.-W. Pan, "Experimental realization of one-way quantum computing with two-photon four-qubit cluster states," Phys. Rev. Lett. **99**, 120503 (2007).
14. G. Vallone, G. Donati, R. Ceccarelli, and P. Mataloni, "Six-qubit two-photon hyperentangled cluster states: characterization and application to quantum computation," Phys. Rev. A **81**, 052301 (2010).
15. W.-B. Gao, C.-Y. Lu, X.-C. Yao, P. Xu, O. Guhne, A. Goebel, Y.-A. Chen, C.-Z. Peng, Z.-B. Chen, and J.-W. Pan, "Experimental demonstration of a hyper-entangled ten-qubit Schrodinger cat state," Nat. Phys. **6**, 331–335 (2010).
16. X.-F. Xu, X.-H. Bao, and J.-W. Pan, "Demonstration of active feedforward one-way quantum computing with photon-matter hyperentanglement," Phys. Rev. A **86**, 050304 (2012).
17. C. Simon and J.-W. Pan, "Polarization entanglement purification using spatial entanglement," Phys. Rev. Lett. **89**, 257901 (2002).
18. H.-J. Briegel, W. Dür, J. I. Cirac, and P. Zoller, "Quantum repeaters: the role of imperfect local operations in quantum communication," Phys. Rev. Lett. **81**, 5932–5935 (1998).
19. L.-M. Duan, M. D. Lukin, J. I. Cirac, and P. Zoller, "Long-distance quantum communication with atomic ensembles and linear optics," Nature **414**, 413–418 (2001).
20. J.-W. Pan, S. Gasparoni, R. Ursin, G. Weihs, and A. Zeilinger, "Experimental entanglement purification of arbitrary unknown states," Nature **423**, 417–422 (2003).
21. P. Walther, K. J. Resch, I. C. V. Brukner, A. M. Steinberg, J.-W. Pan, and A. Zeilinger, "Quantum nonlocality obtained from local states by entanglement purification," Phys. Rev. Lett. **94**, 040504 (2005).
22. C. Clausen, F. Bussières, A. Tiranov, H. Herrmann, C. Silberhorn, W. Sohler, M. Afzelius, and N. Gisin, "A source of polarization-entangled photon pairs interfacing quantum memories with telecom photons," New J. Phys. **16**, 093058 (2014).
23. J. D. Franson, "Bell inequality for position and time," Phys. Rev. Lett. **62**, 2205–2208 (1989).
24. V. B. Verma, B. Korzh, F. Bussières, R. D. Horansky, A. E. Lita, F. Marsili, M. D. Shaw, H. Zbinden, R. P. Mirin, and S. W. Nam, "High-efficiency WSi superconducting nanowire single-photon detectors operating at 2.5 K," Appl. Phys. Lett. **105**, 122601 (2014).
25. M. Afzelius, C. Simon, H. de Riedmatten, and N. Gisin, "Multimode quantum memory based on atomic frequency combs," Phys. Rev. A **79**, 052329 (2009).
26. I. Usmani, M. Afzelius, H. de Riedmatten, and N. Gisin, "Mapping multiple photonic qubits into and out of one solid-state atomic ensemble," Nat. Commun. **1**, 1 (2010).
27. C. Clausen, I. Usmani, F. Bussieres, N. Sangouard, M. Afzelius, H. de Riedmatten, and N. Gisin, "Quantum storage of photonic entanglement in a crystal," Nature **469**, 508–511 (2011).
28. E. Saglamyurek, N. Sinclair, J. Jin, J. A. Slater, D. Oblak, F. Bussières, M. George, R. Ricken, W. Sohler, and W. Tittel, "Broadband waveguide quantum memory for entangled photons," Nature **469**, 512–515 (2011).
29. M. Bonarota, J. Ruggiero, J.-L. Le Gouët, and T. Chanelière, "Efficiency optimization for atomic frequency comb storage," Phys. Rev. A **81**, 033803 (2010).
30. C. Clausen, F. Bussières, M. Afzelius, and N. Gisin, "Quantum storage of heralded polarization qubits in birefringent and

anisotropically absorbing materials," Phys. Rev. Lett. **108**, 190503 (2012).

31. M. Gündoğan, P. M. Ledingham, A. Almasi, M. Cristiani, and H. de Riedmatten, "Quantum storage of a photonic polarization qubit in a solid," Phys. Rev. Lett. **108**, 190504 (2012).

32. Z.-Q. Zhou, W.-B. Lin, M. Yang, C.-F. Li, and G.-C. Guo, "Realization of reliable solid-state quantum memory for photonic polarization qubit," Phys. Rev. Lett. **108**, 190505 (2012).

33. M. Afzelius, M. U. Staudt, H. de Riedmatten, N. Gisin, O. Guillot-Noel, P. Goldner, R. Marino, P. Porcher, E. Cavalli, and M. Bettinelli, "Efficient optical pumping of Zeeman spin levels in $Nd^{3+}:YVO_4$," J. Lumin. **130**, 1566–1571 (2010).

34. J. F. Clauser, M. A. Horne, A. Shimony, and R. A. Holt, "Proposed experiment to test local hidden-variable theories," Phys. Rev. Lett. **23**, 880–884 (1969).

35. R. F. Werner, "Quantum states with Einstein–Podolsky–Rosen correlations admitting a hidden-variable model," Phys. Rev. A **40**, 4277–4281 (1989).

36. I. Usmani, C. Clausen, F. Bussières, N. Sangouard, M. Afzelius, and N. Gisin, "Heralded quantum entanglement between two crystals," Nat. Photonics **6**, 234–237 (2012).

37. N. Timoney, I. Usmani, P. Jobez, M. Afzelius, and N. Gisin, "Single-photon-level optical storage in a solid-state spin-wave memory," Phys. Rev. A **88**, 022324 (2013).

38. N. Sinclair, E. Saglamyurek, H. Mallahzadeh, J. H. Slater, M. George, R. Ricken, M. P. Hedges, D. Oblak, C. Simon, W. Sohler, and W. Tittel, "Spectral multiplexing for scalable quantum photonics using an atomic frequency comb quantum memory and feed-forward control," Phys. Rev. Lett. **113**, 053603 (2014).

"Demonstration of light-matter micro-macro quantum correlations"

A. Tiranov, J. Lavoie, P. C. Strassmann, N. Sangouard, M. Afzelius, F. Bussières & N. Gisin, Phys. Rev. Lett. 116, 190502 (2016)

P H Y S I C A L   R E V I E W   L E T T E R S

Demonstration of Light-Matter Micro-Macro Quantum Correlations

Alexey Tiranov,[1] Jonathan Lavoie,[1] Peter C. Strassmann,[1] Nicolas Sangouard,[2] Mikael Afzelius,[1]
Félix Bussières,[1] and Nicolas Gisin[1]

[1]*Group of Applied Physics, University of Geneva, CH-1211 Geneva 4, Switzerland*
[2]*Department of Physics, University of Basel, CH-4056 Basel, Switzerland*
(Received 14 October 2015; published 11 May 2016)

Quantum mechanics predicts microscopic phenomena with undeniable success. Nevertheless, current theoretical and experimental efforts still do not yield conclusive evidence that there is or is not a fundamental limitation on the possibility to observe quantum phenomena at the macroscopic scale. This question prompted several experimental efforts producing quantum superpositions of large quantum states in light or matter. We report on the observation of quantum correlations, revealed using an entanglement witness, between a single photon and an atomic ensemble of billions of ions frozen in a crystal. The matter part of the state involves the superposition of two macroscopically distinguishable solid-state components composed of several tens of atomic excitations. Assuming the insignificance of the time ordering our experiment indirectly shows light-matter micro-macro entanglement. Our approach leverages from quantum memory techniques and could be used in other systems to expand the size of quantum superpositions in matter.

Quantum mechanics has been tested in many situations with a remarkably excellent agreement between theory and experiments. There remains, however, one interesting challenge, namely, to demonstrate quantum effects at larger and larger scales [1–3]. This is a timely topic, especially with the advance of quantum technologies that allow one to entangle many kinds of systems involving photons, artificial solid-state atoms, trapped ions, atomic ensembles, nanomechanical oscillators, and large molecules, to name but a few. These approaches all involve "individual" quantum systems (even though each system may be composed of a large number of particles) and should be distinguished from ensemble quantum effects such as superconductivity [4]. These individual systems offer a unique approach to study macroscopic quantum effects, which raises interesting questions: How far can entanglement hold in such systems? How can one compare different systems?

There are many approaches trying to define what constitutes a quantum superposition of macroscopic states [5–7]. The one we use is based on the distinguishability between the states forming the superposition, as formalized in Ref. [8]. More precisely, we say that two quantum states are macroscopically distinct if they can be distinguished with a detector that has a coarse-grained resolution, and we use "macroscopic" to mean "macroscopically distinguishable." This introduces some degree of arbitrariness in what should be the minimum level of coarse-graining, which reflects the challenge of defining such a measure. Instead of trying to achieve this, we use a way to compare different kinds of states to assign them an effective size, as detailed in Ref. [9]. Consequently, the number of particles (or photons) is not used to define the macroscopic nature of the superposition state. Rather, the number of particle is a property of the state that, when increasing, makes the two

components easier to distinguish with a given coarse-grained detector (and hence look more like distinct macroscopic objects). Interestingly, the more distinguishable the states become, the more challenging it is to experimentally reveal that they have quantum features (such as entanglement in a micro-macro entangled state) [8], which explains why we do not easily observe such kind of states.

Quantum optics offers a powerful approach to study the quantum features of superpositions of macroscopic states. Purely photonic experiments for example have reported on superposition of coherent states with opposite phases [10–14], squeezing [15,16], and micro-macro entanglement [17–21]. Hybrid systems have also been exploited for micro-macro entanglement where the micro part was an atom and the macro part contained up to 4 photons [22]. It was proposed to use mirror-Bose-Einstein condensate to observe macroscopic quantum superpositions between light and matter [23]. In matter, GHZ-type states have been produced with up to 14 trapped ions [24]. Here we report on the observation of quantum correlations between a single photon and an atomic ensemble containing up to 47 atomic collective excitations. We give evidence that it constitutes genuine light-matter micro-macro entanglement. Hereinafter in the article the term micro-macro entanglement is used assuming the irrelevance of the time order of the measurements. Correctness of this approximation was recently emphasized with a delayed-choice entanglement swapping experiment [25].

Our implementation, inspired from the proposal of Ref. [26] and experiments [18,19], lies within this scenario. More precisely, we start from two photons entangled in polarization and use a local displacement operation to displace, in optical phase space, one polarization mode of

one photon from the pair. The displacement populates one of the polarization modes with a large number of photons, without affecting the amount of entanglement. The displaced photon is then mapped to an atomic ensemble, creating the light-matter micro-macro entangled state.

Our experiment is conceptually represented on Fig. 1(a). First, an entangled photon pair is generated in the micro-micro state

$$|\psi\rangle = \frac{1}{\sqrt{2}}(|1,0\rangle_s|1,0\rangle_i + |0,1\rangle_s|0,1\rangle_i), \qquad (1)$$

where s and i subscripts are two modes corresponding to the generated *signal* and *idler* single photon, while $|1,0\rangle_{s(i)} \equiv |H\rangle_{s(i)}$ and $|0,1\rangle_{s(i)} \equiv |V\rangle_{s(i)}$ correspond to the horizontal polarization state of the signal (idler) photon and the vertical polarization state, respectively. To displace one of the polarization modes of s, the signal photon is superimposed with a horizontally polarized coherent state pulse (CSP) on a highly transmissive beam splitter. This corresponds to a unitary displacement operation $\mathcal{D}_H^s(\alpha)$ on the horizontal mode of the signal photon transmitted through the beam splitter [27]. The average number of photons contained in the displacement pulse is given by $|\alpha|^2$. After displacement, the state is written as

$$|\Psi\rangle = \frac{1}{\sqrt{2}}[(\mathcal{D}_H^s(\alpha)|1,0\rangle)_s|1,0\rangle_i + |\alpha,1\rangle_s|0,1\rangle_i]. \qquad (2)$$

This micro-macro entangled state (denoted with a capital Ψ for emphasis) contains a displaced single-photon state of the form $\mathcal{D}(\alpha)|1\rangle$ in the first term, and a coherent state $|\alpha\rangle = \mathcal{D}(\alpha)|0\rangle$ in the second. The idler photon plays the role of the "micro" component of the entangled state. Importantly, increasing $|\alpha|$ makes these two terms become more and more distinguishable when using a coarse-grained detector (on the signal mode) [9]. This is discussed in detail below.

We use a quantum memory (QM) protocol to coherently map the state of the signal mode to the collective state of an ensemble of neodymium atoms frozen in a crystal host [32]. This creates $\eta_{abs}|\alpha|^2$ atomic excitations on average, where η_{abs} is the absorption probability of the QM. The atomic state obtained after this linear mapping contains the atomic equivalents of the optical states $|\alpha\rangle$ and $\mathcal{D}(\alpha)|1\rangle$ [5]. These atomic states can in principle be directly distinguished using a readout technique that has an intrinsically limited microscopic resolution, as it was shown experimentally in Ref. [33]. Instead, here we analyze the reemission and infer, i.e. indirectly, the atomic state from
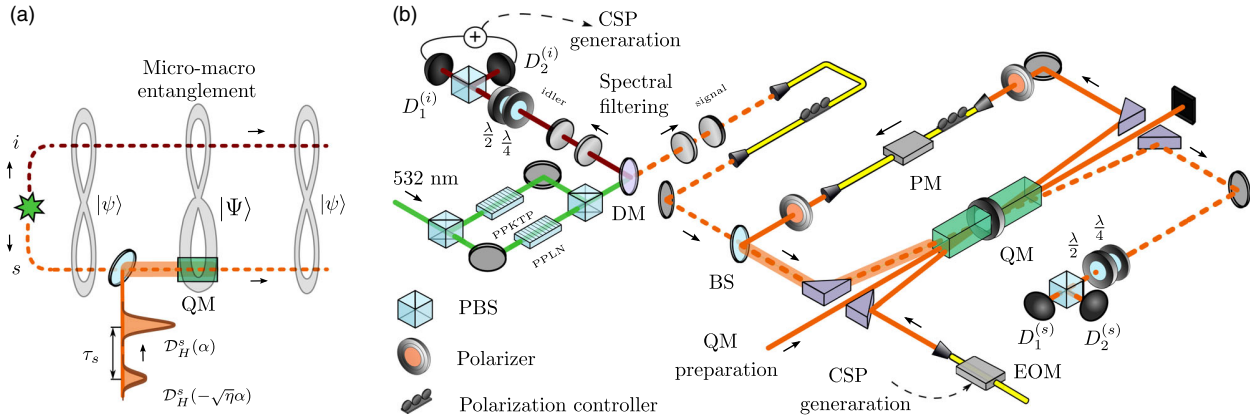

FIG. 1.   Experimental scheme. (a) Conceptual scheme for the creation and analysis of the light-matter micro-macro entangled state $|\Psi\rangle$. First, a displacement operation $\mathcal{D}_H^s(\alpha)$ is applied on the signal mode of the micro-micro polarization entangled state $|\psi\rangle$ using a beam splitter (BS) with high transmittance. The displaced signal photon of the micro-macro state $|\Psi\rangle$ is then mapped inside a solid-state quantum memory (QM) that has a storage and retrieval efficiency η. To characterize the state, it is first displaced back to $|\psi\rangle$ (in the ideal case) when it is retrieved from the memory using $\mathcal{D}_H^s(-\sqrt{\eta}\alpha)$, and is then analyzed using various entanglement witnesses. (b) Detailed setup. A polarization entangled pair of photons is created using spontaneous parametric down-conversion from two periodically poled nonlinear waveguides (PPLN and PPKTP) placed in the arms of a polarization interferometer [28] seeded by a continuous wave laser (532 nm wavelength). Dichroic mirror (DM) is used to separate two photons spatially. After the spectral filtering the idler photon is detected by one of the detectors ($D_1^{(i)}$ or $D_2^{(i)}$). This event heralds a single photon in the signal mode, and it triggers the generation of a coherent state pulse (CSP) using an electro-optical intensity modulator (EOM) that carves a pulse out of a continuous wave laser at 883 nm. The CSP is sent in the QM in a different spatial mode than the signal mode. This further allows preparing both the displacement and back-displacement pulses with the required delay and amplitudes (see text and [29] for details). The relative phase necessary for this is set by an electro-optic phase modulator (PM). The first displacement pulse $\mathcal{D}_H^s(\alpha)$ is synchronized with the heralded single photon on a BS that has a 99.5% transmittance. The resulting state $|\Psi\rangle$ is stored inside the QM and released after a predetermined time of $\tau_s = 50$ ns. The second displacement $\mathcal{D}_H^s(-\sqrt{\eta}\alpha)$ is then applied on the state retrieved from the QM. The state is analyzed, together with the idler photon previously measured, using free-space polarization analyzers composed of quarter-wave ($\lambda/4$) and half-wave ($\lambda/2$) plates followed by polarizing beam splitters (PBS).

a model using independent measurements discussed in the text. Thus, after a predetermined storage time $\tau_s = 50$ ns, the atomic state is mapped back to the optical signal mode. We note that the storage time is much shorter than the 57 μs coherence time and 300 μs lifetime of the optical transition. Hence, the collective atomic state is coherent throughout the whole process.

As part of the measurement of the light-matter entangled state, the state retrieved from the QM is first displaced back with $\mathcal{D}_H^s(-\sqrt{\eta}\alpha)$, where the amplitude is reduced by $\sqrt{\eta}$ to match the limited storage efficiency η of the QM. To achieve this, an optical pulse is sent through the QM. The timing is such that the part of this pulse that is transmitted (i.e. not absorbed) by the QM precisely overlaps with the displaced signal photon retrieved from the QM. This is equivalent to overlapping them on a beam splitter that has a limited transmittance, and thus it corresponds to a displacement operation accompanied by loss (see [29] for details). In the ideal case, the back-displacement would entirely remove the initial displacement and yield the original micro-micro optical entangled state $|\psi\rangle$. In practice, the displacement back is never perfect in amplitude and phase, which creates noise that limits the maximum size of macroscopic component that can be observed. We note that the displacement happens after the detection of the idler photon. This order could be reversed by using a pulsed laser to generate the entangled photons. The formalism of quantum mechanics indicates that this would lead to the same results as the ones observed here (see [29] for details). Under this natural assumption, our results demonstrate light-matter micro-macro entanglement.

As shown in Fig. 1(b) a 532 nm continuous wave laser is coherently pumping two nonlinear waveguides, which probabilistically creates photon pairs at 883 nm (the *signal* photon) and 1338 nm (the *idler* photon). Each photon pair is in superposition of being created in the first waveguide (with horizontal polarizations) and in the second waveguide (with vertical polarizations). Recombination of the output modes of the waveguides leads to a state that is close to the maximally entangled state (1) [28]. The spectrum of the idler photon (the signal photon) is filtered to a Lorentzian linewidth FWHM of 240 MHz (600 MHz) using the combination of a Fabry-Perot cavity (etalon) and a highly reflective volume Bragg grating (see Ref. [28] for details). Detection of the idler photon by detector $D_1^{(i)}$ or $D_2^{(i)}$ heralds a single photon in the signal mode. The detection signal is also used to generate a CSP using an electro-optical intensity modulator which carves a pulse out of a continuous wave laser at 883 nm.

The QM is based on the atomic frequency comb storage protocol [32]. To store light with an arbitrary polarization, we use a configuration consisting of two inline neodymium-doped yttrium orthosilicate crystals $Nd^{3+} : Y_2SiO_5$ separated by a half-wave plate. This configuration was previously used to faithfully store polarization qubits [34–36], to perform

light-to-matter quantum teleportation [37] and to store hyperentanglement [38]. The bandwidth of the prepared QM is 600 MHz and it stores photons for 50 ns with an overall efficiency of $\eta = 4.6(2)\%$. The back-displacement operation is performed with an interference visibility of 99.85%, which is remarkably close to being perfect; this is crucial to maximize the size of the displacement.

To quantify how much of the light contained in the displacement pulse is actually displacing the single photon, we must evaluate to what extent their modes are indistinguishable [9]. This was done using Hong-Ou-Mandel interference and measured a visibility of 74% compared to 85% expected (see [29] for details).

To reveal quantum correlations in the light-matter micro-macro state, we use two methods: the violation of a Clauser-Horne-Shimony-Holt (CHSH) Bell inequality [39] and quantum state tomography.

We first performed the CHSH test without any displacement operations and obtained a parameter $S = 2.59(3)$, which is above the local bound of 2 by 20 standard deviations. This was then repeated with an increasing displacement size $|\alpha|^2$. The results shown on Fig. 2 are in a good agreement with a theoretical model based on independently measured experimental parameters (see [29] for details). We note that the bases used for all CHSH tests are composed of states of even superposition of $|H\rangle$ and $|V\rangle$. A value of $S = 2.099(31)$ is obtained for a displacement containing a mean photon number of $|\alpha|^2 = 13.3(3)$ before mapping the state in the QM. Using the absorption probability $\eta_{\mathrm{abs}} \approx 55\%$, this corresponds to about 7 excited atoms (see [29] for details). Interestingly, violating the
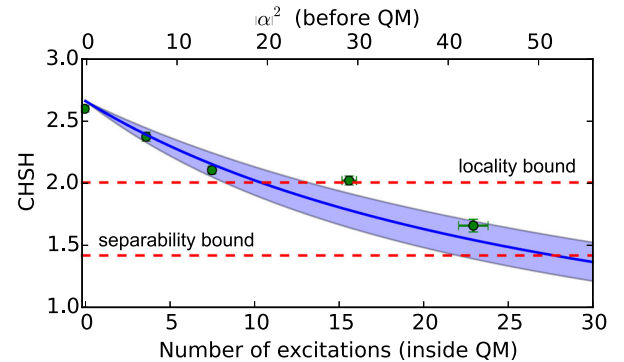
FIG. 2. Measured values of the S parameter of the CHSH-Bell inequality (dots) as a function of the size of the displacement before the QM (top x axis) or as a function of the average number of atomic excitations inside the QM (bottom x axis). CHSH violation values are above the local bound with up to 7 excitations on average, and above the entanglement bound with up to 23 excitations on average. The error bars are estimated assuming Poisson statistics for the detections. The solid line is obtained from a theoretical model based on independently measured parameters, and the shaded area represents a one standard-deviation uncertainty on the predictions of the model.

CHSH inequality shows that the light-matter micro-macro state could lead to the strongest form of quantum correlations, namely, nonlocal correlations. Alternatively, the Bell inequality can be used as an entanglement witness if we find $S \geq \sqrt{2} \approx 1.41$ [40]. We measured $S = 1.65(5)$ with a mean photon number of $|\alpha|^2 = 42(2)$ before the QM, corresponding to ≈ 23 excited atoms inside the QM. This is above the separability bound by 4 standard deviations.

To fully characterize the entanglement of the retrieved micro-micro quantum state, we performed an overcomplete set of tomographic measurements and reconstructed the full density matrix. To prove that the state is still entangled we use two criteria, namely, the positivity under partial transposition (PPT) [41], and the concurrence (which is based on the concept of the entanglement of formation) [42]. Figure 3(a) shows results obtained for increasing the size of the displacement. A negative value of $-0.055(10)$ is obtained for the PPT test and a positive concurrence of $0.246(41)$ is obtained for displacements with $|\alpha|^2 = 86(3)$ photons before the QM. This corresponds to ≈ 47 excited atoms in the atomic ensemble. These results are in a good agreement with our theoretical model described in the SM. We attribute the scatter of the data to the fluctuations of the visibility of the back-displacement operation.

The reported light-matter state can be considered as a micro-macro entangled state for the following reason. Let us illustrate first how the size of a given state can be evaluated from the coarse-grained measure presented in Ref. [9] by focusing on the state (2), which can be rewritten as

$$[\mathcal{D}_H^s(\alpha)(|0\rangle_{sH} + |1\rangle_{sH})](|0\rangle_{sV}|1,0\rangle_i + |1\rangle_{sV}|0,1\rangle_i)$$
$$- [\mathcal{D}_H^s(\alpha)(|0\rangle_{sH} - |1\rangle_{sH})](|0\rangle_{sV}|1,0\rangle_i - |1\rangle_{sV}|0,1\rangle_i),$$

where the normalization is omitted. The state therefore involves the superposition of $\mathcal{D}_H^s(\alpha)(|0\rangle + |1\rangle)$ and $\mathcal{D}_H^s(\alpha)(|0\rangle - |1\rangle)$ in the horizontal mode of the signal photon, and one can obtain one or the other by measuring the idler photon in the basis of diagonal polarizations. Although these two components partially overlap in the photon number space, the distance between their mean photon numbers is given by $2|\alpha|$; see Fig. 3(b). For $|\alpha|^2 \gtrsim 2$, they can be distinguished with a single measurement with a probability of $\approx 91\%$ using a detector that has a perfect resolution [9]. If measured with a coarse-grained detector, this probability is reduced to 50% when the coarse graining is of the order of $|\alpha|$ or more. The effective size of the state (2) can be naturally quantified by the maximum coarse-graining σ_{max} that allows one to distinguish the two components $\mathcal{D}_H^s(\alpha)(|0\rangle + |1\rangle)$ and $\mathcal{D}_H^s(\alpha)(|0\rangle - |1\rangle)$ with a given probability P_g, where P_g should be significantly above 50% to be meaningful for a single-shot measurement. Similarly, the effective size can be evaluated by comparing the results to an archetypical state involving the superposition of $|0\rangle$ and $|N\rangle$ Fock states, where N is the smallest

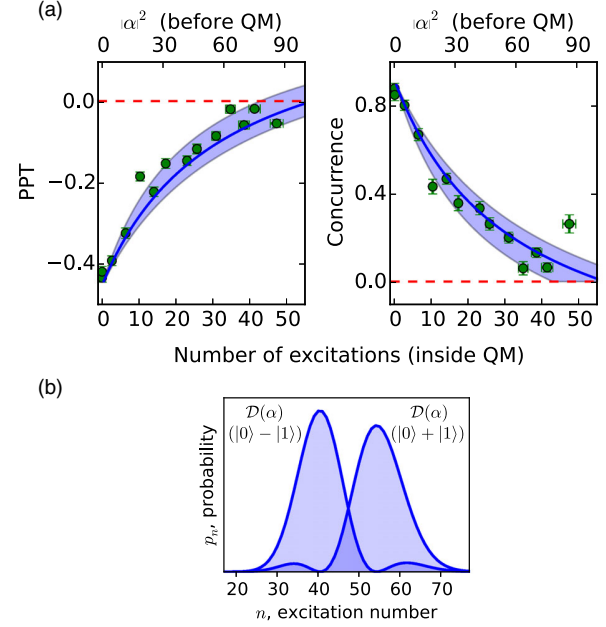FIG. 3.   Quantum state characterization. (a) PPT and concurrence values (obtained from quantum state tomography) as a function of the size of the displacement before the QM (top x axis) or as a function of the average number of atomic excitations inside the QM (bottom x axis). The error bars are estimated from Monte Carlo simulations assuming Poisson noise. The PPT criteria remains negative and the concurrence value remains positive with up to 47 excitations on average. The solid lines in all graphs are obtained from a theoretical model based on the independently measured parameters, and the shaded areas are the uncertainty on these parameters. (b) Distribution of number of atomic excitations of the two macroscopically distinguishable components $\mathcal{D}(\alpha)|1\rangle$ and $|\alpha\rangle$ when expressed in the $\{|0\rangle + |1\rangle, |0\rangle - |1\rangle\}$ basis.

value that allows distinguishing $|0\rangle$ from $|N\rangle$ with a probability P_g and a coarse graining σ_{max}. From our results, which are well reproduced by our theoretical model based on independent measurements, we can confidently give an estimate of the size of the light-matter state from which the entanglement is measured. For $P_g = 2/3$, the state is analogous to the state $|\uparrow\rangle|0\rangle + |\downarrow\rangle|N\rangle$ with $N \approx 13$, where $|\uparrow\rangle$ and $|\downarrow\rangle$ represent microscopic orthonormal states.

Naturally, one must also carefully consider the effect of loss in the signal mode before the beam splitter used for the displacement, as well as the absorption probability in the QM. In the SM we show that if the heralding probability to find the signal photon at the beam splitter is η_h and the absorption in the QM is η_{abs}, the displacement creates a mixture of the state $|\Psi\rangle$ with a displacement of amplitude $\sqrt{\eta_{abs}}\alpha$ with probability $\eta_h \eta_{abs}$, and a separable state with the complimentary probability. In our case we have $\eta_h \eta_{abs} \approx 10\%$, which makes the two macroscopic states nearly indistinguishable, even with a detector with perfect microscopic resolution. This exemplifies that the direct observation of macroscopic features is a very challenging task. Nevertheless, we stress that

the entanglement signature that we directly observe is stemming from the micro-macro state component of the mixture, whose effective size is defined as above. The observation of this entanglement, and its behavior with increasing size, is the main result of this Letter. The direct observation of the size of the superposition with an actual coarse-grained detector is left for future work. This would require reduced loss and a highly efficient quantum memory. Achieving this is certainly conceivable, given the large storage efficiencies that can now be obtained with some quantum memories [43] and with the progress of linear detectors to achieve subshot-noise resolution (e.g. see [44]). Homodyne detection could also prove useful for distinguishing the states, as demonstrated in Ref. [19]. Overall, our approach could certainly be improved with other types of quantum memory, which has the potential to yield larger quantum superpositions in matter.

[1] M. Brune, E. Hagley, J. Dreyer, X. Maître, A. Maali, C. Wunderlich, J. M. Raimond, and S. Haroche, Phys. Rev. Lett. **77**, 4887 (1996).
[2] D. Leibfried, E. Knill, S. Seidelin, J. Britton, R. B. Blakestad, J. Chiaverini, D. B. Hume, W. M. Itano, J. D. Jost, C. Langer, R. Ozeri, R. Reichle, and D. J. Wineland, Nature (London) **438**, 639 (2005).
[3] M. Arndt and K. Hornberger, Nat. Phys. **10**, 271 (2014).
[4] A. J. Leggett, Prog. Theor. Phys. Suppl. **69**, 80 (1980).
[5] F. Fröwis, N. Sangouard, and N. Gisin, Opt. Commun. **337**, 2 (2015).
[6] H. Jeong, M. Kang, and H. Kwon, Opt. Commun. **337**, 12 (2015).
[7] T. Farrow and V. Vedral, Opt. Commun. **337**, 22 (2015).
[8] P. Sekatski, N. Gisin, and N. Sangouard, Phys. Rev. Lett. **113**, 090403 (2014).
[9] P. Sekatski, N. Sangouard, and N. Gisin, Phys. Rev. A **89**, 012116 (2014).
[10] A. Ourjoumtsev, R. Tualle-Brouri, J. Laurat, and P. Grangier, Science **312**, 83 (2006).
[11] J. S. Neergaard-Nielsen, B. M. Nielsen, C. Hettich, K. Mølmer, and E. S. Polzik, Phys. Rev. Lett. **97**, 083604 (2006).
[12] K. Wakui, H. Takahashi, A. Furusawa, and M. Sasaki, Opt. Express **15**, 3568 (2007).
[13] A. Ourjoumtsev, H. Jeong, R. Tualle-Brouri, and P. Grangier, Nature (London) **448**, 784 (2007).
[14] B. Vlastakis, G. Kirchmair, Z. Leghtas, S. E. Nigg, L. Frunzio, S. M. Girvin, M. Mirrahimi, M. H. Devoret, and R. J. Schoelkopf, Science **342**, 607 (2013).
[15] T. Eberle, V. Händchen, and R. Schnabel, Opt. Express **21**, 11546 (2013).
[16] F. A. Beduini, J. A. Zielińska, V. G. Lucivero, Y. A. de Icaza Astiz, and M. W. Mitchell, Phys. Rev. Lett. **114**, 120402 (2015).
[17] F. De Martini, F. Sciarrino, and C. Vitelli, Phys. Rev. Lett. **100**, 253601 (2008).
[18] N. Bruno, A. Martin, P. Sekatski, N. Sangouard, R. T. Thew, and N. Gisin, Nat. Phys. **9**, 545 (2013).
[19] A. I. Lvovsky, R. Ghobadi, A. Chandra, A. S. Prasad, and C. Simon, Nat. Phys. **9**, 541 (2013).
[20] H. Jeong, A. Zavatta, M. Kang, S.-W. Lee, L. S. Costanzo, S. Grandi, T. C. Ralph, and M. Bellini, Nat. Photonics **8**, 564 (2014).
[21] O. Morin, K. Huang, J. Liu, H. Le Jeannic, C. Fabre, and J. Laurat, Nat. Photonics **8**, 570 (2014).
[22] S. Deléglise, I. Dotsenko, C. Sayrin, J. Bernu, M. Brune, J.-M. Raimond, and S. Haroche, Nature (London) **455**, 510 (2008).
[23] F. De Martini, F. Sciarrino, C. Vitelli, and F. S. Cataliotti, Phys. Rev. Lett. **104**, 050403 (2010).
[24] T. Monz, P. Schindler, J. T. Barreiro, M. Chwalla, D. Nigg, W. A. Coish, M. Harlander, W. Hänsel, M. Hennrich, and R. Blatt, Phys. Rev. Lett. **106**, 130506 (2011).
[25] X.-S. Ma, S. Zotter, J. Kofler, R. Ursin, T. Jennewein, Č. Brukner, and A. Zeilinger, Nat. Phys. **8**, 479 (2012).
[26] P. Sekatski, N. Sangouard, M. Stobińska, F. Bussières, M. Afzelius, and N. Gisin, Phys. Rev. A **86**, 060301 (2012).
[27] M. G. Paris, Phys. Lett. A **217**, 78 (1996).
[28] C. Clausen, F. Bussières, A. Tiranov, H. Herrmann, C. Silberhorn, W. Sohler, M. Afzelius, and N. Gisin, New J. Phys. **16**, 093058 (2014).
[29] See Supplemental Material at http://link.aps.org/supplemental/10.1103/PhysRevLett.116.190502, which includes Refs. [30–31].
[30] V. Caprara Vivoli, P. Sekatski, J.-D. Bancal, C. C. W. Lim, B. G. Christensen, A. Martin, R. T. Thew, H. Zbinden, N. Gisin, and N. Sangouard, Phys. Rev. A **91**, 012107 (2015).
[31] V. C. Vivoli, P. Sekatski, J.-D. Bancal, C. C. W. Lim, A. Martin, R. T. Thew, H. Zbinden, N. Gisin, and N. Sangouard, New J. Phys. **17**, 023023 (2015).
[32] M. Afzelius, C. Simon, H. de Riedmatten, and N. Gisin, Phys. Rev. A **79**, 052329 (2009).
[33] S. L. Christensen, J.-B. Béguin, E. Bookjans, H. L. Sørensen, J. H. Müller, J. Appel, and E. S. Polzik, Phys. Rev. A **89**, 033801 (2014).
[34] C. Clausen, F. Bussières, M. Afzelius, and N. Gisin, Phys. Rev. Lett. **108**, 190503 (2012).
[35] M. Gündoğan, P. M. Ledingham, A. Almasi, M. Cristiani, and H. de Riedmatten, Phys. Rev. Lett. **108**, 190504 (2012).
[36] Z.-Q. Zhou, W.-B. Lin, M. Yang, C.-F. Li, and G.-C. Guo, Phys. Rev. Lett. **108**, 190505 (2012).
[37] F. Bussières, C. Clausen, A. Tiranov, B. Korzh, V. B. Verma, S. W. Nam, F. Marsili, A. Ferrier, P. Goldner, H. Herrmann, C. Silberhorn, W. Sohler, M. Afzelius, and N. Gisin, Nat. Photonics **8**, 775 (2014).
[38] A. Tiranov, J. Lavoie, A. Ferrier, P. Goldner, V. B. Verma, S. W. Nam, R. P. Mirin, A. E. Lita, F. Marsili, H. Herrmann, C. Silberhorn, N. Gisin, M. Afzelius, and F. Bussières, Optica **2**, 279 (2015).

[39] J. F. Clauser, M. A. Horne, A. Shimony, and R. A. Holt, Phys. Rev. Lett. **23**, 880 (1969).

[40] S. M. Roy, Phys. Rev. Lett. **94**, 010402 (2005).

[41] A. Peres, Phys. Rev. Lett. **77**, 1413 (1996).

[42] S. Hill and W. K. Wootters, Phys. Rev. Lett. **78**, 5022 (1997).

[43] F. Bussières, N. Sangouard, M. Afzelius, H. de Riedmatten, C. Simon, and W. Tittel, J. Mod. Opt. **60**, 1519 (2013).

[44] T. Gerrits, B. Calkins, N. Tomlin, A. E. Lita, A. Migdall, R. Mirin, and S. W. Nam, Opt. Express **20**, 23798 (2012).

Supplemental Material to "Demonstration of light-matter micro-macro quantum correlations"

Alexey Tiranov[1], Jonathan Lavoie[1], Peter C. Strassmann[1], Nicolas
Sangouard[2], Mikael Afzelius[1], Félix Bussières[1], and Nicolas Gisin[1]
[1]*Group of Applied Physics, University of Geneva, CH-1211 Geneva 4, Switzerland and*
[2]*Department of Physics, University of Basel, CH-4056 Basel, Switzerland*
(Dated: April 15, 2016)

In this Supplemental Material, we provide details on our experiment and we describe the theoretical model. Section I describes the details of the implementation of the displacement operations. Section II presents the Hong-Ou-Mandel dip experiment to prove the indistinguishability of the heralded single photon and the coherent state pulse. Section III presents two theoretical models to compare to our experimental results.

I. IMPLEMENTATION OF THE DISPLACEMENT OPERATION

Displacement with an arbitrary polarization state

Here we show that the polarization state of the displacement pulse can be arbitrary without changing the description of our experiment. Let us consider the case where the polarization of the displacement is expressed as $|\psi\rangle = \alpha|H\rangle + \beta|V\rangle$. The displacement is applied to $\frac{1}{\sqrt{2}}\left(|H\rangle_s|H\rangle_i + e^{i\theta}|V\rangle_s|V\rangle_i\right)$. We note that

$$\frac{1}{\sqrt{2}}\left(|H\rangle_s|H\rangle_i + e^{i\theta}|V\rangle_s|V\rangle_i\right)$$
$$= \frac{1}{\sqrt{2}}\left(|\psi\rangle_s|\phi\rangle_i + e^{i\theta}|\psi^\perp\rangle_s|\phi^\perp\rangle_i\right), \qquad (1)$$

where $|\phi\rangle = \alpha^*|H\rangle + e^{i\theta}\beta^*|V\rangle$, $\langle\phi|\phi^\perp\rangle = \langle\psi|\psi^\perp\rangle = 0$. We see directly that a displacement with polarization $|\psi\rangle$ will produce a state equivalent to displacing $\frac{1}{\sqrt{2}}\left(|H\rangle_s|H\rangle_i + e^{i\theta}|V\rangle_s|V\rangle_i\right)$ with a horizontal polarization.

Displacement with a quantum memory

Here we explain how the quantum memory (QM) can be used to realize the displacement operations. For our purpose, the QM can be seen as a storage loop. As shown on Fig. 1a, light incident on the QM is either absorbed with probability $\eta_{\rm abs} \approx 55\%$ or transmitted with probability $1 - \eta_{\rm abs}$. This is physically equivalent to a beam splitter whose outputs are the directly transmitted optical mode and the atomic mode onto which light is linearly mapped to a collective atomic state [1].

The AFC storage protocol that we use is such that the re-emission process occurs when all the spectral components of the collective atomic state are in phase, which

(a)

(b)
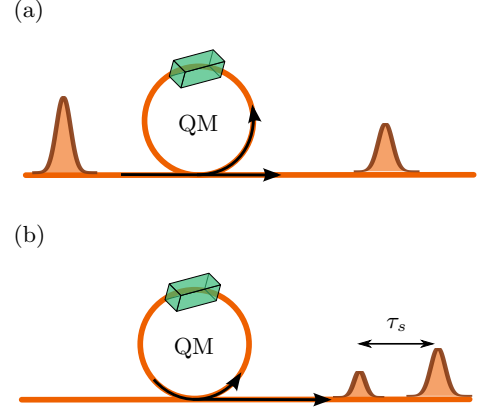
FIG. 1. Quantum memory represented as a storage loop. For our purpose, the AFC quantum memory can be seen as a light-matter beam splitter that loops back onto itself, and the length of the loop corresponds to the storage time τ_s of the QM. (a) When an optical pulse is incident on the QM, it acts like a beam splitter that splits the light on a optically transmitted part and onto the collective state of the atomic ensemble. (b) At the time of re-emission, the QM acts again like a beam splitter that maps the collective atomic state to the optical mode and back onto itself. The number of photons re-emitted is thus accompanied by the corresponding reduction in the number of atomic excitations in the QM.

in our case happens at $\tau_s = 50$ ns after absorption [1]. However, this rephasing is not perfect, and therefore only part of the atomic excitations are converted back to light. In the storage loop representation, the atomic mode is looped back onto the "light-matter" beam splitter after the storage time (see Fig. 1b), albeit with a beam splitting ratio that is different than the one of the absorption process, which is due to the details leading to the rephasing.

To realize a near-perfect back displacement operation one has to achieve the lowest phase and amplitude noise between the two displacements. This is especially difficult to realize with free-space optics for long delays such as 50 ns. However, we note that the QM itself can be used to create the two pulses; see Fig. 2. First, the coherent state pulse (CSP), created whenever an idler photon is detected, is sent through the QM in a spatial mode that is distinct from the one of the signal photon. This creates two pulses delayed by the storage time of the QM ($\tau_s = 50$ ns). The pulses then go through a fibre-
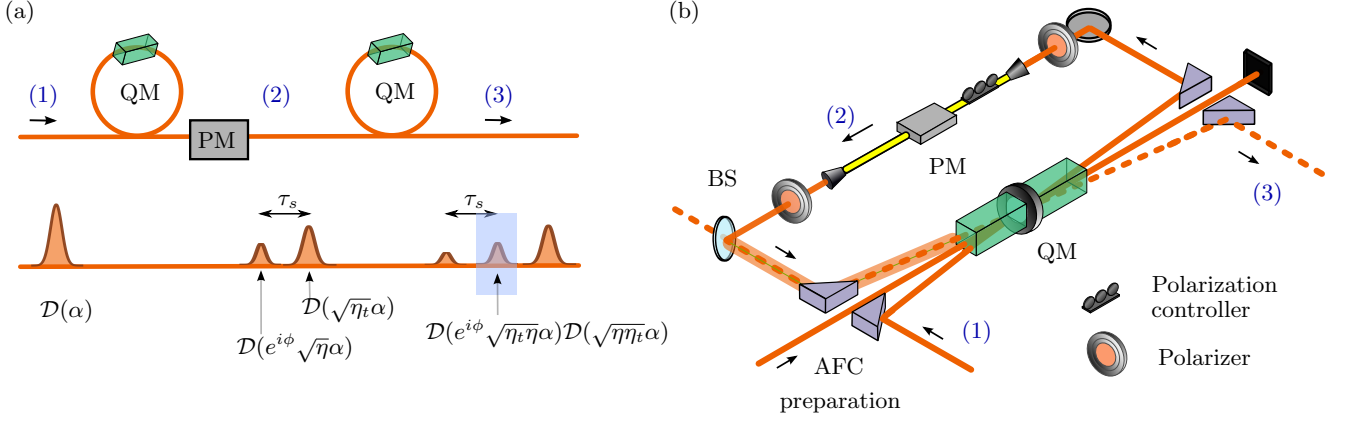
FIG. 2. (a) presents the conceptual evolution of the pulses used for the displacements, and (b) shows how it was implemented. (1) A coherent state pulse is generated by the detection of the idler photon. It corresponds to the displacement $\mathcal{D}(\alpha)$ applied on vacuum. This pulse is incident on the QM in an optical mode that is distinct from the one used to store the signal mode. (2) After the QM and the phase modulator (PM), we obtain two pulses corresponding to the displacements $\mathcal{D}(\sqrt{\eta_t}\alpha)$ and $\mathcal{D}(e^{i\phi}\sqrt{\eta}\alpha)$, where η_t and η are the transmission probability and storage efficiency of the QM, respectively, and ϕ is the phase applied on the second pulse by the PM. (3) After the second passage through the QM, we have three pulses. The middle one corresponds to the displacement $\mathcal{D}(e^{i\phi}\sqrt{\eta_t\eta}\alpha)\mathcal{D}(\sqrt{\eta\eta_t}\alpha)$, and is the one that is applied on the displaced signal photon retrieved from the QM. We see that the amplitudes are perfectly balanced, and setting $\phi = \pi$ will yield destructive interference, which constitutes the back displacement.

pigtailed electrooptic phase modulator (PM) applying a phase of $\phi = \pi$ on the second one. The first displacement operation is performed by combining the heralded signal photon and the first component of the optical signal emerging from the PM. For this we use a non polarizing beam splitter with a transmittance $T = 99.5\%$, resulting in a lossless displacement operation. The back displacement operation corresponds to the interference between the part of the second pulse emerging from the PM that is directly transmitted by the QM, and the part of the atomic excitation that is converted into the optical mode. Because the probability to map the atomic state into the optical state is smaller than 100%, this corresponds to a displacement operation with some loss into the atomic mode. To quantify the quality of the back displacement, we measured the visibility of the interference between the two displacements with the signal photon blocked. We obtained an average visibility of 99.85(2)%, which is very close to being perfect.

To create a representative theoretical model of our experiment, we characterized the polarization of the light that is remaining after back displacement operation. For this the photon pair source was blocked and polarization state tomography was performed on the weak coherent state. We expected to find a pure polarization state, because the remaining light is expected to comes from the well polarized CSP. Surprisingly, we found that the polarization state is almost completely depolarized, having a fidelity of 97(1)% with completely depolarized state. This indicates that the limit to the visibility of the back displacement is at least partly due to some process that we could not identify. This will require further investigation.

Effect of loss

We now describe the effect of loss in our experiment. The first loss to consider is the heralding efficiency η_h, which is the probability to find the heralded signal photon at the beam splitter used for the displacement. If the photon is lost, the displacement pulse is applied on vacuum $|0\rangle$ rather than on $|1\rangle$. In this case, the state ρ created is a mixture of the desired micro-macro entangled state $|\Psi\rangle = \mathcal{D}_H^s(\alpha)|\psi\rangle$, where

$$|\psi\rangle = \frac{1}{\sqrt{2}}(|1,0\rangle_s|1,0\rangle_i + |0,1\rangle_s|0,1\rangle_i),$$

$$|\Psi\rangle = \frac{1}{\sqrt{2}}\left[(\mathcal{D}_H^s(\alpha)|1,0\rangle)_s|1,0\rangle_i + |\alpha,1\rangle_s|0,1\rangle_i\right],$$

with a separable component:

$$\rho = \eta_h|\Psi\rangle\langle\Psi| + (1-\eta_h)|\alpha,0\rangle_s\langle\alpha,0| \otimes \frac{\mathbb{I}_i}{2} \qquad (2)$$

where $\mathbb{I}_i$ is the 2×2 identity matrix representing a completely mixed polarization for the idler photon.

The loss caused by the finite absorption probability in the QM then reduces the size of the displacement and create another separable component to the mixture. Using η_{abs} and $\eta_t = 1 - \eta_{abs}$ to denote the absorption and transmission probabilities, one can show that the light-matter entangled state obtained is

$$\rho' = \eta_{abs}\eta_h\mathcal{D}_H^s(\sqrt{\eta_{abs}}\alpha)|\psi\rangle\langle\psi|\mathcal{D}_H^{s\,\dagger}(\sqrt{\eta_{abs}}\alpha)$$
$$+ (1-\eta_h\eta_{abs})|\sqrt{\eta_{abs}}\alpha,0\rangle_s\langle\sqrt{\eta_{abs}}\alpha,0| \otimes \frac{\mathbb{I}_i}{2}. \quad (3)$$

The first term corresponds to the desired light-matter micro-macro entangled state, where the amplitude of the
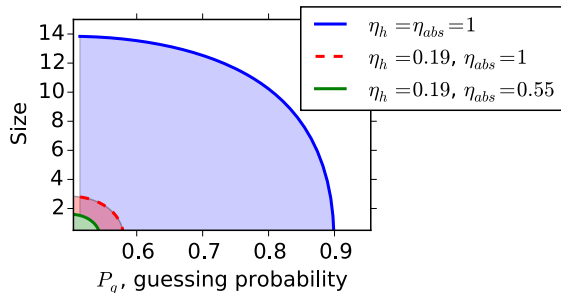
FIG. 3. Size of the light-matter entangled states ρ' (Eq. 3) with $|\alpha|^2 = 47$ atomic excitations on average as a function of the guessing probability P_g to distinguish two macroscopic components of state ρ' for different values of η_h and η_{abs}.

displacement is given by $\eta_{abs}|\alpha|^2$. The other term is separable, and do not contribute to detected signature of entanglement. Rather, they create noise that masks the entanglement signature, which reduces the maximum size of the displacement that we can apply.

One can consider how the loss would affect our ability to directly observe the distinguishability of the macroscopic states of the superposition using a coarse-grained detector. On Fig. 3 we show how loss affects the effective size of the superposition in the cases $\eta_h = 1$ (no loss), $\eta_h = 0.19$ (before the QM) and $\eta_h = 0.19$ with $\eta_{abs} = 0.55$ (inside the QM). The loss and finite absorption probabilities reduce the maximum probability to distinguish the two macroscopic states to a value that is $\approx 53\%$ with a detector that has a perfect single-photon resolution. This exemplifies that the direct observation of the distinguishability of the macroscopic components requires maximizing η_h and η_{abs}, which is a challenging but conceivable task for future work.

Double detection events

We note that in all of our measurements, the probability to detect two photons in the signal mode was at least fifty times smaller than detecting a single photon (which was obtained for the case of 47 atomic excitations). Hence, double detection events could essentially be ignored.

Ordering of detection times

Although the displacement of the signal mode happens after the detection of the idler mode, we here show that this does not prevent us to report on micro-macro light-matter entanglement. All along the manuscript, the optical modes are described through their polarizations. For example $|1,0\rangle_s$ means that the signal mode is filled with one horizontal photon. In order to specify all the degrees of freedom that are relevant for our observables, we can add the information about the detection time. With this

additional information, the state that is ideally detected is given by

$$|1_{t_\ell}, 0_{t_e}\rangle_s |1_{t_e}, 0_{t_e}\rangle_i + |1_{t_\ell}, 0_{t_e}\rangle_s |1_{t_e}, 0_{t_e}\rangle_i \tag{4}$$

where the subscript t_e (t_ℓ) clarifies on the detection of the idler (signal) at an early (late) time. Going backward in time when the signal mode is displaced in phase space, we get

$$[\mathcal{D}_H^s(|0_{t_s}\rangle_{sH} + |1_{t_s}\rangle_{sH})] \tag{5}$$
$$\otimes (|0_{t_s}\rangle_{sV}|1_{t_e}, 0_{t_e}\rangle_i + |1_{t_s}\rangle_{sV}|0_{t_e}, 1_{t_e}\rangle_i)$$
$$-[\mathcal{D}_H^s(|0_{t_s}\rangle_{sH} - |1_{t_s}\rangle_{sH})]$$
$$\otimes (|0_{t_s}\rangle_{sV}|1_{t_e}, 0_{t_e}\rangle_i - |1_{t_s}\rangle_{sV}|0_{t_e}, 1_{t_e}\rangle_i).$$

Defining t_s as the time at which the signal mode is stored in the crystal, the state (5) corresponds to micro-macro light-matter entanglement. Even if the state (4) is not a faithful description of the state obtained experimentally due to noise and loss, the measurement results show unambiguously that the polarization of the idler mode at an early time is entangled with the polarization of the signal mode at a late time. Since the storage protocol is a local operation, entanglement was there before the signal mode was released, i.e. between the idler mode and the doped crystal. We emphasize that the macroscopic character of this light-matter entangled state is inferred by a detailed model of the experimental setup that is validated by independent measurements, c.f. below.

II. HONG-OU-MANDEL INTERFERENCE

To probe for the indistinguishability between the heralded single photon (HSP) and the coherent state pulse (CSP), a Hong-Ou-Mandel (HOM) type interference experiment was performed. This characterization is important to determine the size of the displacement. The reason is simple: if the displacements are not applied on the mode of the HSP, then the single photon is not displaced at all. The case where the modes of the CSP and HSP overlap only partially was theoretically considered in Ref. [3], where it is shown that the ratio $R = V_m/V_e$ between measured V_m and expected V_e HOM visibilities gives a lower bound on the fraction of the CSP that actually displaces the HSP. Hence, if the size of the CSP is $|\alpha|^2$, then the size of the displacement is $R|\alpha|^2$.

In our case, the main mismatch between the modes of the CSP and HSP is due to their temporal modes; see Fig. 4. The mode of the HSP is determined by the energy correlation between the signal and idler photons, combined with filtering bandwidths used in the source of entanglement; see details in Ref. [4]. The CSP has an almost Gaussian temporal profile, which is defined by the high speed pulse generator used to drive the electrooptic EOM that is carving the pulse out of a continuous wave laser at 883 nm. For comparison, the temporal modes of the CSP and the HSP are shown in Fig. 4.
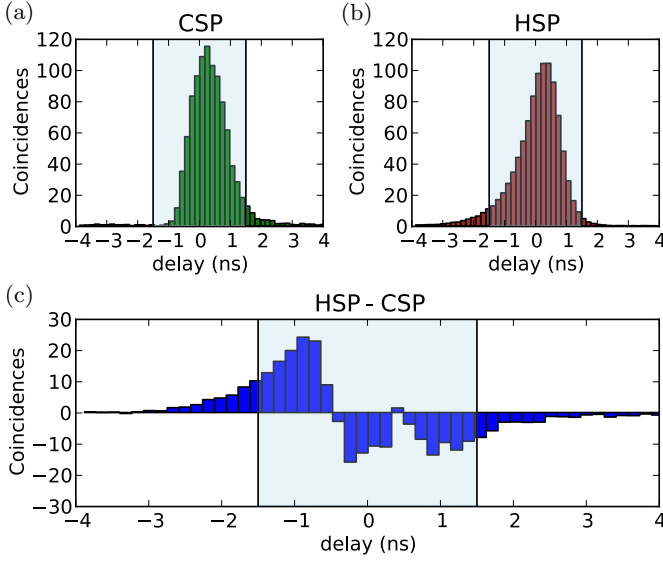
FIG. 4. Temporal profiles of the CSP and HSP. (a) Temporal mode of the coherent state pulse (CSP) shaped from CW laser using electro-optical modulator (EOM). (b) Temporal profile of the heralded single photon (HSP). (c) Difference between two histograms corresponding to the CSP and HSP, where each histogram was normalized. A coincidence window of 3 ns (shaded regions) was used for further analysis.
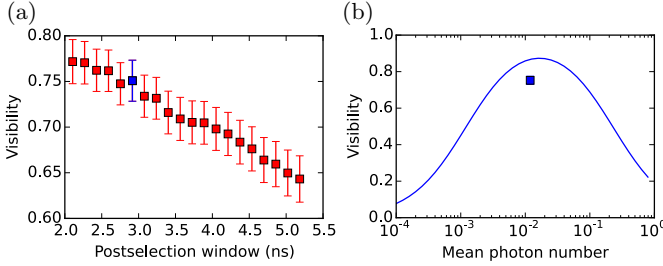

FIG. 5. Hong-Ou-Mandel dip measurement between HSP and CSP. (a) Measured visibility V_{m} of the HOM dip as a function of coincidence window. A window of 3 ns was used during the experiment. The visibility goes down as one increases the postselection window due to the lower overlap between the temporal modes of HSP and CSP. (b) Comparison between experimentally measured visibility of HOM dip (square) and theoretical model (solid line). The mean photon number of the CSP was 0.012(1) and the creation probability of the photon pair was 0.005, while the heralding efficiency was equal to 19%. Since the photon number statistics of HSP and CSP are different the maximum visibility of HOM dip between them for the given photon pair creation probability can be obtained only for certain mean photon number μ of the CSP. The visibility for the low μ of the CSP is limited by the multi photon creation from the photon pair source while for the high μ the higher terms of Poisson distribution of the CSP will reduce the maximum visibility [2].

To measure the HOM dip visibility, the HSP and CPS are combined on a 50/50 beam splitter and synchronized in time. To extract the visibility of the HOM dip, we measure the coincidence rate with the polarization of the CPS either parallel $R_{\parallel}$ or perpendicular $R_{\perp}$ to the HSP. The measured visibility is given by $V_{\mathrm{m}} = (R_{\perp} - R_{\parallel})/R_{\perp}$. This value depends on the temporal width of the coincidence window. This is because using a short window compared to the width of the temporal modes erases differences between them, which increases their indistinguishability, but it also reduces η_h and the detection rate. The value of the measured visibility as a function of the width of the coincidence window is shown in Fig. 5a. A tradeoff value was chosen with a coincidence window of 3 ns, which yielded an heralding efficiency of $\eta_h = 0.19$.

The expected visibility V_{e} is calculated taking into account the heralding efficiency, the photon pair creation probability $p = 5 \times 10^{-3}$ inside the coincidence time window of 3 ns, as a function of the mean photon number contained in the CSP. The result of this calculation is shown on Fig. 5b. For the value $|\alpha|^2 = 0.012$ used with the 3 ns window on Fig. 5a, the expected visibility is $V_{\mathrm{e}} = 85\%$. The measured visibility is $V_{\mathrm{m}} = 74(2)\%$, which shows that we do not have perfect overlap between the HSP and CSP. The difference is due partly to the imperfect spectral-temporal modes overlap between two waveforms, and also to the fluctuations on the central frequency of the HSP, which is due to the small fluctuations on frequency of the pump laser at 532 nm (the latter are caused by the frequency stabilization mechanism that we need to apply to get frequency correlated photons, see [4]).

The measured ratio $R = 0.74/0.85 = 87\%$ is used to correct the size of the displacements that are presented in this work.

III. THEORETICAL MODEL OF THE EXPERIMENT

Simple theoretical model

Here we derive a simple theoretical model to compare to our experimental results. First, we include in our description that actual micro-micro entangled state ρ_{mm} (obtained without any displacement) is itself not an ideal pure state, but can rather be approximated by the Werner state

$$\rho_{mm} = V_{mm}|\psi\rangle\langle\psi| + (1 - V_{mm})\frac{\mathbb{I}}{4} \qquad (6)$$

where $\mathbb{I}$ is the 4×4 identity matrix, and $V_{mm} \approx 94\%$ is the entanglement visibility of the micro-micro entangled state. Next, to include the contribution of the displacement in our description, we recall that we found that light remaining after the imperfect back displacement was almost entirely depolarized. Hence, the actual state ρ'_{mm} emerging from the QM can be seen, at first approximation, as a mixture of ρ_{mm} (obtained when the signal photon was not lost) and the completely mixed

two-qubit state obtained when the signal photon is replaced with a completely mixed polarization photon. We have

$$\rho'_{mm} = (1 - \epsilon)\rho_{mm} + \epsilon \frac{\mathbb{I}}{4}$$
$$= V_{mm}(1 - \epsilon)|\psi\rangle\langle\psi| + [1 - V_{mm}(1 - \epsilon)]\frac{\mathbb{I}}{4} \quad (7)$$

where we denote ϵ as the noise probability.

We then need to properly model ϵ as a function of independently measured experimental parameters. Assuming the interference visibility V between two displacements operations, one can calculate ϵ assuming a Poisson photon number statistics. On the one hand, the probability to detect a photon from the noisy background is proportional to

$$p_n = \mathrm{e}^{-\mu}\sum_{n=1}^{\infty}\frac{\mu^n}{n!}\left[1 - (1 - 2\eta(1 - V))^n\right], \quad (8)$$

where η is the efficiency of the quantum memory and μ is the mean photon number in the back displacement operation. On the other hand, the probability that no photon (other than the heralded signal photon) leaks out of the QM after the back displacement is

$$\bar{p}_n = \mathrm{e}^{-\mu}\sum_{n=1}^{\infty}\frac{\mu^n}{n!}\left[1 - 2\eta(1 - V)\right]^n. \quad (9)$$

Finally, the probability to detect the heralded signal photon while no photon from the noisy background leaks out is proportional to

$$p_s = \eta_h T \eta \bar{p}_n, \quad (10)$$

where $\eta_h = 0.19$ is the heralding efficiency of the signal photon and $T = 99.5\%$ is the transmission of the first beam-splitter. Using these definitions, the noise probability ϵ of the Werner state (7) can be expressed as

$$\epsilon = \frac{p_n}{p_s + p_n}. \quad (11)$$

Using the independently measured parameters $\eta_h = 19(2)\%$, $T = 99.5\%$, $\eta = 4.6(2)\%$, $V = 99.85(2)\%$ and $V_{mm} = 94\%$, we can estimate the expected S-parameter value for the CHSH violation as a function of the size of the displacement. We can also predict the values for the PPT criterion and the value of the concurrence (Fig. 2 and 3 of the main text).

Detailed theoretical model

Here we derive a more detailed model for predicting the expected value of the CHSH S parameter, which can be compared with the result of the simple model. We show that both models produce essentially the same results, and they both correspond very well with our experimental results. This strengthens our claim.

This model starts with a description of the spontaneous parametric down conversion source which produces photons in coupled modes, labelled by the bosonic operators a and b. The photons are created in maximally entangled states in polarization, meaning that each mode splits into two orthogonal polarizations $a - a_\perp$ and $b - b_\perp$. The Hamiltonian of such a process is $\mathcal{H} = i\chi(a^\dagger b_\perp^\dagger - a_\perp^\dagger b^\dagger + \mathrm{h.c})$, where χ is proportional to the non-linear susceptibility of the crystal and to the power of the pump. The expression of the corresponding state $|\psi\rangle$ is obtained by applying $e^{-i\mathcal{H}t}$ on the vacuum $|\underline{0}\rangle$, as we are focusing on spontaneous emissions (0 is underlined to indicate that all modes are in the vacuum). It can be written as [5]

$$|\psi\rangle = \left(1 - T_g^2\right)e^{T_g a^\dagger b_\perp^\dagger}e^{T_g a_\perp^\dagger b^\dagger}|\underline{0}\rangle, \quad (12)$$

where $T_g = \tanh g$, $g = \chi t$ being the squeezing parameter.

For the detectors, we used non-photon number resolving detectors with non-unit efficiency η and dark count probability p_{dc}. The no-click event for the mode a for example, is associated to a positive operator [5]

$$D_{\mathrm{nc}}^a = (1 - p_{\mathrm{dc}})(1 - \eta)^{a^\dagger a}, \quad (13)$$

while the click event corresponds to $D_{\mathrm{c}}^a = \mathbb{1} - D_{\mathrm{nc}}^a$.

We now calculate the conditional state in modes b, $b_\perp$ once the modes a, $a_\perp$ are detected. Note first that the structure of the Hamiltonian is such that we can consider that for any measurement choice, a and $a\perp$ are the eigenmodes of the measurement device. The state that is conditioned on a click in a and no click in $a_\perp$ is given by

$$\rho_{b,b_\perp} = (1 - p_{\mathrm{dc}})\mathrm{tr}_{a,a_\perp}\left((1 - \eta)^{a^\dagger a} \otimes 1_{a_\perp}|\psi\rangle\langle\psi|\right) -$$
$$- (1 - p_{\mathrm{dc}})^2\mathrm{tr}_{a,a_\perp}\left((1 - \eta)^{a^\dagger a} \otimes (1 - \eta)^{a_\perp^\dagger a^\dagger}|\psi\rangle\langle\psi|\right). \quad (14)$$

Using $x^{a^\dagger a}f(a^\dagger) = f(xa^\dagger)x^{a^\dagger a}$, we get [6]

$$\rho_{b,b_\perp} = (1 - p_{\mathrm{dc}})\frac{1 - T_g^2}{1 - T_g^2 R^2}\rho_{\mathrm{th}}^b(Tg)\rho_{th}^{b_\perp}(RT_g) -$$
$$- (1 - p_{\mathrm{dc}})^2\frac{\left(1 - T_g^2\right)^2}{\left(1 - T_g^2 R^2\right)}\rho_{\mathrm{th}}^b(RT_g)\rho_{th}^{b_\perp}(RT_g) \quad (15)$$

with $\rho_{\mathrm{th}}^b(T_g) = \left(1 - T_g^2\right)\sum_{n=0}^{+\infty}T_g^{2k}|k\rangle_b\langle k|$, $\rho_{\mathrm{th}}^{b_\perp}(RT_g) = \left(1 - (RT_g)^2\right)\sum_{n=0}^{+\infty}(RT_g)^{2k}|k\rangle_{b_\perp}\langle k|$ ... i.e. the conditional state can be written as a difference between products of thermal states.

As thermal states are classical states, they can be written as a mixture of coherence states, that is

$$\rho_{\mathrm{th}}^b(T_g) = \int d^2\gamma P^{\bar{n}}(\gamma)|\gamma\rangle_b\langle\gamma| \quad (16)$$

with $P^{\bar{n}}(\gamma) = \frac{1}{\pi \bar{n}} e^{-|\gamma|^2/\bar{n}}$ and $\bar{n} = T_g^2/(1 - T_g^2)$. The result of Bob measurements can thus be deduced from the distribution of results obtained with coherent states. In particular, a state

$$|\alpha\rangle_b \langle\alpha| \otimes |\beta\rangle_{b_\perp} \langle\beta| \qquad (17)$$

becomes

$$|\bar{\alpha} + \cos\theta M\rangle_b \langle\underbrace{\bar{\alpha} + \cos\theta M}_{\hat{\alpha}}| \otimes |\underbrace{\bar{\beta} + \cos\theta M}_{\hat{\beta}}\rangle_{b_\perp} \langle\bar{\beta} + \cos\theta M|$$

(18)

after the memory where $\bar{\alpha} = \alpha T_1 T_2 \sqrt{\eta_c}\sqrt{\eta_d}$ (similarly for $\bar{\beta}$) accounts for the transmission of the beamsplitter used for the displacement operation, η_c for the coupling efficiency and... $M = iT_2\gamma\phi$ where γ^2 is the size of the displacement and ϕ is the error on the relative phase between the two displacements. It is averaged out with gaussian noise to account for the limited accuracy of our back displacement operation. θ accounts for the angle between the measurement setting of Alice and the polarization of the laser used to implement the displacement operation. For Bob's measurement setting with eigenmodes $b^{\theta'} = \cos\theta' b + \sin\theta' b_\perp$ and $b_\perp^{\theta'} = \sin\theta' b - \cos\theta' b_\perp$, the probability to get no click in $b^{\theta'}$ and one click in $b_\perp^{\theta'}$ with the state (18) is given by

$$\mathrm{tr}_{b^{\theta'},b_\perp^{\theta'}} \left[(1-\eta_d)^{b^{\theta'\dagger},b^{\theta'}} \otimes (1 - (1-\eta_d)^{b^{\theta'\dagger},b^{\theta'}}) \right.$$
$$\left| \cos\theta'\hat{\alpha} + \sin\theta'\hat{\beta} \right\rangle_{b'} \left\langle \cos\theta'\hat{\alpha} + \sin\theta'\hat{\beta} \right|$$
$$\left. \left| \sin\theta'\hat{\alpha} - \cos\theta'\hat{\beta} \right\rangle_{b'_\perp} \left\langle \sin\theta'\hat{\alpha} \cos\theta'\hat{\beta} \right| \right]$$
$$= e^{-|\cos\theta'\hat{\alpha} + \sin\theta'\hat{\beta}|^2\eta_d}(1 - e^{-|\sin\theta'\hat{\alpha} - \cos\theta'\hat{\beta}|^2\eta_d}). \quad (19)$$

Attributing the result $+1$ to the events {no click in a and one click in $a_\perp$} and {no click in $b^{\theta'}$ and one click in $b_\perp^{\theta'}$} the joint probability $p(+1 + 1|\theta\theta')$ can be obtained the previous result together with Eqs. (15) and (16). A similar calculations done to compute the three other joint probability $p(-1 + 1|\theta\theta')$, $p(+1 - 1|\theta\theta')$ and $p(-1 - 1|\theta\theta')$ where the result -1 is attributed to events where there is either { a click in a and no click in $a_\perp$ } or { a click in a and a click in $a_\perp$} (similarly for the modes $b^{\theta'}$ and $b_\perp^{\theta'}$). We find

$$p(+1 + 1|\theta\theta') =$$
$$= (1-p_{\mathrm{dc}})\frac{1-T_g^2}{1-(RT_g)^2} [f(\bar{n}, \bar{m}, \zeta) - g(\bar{n}, \bar{m}, \zeta)] -$$
$$- (1-p_{\mathrm{dc}})^2 \frac{(1-T_g^2)^2}{(1-(RT_g)^2)^2} [f(\bar{m}, \bar{m}, \zeta) - g(\bar{m}, \bar{m}, \zeta)],$$
(20)

$$p(+1 - 1|\theta\theta') = [f(\bar{n}, \bar{n}, \zeta) - g(\bar{n}, \bar{n}, \zeta)] -$$
$$- (1-p_{\mathrm{dc}})\frac{(1-T_g^2)}{(1-(RT_g)^2)} [f(\bar{n}, \bar{m}, \zeta) - g(\bar{n}, \bar{m}, \zeta)], \quad (21)$$

$$p(-1 + 1|\theta\theta') =$$
$$= (1-p_{\mathrm{dc}})\frac{1-T_g^2}{1-(RT_g)^2} [1 - f(\bar{n}, \bar{m}, \zeta)] -$$
$$- (1-p_{\mathrm{dc}})^2 \frac{(1-T_g^2)^2}{(1-(RT_g)^2)^2} [1 - f(\bar{m}, \bar{m}, \zeta)], \quad (22)$$

$$p(-1 - 1|\theta\theta') = [1 - f(\bar{n}, \bar{n}, \zeta)] -$$
$$- (1-p_{\mathrm{dc}})\frac{(1-T_g^2)}{(1-(RT_g)^2)} [1 - f(\bar{n}, \bar{m}, \zeta)]. \quad (23)$$

Here

$$f(\bar{n}, \bar{m}, \zeta) = \frac{1}{1 + \cos^2\theta\bar{n}\eta + \sin^2\theta\bar{m}\eta} \left(\frac{1}{1 + 4\zeta\epsilon}\right)^{1/2}, \quad (24)$$

and

$$g(\bar{n}, \bar{m}, \zeta) = \frac{1}{(1 + \bar{n}\eta)(1 + +\bar{m}\eta)} \left(\frac{1}{1 + 4\zeta\epsilon}\right)^{1/2} \quad (25)$$

with

$$\zeta = \frac{T_2^2\gamma^2\eta_d\cos^2(\theta - \theta')}{1 + \cos^2\theta\bar{n}\eta + \sin^2\theta\bar{m}\eta}, \quad (26)$$

$$\bar{\zeta} = T_2^2\gamma^2\eta_d \left(\frac{\cos^2\theta'}{1 + \bar{n}\eta} + \frac{\sin^2\theta'}{1 + \bar{m}\eta}\right) \quad (27)$$

and

$$\eta = \eta_d T_1^2 T_2^2 \eta_c \eta_d, \quad (28)$$

$$\bar{n} = \frac{T_g^2}{1 - T_g^2}, \bar{m} = \frac{(RT_g)^2}{1 - (RT_g)^2} \quad (29)$$

and $\epsilon = 1 - V$ stands for the error on the viability associated to the displacement operation. Note that the experiment is being performed under the fair sampling assumption, the four probabilities $p(\pm1 \pm 1|\theta\theta')$, $p(\pm1 \mp 1|\theta\theta')$ are re-normalized to sum up to one before being used to predict the value of the CHSH inequality.

[1] M. Afzelius, C. Simon, H. de Riedmatten, and N. Gisin, Phys. Rev. A **79**, 052329 (2009).

[2] F. Bussières, C. Clausen, A. Tiranov, B. Korzh, V. B. Verma, S. W. Nam, F. Marsili, A. Ferrier, P. Goldner, H. Herrmann, C. Silberhorn, W. Sohler, M. Afzelius, and N. Gisin, Nature Photon. **8**, 775 (2014).

[3] P. Sekatski, N. Sangouard, M. Stobińska, F. Bussières, M. Afzelius, and N. Gisin, Phys. Rev. A **86**, 060301 (2012).

[4] C. Clausen, F. Bussières, A. Tiranov, H. Herrmann, C. Sil-

berhorn, W. Sohler, M. Afzelius, and N. Gisin, New J. Phys. **16**, 093058 (2014).

[5] V. Caprara Vivoli, P. Sekatski, J.-D. Bancal, C. C. W. Lim, B. G. Christensen, A. Martin, R. T. Thew, H. Zbinden, N. Gisin, and N. Sangouard, Phys. Rev. A **91**, 012107 (2015).

[6] V. C. Vivoli, P. Sekatski, J.-D. Bancal, C. C. W. Lim, A. Martin, R. T. Thew, H. Zbinden, N. Gisin, and N. Sangouard, New Journal of Physics **17**, 023023 (2015).

"Temporal multimode storage of entangled photon pairs"

A. Tiranov, P. C. Strassmann, J. Lavoie, N. Brunner, M. Huber, V. B. Verma, S. W. Nam, R. P. Mirin, A. E. Lita, F. Marsili, M. Afzelius, F. Bussières & N. Gisin arXiv:1606.07774 (2016) (To be published in Phys. Rev. Lett.)

Temporal multimode storage of entangled photon pairs

Alexey Tiranov[1], Peter C. Strassmann[1], Jonathan Lavoie[1],[*] Nicolas Brunner[2],
Marcus Huber[1,3], Varun B. Verma[4], Sae Woo Nam[4], Richard P. Mirin[4], Adriana
E. Lita[4], Francesco Marsili[5], Mikael Afzelius[1], Félix Bussières[1], and Nicolas Gisin[1]

[1]*Groupe de Physique Appliquée, Université de Genève, CH-1211 Genève, Switzerland*
[2]*Département Physique Théorique, Université de Genève, CH-1211 Genève, Switzerland*
[3]*Institute for Quantum Optics and Quantum Information (IQOQI),*
Austrian Academy of Sciences, Boltzmanngasse 3, A-1090 Vienna, Austria
[4]*National Institute of Standards and Technology, 325 Broadway, Boulder, CO 80305, USA and*
[5]*Jet Propulsion Laboratory, California Institute of Technology,*
4800 Oak Grove Dr., Pasadena, California 91109, USA

Multiplexed quantum memories capable of storing and processing entangled photons are essential for the development of quantum networks. In this context, we demonstrate and certify the simultaneous storage and retrieval of two entangled photons inside a solid-state quantum memory and measure a temporal multimode capacity of ten modes. This is achieved by producing two polarization-entangled pairs from parametric down conversion and mapping one photon of each pair onto a rare-earth-ion doped (REID) crystal using the atomic frequency comb (AFC) protocol. We develop a concept of indirect entanglement witnesses, which can be used as Schmidt number witness, and we use it to experimentally certify the presence of more than one entangled pair retrieved from the quantum memory. Our work puts forward REID-AFC as a platform compatible with temporal multiplexing of several entangled photon pairs along with a new entanglement certification method useful for the characterisation of multiplexed quantum memories.

Quantum memories are key elements for developing future quantum networks [1]. Optical quantum memories [2, 3] allow storage of parts of optical quantum states, for instance the storage of one photon out of a pair of entangled photons. This ability can be used to herald entanglement between stored excitations of remote quantum memories [4–6], which is a basic resource for long-distance quantum networks. A prominent example is the quantum repeater [7, 8], which in principle can distribute quantum entanglement over continental distances, thereby allowing long-distance quantum key distribution over scales impossible by current technologies [9].

Most quantum repeater schemes require efficient multiplexing in order to achieve any useful rate of entanglement distribution [10], which in turn requires quantum memories (QM) that are highly multimode [11]. Quantum memories based on ensembles of atoms provide such a resource, where different degrees of freedom can be used to achieve multimode storage, such as spatial [12–16], spectral [17, 18] or temporal modes [19]. The ensemble approach also provides strong collective light-matter coupling [20, 21], making high memory efficiencies possible.

In this work we address the challenge of demonstrating and certifying simultaneous storage of several quantum excitations in different temporal modes of a QM. We focus on temporal multimode storage in a single spatial mode, which is compatible with optical fiber technologies and therefore attractive for long-distance quantum
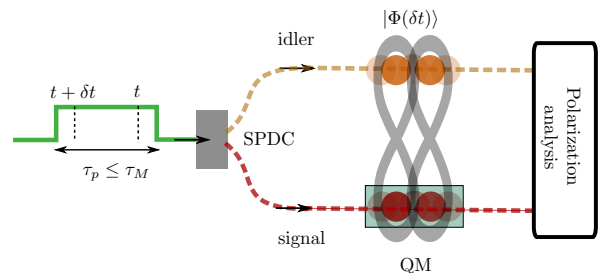
FIG. 1. (color online) Conceptual scheme of the experiment. Temporally multiplexed photon pairs generated from spontaneous parametric down conversion (SPDC) are stored in a multimode quantum memory (QM) and released after a predetermined time τ_M. The pump is pulsed with a 10 MHz repetition rate and with duration τ_p. Two polarization-entangled pairs are generated probabilistically by the same pulse and separated by a time $\delta t \leq \tau_M$. The duration of the pulse equals the storage time such that the stored photons are both in the QM for a time $(\tau_M - \delta t)$. To certify entanglement after absorption and remission by the QM we analyze the correlations in polarization of the four-photon state.

networks. We use the atomic frequency comb (AFC) approach [22], which can achieve multimode storage for much lower optical depths compared to other ensemble-based storage techniques [19]. This protocol is specifically developed for rare-earth-ion doped (REID) crystals [23]. Previous studies have demonstrated temporal highly multimode storage using the AFC scheme, but these experiments have employed either strong [24–26] or attenuated laser pulses [27–29], and true single-photon pulses [30] but without entanglement. Here we demonstrate simultaneous storage of two entangled pho-

ton pairs. The certification of multi-pair entanglement in our experiment requires novel tools, given the limited available data. This is achieved by constructing indirect entanglement witnesses, which we use experimentally to certify the presence of more than one entangled pair retrieved from the quantum memory.

The setup of our experiment is illustrated in Fig. 1. Two independent pairs of entangled signal and idler photons are generated via spontaneous parametric down conversion (SPDC) within a time window shorter than the memory time. The idler photons are at the telecommunication wavelength of 1338 nm, while the signal photons are at 883 nm [31]. The two signal photons are stored in the REID crystal in the same spatial mode, but in two independent temporal modes that differ by up to ten times their coherence time. After a pre-determined storage time, the two photons are re-emitted from the memory and detected by the single-photon detectors (and similarly for the idler photons).

The full characterization of the state of both photon pairs is constrained by the fact that their creation time is much smaller than the dead time of the detectors. This is typical of current single-photon detectors and it can complicate the analysis of temporally multiplexed quantum memories storing short (broadband) single photons. One obvious solution is to double the number of analyzers (and detectors), or use complex multiplexing schemes in space or frequency [32, 33]. Here, instead, we want to use a pair of detectors on each side and apply the same projective measurement needed to analyze a single pair. This leads to a limited set of measurements and outcomes. Previous efforts have been devoted to addressing non-linear functions of density matrix elements, which due to the lack of convexity proved very challenging [34, 35] and still lack assumption-free certification methods. To address this, we develop a new concept of induced witness operators, where an incomplete set of count rates can conclusively certify entanglement, or even Schmidt numbers, without any assumptions about the state. We then apply this new concept to certify the presence of two entangled pairs in our experiment.

First, we demonstrate the capability to generate two independent entangled photon pairs for further quantum storage. For this we generate polarization-entangled photon pairs from SPDC inside two nonlinear waveguides. The continuous pump laser has a central wavelength of 532 nm and is modulated in intensity to obtain a 10 MHz train of 50 ns square pulses (Fig. 1). This modulation defines a temporal window, corresponding to the storage time, inside which two pairs can be generated. The configuration of the nonlinear waveguides, shown in Fig. 2, is such that photons are created in a coherent superposition of $|HH\rangle$, from the first waveguide, or $|VV\rangle$, from the second [31]. We approximate each pair by the state

$$|\phi(t)\rangle = \frac{1}{\sqrt{2}} \left(|H_s, H_i\rangle_t + |V_s, V_i\rangle_t \right), \quad (1)$$

where t is the photon pair creation time within the square
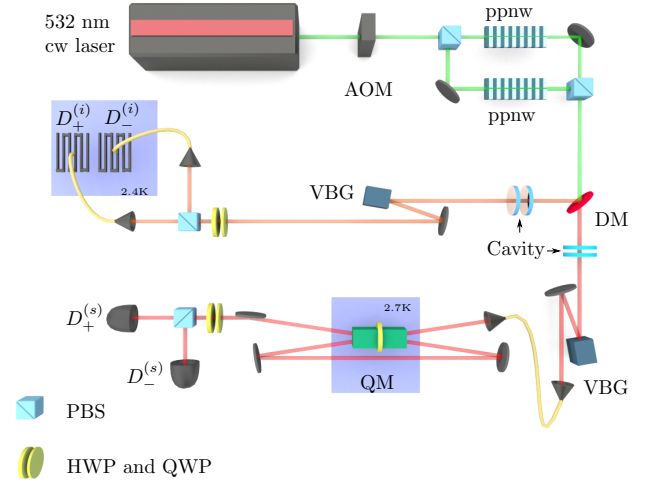

FIG. 2. (color online) Detailed experimental setup. Our source of polarization-entangled photon pairs is based on parametric down conversion inside two periodically poled non-linear waveguides (ppnw) phase matched for Type-0 downconversion. Both crystals are coherently pumped by a 532 nm continuous wave (cw) laser. The pump laser is intensity modulated by an acousto-optic modulator (AOM) at a 10 MHz repetition rate producing a train of 50 ns square pulses. Signal (883 nm) and idler (1338 nm) photons are spatially separated by a dichroic mirror (DM) and spectrally filtered using a cavity and a volume Bragg grating (VBG) in each output mode. The signal mode is coupled to a polarization-preserving solid state quantum memory (QM) based on two Nd^{3+}:Y_2SiO_5 crystals separated by a half-wave plate. To increase the storage efficiency, we use a double-pass configuration through the QM. Finally, we analyze the polarization states of the photon pairs with a set of half-wave (HWP) and quater-wave (QWP) plates, polarizing beamsplitter (PBS) and single photon detectors $D_{\pm}^{(s,i)}$; fiber-coupled superconducting nanowires on the idler side and free-space APDs on the signal side.

pump window, s and i subscripts label signal and idler modes, while $|H\rangle$ and $|V\rangle$ designate horizontal and vertical polarization states of a single photon, respectively.

Two independent polarization-entangled pairs can be generated from the same pulse, in condition that the delay between the pairs, δt, is sufficiently larger than the coherence time of one pair [36]. In this case, the joint state of two pairs is described by

$$|\Phi(\delta t)\rangle = |\phi(t)\rangle \otimes |\phi(t + \delta t)\rangle. \quad (2)$$

The measured coherence time of a photon pair, $\tau_c = 1.9$ ns, is defined by the filtering system which is applied to the both photons (for the details see [31]). Overall, the rate of two-fold coincident detections after storage is 200 Hz for an average pump power of 4 mW (2 mW at the input of each waveguide).

The signal mode of each pair is coupled to the QM. The latter consists of two Nd^{3+}:Y_2SiO_5 crystals mounted around a half-wave plate, together enabling high-fidelity

polarization storage [37–39]. The absorption profile of the broad resonant frequency transition of the atomic ensemble is tailored in a frequency comb using optical pumping techniques [39]. The prepared AFC fixes the storage time to $\tau_M = 50$ ns [22] and the measured total memory efficiency of the single photon is $\eta = 7(1)\%$ in the double-pass configuration depicted in Fig. 2. To analyze the correlations between the released signal and idler photons, we use a combination of quarter-wave, half-wave plates and a polarizing beam splitter (PBS) on each side.

To detect the stored signal and the idler photons from each pair we put two single-photon detectors (SPDs) at the output ports of the PBS on each side (denoted as "+" and "−" in Fig. 2). We use superconducting nanowire SPDs ($D_\pm^{(i)}$) with 75% efficiency, 100 ns dead time and 300 ps jitter (WSi superconducting nanowire [40]) for the idler photons. The signal photons are detected with two free-space free-running silicon avalanche photodiode ($D_\pm^{(s)}$) with 40% efficiency, 1 μs dead time and 400 ps jitter.

Figure 3(a) shows two-fold coincidences as a function of the delay between the detections of a signal and an idler photons. The temporally resolved peak structure corresponds to the transmitted (0 ns) and stored signal photon in the QM (50 ns) from a single photon pair (Eq. (1)). However, to detect and analyze the four-photon state (Eq. (2)) one has to look at coincidences between all four detectors (four-folds). Our main limitation comes from the ~ 1 μs dead time of the signal mode detectors. Given that one photon of the first pair is detected at one output port of the PBS, the photon of the second pair cannot be detected in the same output port, as the separation is smaller than the dead time. For example, if the first photon pair is detected in ($D_+^{(s)}, D_+^{(i)}$), the only way to detect the following photon pair is with the complementary detector combination ($D_-^{(s)}, D_-^{(i)}$). For a given pair of measurement settings (denoting x and y the choice of measurement setting for Alice and Bob, respectively), there are thus four accessible event rates labelled $N_{ab,\bar{a}\bar{b}|xy}$, where $a, b = \pm$. Figure 3(b) shows the histogram of measured four-fold events, for different delays δt between pairs. The triangular shape is caused by the square wave pumping of the SPDC: the probability to generate two photon pairs with the delay between them equal to the pump length (in our case 50 ns) is much smaller for smaller delays.

Two detections on the idler's side, with delay δt, herald two signal photons, also with delay δt (within their coherence times), counted and analyzed after storage in the QM. In the data analysis, the delay between two pairs is bounded by the storage time $\tau_M = 50$ ns. Hence, we only consider the overall range delimited by two dotted vertical lines on Fig. 3(b). Importantly, by comparing the histograms corresponding to different delays between photon pairs, we see that the presence of two excitations does not change the efficiency of the QM. The multimode capacity of the QM is given by the number of modes (bins
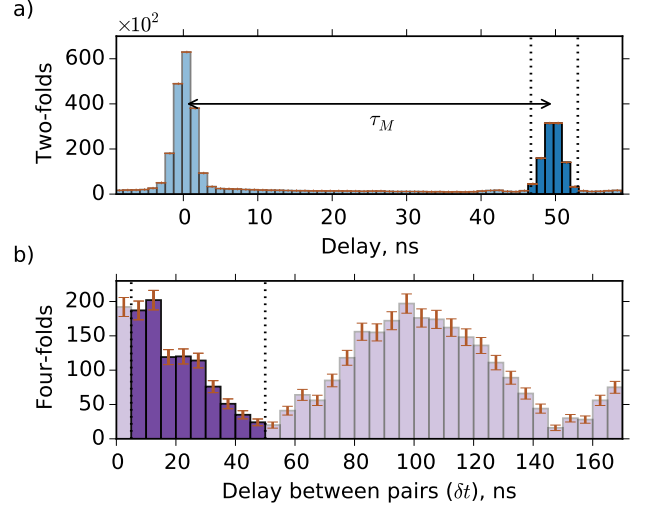

FIG. 3. (color online) Temporal multimode storage. (a) The two-fold coincidences between detections of the signal and idler photons as a function of the delay between two detection events. The first peak at 0 ns stems from the signal photons not absorbed by the QM while the second peak at 50 ns corresponds to the signal photons absorbed by the QM and released after the storage time. Such an histogram is accumulated for each pair of detectors between signal and idler photons. A coincidence window of 4 ns (depicted by the dotted lines) is used to calculate the rates. (b) The total four-fold coincidences collected during the experiment is plotted as a function of the delay δt between photon pairs. The events corresponding to the stored state (2) inside the storage time of the QM are delimited by dotted vertical lines from 5 to 50 ns. There are 9 distinguishable time divisions, demonstrating storage of 10 modes containing single photon excitations. For longer delay (> 50 ns), two photons do not overlap at any time in the QM. Error bars represent one standard deviation assuming Poisson noise for the counts.

on the histogram) and equal to 10. Those results are direct signatures of temporal multimode capacity of our QM using simultaneous storage of two single photons.

The limited set of projection measurements used in this experiment does not allow us to probe entanglement of the four-photon state (Eq. (2)) using standard tools. To certify the presence of two entangled pairs in different temporal modes we therefore devise an entanglement witness based on the event rates $N_{ab,\bar{a}\bar{b}|xy}$ for different pairs of measurement settings.

To distinguish the different temporal modes the overlap between adjacent modes should be minimized. The size of the temporal bins must be larger than the coherence time of the photon pair generated from the SPDC (~ 2 ns). For this reason, we consider only the events when photon pairs are separated more than 5 ns (Fig. 3(b)), which corresponds to 2.5 times the temporal width of a photon pair. Specifically, we denote the final quantum state (after the memory) ρ, which is of
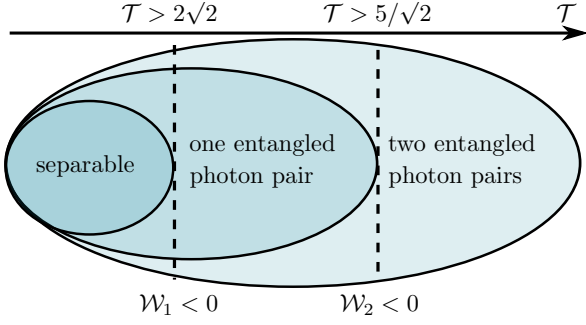
FIG. 4. (color online) Entanglement witness. From the measured four-fold correlations we can compute our central figure of merit $\mathcal{T}$ (Eq. (3)). A value of $\mathcal{T}$ implies that the operator $\mathcal{W}_k(\mathcal{T})$ has an expectation value equal to exactly zero. For a sufficiently large value of $\mathcal{T}$ this implies that the expectation value of $W_1(\mathcal{T})$ (or $W_2(\mathcal{T})$) is negative. Since we can prove that $\mathcal{W}_1$ is an entanglement witness and $\mathcal{W}_2$ a Schmidt number witness, we can thus conclude on one or two entangled pairs.

dimension 4×4. Our goal is to prove that ρ contains two entangled pairs (Fig. 4) and do not have to assume *a priori* that ρ consists of two independent pairs (as in Eq. (2)). That is, violation of our entanglement witness certifies the presence of more than one entangled pair, even if the two pairs may have become correlated inside the QM. Surprisingly this is achieved even without direct access to density matrix elements, but only proportionality relations between them [41].

Our witness involves two local measurement settings per party. Using Bloch vector notation, Alice's measurements are given by vectors $\hat{\sigma}_x$ (for $x = 0$) and $\hat{\sigma}_y$ (for $x = 1$), while Bob's measurements are $(\hat{\sigma}_x + \hat{\sigma}_y)/\sqrt{2}$ (for $y = 0$) and $(\hat{\sigma}_x - \hat{\sigma}_y)/\sqrt{2}$ (for $y = 1$). Note that this choice of measurements is typical for Bell-CHSH tests [39] and suitable for the entanglement witness described below. For a given choice of local measurements, the event rates $N_{ab:\bar{a}\bar{b}}$ are thus proportional to $\mathrm{Tr}(P_a \otimes P_{\bar{a}} \otimes P_b \otimes P_{\bar{b}}\rho)$, where $P_a = (\mathbb{1} + a\hat{v}\cdot\hat{\vec{\sigma}})/2$ denote qubit projectors. Our entanglement witness is based on the expression

$$\mathcal{T} = \frac{1}{N}(\mathcal{C}_{00} + \mathcal{C}_{01} + \mathcal{C}_{10} - \mathcal{C}_{11}) \qquad (3)$$

where we have defined correlation functions

$$\mathcal{C}_{xy} = \sum_{a,b=\pm 1} ab\, N_{ab,\bar{a}\bar{b}|xy} \qquad (4)$$

and a normalization factor

$$N = \frac{1}{4} \sum_{x,y=0,1} \sum_{a,b=\pm 1} N_{ab,\bar{a}\bar{b}|xy}. \qquad (5)$$

In the case ρ contains one entangled pair (or less), the expression $\mathcal{T}$ is upper-bounded by

$$\mathcal{T} \leq \frac{5}{\sqrt{2}} \simeq 3.535. \qquad (6)$$

Hence any violation of the witness, i.e. $\mathcal{T} > 5/\sqrt{2}$, implies the presence of more than one entangled pair in the output state ρ. For any separable state ρ we prove that the expression $\mathcal{T}$ has an upper bound of $2\sqrt{2}$. This allows to use the actual value of the witness to certify the presence of entanglement in general (Fig. 4); the value of $\mathcal{T}$ can be attributed to the expectation value of an induced operator $\mathcal{W}(\mathcal{T})$. Depending on the value of $\mathcal{T}$ the fact that this operator has a vanishing expectation value certifies entanglement of one or more entangled photon pairs. The details of the derivation of the bounds are given in [41].

$\mathcal{C}_{00}$	$\mathcal{C}_{01}$	$\mathcal{C}_{10}$	$\mathcal{C}_{11}$	$\mathcal{T}$	$\tilde{\mathcal{T}}$
0.98(6)	0.92(7)	0.88(6)	-0.88(6)	3.67(6)	3.64(2)

TABLE I. Experimental certification of two entangled pairs after storage. Each correlator $\mathcal{C}_{xy}$ is measured as described in the main text and used to compute the parameter $\mathcal{T}$ of Eq. (3). $\tilde{\mathcal{T}}$ is a model-based estimation of the expected $\mathcal{T}$ value in our experiment (see text). There is a good agreement between the two. These results above the bound (6) of 3.535 certify entanglement for each photon pair released from the QM. The uncertainties represent one standard deviation assuming Poisson statistics for the counts.

With the recorded four-fold events in hand, we use the entanglement witness to show that the two pairs used to probe the multimode properties of the memory are polarization entangled. Each correlator of Eq. (3) is measured for 900 seconds and the sequence is repeated many times (see Table I). The experimental value of the entanglement witness is $\mathcal{T} = 3.67 \pm 0.06$, two standard deviations above the upper bound (6) of 3.535 attainable when only one pair is entangled while the other is separable. One can find all the counts to reconstruct the witness in the [41].

To understand what limits our measured value of $\mathcal{T}$, we developed a simple model to predict it using only the measurement of the Bell–CHSH parameter S for a single entangled pair (see the details in the [41]). For this we assume that we are measuring two independent pairs and a total quantum state of the form $\rho(\mathcal{V}) = \rho_W(\mathcal{V}) \otimes \rho_W(\mathcal{V})$, where $\rho_W(\mathcal{V}) = \mathcal{V}|\phi_+\rangle\langle\phi_+| + (1-\mathcal{V})\mathbb{1}/4$ is a two-qubit Werner state with visibility $\mathcal{V}$. We should measure the value $S = 2\sqrt{2}\mathcal{V}$ for a single entangled pair in the state $\rho_W(\mathcal{V})$, and we can use this to calculate the expected value of $\tilde{\mathcal{T}}$. With the photons retrieved from the QM, we found $S = 2.58 \pm 0.02$ corresponding to a visibility of $\mathcal{V} = 0.912 \pm 0.007$, which leads to an expected value of $\tilde{\mathcal{T}} = 3.64 \pm 0.02$, in agreement with experimentally measured value of $\mathcal{T}$. We note that in this model, a minimum visibility of $\mathcal{V} \simeq 0.85$ (for each identical pair) is required to certify more than one entangled pair, which is more stringent than the case where all measurement outcomes are accessible. The maximum value reachable with a state of the form ρ_W is $\mathcal{T} = 8\sqrt{2}/3 \simeq 3.77$

with $\mathcal{V} = 1$. The visibility $\mathcal{V}$ in our experiment was limited equally by the imperfect preparation of the polarization entangled state and multi-pair generation from the SPDC source [31].

In conclusion, we quantified the temporal multimode capacity of our solid-state QM using two entangled photon pairs as a probe. To ascertain the high-fidelity storage, we developed an entanglement certification method that can also be used as a Schmidt number witness. The latter does not require any assumptions on the quantum state and works even with a limited set of projective measurements. Our approach can be adapted to certify entanglement involving multiple stored excitations in multiplexing quantum memories harnessing other degrees of freedom such as frequency and spatial modes of light.

Progress towards a quantum repeater requires the use of a quantum memory that can retrieve photons on-demand using a complete long-duration AFC spin-wave storage [28, 29, 46] with high multimode capacity [47]. Alternatively, a scheme based on spectral multiplexing which does not require temporal on-demand readout could be used [17]. Our experiment demonstrating storage of several entangled excitations in ten different temporal modes of a quantum memory together with previous demonstrations open promising perspectives in the direction of long-distance quantum communication.

[1] H. J. Kimble, Nature **453**, 1023 (2008).

[2] A. I. Lvovsky, B. C. Sanders, and W. Tittel, Nat Photon **3**, 706 (2009).

[3] F. Bussières, N. Sangouard, M. Afzelius, H. de Riedmatten, C. Simon, and W. Tittel, Journal of Modern Optics **60**, 1519 (2013).

[4] C. W. Chou, H. de Riedmatten, D. Felinto, S. V. Polyakov, S. J. van Enk, and H. J. Kimble, Nature **438**, 828 (2005).

[5] D. L. Moehring, P. Maunz, S. Olmschenk, K. C. Younge, D. N. Matsukevich, L.-M. Duan, and C. Monroe, Nature **449**, 68 (2007).

[6] Z.-S. Yuan, Y.-A. Chen, B. Zhao, S. Chen, J. Schmiedmayer, and J.-W. Pan, Nature **454**, 1098 (2008).

[7] H.-J. Briegel, W. Dür, J. I. Cirac, and P. Zoller, Phys. Rev. Lett. **81**, 5932 (1998).

[8] L.-M. Duan, M. D. Lukin, J. I. Cirac, and P. Zoller, Nature **414**, 413 (2001).

[9] B. Korzh, C. C. W. Lim, R. Houlmann, N. Gisin, M. J. Li, D. Nolan, B. Sanguinetti, R. Thew, and H. Zbinden, Nat Photon **9**, 163 (2015).

[10] N. Sangouard, C. Simon, H. de Riedmatten, and N. Gisin, Rev. Mod. Phys. **83**, 33 (2011).

[11] C. Simon, H. de Riedmatten, M. Afzelius, N. Sangouard, H. Zbinden, and N. Gisin, Phys. Rev. Lett. **98**, 190503 (2007).

[12] S.-Y. Lan, A. G. Radnaev, O. A. Collins, D. N. Matsukevich, T. A. Kennedy, and A. Kuzmich, Opt. Express **17**, 13639 (2009).

[13] Z.-Q. Zhou, Y.-L. Hua, X. Liu, G. Chen, J.-S. Xu, Y.-J. Han, C.-F. Li, and G.-C. Guo, Phys. Rev. Lett. **115**, 070502 (2015).

[14] V. Parigi, V. D'Ambrosio, C. Arnold, L. Marrucci, F. Sciarrino, and J. Laurat, Nature Communications **6**, 7706 (2015).

[15] H.-N. Dai, H. Zhang, S.-J. Yang, T.-M. Zhao, J. Rui, Y.-J. Deng, L. Li, N.-L. Liu, S. Chen, X.-H. Bao, X.-M. Jin, B. Zhao, and J.-W. Pan, Phys. Rev. Lett. **108**, 210501 (2012).

[16] Y. Wu, L. Tian, Z. Xu, W. Ge, L. Chen, S. Li, H. Yuan, Y. Wen, H. Wang, C. Xie, and K. Peng, Phys. Rev. A **93**, 052327 (2016).

[17] N. Sinclair, E. Saglamyurek, H. Mallahzadeh, J. H. Slater, M. George, R. Ricken, M. P. Hedges, D. Oblak, C. Simon, W. Sohler, and W. Tittel, Phys. Rev. Lett. **113**, 053603 (2014).

[18] E. Saglamyurek, M. Grimau Puigibert, Q. Zhou, L. Giner, F. Marsili, V. B. Verma, S. Woo Nam, L. Oesterling, D. Nippa, D. Oblak, and W. Tittel, Nature Communication **7**, 11202 (2016).

[19] J. Nunn, K. Reim, K. C. Lee, V. O. Lorenz, B. J. Sussman, I. A. Walmsley, and D. Jaksch, Phys. Rev. Lett. **101**, 260502 (2008).

[20] A. V. Gorshkov, A. André, M. Fleischhauer, A. S. Sørensen, and M. D. Lukin, Phys. Rev. Lett. **98**, 123601 (2007).

[21] K. Hammerer, A. S. Sørensen, and E. S. Polzik, Rev. Mod. Phys. **82**, 1041 (2010).

[22] M. Afzelius, C. Simon, H. de Riedmatten, and N. Gisin, Phys. Rev. A **79**, 052329 (2009).

[23] W. Tittel, M. Afzelius, T. Chanelière, R. Cone, S. Kröll, S. Moiseev, and M. Sellars, Laser & Photonics Reviews **4**, 244 (2010).

[24] M. Bonarota, J.-L. L. Gout, and T. Chanelire, New Journal of Physics **13**, 013013 (2011).

[25] M. Gündoğan, M. Mazzera, P. M. Ledingham, M. Cristiani, and H. de Riedmatten, New Journal of Physics **15**, 045012 (2013).

[26] P. Jobez, N. Timoney, C. Laplane, J. Etesse, A. Ferrier, P. Goldner, N. Gisin, and M. Afzelius, Phys. Rev. A **93**, 032327 (2016).

[27] I. Usmani, M. Afzelius, H. de Riedmatten, and N. Gisin, Nat Commun **1**, 12 (2010).

[28] P. Jobez, C. Laplane, N. Timoney, N. Gisin, A. Ferrier, P. Goldner, and M. Afzelius, Phys. Rev. Lett. **114**, 230502 (2015).

[29] M. Gündoğan, P. M. Ledingham, K. Kutluer, M. Mazzera, and H. de Riedmatten, Phys. Rev. Lett. **114**, 230501 (2015).

[30] J.-S. Tang, Z.-Q. Zhou, Y.-T. Wang, Y.-L. Li, X. Liu, Y.-L. Hua, Y. Zou, S. Wang, D.-Y. He, G. Chen, Y.-N. Sun, Y. Yu, M.-F. Li, G.-W. Zha, H.-Q. Ni, Z.-C. Niu, C.-F. Li, and G.-C. Guo, Nat. Commun. **6**, 9652 (2015).

[31] C. Clausen, F. Bussières, A. Tiranov, H. Herrmann, C. Silberhorn, W. Sohler, M. Afzelius, and N. Gisin, New Journal of Physics **16**, 093058 (2014).

[32] M. J. Collins, C. Xiong, I. H. Rey, T. D. Vo, J. He, S. Shahnia, C. Reardon, T. F. Krauss, M. J. Steel, A. S. Clark, and B. J. Eggleton, Nature Communications **4**, 2582 (2013).

[33] J. M. Donohue, J. Lavoie, and K. J. Resch, Physical Review Letters **113**, 163602 (2014).

[34] M. Krenn, R. Fickler, M. Huber, R. Lapkiewicz, W. Plick, S. Ramelow, and A. Zeilinger, Phys. Rev. A **87**, 012326 (2013).

[35] M. Krenn, M. Huber, R. Fickler, R. Lapkiewicz, S. Ramelow, and A. Zeilinger, Proceedings of the National Academy of Sciences **111**, 6243 (2014).

[36] H. de Riedmatten, V. Scarani, I. Marcikic, A. Acín, W. Tittel, H. Zbinden, and N. Gisin, Journal of Modern Optics **51**, 1637 (2004).

[37] C. Clausen, F. Bussières, M. Afzelius, and N. Gisin, Phys. Rev. Lett. **108**, 190503 (2012).

[38] Z.-Q. Zhou, W.-B. Lin, M. Yang, C.-F. Li, and G.-C. Guo, Phys. Rev. Lett. **108**, 190505 (2012).

[39] A. Tiranov, J. Lavoie, A. Ferrier, P. Goldner, V. B. Verma, S. W. Nam, R. P. Mirin, A. E. Lita, F. Marsili, H. Herrmann, C. Silberhorn, N. Gisin, M. Afzelius, and F. Bussières, Optica **2**, 279 (2015).

[40] V. B. Verma, B. Korzh, F. Bussières, R. D. Horansky, A. E. Lita, F. Marsili, M. D. Shaw, H. Zbinden, R. P. Mirin, and S. W. Nam, Applied Physics Letters **105**, 122601 (2014).

[41] See Supplemental Material at http://link.aps.org, which includes Refs. [42-45].

[42] A. Sanpera, D. Bruß, and M. Lewenstein, Phys. Rev. A **63**, 050301 (2001).

[43] C. Lancien, O. Ghne, R. Sengupta, and M. Huber, Journal of Physics A: Mathematical and Theoretical **48**, 505302 (2015).

[44] C. Eltschka and J. Siewert, Phys. Rev. Lett. **111**, 100503 (2013).

[45] J. Löfberg, Proceedings of the CACSD Conference (2004).

[46] C. Laplane, P. Jobez, J. Etesse, N. Timoney, N. Gisin, and M. Afzelius, New Journal of Physics **18**, 013006 (2016).

[47] P. Jobez, N. Timoney, C. Laplane, J. Etesse, A. Ferrier, P. Goldner, N. Gisin, and M. Afzelius, Phys. Rev. A **93**, 032327 (2016).

Supplemental material for "Temporal multimode storage of entangled photon pairs"

Alexey Tiranov[1], Peter C. Strassmann[1], Jonathan Lavoie[1], Nicolas Brunner[2],
Marcus Huber[1,3], Varun B. Verma[4], Sae Woo Nam[4], Richard P. Mirin[4], Adriana
E. Lita[4], Francesco Marsili[5], Mikael Afzelius[1], Félix Bussières[1], and Nicolas Gisin[1]

[1]*Groupe de Physique Appliquée, Université de Genève, CH-1211 Genève, Switzerland*
[2]*Département Physique Théorique, Université de Genève, CH-1211 Genève, Switzerland*
[3]*Institute for Quantum Optics and Quantum Information (IQOQI),*
Austrian Academy of Sciences, Boltzmanngasse 3, A-1090 Vienna, Austria
[4]*National Institute of Standards and Technology, 325 Broadway, Boulder, CO 80305, USA and*
[5]*Jet Propulsion Laboratory, California Institute of Technology,*
4800 Oak Grove Dr., Pasadena, California 91109, USA

I. INDIRECT ENTANGLEMENT WITNESSES

Here we present the details of the derivation of the entanglement witness used in the main text. Although we expect the final state to be a product of two highly entangled states, we obviously do not want to make this assumption in the derivation of its entanglement certification. For that purpose we treat the underlying events as originating from a 4×4 dimensional Hilbert space without any assumption in its internal structure. In the ideal case that state should correspond to a tensor product of two Bell states and thus have a Schmidt number of 4. If only one of the pairs could retain its entanglement through the storage in the quantum memory its Schmidt number would be at most 2. If, on the other hand all the entanglement had been destroyed, the resulting state would be completely separable (i.e. Schmidt number 1).

Ideally we could now derive a Schmidt number witness W_k [1], tailored towards this state. One could then decompose this witness into a linear combination of local measurements and acquire all the required coincidences until that witness is constructed and assumption-free entanglement of both pairs is certified. As pointed out in the main text, however, the dead times between the two signals prohibit the acquisition of complete counts in any basis. It is thus impossible to follow the canonical approach of obtaining density matrix elements through local projective coincidences as:

$$\langle \alpha, \beta | \rho | \alpha, \beta \rangle = \frac{N_{\alpha,\beta}}{\sum_i \sum_j N_{i,j} := N_{tot}}, \quad (1)$$

since N_{tot} inevitably contains terms that cannot be measured in the current setup. What we can measure instead are proportionality constants $\mathcal{T}$ between different count rates, i.e.

$$\frac{\sum_{\{a,b\} \in X} c_{a,b} N_{a,b}}{\sum_{\{a,b\} \in Y} d_{a,b} N_{a,b}} = \mathcal{T}, \quad (2)$$

with arbitrary real coefficients $c_{a,b}$ and $d_{a,b}$. Even though we do not have access to N_{tot} we can now use it to rewrite the above as a fraction of corresponding density matrix elements.

$$\mathcal{T} = \frac{\frac{1}{N_{tot}} \sum_{\{a,b\} \in X} N_{a,b}}{\frac{1}{N_{tot}} \sum_{\{a,b\} \in Y} N_{a,b}} = \frac{\sum_{\{a,b\} \in X} \langle a, b | \rho | a, b \rangle}{\sum_{\{a,b\} \in Y} \langle a, b | \rho | a, b \rangle}. \quad (3)$$

Through the linearity of the trace we can conclude that the operator

$$\mathcal{W}(\mathcal{T}) = \sum_{\{a,b\} \in X} |a, b\rangle\langle a, b| - \mathcal{T} \sum_{\{a,b\} \in Y} |a, b\rangle\langle a, b|, \quad (4)$$

has expectation value zero, i.e. $\mathrm{Tr}(\mathcal{W}(\mathcal{T})\rho) = 0$. Now we can continue to look at the following optimization problem

$$\min_{\sigma \in SEP} \mathrm{Tr}(\mathcal{W}(\mathcal{T})\sigma) := E_{min}. \quad (5)$$

If we can prove that $E_{min} > 0$, we have thus proven entanglement of the state ρ, through the induced witness $\mathcal{W}(\mathcal{T})$. Even though the above optimization problem is convex, it may nonetheless be hard to solve. We can however use the concept of positive maps to address it through a relaxation (even in the multipartite case, see [2]). As an exemplary case consider the partial transpose map, i.e.

$$\min_{\sigma \in PPT} \mathrm{Tr}(\mathcal{W}(\mathcal{T})\sigma) := E_{PPT} \leq E_{min}. \quad (6)$$

Since the explicit form of the above optimization problem is a semi-definite program (SDP), it can be easily solved using SDP solvers, where the maximization of the dual yields analytic lower bounds on the minimum. It is even possible to address the dimensionality of entanglement in this context. Since the negativity $\mathcal{N}(\rho)$ is bounded for states of Schmidt rank k as $\frac{k-1}{2}$ [3], we can make use of its variational form $\mathcal{N}(\rho) = \min(\mathrm{Tr}(M_-))$, s.t. $\rho^{T_A} = M_+ - M_-, M_\pm \geq 0$ to introduce the following SDP

$$\min_{\sigma} \mathrm{Tr}(\mathcal{W}(\mathcal{T})\sigma) := E_k, \quad (7)$$

$$\text{s.t. } \sigma^{T_A} = M_+ - M_-, M_\pm \geq 0, \mathrm{Tr}(M_-) \leq \frac{k-1}{2}. \quad (8)$$

This is again an SDP, and thus possible to compute analytic bounds. Now it is obvious that if $E_k > 0$ the

Schmidt number (i.e. entanglement dimensionality) of the experimental state ρ has to be greater than k.

Now applying the above formalism to the two-photon pair experiment we can use

$$\mathcal{T} = \frac{1}{N}(C_{00} + C_{01} + C_{10} - C_{11}) \qquad (9)$$

where we have defined correlation functions

$$C_{xy} = \sum_{a,b=\pm 1} ab\, N_{ab,\bar{a}\bar{b}|xy} \qquad (10)$$

and a normalization factor

$$N = \frac{1}{4} \sum_{x,y=0,1} \sum_{a,b=\pm 1} N_{ab,\bar{a}\bar{b}|xy}. \qquad (11)$$

Now we can optimize over all T such that:

$$\mathcal{T}_{PPT} := \max \mathcal{T} \qquad (12)$$
$$\text{s.t. } E_{PPT} \le 0 \qquad (13)$$

and

$$\mathcal{T}_{1-photon} := \max \mathcal{T} \qquad (14)$$
$$\text{s.t. } E_2 \le 0 \qquad (15)$$

In the last program we can furthermore add Schmidt number witnesses [1] to be non-violated as a linear constraint. We have implemented these programs with MATLAB using the SDPT3 solver and the YALMIP package [4] and found that $\mathcal{T}_{PPT} = 2\sqrt{2}$ and with a bounded negativity and choosing the optimal Schmidt number witness for the unconstrained state the value for one photon is $\mathcal{T} \approx 3.535$, thus showing that the induced entanglement witnesses $\mathcal{W}(\mathcal{T})$ indeed proves that more than one entangled pair is required to explain the observed correlations.

II. CONSISTENCY CHECK

The consistency of the experimentally obtained value of $\mathcal{T}$ can be verified with the following model. Assume two independent photon pairs, each pair being in a Werner state with visibility $\mathcal{V}$: $\rho_W(\mathcal{V}) = \mathcal{V}|\phi_+\rangle\langle\phi_+| + (1-\mathcal{V})\mathbb{1}/4$, where $|\phi_+\rangle = \frac{1}{\sqrt{2}}(|00\rangle + |11\rangle)$ is a Bell state. Hence the total state is of the form $\rho(\mathcal{V}) = \rho_W(\mathcal{V}) \otimes \rho_W(\mathcal{V})$. For such a state, the witness value $\mathcal{T}$ can be directly expressed in function of the visibility

$$\mathcal{T} = \frac{4\sqrt{2}\mathcal{V}}{1 + \mathcal{V}^2/2}. \qquad (16)$$

Equivalently, this can be expressed in terms of the Bell-CHSH parameter S for a single photon pair:

$$\mathcal{T} = \frac{2S}{1 + S^2/16}. \qquad (17)$$

	Stored				Transmitted			
	x_0,y_0	x_0,y_1	x_1,y_0	x_1,y_1	x_0,y_0	x_0,y_1	x_1,y_0	x_1,y_1
$N_{++,--}$	76	70	61	4	195	220	200	6
$N_{--,++}$	112	113	112	6	216	227	198	11
$N_{+-,-+}$	1	2	5	92	10	12	11	222
$N_{-+,+-}$	2	7	4	82	9	10	13	223

TABLE I. Experimental certification of two entangled pairs. The total number of four-fold events detected for each combination of four detectors (two detectors on each side of the experiment). The data was collected for the maximum delay between photon pairs of 50 ns. For this reason only 4 detector combinations are available due to their deadtime. Each column is used to calculate the correlators $\mathcal{C}_{xy}$ (Eq. (10)) for different sets of projective measurements as described in the main text. Their values are used to compute the parameter T of Eq. (9) for stored entangled photon pairs or transmitted through the QM. For stored photons we obtained the value of entanglement witness of $\mathcal{T} = 3.67(6)$, while for the transmitted part it is $3.63(4)$. Both values are above the entanglement bound to certify two entangled pairs.

Here the CHSH parameter is given by

$$S = \sum_{x,y=0,1} (-1)^{xy} E_{xy} \qquad (18)$$

where we have defined the usual correlators $E_{xy} = \sum_{a,b=\pm 1} abp(ab|xy)$. For a single photon pair in a Werner state $\rho_W(\mathcal{V})$, the CHSH value is a simple function of the visibility: $S = 2\sqrt{2}\mathcal{V}$. Notice that the measurement settings used in our witness are the optimal settings for testing CHSH on the Bell state $|\phi_+\rangle$.

Experimentally, we measured for a single photon pair $S = 2.58 \pm 0.02$. Given the above model, we thus expect a witness value of $\tilde{\mathcal{T}} = 3.64 \pm 0.02$, in excellent agreement with our data.
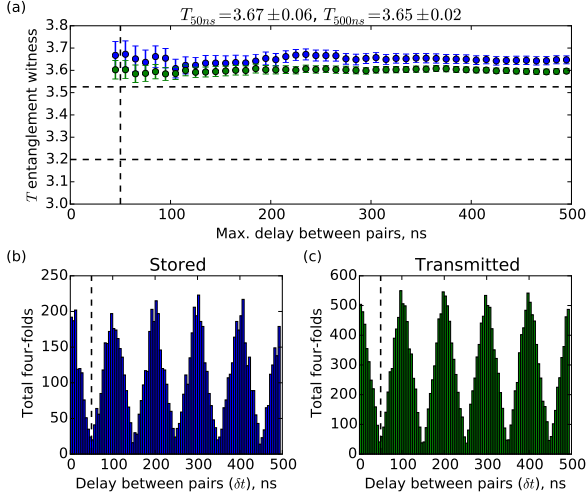
FIG. 1. (a) The value of entanglement witness as a function of the delay between photon pairs which were transmitted or stored in the quantum memory. Bigger delay decreases standard deviation due to the bigger statistics. All the values are above entanglement bound (dash line), which certifies the presence of entanglement for both photon pairs. The values for 50 ns and 500 ns maximum delay are equal inside standard deviation. (b) The total number of quadruples is plotted in function of the delay between photon pairs which were transmitted (right graph) or stored in the quantum memory (left). Triangular shape comes from the square shape of the pump and convolution. To certify storage of both photon pairs we consider a maximum delay of 50 ns between two photon pairs. For longer delay, one cannot certify that two stored for at least some time. The number of stored quadruples from the first pulse or any other is the same which underlines that the efficiency of the QM doesn't depend on the number of stored excitations.

[1] A. Sanpera, D. Bruß, and M. Lewenstein, Phys. Rev. A **63**, 050301 (2001).

[2] C. Lancien, O. Ghne, R. Sengupta, and M. Huber, Journal of Physics A: Mathematical and Theoretical **48**, 505302 (2015).

[3] C. Eltschka and J. Siewert, Phys. Rev. Lett. **111**, 100503 (2013).

[4] J. Löfberg, Proceedings of the CACSD Conference (2004).
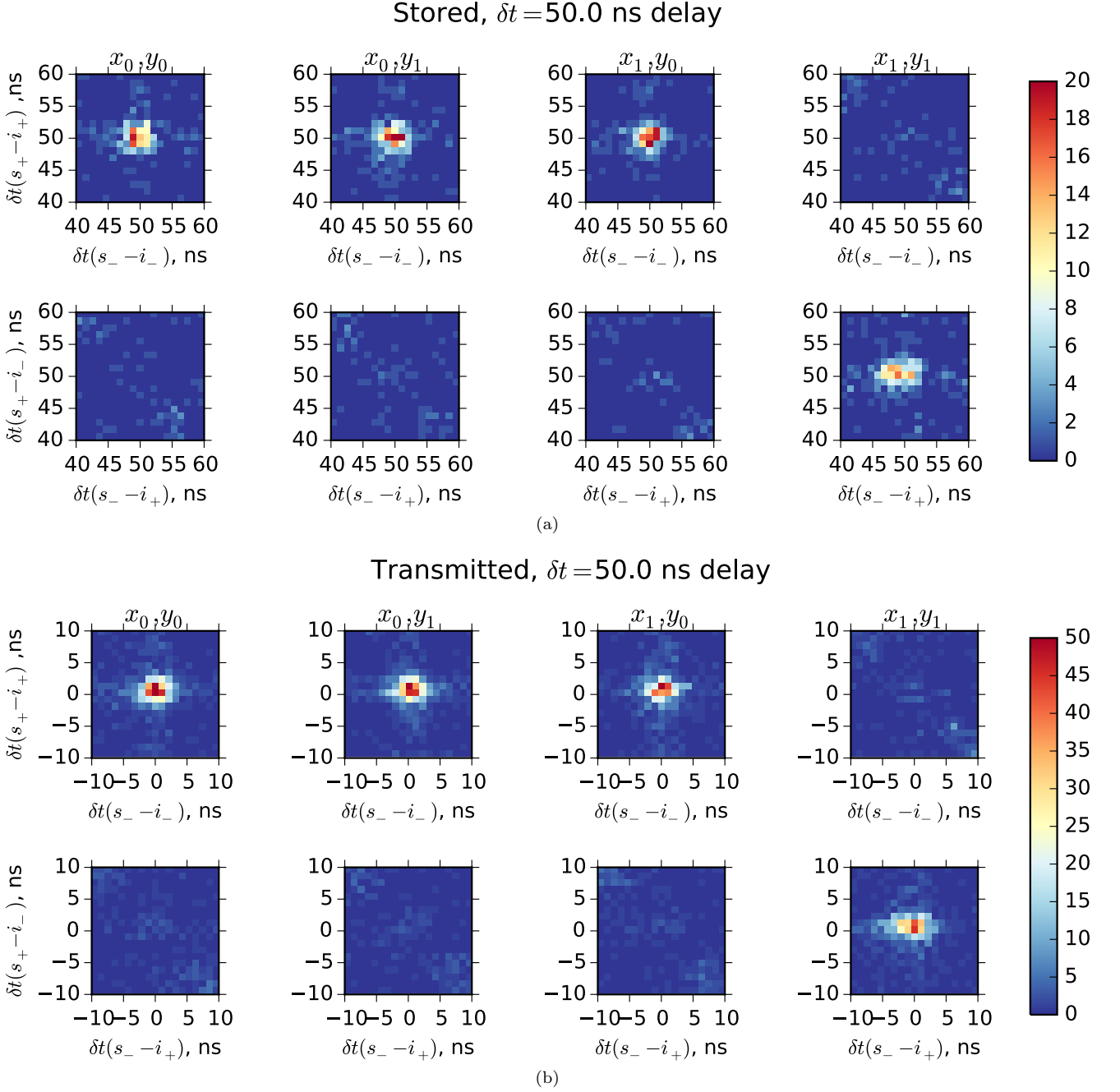
FIG. 2. Histograms of the number of four-fold coincidences with the stored (a) and transmitted (b) signal photon that were used to verify entanglement for both photon pairs. They are shown as a function of delays $\delta t(s_k - i_l)$ between detector $D_k^{(s)}$ of the signal analyzer ($k = +; -$) and detector $D_l^{(i)}$ ($l = +; -$), where $D^{(i)}$ is one of the two SNSPDs used to detect idler photon. The histograms were measured in four different bases that are equivalent to the CHSH inequality violation. The binning of the histogram in each direction was set to be 0.486 ps. The coincidence window of 5 ns around the center of the histograms was used to collect the four fold events and calculate entanglement witness (9).
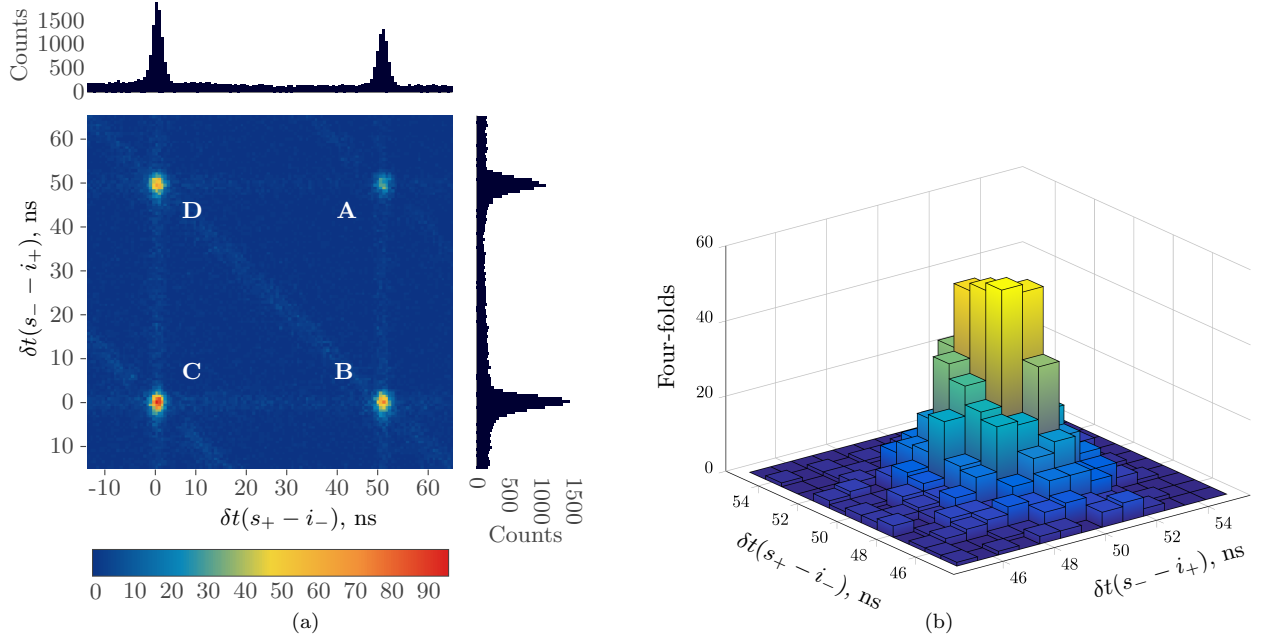
FIG. 3. (a) The total number of quadruple events plotted as a function of the delays between different pairs of detectors by which they were detected. The maximum delay of 500 ns was considered. Four different coincidence peaks correspond to four different cases: (A) both signal photons were stored in the QM, (C) both signal photons were transmitted without absorption in the crystal and two cases (B, D) where only one of the signal photon was stored while other was transmitted. (b) The total number of stored quadruples (case A) as a function of the delays between different pairs of detectors.

"Quantification of multi-dimensional photonic entanglement stored in a quantum memory based on sparse data"

A. Tiranov, S. Designolle, E. Zambrini Cruzeiro, J. Lavoie, N. Brunner, M. Afzelius, M. Huber & N. Gisin, arXiv:1609.05033 (2016)

Quantification of multi-dimensional photonic entanglement stored in a quantum memory based on sparse data

Alexey Tiranov[1],[*] Sébastien Designolle[1], Emmanuel Zambrini Cruzeiro[1], Jonathan Lavoie[1],[†] Nicolas Brunner[1], Mikael Afzelius[1], Marcus Huber[1],[2],[‡] and Nicolas Gisin[1]

[1] *Groupe de Physique Appliquée, Université de Genève, CH-1211 Genève, Switzerland and*
[2] *Institute for Quantum Optics and Quantum Information,*
Austrian Academy of Sciences, A-1090 Vienna, Austria
(Dated: September 19, 2016)

Multi-dimensional entanglement offers interesting possibilities in quantum information e.g. quantum cryptography. Here we report the characterization of two-photon multi-dimensional energy-time entanglement between many temporal modes, after one photon has been stored in a solid-state quantum memory. We develop a method for entanglement quantification which makes use of only very sparse data, namely coincidences in the time-of-arrival basis and coherences between two neighboring temporal modes. This allows us to certify that the quantum state after storage in our experiment features at least 1.18 $e$bits of entanglement of formation. The theoretical methods we develop can be readily extended to a wide range of experimental platforms, while our experimental results demonstrate the suitability of energy-time multi-dimensional entanglement for a quantum repeater architecture.

Quantum entanglement represents a key resource for quantum information processing, e.g. in quantum communications. Of particular interest is the possibility of using multi-dimensional entangled states, which are proven to outperform standard two-qubit entangled states for a wide range of applications. In particular, high-dimensional entanglement can increase the quantum communication channel capacity [1], as well as enhance key rate and resilience to errors in quantum key distribution [2–4]. Moreover, it is also relevant for the implementation of device-independent quantum communication protocols [5], allowing for more robust Bell tests [6] and enhanced security [7].

In recent years a strong effort has been devoted to the experimental implementation of multi-dimensional entangled systems, in particular in the context of photonic experiments. Different degrees of freedom were considered, such as orbital angular momentum [8–10], frequency [11–14], spatial modes [15–17], time-bins [18–20] and energy-time [21, 22]. Several experiments also demonstrated the potential of multi-dimensional entanglement for quantum cryptography [23–26]. For this time-bins and energy-time entangled systems are suitable for implementations using optical fibres [27].

While these works open promising perspectives, the use of multi-dimensional entanglement for practical and efficient quantum communications still faces important challenges. Unavoidable losses in optical fibers require the use of quantum repeater schemes featuring quantum memories in order to reach long distances [28]. First steps were taken in realizing quantum memories beyond

qubits. Notable experiments demonstrated the storage of three-dimensional entanglement of orbital angular momentum [29, 30], as well as the implementation of a temporal multimode quantum memory capable of storing multiple entangled two-qubit pairs [31], a key step for achieving efficient entanglement distribution [32].

An important challenge consists of certifying and characterizing multi-dimensional entanglement. Indeed, the complexity of these systems (i.e. in terms of the number of parameters for characterizing their quantum state) renders usual methods, such as quantum state tomography, completely unpractical. More efficient techniques have been developed, based e.g. on compressed sensing [33, 34], but usually require partial prior knowledge of the state. In general the problem of developing reliable and efficient methods for characterizing high-dimensional entanglement based on experimentally accessible data, which is typically limited, is an active area of research [35–37].

In the present work we address both of these challenges by demonstrating the characterization of multi-dimensional energy-time entanglement stored in a solid-state quantum memory based on very sparse data. We first develop a method for quantifying multi-dimensional entanglement based on the knowledge of the diagonal elements of the density matrix, and a few off-diagonal elements. In our experiment, this corresponds to measuring in the time-of-arrival basis, and observing the coherence between neighboring temporal modes. From simple positivity constraints, our method imposes strong constraints on the remaining elements of the density matrix, despite the limited knowledge.

We demonstrate the practical relevance of the method in our quantum storage experiment, involving energy-time entanglement of a photon pair containing up to 9 temporal modes. In particular we certify that the quantum state after storage has an entanglement of formation of at least 1.18 $e$bits. To the best of our knowledge,

---

[*] alexey.tiranov@unige.ch
[†] Present address: Department of Physics and Oregon Center for Optical Molecular & Quantum Science, University of Oregon, Eugene, OR 97403, USA
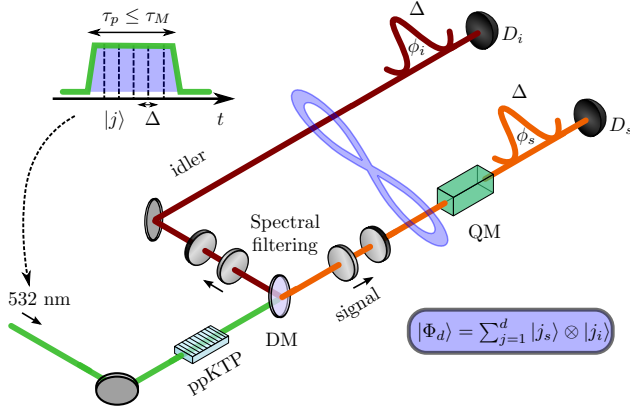[‡] marcus.huber@univie.ac.at

FIG. 1. Experimental setup. A pair of photons (signal and idler) is generated in a ppKTP waveguide via SPDC of a 532 nm pump photon. Both photons are spectrally filtered using optical cavities. Since the resulting coherence time of the photon pair is much smaller than the coherence time of the pump laser, this leads to the generation of two-photon energy-time entanglement. The signal photon is sent to a quantum memory (QM) based on a Nd^{3+}:Y_2SiO_5 crystal and stored for τ_M=50 ns. The pump laser intensity is modulated using an acousto-optic modulator to generate a square pulse with duration τ_p smaller than the storage time of the QM. Finally the photon pair is analyzed via an unbalanced interferometers, with controllable phases ϕ_s and ϕ_i and identical delays $\Delta = 5.5$ ns, and single-photon detectors (D_s and D_i). Hence the entangled state generated and measured in our experiment can be compactly described by an entangled state of d temporal modes of the form $|\Phi_d\rangle$. The experimental parameters allow for up to $d = 9$ modes.

this is the highest value certified so far in any experiment (even without storage). These results demonstrate the potential of energy-time entanglement combined with multimode quantum memories for creating and certifying multi-dimensional entanglement on long distances.

We start by presenting our experimental scheme. Energy-time entanglement between two single photons at different wavelengths is generated using spontaneous parametric down conversion (SPDC). A monochromatic continuous-wave 532 nm laser pumps a nonlinear optical waveguide (periodically poled potassium titanyl phosphate (ppKTP) waveguide) to generate the signal and idler photons at 883 nm and 1338 nm, respectively (Fig. 1). The two down-converted photons are created simultaneously and are well correlated in energy. However, the use of a monochromatic pump laser leads to an uncertainty on the photon pair creation time. This uncertainty is defined by the coherence time of the pump laser $\sim$ 1 ms and leads to energy-time entanglement between the two down-converted photons.

The entangled photon pair is filtered down to 200 MHz which corresponds to a coherence time $\tau_c \approx 2.0$ ns (the details about the SPDC source can be found in [38]). The fact that τ_c is much smaller than the coherence time of the pump laser, combined with the detection scheme

we use (see below), allow us to describe the entangled two-photon state as

$$|\Phi_d\rangle = \frac{1}{\sqrt{d}} \sum_{j=1}^{d} |j\rangle_i \otimes |j\rangle_s \ , \qquad (1)$$

where $|j\rangle_i$ ($|j\rangle_s$) denotes the state of the idler (signal) photon in temporal mode $j = 1, ..., d$.

The signal photon is coupled to the quantum memory, which is based on a rare-earth ion-doped orthosilicate crystal, Nd^{3+}:Y_2SiO_5, which is cooled down to 3 K. Photon storage is achieved via the atomic frequency comb (AFC) quantum memory protocol, implemented on the optical transition $^4I_{9/2} \longleftrightarrow ^4 F_{3/2}$ of Nd^{3+} ions. The storage time of $\tau_M = 50$ ns is predetermined, with an overall efficiency of 15%. More details about the quantum memory can be found in [39].

Finally, local measurements are performed on each photon using unbalanced interferometers (see Fig. 1). The delay $\Delta = 5.5$ ns between the short and long arms of the interferometers is bigger than the coherence time of the photon pair τ_c. In this case, the situation in which both photons passed through the short arm is indistinguishable from one where both photons travel through the long arm, leading to quantum interference in the coincidence rate [40]. In practice, two Michelson interferometers (bulk for the signal photon and fiber-based for the idler photon) with controllable phases (ϕ_s and ϕ_i on Fig. 1) and identical delays $\Delta_s = \Delta_i = \Delta$ were implemented and actively phase stabilised [41].

The experiment thus generates an energy-time entangled state between d temporal modes, of the form (1), which can also be viewed as a post-selected time-bin entangled state. The maximum number of temporal modes that is possible to couple to the QM is defined by its storage time τ_M. Thus the ratio τ_M/Δ corresponds to the maximum dimension of $d \sim 9$ for the state (1) which can be stored and certified in our experiment.

Our goal now is to characterize the multi-dimensional entanglement at the output of the quantum memory by reconstructing part of the $d^2 \times d^2$ density matrix ρ, with elements $\langle j, k|\rho|j', k'\rangle = \text{Tr}[\rho(|j\rangle_i\langle j'|_i \otimes |k\rangle_s\langle k'|_s)]$. Note however, that the measurement information at our disposal is very limited, due to the simplicity of our measurement setup. Hence we can obtain only very few elements of ρ. Specifically, we can measure: i) the diagonal of the density matrix, i.e. terms $\langle j, k|\rho|j, k\rangle$, via the time-coincide measurement, and ii) the visibility $\mathcal{V}$ between two neighboring temporal modes, i.e. terms $\langle j, j|\rho|j + 1, j + 1\rangle$, via the interference measurements. Note that a full state reconstruction of ρ would require the use of d different interferometers, and is extremely cumbersome and unpractical.

Nevertheless we will see that the limited information at our disposal is already enough to partly characterize the state, in particular leading to strong lower bounds on the entanglement of formation of ρ, E_{oF}. The latter is an operationally meaningful measure of entanglement, quanti-
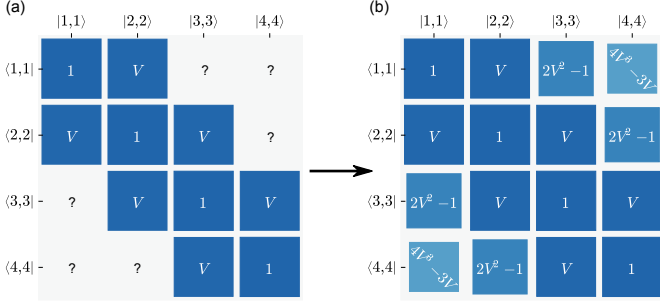
FIG. 2. Illustration of the method. Given a sub matrix where only the diagonal and first off diagonal are known (a), the method allows us to complete the matrix (b), giving lower bounds (7) on all unknown elements based on positivity constraints. Finally this construction leads to a lower bound on the entanglement of formation via relation (2).

fying how much pure entanglement (counted in $e$bits, i.e. the number of maximally entangled two-qubit pairs) is required in order to prepare ρ via an arbitrary LOCC procedure. Following Ref. [42], we have that

$$E_{oF} \geq -\log_2(1 - \frac{B^2}{2}) \;, \tag{2}$$

where we have defined the quantity B as

$$\frac{2}{\sqrt{|C|}} \left(\sum_{\substack{(j,k) \in C \\ j<k}} |\langle j,j|\rho|k,k\rangle| - \sqrt{\langle j,k|\rho|j,k\rangle\langle k,j|\rho|k,j\rangle} \right). \tag{3}$$

Note that the indices (j,k) are taken from a set C that can be chosen at will. The quantity B puts a lower bound on the concurrence of ρ [43]. For a $d\times d$ maximally entangled pure state $|\Phi_d\rangle$ one has $B = \sqrt{2(d-1)/d}$, leading to the tight bound $E_{oF} = \log_2(d)$.

Note that the evaluation of B requires only $O(d^2)$ elements of the density matrix, comparing to the total number of $d^4 - 1$. While the diagonal elements, i.e. $\langle j,k|\rho|j,k\rangle$, can be estimated in the experiment (see below), measuring all coherence terms $\langle j,j|\rho|k,k\rangle$ is still challenging and unpractical, as it requires many interferometers (with time delays $n\Delta$ with $n = 2,...,d$) with controllable phases. Nevertheless we will see now that all unknown coherence terms (e.g. $\langle j,j|\rho|k,k\rangle$ with $|k-j| \geq 2$) can in fact be efficiently lower bounded based only on accessible data.

These bounds simply follow from the requirement of the density matrix ρ to be positive semi-definite, i.e. representing a physical quantum state. We first notice that if a matrix is positive semi-definite, then it is also the case for its real part and all of its sub-matrices. Hence,

the following sub-matrix of ρ is positive semi-definite

$$\begin{pmatrix} r_{1,1} & r_{1,2} & \cdots & & r_{1,d} \\ r_{1,2} & r_{2,2} & \ddots & & \vdots \\ \vdots & \ddots & \ddots & & r_{d-1,d} \\ r_{1,d} & \cdots & r_{d-1,d} & & r_{d,d} \end{pmatrix} \tag{4}$$

where $r_{j,k} = r_{k,j} = \Re(\langle j,j|\rho|k,k\rangle)$. From Sylvester's criterion it follows that every sub-determinant of a positive semi-definite matrix should be non-negative. In particular, the following determinant of any 3×3 sub-matrix of (4) is non-negative, i.e.

$$\begin{vmatrix} r_{j,j} & r_{j,k} & r_{j,l} \\ r_{j,k} & r_{k,k} & r_{k,l} \\ r_{j,l} & r_{k,l} & r_{l,l} \end{vmatrix} \geq 0 \;, \tag{5}$$

for all $j < k < l$. We thus get the lower bound:

$$r_{j,l} \geq \frac{r_{j,k}r_{l,l} - \sqrt{(r_{j,j}r_{k,k} - r_{j,k}^2)(r_{k,k}r_{l,l} - r_{k,l}^2)}}{r_{k,k}} \;. \tag{6}$$

Notice that the square root in the above equation is real since its arguments are 2×2 sub-determinants of (5) and therefore non-negative. Moreover, even if we do not know the exact value of $r_{j,k}$ or $r_{k,l}$, but only a non-negative lower bound on them, the formula (6) remains valid. This property allows us to iteratively compute a lower bound on every element of the matrix (4), based only on its diagonal and its first off-diagonal. Finally, we can lower bound B and eventually the entanglement of formation E_{oF} via inequality (2).

Let us now focus on the situation of our experiment, for which we expect the following form of the density matrix (omitting normalization): $r_{j,j} = 1$ for $j = 1,...,d$ and $r_{j,j+1} = \mathcal{V}$ for $j = 1,...,d-1$. The bounds on the first unknown off-diagonal elements read:

$$r_{j,j+2} \geq 2\mathcal{V}^2 - 1 \quad , \quad r_{j,j+3} \geq \mathcal{V}(4\mathcal{V}^2 - 3)\,. \tag{7}$$

Hence the matrix (4), containing initially many unknown elements, can be filled iteratively, as illustrated in Fig. 2. Finally, by computing parameter B, we get a lower bound on the entanglement of formation depending on the visibility, see Fig. 3(b). In particular, for a perfect visibility $\mathcal{V} = 1$, the only compatible state is the maximally entangled one (1), and the bound becomes tight, i.e. $E_{oF} = \log_2(d)$. See Appendix B for more details.

Notice that the bounds become worse when one moves away from the diagonal. In fact, depending on the value of $\mathcal{V}$, the bound (6) becomes negative at some point, and thus the corresponding (and following) off-diagonal elements cannot be lower bounded anymore. Nevertheless, until that point, the bounds computed are useful and it can be verified that the corresponding matrix is semi-definite positive. Hence the bound on the entanglement of formation we obtain is tight. Notice also that we can play with the subset C in Eq. (3) to improve the final
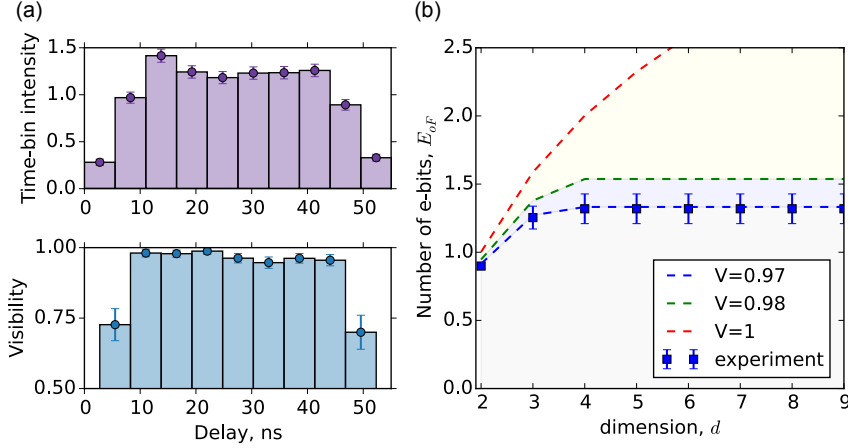
FIG. 3. Results for one experimental run. (a) The measured intensities in the time-of-arrival basis (diagonal elements $r_{j,j}$) and visibilities (first off-diagonal $r_{j,j+1}$) for 10 temporal modes, separated by $\Delta = 5.5$ ns. (b) Lower bounds for the entanglement of formation (number of $e$bits) as a function of the number d of temporal modes taken into account when reconstructing the density matrix. Here the optimal value is $\sim$1.25(11) $e$bits. The data shows good agreement with our model considering the measured visibility of $\mathcal{V}$ of 97%. The case $\mathcal{V} = 1$, corresponding to the maximally entangled state (1), gives $\log_2(d)$ $e$bits.

bound on E_{oF}. This comes from the fact that, while taking a larger set C makes the sum in Eq. (3) larger, the denominator $\sqrt{|C|}$ also grows. We find that in certain cases, better bounds on E_{oF} are obtained when considering small sets C.

To apply the above method to our experiment, we start by measuring the coherence between neighboring temporal modes, giving access to $r_{j,j+1}$. In order to do this, we use the two interferometers (Fig. 1) to extract coherences between temporal modes $|j\rangle$ and $|j + 1\rangle$. The phase of the idler interferometer ϕ_i is fixed while the phase of the signal interferometer ϕ_s is scanned over the interval $[0, 2\pi]$. For each time-bin the phase scan is done by measuring 15 points with 2 minutes per point. The coincidence rates are recorded, which correspond to local projections onto $e^{\phi_s + \phi_i}|j, j\rangle + |j + 1, j + 1\rangle$ for all $j = 1, ..., d - 1$. The visibility values are extracted by comparing number of coincidences corresponding to constructive (maximum) and destructive (minimum) interference. Results are given in Fig. 3(a). Note that the visibilities for the first and the last temporal modes are lower due to a significant change of the intensity between the two neighboring modes. The average visibility for the central temporal modes is $\sim$97%, and is limited by the interferometric stability and the multi-pair contribution from the SPDC process.

We then measure correlations in the time basis, leading to the diagonal terms $r_{j,j}$ for $j = 1, ..., d$. For this, we block the short (or long) arm of the signal interferometer to project on states $|j, j\rangle$ (or $|j + 1, j + 1\rangle$) using a mechanical switch. The results for one of the measurements is depicted in Fig. 3(a). The remaining terms of the diagonal of ρ, i.e. $\langle j, k|\rho|j, k\rangle$ are also estimated. Essentially the only contributions to these elements are the multi-pair emission of the SPDC and noise of the detectors. Since these processes are independent of the temporal

mode we assume that all diagonal terms $\langle j, k|\rho|j, k\rangle$ are equal when $j \neq k$. Based on this assumption and using our interferometers we then measure contributions from neighboring modes $\langle j, j + 1|\rho|j, j + 1\rangle$ which is approximately equal to $\approx 1\%$ and use these values for all other terms.

We analyze the data via the method discussed above in order to estimate the entanglement of formation of the state. We first lower bound each element in the submatrix (4); details are given in the Appendix. We consider all possible sub-matrices of ρ (of different sizes) and keep the one leading to the best bound on E_{oF}, see Fig. 3(b). The maximum number of $e$bits corresponds to the cases where both the measured visibilities and intensities are large and relatively constant. This is achieved by considering the central region of the pulse, excluding the edges where the intensity variation is limiting the visibility (Fig. 3(a)).

Finally we obtain a lower bound for the entanglement of formation $E_{oF} \geq 1.18(4)$ $e$bits, based on a dozen repetitions of the measurement procedure and analysis. The statistical error was measured for each experimental set and after propagated for all measurements. Moreover, this result also certifies a genuinely 3×3 entangled state, as any two-qubit state contains at most one $e$bit. More generally, our approach can be used to place lower bounds on the entanglement dimensionality given by $\log_2(d) \geq E_{oF}$.

In the above analysis we certified a minimal degree of entanglement considering all possible quantum states (density matrices) compatible with our data. It is also relevant to estimate the entanglement based on a more physical model of our experiment. Indeed, this is expected to provide a much higher estimate of the entanglement, given that we consider here only quantum states of a specific form. Specifically, considering gaussian phase

noise of the pump laser (with linewidth $\sim$1 kHz), we find that the visibility remains essentially constant for all temporal modes stored in the memory (see Appendix for details). Hence we get that $r_{j,j+n} \approx \mathcal{V}$, where $\mathcal{V}$ is the measured visibility between two neighboring modes. This allows us to get a lower bound on the entanglement of formation of 2.6 $e$bits from our measurement data which is limited by the visibility $\mathcal{V}$.

In conclusion, we characterized multi-dimensional energy-time entanglement between two photons where one photon was stored in a quantum memory and the other photon is at telecom wavelength. In particular, we certified an entanglement of formation of 1.18(4) $e$bits by developing a general method for characterizing multidimensional entangled state based on very sparse measurement data. The generality of our method may find application in other physical platforms. Combined with the use of a quantum memory our approach offers promising perspectives for quantum communications based on multi-dimensional entanglement.

Our method also serves as tool for certifying the dimensionality of entanglement. While we could certify 3×3 entanglement, higher dimension could be reached by improving the state preparation and the measurement apparatus to achieve higher visibilities, or even use additional interferometers. Another possible direction would be to perform device-independent tests of the degree of entanglement [44] and its dimensionality [45].

ACKNOWLEDGEMENTS

[1] C. H. Bennett, P. W. Shor, J. A. Smolin, and A. V. Thapliyal, Phys. Rev. Lett. 83, 3081 (1999).

[2] H. Bechmann-Pasquinucci and W. Tittel, Phys. Rev. A 61, 062308 (2000).

[3] N. J. Cerf, M. Bourennane, A. Karlsson, and N. Gisin, Phys. Rev. Lett. 88, 127902 (2002).

[4] L. Sheridan and V. Scarani, Phys. Rev. A 82, 030301 (2010).

[5] A. Acín, N. Brunner, N. Gisin, S. Massar, S. Pironio, and V. Scarani, Phys. Rev. Lett. 98, 230501 (2007).

[6] T. Vértesi, S. Pironio, and N. Brunner, Phys. Rev. Lett. 104, 060401 (2010).

[7] M. Huber and M. Pawłowski, Phys. Rev. A 88, 032309 (2013).

[8] A. Mair, A. Vaziri, G. Weihs, and A. Zeilinger, Nature 412, 313 (2001).

[9] A. Dada, J. Leach, G. Buller, M. Padgett, and E. Andersson, Nature Physics 7, 677 (2011).

[10] M. Krenn, M. Huber, R. Fickler, R. Lapkiewicz, S. Ramelow, and A. Zeilinger, Proceedings of the National Academy of Sciences USA 111, 6243 (2014).

[11] L. Olislager, J. Cussey, A. T. Nguyen, P. Emplit, S. Massar, J.-M. Merolla, and K. P. Huy, Phys. Rev. A 82, 013804 (2010).

[12] C. Bernhard, B. Bessire, T. Feurer, and A. Stefanov, Phys. Rev. A 88, 032322 (2013).

[13] X. Xing, A. Feizpour, A. Hayat, and A. M. Steinberg, Optics express 22, 25128 (2014).

[14] R.-B. Jin, R. Shimizu, M. Fujiwara, M. Takeoka, R. Wakabayashi, T. Yamashita, S. Miki, H. Terai, T. Gerrits, and M. Sasaki, arXiv 1603.07887 (2016).

[15] M. Edgar, D. Tasca, F. Izdebski, R. Warburton, J. Leach, M. Agnew, G. Buller, R. Boyd, and M. Padgett, Nature Communications 3, 984 (2012).

[16] R. Fickler, R. Lapkiewicz, M. Huber, M. P. Lavery, M. J. Padgett, and A. Zeilinger, Nature Communications 5, 5 (2014).

[17] C. Schaeff, R. Polster, M. Huber, S. Ramelow, and A. Zeilinger, Optica 2, 7 (2015).

[18] H. de Riedmatten, I. Marcikic, H. Zbinden, and N. Gisin, Quant. Inf. Comp. 2, 425 (2002).

[19] D. Stucki, H. Zbinden, and N. Gisin, Journal of Modern Optics 52, 2637 (2005).

[20] T. Ikuta and H. Takesue, Phys. Rev. A 93, 022307 (2016).

[21] R. T. Thew, A. Acín, H. Zbinden, and N. Gisin, Physical Review Letters 93, 010503 (2004).

[22] D. Richart, Y. Fischer, and H. Weinfurter, Applied Physics B 106, 543 (2012).

[23] S. Gröblacher, T. Jennewein, A. Vaziri, G. Weihs, and A. Zeilinger, New Journal of Physics 8, 75 (2006).

[24] I. Ali-Khan, C. J. Broadbent, and J. C. Howell, Phys. Rev. Lett. 98, 060503 (2007).

[25] M. Mirhosseini, O. S. Magaa-Loaiza, M. N. OSullivan, B. Rodenburg, M. Malik, M. P. J. Lavery, M. J. Padgett, D. J. Gauthier, and R. W. Boyd, New Journal of Physics 17, 033033 (2015).

[26] T. Zhong, H. Zhou, R. D. Horansky, C. Lee, V. B. Verma, A. E. Lita, A. Restelli, J. C. Bienfang, R. P. Mirin, T. Gerrits, S. W. Nam, F. Marsili, M. D. Shaw, Z. Zhang, L. Wang, D. Englund, G. W. Wornell, J. H. Shapiro, and F. N. C. Wong, New Journal of Physics 17, 022002 (2015).

[27] I. Marcikic, H. de Riedmatten, W. Tittel, V. Scarani, H. Zbinden, and N. Gisin, Phys. Rev. A 66, 62308 (2002).

[28] N. Sangouard, C. Simon, H. de Riedmatten, and N. Gisin, Rev. Mod. Phys. 83, 33 (2011).

[29] Z. Q. Zhou, Y. L. Hua, X. Liu, G. Chen, J. S. Xu, Y. J. Han, C. F. Li, and G. C. Guo, Physical Review Letters **115**, 1 (2015).

[30] D.-S. Ding, W. Zhang, S. Shi, and Z.-Y. Zhou, arXiv:1412.6188 (2014).

[31] A. Tiranov, P. C. Strassmann, J. Lavoie, N. Brunner, M. Huber, V. B. Verma, S. W. Nam, R. P. Mirin, A. E. Lita, F. Marsili, M. Afzelius, F. Bussires, and N. Gisin, arXiv:1606.07774 (2016).

[32] C. Simon, H. de Riedmatten, M. Afzelius, N. Sangouard, H. Zbinden, and N. Gisin, Phys. Rev. Lett. **98**, 190503 (2007).

[33] D. Gross, Y.-K. Liu, S. T. Flammia, S. Becker, and J. Eisert, Phys. Rev. Lett. **105**, 150401 (2010).

[34] F. Tonolini, S. Chan, M. Agnew, A. Lindsay, and J. Leach, Scientific Reports **4**, 6542 EP (2014).

[35] D. Giovannini, J. Romero, J. Leach, A. Dudley, A. Forbes, and M. J. Padgett, Phys. Rev. Lett. **110**, 143601 (2013).

[36] G. A. Howland, S. H. Knarr, J. Schneeloch, D. J. Lum, and J. C. Howell, Phys. Rev. X **6**, 021018 (2016).

[37] P. Erker, M. Krenn, and M. Huber, arXiv:1512.05315 (2015).

[38] C. Clausen, F. Bussières, A. Tiranov, H. Herrmann, C. Silberhorn, W. Sohler, M. Afzelius, and N. Gisin, New Journal of Physics **16**, 093058 (2014).

[39] C. Clausen, I. Usmani, F. Bussières, N. Sangouard, M. Afzelius, H. de Riedmatten, and N. Gisin, Nature **469**, 508 (2010).

[40] J. D. Franson, Phys. Rev. Lett. **62**, 2205 (1989).

[41] A. Tiranov, J. Lavoie, A. Ferrier, P. Goldner, V. B. Verma, S. W. Nam, R. P. Mirin, A. E. Lita, F. Marsili, H. Herrmann, C. Silberhorn, N. Gisin, M. Afzelius, and F. Bussières, Optica **2**, 279 (2015).

[42] M. Huber and J. I. de Vicente, Physical Review Letters **110**, 030501 (2013).

[43] W. K. Wootters, Quantum Info. Comput. **1**, 27 (2001).

[44] T. Moroder, J.-D. Bancal, Y.-C. Liang, M. Hofmann, and O. Gühne, Phys. Rev. Lett. **111**, 030501 (2013).

[45] N. Brunner, S. Pironio, A. Acin, N. Gisin, A. A. Méthot, and V. Scarani, Phys. Rev. Lett. **100**, 210503 (2008).

[46] J. Minář, H. de Riedmatten, C. Simon, H. Zbinden, and N. Gisin, Phys. Rev. A **77**, 052325 (2008).

APPENDIX FOR "QUANTIFICATION OF MULTI-DIMENSIONAL PHOTONIC ENTANGLEMENT STORED IN A QUANTUM MEMORY BASED ON SPARSE DATA"

In this Appendix we provide more details about experimental results and theoretical method that was implemented to quantify multi-dimensional entanglement.

Appendix A: Details of experimental results

We have performed 12 complete experiments following the method explained in the main text. Here we describe in more details one of these runs and provide details about final results.

First, we provide details about the measurement of the visibility between the neighboring temporal modes. Fig. 5 illustrates 2D image representing the coincidence measurement for different temporal modes (Delay 1) as a function of delay between two detectors D_s and D_i (Delay 2). The coincidence histograms between detectors D_s and D_i shows three peaks corresponding to different path combinations for travelling idler and signal photon after storage. By varying the phase of the interferometer ϕ_s we observe the interference for central peak which represents post-selected time-bin entangled state

$$|\Phi_d\rangle = \frac{1}{\sqrt{d}} \sum_{j=1}^{d} c_j |j\rangle_i \otimes |j\rangle_s . \qquad (A1)$$

The separation between peaks is equal to the travel-time difference between different arms of the interferometer Δ =5.5 ns (Fig. 5). The central peak is post-selected using 3 ns temporal window (Delay 2) illustrated by dashed line. We define different temporal modes by discretizing temporal pulse using period Δ (Delay 1 in Fig. 5).

We measure the visibility for each pair of neighboring temporal modes by comparing number of coincidences corresponding to destructive (Fig. 5(a)) and constructive (Fig. 5(b)) interferences between different temporal modes. The visibility is reduced at the edges of the pulse which can be seen from increased number of coincidences for destructive interference for first and last histogram bin (Fig. 5). This is explained by fast intensity variation at the beginning and at the end of the pulse which reduces the maximum achievable visibility. To measure intensity of each temporal mode c_j we block one of the arms of the signal interferometer and repeat coincidence measurement described above.

After we show the full sub-matrix reconstruction. Fig. 4 shows the sub-matrix before and after application of the theoretical method. Only elements from the first $r_{j,j}$ and second $r_{j,j+1}$ diagonals were measured experimentally using a pair of interferometers. Application of the method based on the positivity of the density matrix (described in the main text) gives a lower bound on the elements for all other diagonals ($r_{j,j+2}, r_{j,j+3}$ and so on).

(a)

	|1,1⟩	|2,2⟩	|3,3⟩	|4,4⟩	|5,5⟩	|6,6⟩	|7,7⟩	|8,8⟩	|9,9⟩	|10,10⟩
⟨1,1|	0.28	0.38								-
⟨2,2|	0.38	0.97	1.14							
⟨3,3|	-	1.14	1.41	1.29						
⟨4,4|	-		1.29	1.24	1.19					-
⟨5,5|	-			1.19	1.18	1.16				-
⟨6,6|	-				1.16	1.23	1.16			-
⟨7,7|	-					1.16	1.23	1.19		-
⟨8,8|	-						1.19	1.26	1.01	-
⟨9,9|	-							1.01	0.89	0.38
⟨10,10|	-								0.38	0.33

(b)

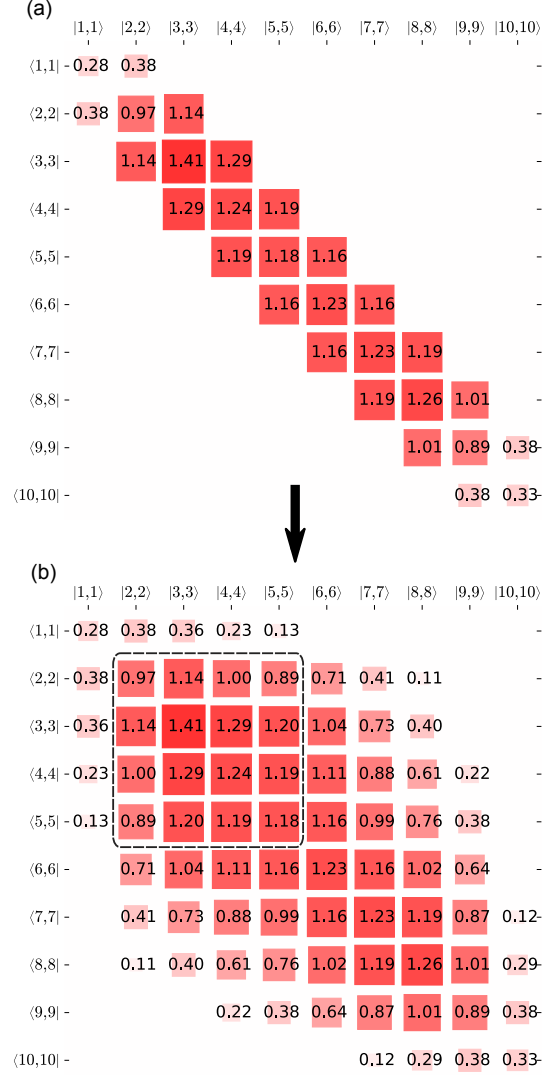|	|1,1⟩	|2,2⟩	|3,3⟩	|4,4⟩	|5,5⟩	|6,6⟩	|7,7⟩	|8,8⟩	|9,9⟩	|10,10⟩
⟨1,1|	0.28	0.38	0.36	0.23	0.13					-
⟨2,2|	0.38	0.97	1.14	1.00	0.89	0.71	0.41	0.11		
⟨3,3|	0.36	1.14	1.41	1.29	1.20	1.04	0.73	0.40		
⟨4,4|	0.23	1.00	1.29	1.24	1.19	1.11	0.88	0.61	0.22	-
⟨5,5|	0.13	0.89	1.20	1.19	1.18	1.16	0.99	0.76	0.38	-
⟨6,6|	-	0.71	1.04	1.11	1.16	1.23	1.16	1.02	0.64	-
⟨7,7|	-	0.41	0.73	0.88	0.99	1.16	1.23	1.19	0.87	0.12
⟨8,8|	-	0.11	0.40	0.61	0.76	1.02	1.19	1.26	1.01	0.29
⟨9,9|	-			0.22	0.38	0.64	0.87	1.01	0.89	0.38
⟨10,10|	-						0.12	0.29	0.38	0.33

FIG. 4. Illustration of the sub matrix reconstruction for experimental data of one run. The values were normalized with respect to the maximum dimension (10 in this case).

These elements are further used to give a lower bound on the entanglement of formation E_{oF} based on expression from Ref. [42]

$$E_{oF} \geq -\log_2(1 - \frac{B^2}{2}) , \qquad (A2)$$

where we have defined the quantity B as

$$\frac{2}{\sqrt{|C|}} \left(\sum_{\substack{(j,k)\in C \\ j<k}} |\langle j,j|\rho|k,k\rangle| - \sqrt{\langle j,k|\rho|j,k\rangle\langle k,j|\rho|k,j\rangle} \right) . \qquad (A3)$$

The sub-matrix which gives maximum value of E_{oF} is indicated by a dashed line.

Same set of data was accumulated many times and for each the certified number of $e$bits was calculated. Due to
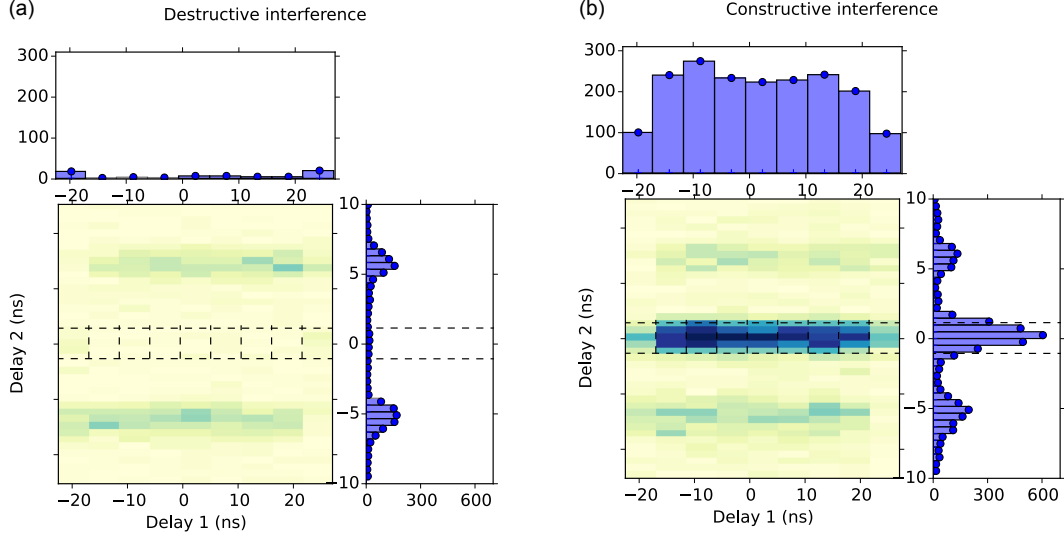
FIG. 5. Example of the interference measurement corresponding to destructive and constructive interference between neighboring temporal modes. From this measurement we extract the visibilities corresponding to different pairs of neighboring temporal modes.
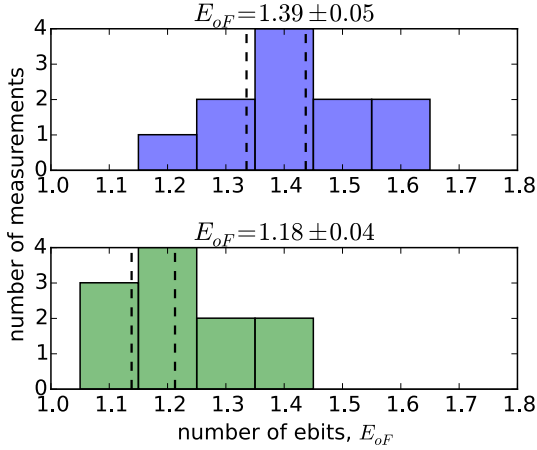

FIG. 6. Summary of all results without (a) and including white noise contribution (b).

the instability of each interferometer the visibility value varied from time to time. The average visibility of 97% was measured. Final certified values of entanglement of formation are given in Fig. 6 and are all above one for both cases without or including white noise contribution which modifies the diagonal element of the density matrix and reduces certified number of *e*bits.

Appendix B: Bounds on entanglement: noise sensitivity

We discuss here in more details the characterization of the density matrix obtained via the method described in the main text. In particular we consider again the

situation expected from our experiment, that is, $r_{j,j} = 1$ and $r_{j,j+1} = \mathcal{V}$. Applying the method, we get the following bounds for the (unmeasured) coherence terms

$$
\begin{aligned}
r_{j,j+2} &\geq 2\mathcal{V}^2 - 1 \\
r_{j,j+3} &\geq \mathcal{V}(4\mathcal{V}^2 - 3) \\
r_{j,j+4} &\geq 8\mathcal{V}^4 - 8\mathcal{V}^2 + 1 \\
r_{j,j+5} &\geq \mathcal{V}(16\mathcal{V}^4 - 20\mathcal{V}^2 + 5).
\end{aligned}
\tag{B1}
$$

Based on these bounds, one can then obtain a lower on the entanglement of formation, as discussed in the main text. In Fig. (7) we plot the obtained bound on E_{oF} as a function of the dimension of the quantum state. We consider different values of the visibility $\mathcal{V}$. For $\mathcal{V} = 1$, one obtains $E_{oF} = \log_2(d)$, which corresponds to the maximally entangled state of dimension $d \times d$, i.e. $|\Phi_d\rangle$. Notice that the maximally entangled state is here the only quantum state compatible with the requirement that $\mathcal{V} = 1$. For $\mathcal{V} < 1$, one can see that the bound on E_{oF} reaches a maximum (for some dimension, which depends on the value of $\mathcal{V}$) and then remains constant. Hence for limited visibility $\mathcal{V} < 1$, there is a maximal amount of E_{oF} that can be certified, independent of the Hilbert space dimension.

Appendix C: Physical model of the phase noise

The visibility measured for bigger interferometric delays will monotonically decrease due to the finite linewidth of the pump laser. The phase noise of the pump laser can be approximated by gaussian distribution with standard deviation $\delta\phi$. In this case the visibility scales as $\mathcal{V} \sim e^{-\delta\phi^2/2}$ [46]. In our case for different temporal
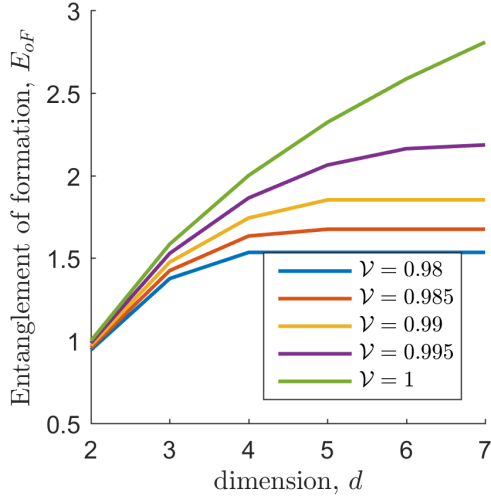
FIG. 7. Lower bound on the entanglement of formation (in terms of number of ebits) as a function of the dimension d, for visibilities $\mathcal{V}$ from 1 to 0.98.

modes separated by $n\Delta$ delay we can rewrite it as

$$\mathcal{V}_n = \mathcal{V}_1 e^{-2(\pi\delta\nu n\Delta)^2}, \tag{C1}$$

where $\delta\nu$ is the spectral linewidth of the pump laser and $\mathcal{V}_1$ is the visibility between neighboring modes.

Assuming a full-width half-maximum linewidth of the pump laser of 1 kHz and a maximum delay between temporal modes of 50 ns, the expected visibility remains almost constant decreasing only by a factor 0.999. This verifies our approximation of coherent sum between all temporal modes generated and stored in the quantum memory.

"Spectral hole lifetimes and spin population relaxation dynamics in neodymium-doped yttrium orthosilicate"

E. Zambrini Cruzeiro, A. Tiranov, I. Usmani, C. Laplane, J. Lavoie, A. Ferrier, P. Goldner, N. Gisin & M. Afzelius, arXiv:1611.05444 (2016)

Spectral hole lifetimes and spin population relaxation dynamics in neodymium-doped yttrium orthosilicate

E. Zambrini Cruzeiro,[1] A Tiranov,[1] I. Usmani,[2] C. Laplane,[1]
J. Lavoie,[1, *] A. Ferrier,[3, 4] P. Goldner,[3] N. Gisin,[1] and M. Afzelius[1, †]

[1]*Groupe de Physique Appliquée, Université de Genève, CH-1211 Genève 4, Switzerland*
[2]*Laboratoire Charles Fabry, Institut d'Optique Graduate School, CNRS, Université Paris-Saclay, 91127 Palaiseau, France*
[3]*PSL Research University, Chimie ParisTech, CNRS, Institut de Recherche de Chimie Paris, 75005, Paris, France*
[4]*Sorbonne Universites, UPMC Univ Paris 06, 75005, Paris, France*
(Dated: November 15, 2016)

We present a detailed study of the lifetime of optical spectral holes due to population storage in Zeeman sublevels of Nd^{3+}:Y_2SiO_5. The lifetime is measured as a function of magnetic field strength and orientation, temperature and Nd^{3+} doping concentration. At the lowest temperature of 3 K we find a general trend where the lifetime is short at low field strengths, then increases to a maximum lifetime at a few hundreds of mT, and then finally decays rapidly for high field strengths. This behaviour can be modelled with a relaxation rate dominated by Nd^{3+}-Nd^{3+} cross relaxation at low fields and spin lattice relaxation at high magnetic fields. The maximum lifetime depends strongly on both the field strength and orientation, due to the competition between these processes and their different angular dependencies. The cross relaxation limits the maximum lifetime for concentrations as low as 30 ppm of Nd^{3+} ions. By decreasing the concentration to less than 1 ppm we could completely eliminate the cross relaxation, reaching a lifetime of 3.8 s at 3 K. At higher temperatures the spectral hole lifetime is limited by the magnetic-field independent Raman and Orbach processes. In addition we show that the cross relaxation rate can be strongly reduced by creating spectrally large holes of the order of the optical inhomogeneous broadening. Our results are important for the development and design of new rare-earth-ion doped crystals for quantum information processing and narrow-band spectral filtering for biological tissue imaging.

I. INTRODUCTION

Rare-earth (RE) ions doped into solid-state materials (amorphous or crystalline) are currently investigated in the domain of quantum technology for both storing and processing quantum information [1, 2]. A strong motivation behind this effort is the long optical and spin coherence times that can be achieved at low temperatures [3, 4]. The large number of RE ions that can be considered (RE = Eu, Pr, Tm, Nd, Er, Yb, Ce, etc.) also implies a wide range of possibilities in terms of optical wavelength (ultraviolet to near-infrared), spin transition frequencies (MHz to GHz) and transition dipole moments of the relevant optical and spin transitions [5].

The RE ions can be grouped into Kramers or non-Kramers ions, depending on the number of $4f^N$ electrons in the RE^{3+} state of the ion [5]. Kramers ions have an odd number of electrons, while non-Kramers ions have an even number of electrons. In low-symmetry crystallographic sites, the non-Kramers ions have a completely lifted J degeneracy and the ground state spin structure results from nuclear Zeeman and nuclear quadrupole type interactions. These nuclear states generally have long coherence times [4, 6] and can be used as qubits [7, 8] or as long-duration storage states for optical quantum memo-

ries [9–11]. However, the spin transition frequencies are low, in the 10-100 MHz range, which limits the useful bandwidth and the speed with which one can manipulate the spin states.

In Kramers ions the degeneracy is not completely lifted by the interaction with the crystal lattice. In low-symmetry crystallographic sites, Kramers ions have a two-fold J degeneracy of the ground state (a Kramers doublet). The doublet can often be treated as an effective $S = 1/2$ spin with a magnetic moment in the range of 1 - 10 Bohr magnetons μ_B (in erbium as high as $15\mu_B$). This effective spin model can break down at high magnetic fields and/or low crystal-field splittings [12]. Using Kramers doublets one can achieve spin transition frequencies in the GHz range by applying a moderate magnetic field, which implies large bandwidth and fast operations. Several Kramers ions also have relevant optical transitions that are easily accessible with diode lasers, such as Nd (883 nm), Yb (980 nm) or Er (1530 nm), an important practical aspect. On the other hand, the large magnetic moments of Kramers ions couple more strongly to lattice phonons and to other magnetic ions in the lattice, which might shorten the spin population (T_1) and coherence (T_2) times, as well as the optical coherence lifetimes, with respect to non-Kramers ions. To fully exploit the advantages of Kramers ions it is therefore important to understand and optimise their spin properties.

In this article the focus is on the spin relaxation mechanisms of a Kramers ion. The relaxation processes strongly affect the degree of spin polarization that can be achieved through optical pumping, which is a crucial step

---

for quantum processing and storage schemes using both single spins and ensembles of spins. The spin population lifetime also puts an upper limit on the achievable spin coherence time such that $T_2 \leq 2T_1$. A long spin population time is thus a basic requirement for many quantum applications.

Optical pumping and partial spin polarization in Kramers doublets was first observed by Macfarlane and Vial in Nd^{3+}:LaF_3 [13]. Specifically, they used spectral hole burning (SHB) to optically pump ions into a Kramers sub-level for a small sub-ensemble of ions in the large optical inhomogeneous broadening. Only recently, however, the optical pumping using Kramers doublets received renewed interest in the context of quantum light storage experiments [14–16]. There, efficient optical pumping using SHB is a requirement for achieving high storage efficiencies. This led to a few limited studies of spin population lifetimes measured using SHB. In both neodymium and erbium doped single crystals the lifetimes have been limited to about 100 ms [14, 17, 18], which in turn reduces the maximum efficiency of quantum storage protocols [19]. In general the lifetime limitation is thought to be due to the spin-lattice relaxation (SLR) and/or spin cross relaxation (flip-flop or FF) processes [20, 21]. But the relative importance of these two processes remains unknown, particularly at the low doping concentrations often used in the context of quantum storage experiments (<100 ppm).

In this article we experimentally characterize the spin population dynamics of a Kramers ion, as a function of the applied magnetic field, temperature and dopant concentration. Specifically, we study neodymium-doped Y_2SiO_5 crystals, which is a typical Kramers case that we believe is representative of a large class of Kramers-ion doped crystals. One of our main findings is that the spin FF process is limiting the spectral hole lifetime at concentrations as low as 30 ppm. Only in a extremely low-doped sample (< 1 ppm) did we measure a spectral hole lifetime solely limited by the SLR, where the lifetime approaches 4 seconds at low magnetic fields. As the neodymium ion has a moderate magnetic moment among Kramers ions, we expect that the spin FF process has a large impact on the spectral hole lifetime of many Kramers doublets.

The article is organized as follows. In Sec. II we discuss the different relaxation processes (SLR and spin FF) and their expected dependence on relevant experimental parameters. We also discuss the difference in measuring the population lifetime using SHB and more conventional electron paramagnetic resonance (EPR) experiments. In Sec. III, we discuss basic properties of neodymium-doped Y_2SiO_5 and the employed experimental methods. In Sec. IV we present measurements of the spectral hole lifetime as a function of the external magnetic field (in Sec. IV A), temperature (Sec. IV B), neodymium concentration (Sec. IV C) and overall spin polarization (Sec. IV D). In Sec. V we summarize our results and give an outlook on possible future experiments.
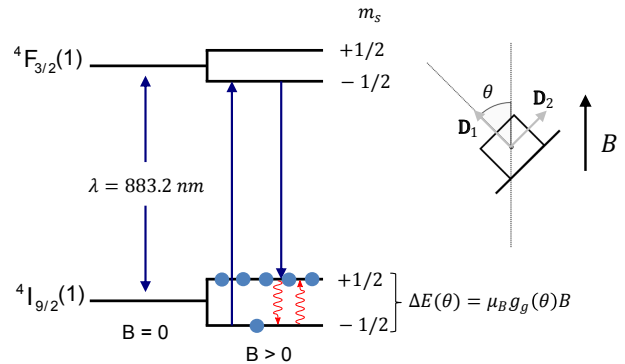

FIG. 1. Kramers doublet splitting under an external magnetic field B for the case of Nd^{3+}:Y_2SiO_5. Each crystal field level within the electronic states $^4I_{9/2}$ and $^4F_{3/2}$ consists of two magnetic sublevels $m_s = \pm 1/2$. Note that only the lowest crystal field level of each electronic state is shown here. The magnetic sublevels become non-degenerate under the presence of a magnetic field. The splitting in energy depends linearly on the magnetic field B and on the effective g factor $g(\theta)$, which characterizes the angular dependence of the splitting. On the right, the convention used for the magnetic field angle θ is shown. The magnetic field is static and is applied in the D_1-D_2 plane, where D_1 and D_2 are the so-called polarization extinction axes of Y_2SiO_5 crystal. Absorption is maximal when the polarization of light is linear and aligned with D_1.

II. THEORY

A. Kramers doublets

We here consider the electronic ground state $^{2S+1}L_J$ of a Kramers ion such as neodymium, ytterbium or erbium. If the site symmetry of the ion is sufficiently low, then the interaction with the crystal lattice splits the $2J + 1$ magnetic sublevels into $J + 1/2$ Kramers doublets. At the low temperatures considered here ($3 \leq T \leq 5.5$ K), only the lowest Kramers doublet is populated. Moreover, only the doublet with the lowest energy typically has long population lifetimes, while the other doublets have very short lifetimes due to fast phonon emission towards the lowest doublet. We note also that the optically excited state is also a Kramers doublet, although its spin dynamics is not characterized in this work. In the following, all experimental data relates to the lowest doublet in the electronic ground state (Fig. 1).

Under application of a magnetic field each doublet splits into two levels. The doublet can be modelled as a spin-half system $S = 1/2$ with a corresponding spin Hamiltonian $\mathbf{H} = \mu_B \mathbf{B} \cdot \tilde{g} \cdot \mathbf{S}$ [22]. Here μ_B is the Bohr magneton, $\mathbf{B}$ is the magnetic field vector, $\tilde{g}$ the g factor matrix and $\mathbf{S}$ the spin operator vector. The $\tilde{g}$ matrix is often highly anisotropic, which results in a strong angular dependence of the Zeeman energy split ΔE. In this work we vary the magnetic field in a certain plane (see Fig. 1), such that the energy split can be written in

terms of an effective, angle-dependent g factor $g(\theta)$, i.e. $\Delta E(\theta) = \mu_B g(\theta) B$.

At a given temperature T, the ratio of spins in the two levels is given by the Boltzmann distribution for a system in thermal equilibrium. At 3 K, and for magnetic fields around 1 T, these levels are roughly equally populated, given that $g(\theta)$ varies between 1.5 and 2.7 in the plane of interest (see Fig. 1) [23]. The goal of optical pumping is to create a population distribution far from thermal equilibrium, such as a completely spin-polarized state with all ions in one of the doublet states. After the optical pumping the spins will rethermalize because of the different population relaxation mechanisms. This, in turn, will limit both the time during which the desired state can be used and the maximum degree of spin polarization that can be achieved. We will therefore start by discussing the different relaxation mechanisms that are relevant for Kramers ions at low temperatures.

B. Spin lattice relaxation

The Kramers doublet states can thermalize to the bath temperature through different interactions with phonons, which together are denoted as spin lattice relaxation (SLR) [24–27]. The SLR rate is a single-ion property, i.e. it has no dependence on the concentration of paramagnetic ions. In some rarer cases, however, a spin concentration dependence can be observed due to the "phonon bottleneck" phenomenon [25].

There are three main types of SLR processes; direct, Raman and Orbach. The direct process involves the absorption or emission of a phonon with the same energy as the doublet energy separation $\Delta E(\theta)$. This process is thus strongly dependent on the density of phonons at a given energy, which scales as $\Delta E^2(\theta)$. The Raman and Orbach processes, on the other hand, are two-phonon processes. The Raman process only requires a two-phonon resonance and therefore uses a larger range of the phonon spectrum. The Orbach process is resonantly enhanced by also involving a one-phonon resonance with a second Kramers doublet, with an energy separation Δ_O with respect to the ground state doublet. The three processes add up to a total SLR rate that can be written as [26, 27],

$$R_{SLR} = \alpha_D(\theta)g^3(\theta)(\mu_B B)^5 \coth\left(\frac{\Delta E(\theta)}{2k_B T}\right) + \alpha_R T^9 + \alpha_O e^{-\frac{\Delta_O}{k_B T}}, \quad (1)$$

where α_D, α_R, α_O are the coupling parameters for the direct, Raman and Orbach processes, respectively.

The Raman and Orbach processes are strongly temperature dependent, but they normally have no magnetic-field dependence. A field dependence might appear, however, if the Zeeman split $\Delta E(\theta)$ becomes comparable to the crystal-field split with respect to the first excited crystal-field level [27]. Since all experiments presented in this article are far from this regime we consider the Raman and Orbach processes to be field-insensitive.

Kurkin and Chernov [28] have measured the Raman and Orbach coupling parameters in Nd^{3+}:Y_2SiO_5 using EPR techniques. They found $\alpha_R = 1.2 \cdot 10^{-5}$, $\alpha_O = 3.8 \cdot 10^{10}$ and $\Delta_O/k_B = 97$ K (for the crystallographic site relevant to this article, see Sec. III A). Using these parameters we calculate that, for temperatures of 3 and 5 K, the Raman and Orbach processes combined amount to a SLR rate of 0.24 and 166 Hz, respectively. These rates correspond to population lifetimes of 4.2 s and 6 ms, respectively. For efficient optical pumping the population lifetime must be much longer than the radiative lifetime of the optically excited state (see Sec. III B), which is 300 μs in Nd^{3+}:Y_2SiO_5 [14]. One can thus immediately conclude that for Nd^{3+}:Y_2SiO_5 pumping cannot be efficient at a temperature of 5 K or above. Since Raman and Orbach parameters have been measured for many Kramers ions in different host crystals, such a simple analysis permits to evaluate below which temperature efficient optical pumping could potentially be achieved.

The direct process is only weakly dependent on temperature, as compared to Raman and Orbach, but displays a strong dependence on both the angle and magnitude of the magnetic field. As a consequence much less information can be found in the literature, typically the direct contribution to the relaxation rate is characterized only for a fixed angle and magnetic field, such as for Nd^{3+}:Y_2SiO_5 [29]. In the limit where $\Delta E \ll 2k_B T$, which holds for most of the data presented in this article, the direct process scales as $\alpha_D(\theta)g^2(\theta)B^4$. There is thus often a known angular dependence due to $g^2(\theta)$, but the angular dependence in the coupling parameter $\alpha_D(\theta)$ is generally unknown. One of the goals of this work is to measure $\alpha_D(\theta)$ in Nd^{3+}:Y_2SiO_5.

C. Cross relaxation

Another type of spin relaxation process is the cross relaxation between two spins [27, 30, 31], which is also called the spin flip-flop (FF) process. If two spins with the same energy splitting ΔE are spatially close enough they can swap excitation through a magnetic dipole-dipole interaction. As a consequence it depends on the concentration of spins. In EPR experiments the cross relaxation process is often considered between two different types of paramagnetic ions, ensembles A and B, which are tuned into resonance by making their $g(\theta)$ factors similar for specific angles of the magnetic field [27]. If ensemble A has been saturated by an initial microwave pulse, its spins can relax by flip-flopping with the ensemble B spins, causing an increased relaxation rate at those specific angles of the magnetic field.

In our experiment we perform optical pumping using spectral hole burning and we need to consider how cross-relaxation can affect the lifetime of the spectral hole. The spectral hole burning creates a strongly spin-polarized

ensemble A for a small frequency range within the large optical inhomogeneous broadening. All other spins, ensemble B, remain, however, in a thermal distribution between the two spin states (see Fig. 2). We stress that ensembles A and B both contain Nd^{3+} ions with identical spin properties, but whose optical frequencies are different (Fig. 2). In typical spectral hole lifetime measurements [17, 32], ensemble A contains much less than 1% of the total number of spins. For some broadband quantum memory applications, this fraction can approach 10% [33, 34]. We note that the effect of spin flip-flops on the spectral hole lifetime has also been considered in EPR experiments [31]. There, however, only off-resonant flip-flops can cause a decay of the *spin* hole, while in our case resonant spin flip-flops can cause a decay of the *optical* hole.

In our spin flip-flop model we assume that there is no correlation between the inhomogeneous broadening of the spin transition and the optical transition. Hence, the spectral hole only appears on the optical transition and not on the spin transition where the A and B spins cannot be distinguished in frequency, i.e. in ΔE. As a consequence there are always many spins within ensemble B that can resonantly spin flip-flop with the initially spin-polarized ensemble A, effectively causing a fast relaxation and a limitation in the initial spin polarization that can be achieved for ensemble A. This is true as long as $\Delta E \ll 2k_B T$, while in the opposite limit a very different behaviour can be expected depending on if spins A are polarized into the upper or lower energy level.

The calculation of the cross-relaxation rate between identical spins having isotropic g tensors was first considered by Portis [30], in the limit of equally populated spin states ($\Delta E \ll 2k_B T$). Böttger et al. [20] proposed a modified formula which is valid for any temperature range, which can be written as,

$$R_{FF} = \alpha_{FF} \frac{g^4 n^2}{\Gamma} \operatorname{sech}^2\left(\frac{\Delta E(\theta)}{2k_B T} \right), \qquad (2)$$

where α_{FF} is the coupling parameter, Γ is the inhomogeneous spin linewidth and n is the concentration of dopant ions.

In the case of spins with anisotropic g tensors the calculations are much more complicated [35]. In the Supplementary Material we use a simpler approach to calculate the expected angular dependence of the average spin flip-flop rate. It is based on a dipole-dipole interaction and Fermi's golden rule. Our calculations show that one can not simply replace the isotropic g factor in Eq. (2) with the effective $g(\theta)$ factor for anisotropic spins. In some cases one can still derive simple formulas for the angular dependence, such as for g tensors with axial symmetry and measurements in planes containing the principal axes of the g tensor. In general, however, the angular dependence of the rate cannot be written as a simple formula. Therefore we henceforth write the FF rate as

$$R_{FF} = \beta_{FF}(\theta) \frac{n^2}{\Gamma} \operatorname{sech}^2\left(\frac{\Delta E(\theta)}{2k_B T} \right), \qquad (3)$$
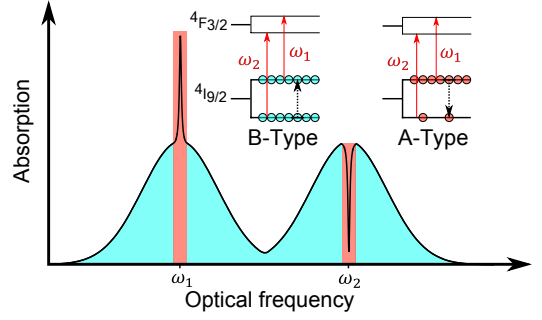

FIG. 2. Illustration of the creation of two spin populations by spectral hole burning on an optical transition within a four-level system as shown in Fig. 1. For simplicity we assume that only two transitions are allowed, originating from each $^4I_{9/2}$ spin level. These optical transitions are inhomogeneously broadened with average frequencies ω_1 and ω_2. A narrow hole is burnt into the ω_2 absorption line by optically pumping the spins into the upper $^4I_{9/2}$ spin level. This creates a highly polarized spin ensemble in that narrow spectral region, denoted ensemble as A (in red), while the remaining ions have a thermal distribution, denoted ensemble as B (in cyan). A spin of ensemble A can flip-flop with a spin of ensemble B, as depicted by dashed arrows. This causes a decrease in the spin polarization of ensemble A and a time-dependent decay of the spectral hole. The associated increase in absorption on the ω_1 line is not measurable since it is distributed over the large spectral region made up of ensemble B spins.

where the angular dependence is in the parameter $\beta_{FF}(\theta)$.

We further note that for the range of fields and temperatures considered here, the $\operatorname{sech}^2(\Delta E/2k_B T)$ term is close to 1, such that one would expect a very weak B-field dependence of the FF rate. But on the contrary we will show experimental evidence of a strong B dependence of the FF process, prompting a modification of Eq. (3). Similar results were recently observed in an erbium-doped silicate fiber [21] and we will discuss the similarities and differences with respect to that work in relation to the experimental results in Sec. IV A.

III. EXPERIMENTAL DETAILS

A. Nd^{3+}-doped Y_2SiO_5

The Y_2SiO_5 host crystal is interesting because its low nuclear spin density generally results in long optical and hyperfine coherence times when doped with RE ions [4, 6, 20, 36]. The optical properties of $Nd^{3+}:Y_2SiO_5$ have been studied since the mid 1980s for its use as a laser medium [37–40]. The $Nd^{3+}:Y_2SiO_5$ crystal was first introduced in the field of quantum information with the demonstration of storage of light at the single-photon level in 2010 [14]. Since then it has been used in numerous quantum storage experiments [15, 33, 41–43] and in coherent storage of microwave excitations [23]. A nanophotonic cavity has also been fabricated in a $Nd^{3+}:Y_2SiO_5$

crystal, showing enhanced interaction between Nd^{3+} ions and light [44].

The optical transition of interest for coherent light-matter interactions is between the lowest Kramers doublet in the electronic ground state $^4I_{9/2}$ and in the electronically excited state $^4F_{3/2}$. The radiative lifetime of the excited state is about 300 µs [14], one of the shortest of any RE ion with an optical transition having good coherence properties. The short lifetime makes optical pumping more efficient, given a fixed spin population lifetime, as compared to RE ions having long radiative lifetimes such as erbium (about 10 ms).

The Nd^{3+} ions replace Y^{3+} ions in two possible crystallographic sites in the lattice [29], both having a site symmetry of C_1. In this work only ions in site 1 are studied, following the site notation of Ref. [38], since the corresponding absorption coefficient is higher. The transition wavelength for site 1 is 883.0 nm (11325 cm^{-1}). We note that this site notation is inverted with respect to the EPR notation introduced in Ref. [29].

All crystals we use have a natural abundance of Nd^{3+} isotopes, hence 80% with zero nuclear spin $I = 0$ (with even atomic mass number) and 20% with nuclear spin $I = 7/2$ (12.2% ^{143}Nd and 8.3% ^{145}Nd). For the isotopes with $I = 7/2$ the ground state has more than the two levels of the simple Kramers doublet. The coupling to the nuclear spin also affects the population lifetime and opens up more decay channels. In this work we aimed at only characterizing even isotopes with $I = 0$. In Sec. III B we discuss how we could extract lifetimes that, to a high confidence, only pertain to even isotopes.

Part of this work concerns the concentration dependence of the spectral hole lifetime, therefore we study three crystals with different concentrations. We use a crystal nominally doped with 30 ppm Nd^{3+} grown by Scientific Materials and another one with 75 ppm grown by us. The latter crystal was grown by the Czochralski method using an inductively heated irridium crucible. The starting oxides were of at least 99.99% purity (Alfa Aesar). We also used a crystal more strongly doped with Eu^{3+} (1000 ppm), which contains a residual concentration of Nd^{3+}. Using absorption spectroscopy we estimated the Nd^{3+} concentration to be 0.5 ± 0.3 ppm. Since we expect no cross relaxation between Nd^{3+} and Eu^{3+} ions this crystal represents in a good approximation a pure Nd^{3+}:Y_2SiO_5 crystal with extremely low Nd^{3+} concentration.

All crystals were cut along the polarization extinction axes $\mathbf{D_1}$,$\mathbf{D_2}$ and $\mathbf{b}$ [45], where $\mathbf{b}$ coincides with the unit cell axis that has C_2 symmetry. Light was propagating along $\mathbf{b}$ with its polarization along $\mathbf{D_1}$ for highest absorption. The crystals had peak absorption coefficients of $\alpha_{30} = 3$ cm^{-1} [14], $\alpha_{75} = 7.4$ cm^{-1} [33] and $\alpha_{0.5} = 0.05$ cm^{-1} (at zero magnetic field). The magnetic field was applied in the $\mathbf{D_1}$-$\mathbf{D_2}$ plane where all ions are magnetically equivalent. Out of this plane the ions split into two magnetically non-equivalent sub-ensembles, related by the C_2 symmetry around $\mathbf{b}$, having different

Zeeman splittings $\Delta E(\theta)$. This would complicate the interpretation of the data, since these are expected to have different spin population lifetimes.

B. Spectral hole decay measurements

Spectral hole burning (SHB) is a common technique to measure spin dynamics of RE ions at low temperatures [17, 21, 32, 46, 47]. It consists of a burn pulse that optically pumps ions out of a specific ground state, either to the optically excited state or to another ground state through spontaneous emission. By pumping for a long time with respect to the excited state lifetime T_1^{opt} one can polarize most of the spins in a particular ground state, as shown in Fig. 1. This requires that the spectral hole lifetime $T_1^{\text{SHB}} = 1/(R_{\text{FF}} + R_{\text{SLR}})$ is much longer than T_1^{opt} and that the branching ratio of the two optical transitions is high enough as discussed thoroughly in Refs [19, 48, 49].

To probe the hole a second optical pulse measures the population of the optically pumped state after some delay, which allows one to measure the recovery of the thermal population. In our case the shortest delay was much longer than T_1^{opt}, such that the recovery only involved spin dynamics. We also emphasize that we measure the spectral hole area, such that we are not sensitive to spectral diffusion which can decrease the hole amplitude through a time-dependent broadening of the hole. In general we did not observe spectral diffusion in these measurements. Therefore, measuring the decay of the hole area or the hole depth is equivalent in our case.

For all the measurements presented in this article we observed recovery signals consisting of a short decay on the scale of 100 ms or less and a long decay of a few seconds. The hole depth related to the short decay depends strongly on the magnetic field strength, for a fixed angle, and there is a clear correlation with the lifetime given by the decay constant. For some fields this depth corresponded to almost the entire optical depth, which means that it cannot stem from odd isotopes with nuclear spin $I = 7/2$ as these only make up 20% of the ensemble (and hence the total optical depth). In general we can be certain that holes deeper than about 20% cannot come from odd isotopes. We therefore assume that the short decays with large amplitudes stem from even isotopes with no nuclear spin $I = 0$. Each data set for a fixed field angle was examined in this way and only the decay constants of sufficiently deep holes were selected for the final analysis. This limited our measurements to a certain magnetic field range, depending on the crystal (i.e. doping concentration) and the field angle θ.

The long decay is related to a much smaller relative fraction of the hole depth which is consistent with a contribution to the hole from odd isotopes with $I = 7/2$. The related hole depth is much less dependent on the magnetic field strength and angle, which is also consistent with its much longer lifetime that would make optical

pumping efficient for any field configuration. We have also performed a few SHB measurements on an isotopically enriched ^{145}Nd^{3+}:Y$_2$SiO$_5$ crystal, supporting this hypothesis. The characterization of hyperfine population lifetimes is out of the scope of this article.

C. Experimental setup

The crystal is placed in an optical cryostat which can be cooled down to 3 K. A superconducting magnet mounted inside can produce a variable magnetic field between 0 and 2 T. The crystal is rotated with respect to the magnetic field using a piezo stage. In the center of the rotator there is a small 1.5 mm hole such that a laser beam can pass through the crystal and rotator. The 883.0 nm laser beam is derived from a continuous-wave external cavity diode laser. An acousto-optic modulator (AOM) is used to modulate the intensity and frequency of light. The AOM was used to create the burn and probe pulses, and to scan the probe pulse a few tens of MHz around the spectral hole. A digital-delay generator creates all the trigger signals for the experiment, while an arbitrary function generator drives the AOM.

IV. RESULTS AND DISCUSSION

A. Magnetic field dependence

In a first series of measurements we study the spectral hole lifetime T_1^{SHB} as a function of the magnetic field strength for eight fixed angles. The Nd^{3+} concentration was 30 ppm and the crystal was cooled to the temperature of 3 K. Three examples of experimental data sets are shown in Fig. 3 for $\theta = 0°$ ($\mathbf{D}_1$ axis), $\theta = 90°$ ($\mathbf{D}_2$ axis) and $\theta = 120°$.

All measurements display the same general trend as a function of field strength. At low fields the lifetime is small, typically below 10 ms. By increasing the magnetic field one can reach the maximal lifetime at a certain point in the range 0.3-0.6 T, depending on the angle, after which it starts to decrease again. Note that in Fig. 3 we show the data that was retained for the final fit to the model, using the procedure discussed in Sec. III B, but the general trend of a reduction in hole lifetime with decreasing field continues towards zero field. For lower fields, however, it becomes increasingly difficult to use our method for extracting lifetimes of even isotopes with respect to odd isotopes (see Sec. III B).

The decrease in spectral hole lifetime in the high-field limit is well understood. It is due to the increase in the SLR rate caused by the direct phonon process. As discussed in Sec. II B the spectral hole lifetime is expected to scale as $T_1^{\mathrm{SHB}} \propto 1/(\alpha_{\mathrm{D}}(\theta)g^2(\theta)B^4)$ in this region. All experimental data sets fits well to the SLR theory in the high-field limit, as shown in Fig. 3.
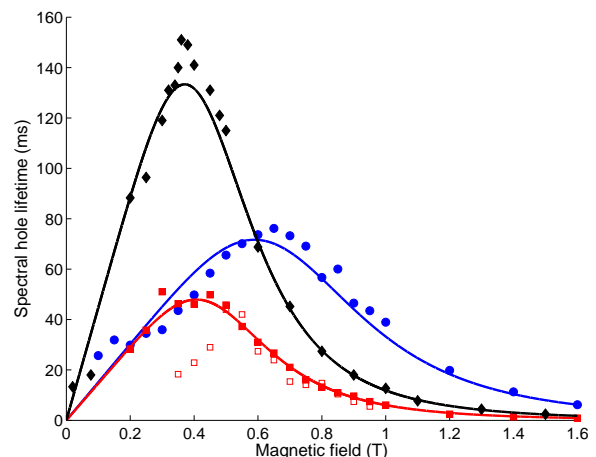

FIG. 3. Lifetime of the spectral hole versus magnetic field strength, for a Nd^{3+} concentration of 30 ppm and at three different angles $\theta = 0°$ (blue circles), $\theta = 90°$ (red filled squares), and $\theta = 120°$ (black diamonds). Data for $\theta = 90°$ and the crystal with 75 ppm Nd^{3+} concentration is also shown (red open squares). The figure shows both experimental data and fits from the model based on SLR and FF (see Sec. IV A for details). The temperature was 3 K for all data sets.

In the low-field limit the reduction in lifetime cannot be explained by the cross relaxation rate given by Eq. (3). Indeed, as already discussed in Sec. II C the B-field dependence should be weak, because the thermal population distribution does not change significantly over the relevant range of magnetic fields at 3 K. Yet, by comparing the lifetimes measured for the samples doped with 30 and 75 ppm of Nd^{3+} at the angle of $\theta = 90°$ ($\mathbf{D}_2$ axis), see Fig. 3, it is clear that the T_1^{SHB} is concentration dependent in the low-field region. Further data showing the concentration dependence are presented in Figs 6 and 7. There is thus a strong indication of cross-relaxation being the dominant process at low fields.

A similar trend was observed in recent measurements of the spectral hole lifetime in erbium-doped silica glass fibers [21]. There it was proposed that the inhomogeneous spin linewidth increases linearly with the magnetic field, which results in an inverse dependence on the field for the cross relaxation rate $R_{\mathrm{FF}} \propto 1/\Gamma \propto 1/(\Gamma_0 + \kappa B)$, cf. Eq. (3), where κ is a constant and Γ_0 is the inhomogeneous spin linewidth at zero field. This assumption is justified for an amorphous glass where the inhomogeneous spin linewidth stems from the anisotropy of the g-tensor, which generally is large for Kramers ions. In our case a similar linear dependence of the spin linewidth could arise from an inhomogeneity in the g factor, caused by strain or defects [50].

There is some experimental support for an increase in the spin linewidth with increasing magnetic field. We performed optically-detected (OD) EPR in the sample with 30 ppm Nd^{3+} concentration, using a method we re-
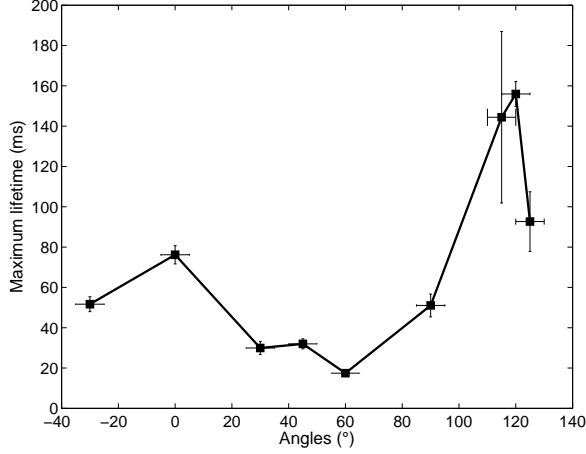
FIG. 4. Maximum spectral hole lifetime for each of the measured angles in the crystal with 30 ppm Nd^{3+} concentration at a temperature of 3 K. We can distinguish a global maximum at $\theta = 120°$ and a local maximum at $\theta = 0°$. As discussed in Sec. IV A, the global maximum is at $\theta = 120°$ because the FF rate is minimal at this angle.
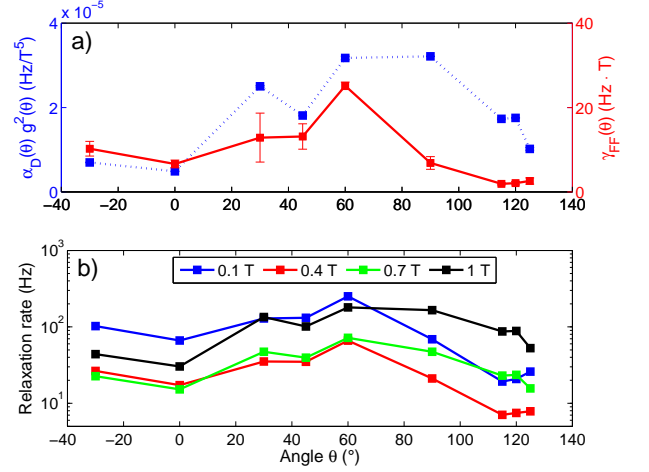

FIG. 5. Angular dependence of the coupling parameters presented in the main text and the relaxation rate. In (a) we show the angular variation of $\alpha_D(\theta)g(\theta)^2$ (in units of Hz/T^5) and $\gamma_{FF}(\theta)$ (in units of Hz·T). The direct SLR process varies somewhat like a sine function, with a minimum around $\mathbf{D}_1$, while the FF appears to have two minima, at $\mathbf{D}_1$ and $\theta = 120°$, respectively. In (b) we show the angular dependence of the total relaxation rate $R_{SLR} + R_{FF}$ for $B = 0.1$, 0.4, 0.7 and 1 T. The minimum rate at about $\theta = 120°$, for a field of 0.4 T, explains the maximum lifetime of 156 ms observed for this field strength (cf Fig. 4).

cently presented in Ref. [51], which gave a spin linewidth of 5 MHz for a low field ($<$ 10 mT) along $\mathbf{D}_2$. In Ref. [23] conventional EPR gave a linewidth of 12 MHz for 561.5 mT along $\mathbf{D}_1$, in a sample with 10 ppm Nd^{3+} concentration. But due to the difference in field direction and Nd^{3+} concentration used in the two experiments we cannot make any quantitative estimations of the increase in linewidth. We also note that a field-dependent spin linewidth has been observed in Er^{3+}:Y_2SiO_5 [52]. Even more recent EPR measurements of the angular dependence of the spin linewidth in Er^{3+}:Y_2SiO_5 also support our hypothesis of a strain-induced field-dependent spin linewidth [53].

For a spin linewidth of the form $\Gamma = \Gamma_0 + \kappa B$ we would expect a weak dependence of the FF rate with the field for sufficiently low fields, hence the T_1^{SHB} would reach a plateau for low fields. Since we do not observe this (see Fig. 3) we cannot fit Γ_0 using our data. By using $\Gamma = \kappa B$ as a model, Eq. (3) can then be written as

$$R_{FF} = \frac{\gamma_{FF}(\theta)}{B} \operatorname{sech}^2 \left(\frac{\Delta E(\theta)}{2k_B T} \right) \qquad (4)$$

where $\beta_{FF}(\theta)$, κ and n have been included in the effective coupling parameter $\gamma_{FF}(\theta) = \beta_{FF}(\theta)n^2/\kappa$.

The spectral hole lifetimes measured as a function of magnetic field strength were fitted to the theoretical model using Eqs. (1), (4) and $T_1^{SHB} = 1/(R_{FF} + R_{SLR})$. The model yielded a good fit for all eight angles, as shown for three of the angles in Fig. 3. This supports our assumption that there is a linear increase of the spin linewidth as a function of field strength, which causes a reduction of the cross relaxation in the low-field limit. To further strengthen this conclusion it would be highly

interesting to measure the spin linewidth as function of strength and angle of the magnetic field, for instance using the methods applied in Ref. [51]. Recently, Welinski *et al.* took steps in this direction by measuring the angular dependence of the spin linewidth in erbium-doped Y_2SiO_5. We also note that different Kramers ions could display different field dependence of the spectral hole lifetime, in the low-field limit, if the field-independent part of the spin linewidth Γ_0 is larger than κB.

As a result of the competition between the cross relaxation and the SLR direct process there is a maximum spectral hole lifetime for each magnetic field angle (Fig. 3). This maximum has a strong angular dependence and the field strength at which it is reached also depends on the angle. As shown in Fig. 4 the maximum lifetime goes from 17.5 ± 1.1 ms at $B = 0.55$ T for $\theta = 60°$, to 156 ± 6 ms at $B = 0.4$ T for $\theta = 120°$, as shown in Fig. 4. There is also a local maximum of 76 ± 4 ms at $B = 0.65$ T for an angle of $\theta = 0°$. In the following we will discuss how the maximum lifetime, and the field at which it is reached, is a complex interplay between the angular variations in the g factor and in the coupling parameters for SLR and FF.

For the cross relaxation process the angular dependence is given by the FF coupling parameter $\gamma_{FF}(\theta)$. For the SLR direct process we need to consider the product of the coupling parameter and the $g(\theta)^2$ factor, as discussed in Sec. II B. For both processes we neglect, for

simplicity, the dependence on the ratio $\Delta E(\theta)/(2k_\mathrm{B}T)$. This is a good approximation for fields of 1 T or less. In Fig. 5(a) we thus show $\alpha_\mathrm{D}(\theta)g(\theta)^2\mu_B^5$ and $\gamma_\mathrm{FF}(\theta)$. The SLR direct process alone has a minimum rate at $\theta = 0°$ and maximum rate at $\theta = 90°$, suggesting that in absence of cross relaxation the optimal field orientation would be along the $\mathbf{D}_1$ rather than at $\theta = 120°$ (see Fig. 4). The cross relaxation has a very different behaviour, with two local minima at $\theta = 0°$ and $\theta = 120°$, and a maximum rate at $\theta = 60°$.

The angular dependencies of the two processes show that there should be two local minima of the total rate, at $\theta = 0°$ and $\theta = 120°$, which corresponds well to the observed maxima of the spectral hole lifetime at those angles (see Fig. 4). We also note that the particularly short lifetimes around $\theta = 60°$ are due to the fact that both coupling parameters are large in this region. Looking at Fig. 5(a) it is not directly evident, however, why the maximum at $\theta = 120°$ gives a particularly long lifetime. It is not surprising that it cannot be deduced directly from Fig. 5(a), as both processes have a different dependence on the field strength B. To better understand the maximum at $\theta = 120°$ we plot the total relaxation rate $R_\mathrm{SLR} + R_\mathrm{FF}$ as a function of angle for several magnetic field strengths, see Fig. 5(b). At the lowest field (0.1 T) the rate is entirely dominated by the FF process and the lowest rate is reached around $\theta = 120°$. Increasing the field to 0.4 T results in a similar angle dependence, hence the rate is dominated by the FF process, but with significantly lower rate. Since 0.4 T is the field strength at which the longest lifetime of 156 ms is reached, we can conclude that it is given by the low FF coupling parameter at $\theta = 120°$. Further increasing the field increases the SLR rate and progressively shifts the minimum rate towards $\theta = 0°$. At the highest field of 1 T it is entirely dominated by the SLR process.

The angular variation of the direct SLR relaxation is defined by the wavefunctions of the Kramers doublets within the $^4\mathrm{I}_{9/2}$ ground state [26]. Therefore one requires knowledge of the crystal-field Hamiltonian of Nd^{3+}:$\mathrm{Y}_2\mathrm{SiO}_5$ in order to make a comparison with our experimental results. To our knowledge, however, the crystal-field Hamiltonian has not been determined. Concerning the angular dependence of the flip-flop process, we have made comparisons with the simple theoretical model discussed in Sec. II C and further developed in the Supplemental Material. The model predicts a minimum rate in the region around $\theta = 110°$, in rather good agreement with the data in Fig. 5(a). It completely fails to describe, however, the second minimum at $\theta = 0°$. A possible explanation could be that the spin linewidth Γ has an angular dependence, as recently observed in erbium-doped $\mathrm{Y}_2\mathrm{SiO}_5$ [53], which is not included in our simple model. To make further progress one would need to experimentally measure the spin linewidth as a function of magnetic field and its orientation in neodymium-doped $\mathrm{Y}_2\mathrm{SiO}_5$.

We conclude this section by emphasizing that opti-

mization of both the magnetic field magnitude and its direction is important when both cross relaxation and SLR play a role in the spectral hole lifetime. The importance of the spin linewidth also suggests that the flip-flop rate could be reduced by co-doping the sample with another rare-earth ion. An increase in the spin linewidth due to co-doping was observed in Er^{3+}:$\mathrm{Y}_2\mathrm{SiO}_5$ [53], by co-doping with Sc^{3+}. However, co-doping also results in an increase in the optical inhomogeneous broadening [53, 54]. It is an open question, then, if it is possible to reduce the spin flip-flop rate significantly by co-doping, without causing a large decrease in the optical depth due to a simultaneous increase in the optical linewidth.

B. Temperature dependence

We now turn to the temperature dependence of the spectral hole lifetime. We measured the lifetime at different temperatures ranging from 3 to 5.5 K, for the crystals with 30 ppm and 75 ppm Nd^{3+} concentrations, see Fig. 6. The measurements were made for the optimal angle of $\theta = 120°$ (cf. Fig. 4). The static magnetic field in these measurements was given by a permanent magnet installed inside the cryostat, as opposed to the superconducting magnet used for all other measurements. The field was estimated to be 300 mT, but the exact value could be a few tens of mT higher or lower.

At the lowest temperatures the lifetimes in the 30 ppm doped crystal are about twice as long as compared to the 75 ppm doped crystal, which shows that also at the op-
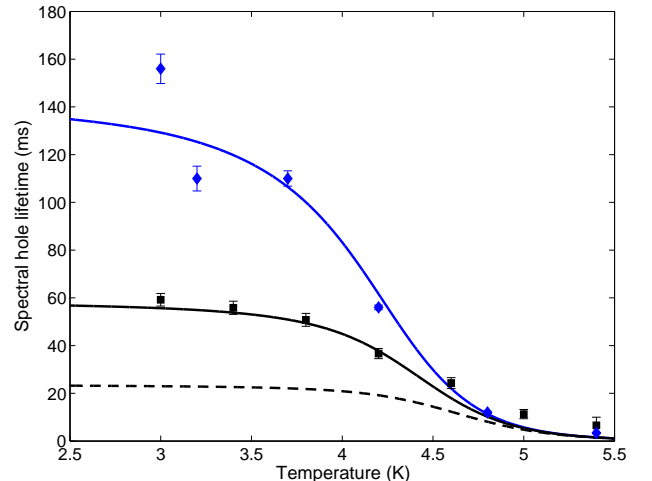

FIG. 6. Spectral hole lifetime as a function of temperature for the $\mathrm{Y}_2\mathrm{SiO}_5$ crystals doped with 30 ppm (blue diamonds) and 75 ppm (black squares) of Nd^{3+} ions. The magnetic field strength was $B = 0.3$ T, oriented with an angle of $\theta = 120°$ with respect to the $\mathbf{D}_1$ axis. Both full and dashed lines represent different models used to interpret the data, and are discussed in detail in Sec. IV B.

timal angle the spin FF process is important for these low concentrations. This concentration dependence is a further strong indication that the lifetimes depend on the FF process at this field strength. For both concentrations the lifetime decreases rather slowly at the lowest temperatures, which is due to the linear temperature dependence of the direct SLR process. Above 4 K the lifetimes decrease more rapidly and both samples reach similar lifetimes of less than 20 ms at around 5 K. The rapid decrease is due to the Raman and Orbach processes, which have strong temperature dependence as discussed in Sec. II B. It is also expected that the lifetimes at temperatures higher than 5 K do not depend on the Nd^{3+} concentration, since neither the Raman process nor the Orbach process depend on the concentration.

For the 30 ppm doped crystal we compare the data with the model as fitted to the field-dependent data in Sec. IV A, including the Raman and Orbach contributions, with no further tuning of the parameters. As discussed in Sec. II B we use the Raman and Orbach parameters measured independently by Kurkin and Chernov [29] using EPR. The agreement with our spectral hole lifetime measurements is rather good (Fig. 6).

One can now use the model developed for the 30 ppm doped crystal in order to predict the spectral hole lifetimes for the 75 ppm doped crystal. The SLR processes do not have a concentration dependence, while the FF process is expected to have a quadratic dependence n^2, see Eq. (3) in Sec. II C. In Fig. 6 we compare the predicted lifetimes with the experimental data by only scaling the flip-flop parameter $\gamma_{FF}(\theta)$ for the 30 ppm crystal by $(75/30)^2$. This model predicts too short lifetimes at low temperatures, as shown by the dashed line in the graph, which suggests a different concentration dependence. In Fig. 6 we also show the prediction based on a linear scaling $(75/30)$ of the $\gamma_{FF}(\theta)$ parameter, which perfectly reproduces the experimental data.

The discrepancy with Eq. (3) is possibly due to a concentration dependence of the spin linewidth Γ. Kittel and Abrahams have shown, for instance, that the dipolar broadening of a spin resonance line depends linearly on the concentration (at low concentrations) [55]. It is also possible that the linear coefficient κ is concentration dependent. We again emphasize that measurements of the spin linewidth as a function of field strength, field angle and concentration would be highly valuable for understanding the details of the cross relaxation process. To this end, one could do OD-EPR measurements using the method developed in [51].

C. Concentration dependence

To further investigate the concentration dependence of the spectral hole lifetimes we compare the lifetimes for three different Nd^{3+} concentrations. In addition to the crystals doped with 30 and 75 ppm of Nd^{3+} ions, we also include a comparison with the Eu^{3+}:Y_2SiO_5 crystal
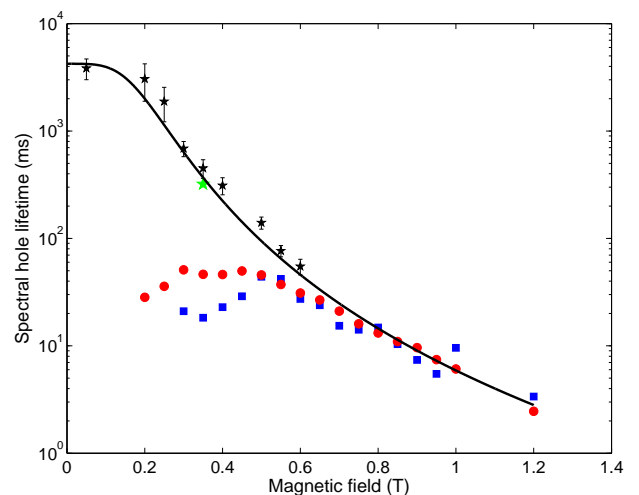

FIG. 7. Spectral hole lifetimes for the crystals with 30 ppm (red circles), 75 ppm (blue squares) and ≤ 1 ppm (black stars) Nd^{3+} doping concentrations. The temperature was 3 K and the field was oriented along the $\mathbf{D}_2$ axis ($\theta = 90°$). We also provide an extrapolation of the model for the spectral hole lifetime (solid line) for a crystal where there is no flip-flop mechanism (see Sec. IV C for details). The green star shows the lifetime achieved by burning a very large spectral hole in the 30 ppm crystal, as discussed in Sec. IV D.

containing a small Nd^{3+} impurity concentration of less than 1 ppm (see Sec. III A).

In Fig. 7 we compare the spectral hole lifetimes as a function of magnetic field strength for all three crystals. The field was oriented along the $\mathbf{D}_2$ axis ($\theta = 90°$) and the temperature was 3 K. We emphasize that the measurement data for the 30 and 75 ppm of Nd^{3+} crystals are identical to those shown in Fig. 3.

The spectral hole lifetimes measured in the crystal doped with ≤ 1 ppm of Nd^{3+} ions shows a radically different behaviour with respect to the crystals with higher doping. The lifetime increases monotonically as the field strength is reduced and reaches a plateau at low fields. The maximum lifetime is 3.8±0.8 s, which is a 75-fold increase with respect to the maximum lifetime of 51±6 ms obtained in the 30 ppm Nd^{3+} doped crystal, for this orientation of the field (cf. Fig. 4). Clearly the cross-relaxation process at low magnetic fields poses a serious limitation on the maximum achievable lifetime, even at doping concentrations as low as 30 ppm. Although the extremely low-doped crystal results in long-lived spectral holes, the associated low optical depth prevents it from being used directly in quantum memory applications, as it would lead to very low storage efficiencies. A potential solution is to use cavity-enhanced quantum memory schemes [56, 57], or a slightly more doped sample, or even a combination of both these approaches.

In Fig. 7 we also show an extrapolation of the model fitted to the field-dependent data obtained for the crys-

tal doped with 30 ppm of Nd^{3+} ions. Specifically we use the fitted $\alpha_D(\theta)$ parameter at $\theta = 90°$ to calculate the direct process, to which we add the Raman and Orbach rate contributions. The flip-flop contribution is not included, such that the spectral hole lifetime is calculated using only $T_1^{\text{SHB}} = 1/R_{\text{SLR}}$ and Eq. (1). The agreement with the lifetimes measured in the extremely low-doped sample is excellent, for all measured field strengths. Note that the signal-to-noise ratio was too low to measure the lifetime beyond 0.6 T, due to the low optical depth.

We conclude that the flip-flop process has been completely eliminated at a concentration of ≤ 1 ppm of Nd^{3+} ions. We estimate that the already observed linear dependence of the lifetime on concentration can in itself explain this effect (see Sec. IV B). In addition one could expect that the presence of Eu^{3+} ions further reduces the flip-flop rate by increasing the Nd^{3+} spin linewidth.

D. Lifetime of a spectrally large hole

In the previous sections we have seen strong evidence for a concentration dependence of the spectral hole lifetimes due to cross relaxation. As explained in Sec. II C this decay process is possible because only a small spectral region is spin polarized during the pumping process (ensemble A), while the majority of spins (typically 99% or more) are not affected by the pumping process (ensemble B). As a consequence one would expect that the spectral hole lifetime would change if a very large spectral hole was burnt into the optical linewidth, cf. Fig. 2, which would largely reduce the number of spins in ensemble B and increase the spins in ensemble A. The result should be a strongly reduced spin flip-flop probability and long spectral hole lifetime.

We investigated this possibility in the crystal doped with 30 ppm of Nd^{3+} ions. The magnetic field strength was 350 mT, oriented along $\mathbf{D}_2$ ($\theta = 90°$), and the temperature was 3 K. It is important to note that a minimum magnetic field strength is required to be able to split the ground state doublet more than the optical inhomogeneous broadening, as illustrated in Fig. 2. This is a condition in order to be able to optically spin polarize a large part of the inhomogeneous spectrum. This prevents the technique to be used at very low fields, where the flip-flop process dominates, unless the inhomogeneous broadening is particularly weak.

In Fig. 8 we show the decay curve of both a narrow hole and a large and deep spectral hole where about half of the inhomogeneous broadening has been optically pumped. The spectral hole lifetime increases from 50 ms to 320 ms by burning a large hole, a rather spectacular increase. If we compare this lifetime with the one obtained for the extremely low-doped crystal it actually gives a similar lifetime, as shown by the green star in Fig. 7. This is rather surprising since we estimate that only about 50% of the spins where polarized by burning a large hole.

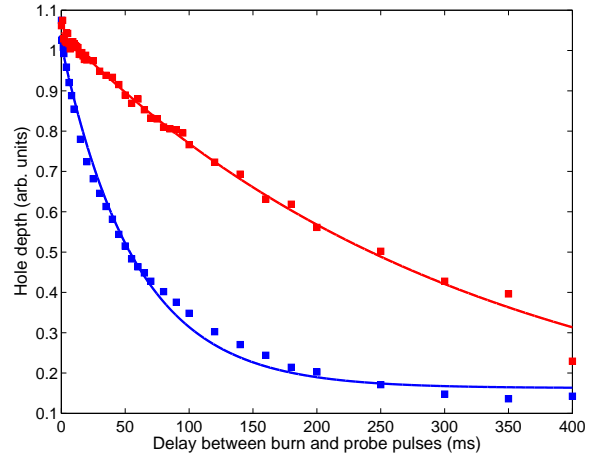While this experiment shows the potential of modify-

FIG. 8.   Spectral hole decay measurements for a narrow spectral hole (blue squares) and a large spectral hole (red diamonds). The narrow hole has a linewidth of a few MHZ, while the large hole represents optical pumping of about 50% of the ions within the optical inhomogeneous linewidth of about 6 GHz. The solid lines show the fitted single-exponential curves, which give lifetimes of 50 ms (blue line) and 320 ms (red line), respectively.

ing the cross relaxation rate by optical pumping, the detailed underlying mechanism is not well understood and further experiments will be necessary to be able to apply this method to various quantum memory schemes. Another interesting perspective is to decrease spectral diffusion using optical pumping of large spectral regions. Indeed, in many cases the optical coherence times of Kramers ions are limited by spectral diffusion driven by spin flip-flops at low fields [20].

A related and interesting question is if the cross-relaxation rate can be suppressed by decreasing the temperature such that all spins point in the same direction. This limit is reached when $\Delta E(\theta) \ll (2k_B T)$ where all the spins would polarize into the lower Zeeman state (cf. Fig. 2) by the low temperature. Looking at Eq. (3) one would naively conclude that the cross relaxation rate would be highly suppressed. However, if a small fraction of the spins are excited to the higher Zeeman state, then rapid spin flip-flops will occur with the spins in the lower Zeeman state. As the SLR rate should be very weak at such temperatures, we expect the flip-flop rate to be the limiting process for storage of quantum information. Similarly any narrow spectral features created through SHB using these Zeeman states would also decay due to flip-flop rates. But as our results show one could go to much lower concentration to mitigate this problem, or possibly co-dope the material in order to increase the spin linewidth and reduce the cross relaxation rate. We also emphasize that the overall population difference between the two states will of course not be affected by cross relaxation, which is the typical measure of spin popula-

tion lifetimes at extremely low temperatures (tens of mK) [52]. Hence, some caution has to be exercised when using such measurements to predict useful spin coherence times, which are likely to be affected by spin flip-flops, rather than SLR processes, at low temperatures.

V. CONCLUSIONS AND OUTLOOK

We have studied the relaxation mechanisms of spectral holes in neodymium-doped orthosilicate under different magnetic fields, temperatures and dopant concentrations. Our main finding is that the limiting factor in achieving long-lived spectral holes is the spin cross relaxation, or flip-flop, process. We have also shown that both the strength and angle of the magnetic field must be carefully optimized to maximize the hole lifetime. By decreasing the concentration to as low as ≤ 1 ppm of Nd^{3+} ions, we could eliminate the flip-flop process and reach a hole lifetime of 3.8 s at 3 K. Our results show that optimization of the dopant concentration is crucial in order to find a compromise between the spectral hole lifetime and optical absorption coefficient. We have also shown

that the cross relaxation rate can be drastically reduced by creating very large spectral holes, which could open up new ways of engineering spectral hole lifetimes in a given crystal and to improve optical pumping in crystals doped with rare-earth Kramers ions. We also argue that lowering the temperature to the mK regime would not suppress the effect of cross relaxation on quantum coherence measurements. We believe that these results should allow better optimization of these crystals for applications in quantum memories [1, 2] and narrow-band spectral filtering for biological tissue imaging [58–60].

VI. ACKNOWLEDGEMENTS

[1] F. Bussières, N. Sangouard, M. Afzelius, H. de Riedmatten, C. Simon, and W. Tittel, Journal of Modern Optics **60**, 1519 (2013).

[2] M. Afzelius and H. de Riedmatten, "Quantum light storage in solid state atomic ensembles," in *Engineering the Atom-Photon Interaction: Controlling Fundamental Processes with Photons, Atoms and Solids*, Nano-Optics and Nanophotonics, edited by A. Predojević and M. W. Mitchell (Springer International Publishing, 2015) pp. 241–268.

[3] Y. Sun, C. W. Thiel, R. L. Cone, R. W. Equall, and R. L. Hutcheson, J. Lumin. **98**, 281 (2002).

[4] M. Zhong, M. P. Hedges, R. L. Ahlefeldt, J. G. Bartholomew, S. E. Beavan, S. M. Wittig, J. J. Longdell, and M. J. Sellars, Nature **517**, 177 (2015).

[5] W. Tittel, M. Afzelius, T. Chanelière, R. Cone, S. Kröll, S. Moiseev, and M. Sellars, Laser & Photonics Reviews **4**, 244 (2010).

[6] E. Fraval, M. J. Sellars, and J. J. Longdell, Phys. Rev. Lett. **92**, 077601 (2004).

[7] E. Fraval, M. J. Sellars, and J. J. Longdell, Phys. Rev. Lett. **95**, 030506 (2005).

[8] L. Rippe, B. Julsgaard, A. Walther, Y. Ying, and S. Kröll, Phys. Rev. A **77**, 022307 (2008).

[9] G. Heinze, C. Hubrich, and T. Halfmann, Phys. Rev. Lett. **111**, 033601 (2013).

[10] M. Gündoğan, P. M. Ledingham, K. Kutluer, M. Mazzera, and H. de Riedmatten, Phys. Rev. Lett. **114**, 230501 (2015).

[11] C. Laplane, P. Jobez, J. Etesse, N. Timoney, N. Gisin, and M. Afzelius, New Journal of Physics **18**, 013006 (2016).

[12] R. Marino, I. Lorgeré, O. Guillot-Noël, H. Vezin, A. Toncelli, M. Tonelli, J.-L. Le Gouët, and P. Goldner, Journal

of Luminescence **169**, 478 (2016).

[13] R. M. Macfarlane and J. C. Vial, Phys. Rev. B **36**, 3511 (1987).

[14] I. Usmani, M. Afzelius, H. de Riedmatten, and N. Gisin, Nat Commun **1**, 12 (2010).

[15] C. Clausen, I. Usmani, F. Bussieres, N. Sangouard, M. Afzelius, H. de Riedmatten, and N. Gisin, Nature **469**, 508 (2011).

[16] Z.-Q. Zhou, W.-B. Lin, M. Yang, C.-F. Li, and G.-C. Guo, Phys. Rev. Lett. **108**, 190505 (2012).

[17] S. R. Hastings-Simon, B. Lauritzen, M. U. Staudt, J. L. M. van Mechelen, C. Simon, H. de Riedmatten, M. Afzelius, and N. Gisin, Phys. Rev. B **78**, 085410 (2008).

[18] M. Afzelius, I. Usmani, A. Amari, B. Lauritzen, A. Walther, C. Simon, N. Sangouard, J. Minář, H. de Riedmatten, N. Gisin, and S. Kröll, Phys. Rev. Lett. **104**, 040503 (2010).

[19] B. Lauritzen, S. R. Hastings-Simon, H. de Riedmatten, M. Afzelius, and N. Gisin, Phys. Rev. A **78**, 043402 (2008).

[20] T. Böttger, C. W. Thiel, Y. Sun, and R. L. Cone, Phys. Rev. B **73**, 075101 (2006).

[21] E. Saglamyurek, T. Lutz, L. Veissier, M. P. Hedges, C. W. Thiel, R. L. Cone, and W. Tittel, Phys. Rev. B **92**, 241111 (2015).

[22] A. Abragam and B. Bleaney, *Electronic Paramagnetic Resonance of Transition Ions* (Clarendon Press, Oxford UK, 1970).

[23] G. Wolfowicz, H. Maier-Flaig, R. Marino, A. Ferrier, H. Vezin, J. J. L. Morton, and P. Goldner, Phys. Rev. Lett. **114**, 170503 (2015).

[24] R. Orbach, Proc. R. Soc. Lond. Ser. A **264**, 458 (1961).

[25] P. L. Scott and C. D. Jeffries, Phys. Rev. **127**, 32 (1962).

[26] G. H. Larson and C. D. Jeffries, Phys. Rev. **141**, 461 (1966).

[27] G. H. Larson and C. D. Jeffries, Phys. Rev. **145**, 311 (1966).

[28] I. Kurkin, Y. K. Chirkin, and V. Shlenkin, Fizika Tverdogo Tela **14**, 2719 (1972).

[29] I. Kurkin and K. Chernov, Physica B+C **101**, 233 (1980).

[30] A. M. Portis, Phys. Rev. **104**, 584 (1956).

[31] N. Bloembergen, S. Shapiro, P. S. Pershan, and J. O. Artman, Phys. Rev. **114**, 445 (1959).

[32] S. R. Hastings-Simon, M. Afzelius, J. Minář, M. U. Staudt, B. Lauritzen, H. de Riedmatten, N. Gisin, A. Amari, A. Walther, S. Kröll, E. Cavalli, and M. Bettinelli, Phys. Rev. B **77**, 125111 (2008).

[33] F. Bussières, C. Clausen, A. Tiranov, B. Korzh, V. B. Verma, S. W. Nam, F. Marsili, A. Ferrier, P. Goldner, H. Herrmann, C. Silberhorn, W. Sohler, M. Afzelius, and N. Gisin, Nat. Photon. **8**, 775 (2014).

[34] E. Saglamyurek, N. Sinclair, J. Jin, J. A. Slater, D. Oblak, F. Bussières, M. George, R. Ricken, W. Sohler, and W. Tittel, Nature **469**, 512 (2011).

[35] J. H. Van Vleck, Phys. Rev. **74**, 1168 (1948).

[36] R. W. Equall, Y. Sun, R. L. Cone, and R. M. Macfarlane, Phys. Rev. Lett. **72**, 2179 (1994).

[37] A. Tkachuk, A. Przhevusskii, L. Morozova, A. Poletimova, M. Petrov, and A. Korovkin, Opt. Spectrosc. **60**, 176 (1986).

[38] R. Beach, M. Shinn, L. Davis, R. Solarz, and W. Krupke, IEEE J. Quantum Electron **26**, 1405 (1990).

[39] R. Beach, C. Brandle, G. Berkstresser, G. Albrecht, R. Solarz, W. Krupke, B. Comaskey, and S. Mitchell, Opt. Lett. **15**, 1020 (1990).

[40] B. Comaskey, G. F. Albrecht, R. J. Beach, B. D. Moran, and R. W. Solarz, Opt. Lett. **18**, 2029 (1993).

[41] I. Usmani, C. Clausen, F. Bussières, N. Sangouard, M. Afzelius, and N. Gisin, Nat Photon **6**, 234 (2012).

[42] A. Tiranov, J. Lavoie, A. Ferrier, P. Goldner, V. B. Verma, S. W. Nam, R. P. Mirin, A. E. Lita, F. Marsili, H. Herrmann, C. Silberhorn, N. Gisin, M. Afzelius, and F. Bussières, Optica **2**, 279 (2015).

[43] A. Tiranov, J. Lavoie, P. C. Strassmann, N. Sangouard, M. Afzelius, F. Bussières, and N. Gisin, Phys. Rev. Lett. **116**, 190502 (2016).

[44] T. Zhong, J. M. Kindem, E. Miyazono, and A. Faraon, Nat Commun **6**, (2015).

[45] C. Li, C. Wyon, and R. Moncorge, IEEE Journal of Quantum Electronics **28**, 1209 (1992).

[46] F. Könz, Y. Sun, C. W. Thiel, R. L. Cone, R. W. Equall, R. L. Hutcheson, and R. M. Macfarlane, Phys. Rev. B **68**, 085109 (2003).

[47] N. Ohlsson, M. Nilsson, S. Kröll, and R. K. Mohan, Opt. Lett. **28**, 450 (2003).

[48] A. Louchet, J. S. Habib, V. Crozatier, I. Lorgeré, F. Goldfarb, F. Bretenaker, J.-L. L. Gouët, O. Guillot-Noël, and P. Goldner, Phys. Rev. B **75**, 035131 (2007).

[49] M. Afzelius, M. U. Staudt, H. de Riedmatten, N. Gisin, O. Guillot-Noël, P. Goldner, R. Marino, P. Porcher, E. Cavalli, and M. Bettinelli, Journal of Luminescence **130**, 1566 (2010).

[50] A. M. Stoneham, Rev. Mod. Phys. **41**, 82 (1969).

[51] C. Laplane, E. Zambrini Cruzeiro, F. Fröwis, P. Goldner, and M. Afzelius, Phys. Rev. Lett. **117**, 037203 (2016).

[52] S. Probst, H. Rotzinger, S. Wünsch, P. Jung, M. Jerger, M. Siegel, A. V. Ustinov, and P. A. Bushev, Phys. Rev. Lett. **110**, 157001 (2013).

[53] S. Welinski, C. Thiel, J. Dajczgewand, A. Ferrier, R. Cone, R. Macfarlane, T. Chanelière, A. Louchet-Chauvet, and P. Goldner, Optical Materials (2016), http://dx.doi.org/10.1016/j.optmat.2016.09.039.

[54] T. Böttger, C. W. Thiel, R. L. Cone, and Y. Sun, Phys. Rev. B **77**, 155125 (2008).

[55] C. Kittel and E. Abrahams, Phys. Rev. **90**, 238 (1953).

[56] S. A. Moiseev, S. N. Andrianov, and F. F. Gubaidullin, Phys. Rev. A **82**, 022311 (2010).

[57] M. Afzelius and C. Simon, Phys. Rev. A **82**, 022310 (2010).

[58] Y. Li, P. Hemmer, C. Kim, H. Zhang, and L. V. Wang, Opt. Express **16**, 14862 (2008).

[59] D. L. McAuslan, L. R. Taylor, and J. J. Longdell, Applied Physics Letters **101** (2012).

[60] H. Zhang, M. Sabooni, L. Rippe, C. Kim, S. Kröll, L. V. Wang, and P. R. Hemmer, Applied Physics Letters **100** (2012).

Supplementary Material for "Spectral hole lifetimes and spin population relaxation dynamics in Neodymium-doped yttrium orthosilicate"

E. Zambrini Cruzeiro,[1] A Tiranov,[1] I. Usmani,[2] C. Laplane,[1]
J. Lavoie,[1, *] A. Ferrier,[3, 4] P. Goldner,[3] N. Gisin,[1] and M. Afzelius[1, †]

[1] *Groupe de Physique Appliquée, Université de Genève, CH-1211 Genève 4, Switzerland*
[2] *Laboratoire Charles Fabry, Institut d'Optique Graduate School, CNRS, Université Paris-Saclay, 91127 Palaiseau, France*
[3] *PSL Research University, Chimie ParisTech - CNRS Institut de Recherche de Chimie Paris, 75005, Paris, France*
[4] *Sorbonne Universites, UPMC Univ Paris 06, 75005, Paris, France*

In this Supplementary Material we provide a model for spin-spin relaxation due to flip-flop transitions, in a special case of anisotropic g-tensor in Sec I. In Sec. II also give extended experimental results presented in the main text.

I. SPIN FLIP-FLOPS IN ANISOTROPIC MEDIA

The average flip-flop rate for spins under a magnetic field B and temperature T, is usually written in the form of Eq. (3) of Section II in the main text, where β_{ff} is a constant that depends on the details of the crystal structure, its magnetic properties and spin resonance line shape [1]. The temperature and field dependence of the flip-flop process arises from the probability for each spin pair in the lattice to be antiparallel and causes the flip-flop rate to decrease rapidly with increasing field or decreasing temperature. In the case of an isotropic $\hat{g}$-tensor the rate has been shown to be proportional to $\beta_{\text{ff}} \propto g^4$. However, in the case of strong anisotropy, which is the case for most rare-earth ion doped crystals, this does not hold any more and the equation has to be modified. Anisotropic magnetic properties of the rare earth Kramers ion-doped crystals were confirmed for many materials and ions (for example Er^{3+}, Nd^{3+} and Yb^{3+} in YSO crystal) [2–4].

The easiest way to derive the expression for β_{ff} in the anisotropic case is to follow the same approach as for the isotropic one and to consider the dipole dipole interaction as an perturbation for Zeeman Hamiltonian. To further calculate the average flip-flop rate one has to integrate it around some crystal volume, taking into account the angular dependence of the dipole-dipole interaction. The resulting Hamiltonian for the simplest case of a spin pair S_1 and S_2 interacting with the external magnetic field B and between each other through magnetic dipole-dipole interaction $\hat{H}_{dd}$ is

$$\hat{H} = \mu_B \vec{B} \hat{g} \vec{S}_1 + \mu_B \vec{B} \hat{g} \vec{S}_2 + \hat{H}_{dd} + c.c. \qquad (1)$$

In the case of identical spins and parallel principal axes

———

* Current address: Present address: Department of Physics and Oregon Center for Optical Molecular & Quantum Science, University of Oregon, Eugene, OR 97403, USA
† Correspondance: mikael.afzelius@unige.ch

of their respective $\hat{g}$-tensors, H_{dd} can be written as

$$
\begin{aligned}
\hat{H}_{dd} = \mu_B^2 r^{-3} \Big[& (1 - 3l^2) g_x^2 \hat{S}_{1x} \hat{S}_{2x} + \qquad (2) \\
& + (1 - 3m^2) g_y^2 \hat{S}_{1y} \hat{S}_{2y} + (1 - 3n^2) g_z^2 \hat{S}_{1z} \hat{S}_{2z} - \\
& - 3lm g_x g_y (\hat{S}_{1x} \hat{S}_{2y} + \hat{S}_{1y} \hat{S}_{2x}) - \\
& - 3ln g_x g_z (\hat{S}_{1x} \hat{S}_{2z} + \hat{S}_{1z} \hat{S}_{2x}) - \\
& - 3mn g_y g_z (\hat{S}_{1y} \hat{S}_{2z} + \hat{S}_{1z} \hat{S}_{2y}) \Big],
\end{aligned}
$$

where $\{l, m, n\}$ are the direction cosines of the vector $\vec{r}$ connecting two spins 1 and 2, and $\hat{g}$-tensor is of the diagonal form

$$\hat{g} = \begin{pmatrix} g_x & 0 & 0 \\ 0 & g_y & 0 \\ 0 & 0 & g_z \end{pmatrix}. \qquad (3)$$

We consider the dipole-dipole interaction $\hat{H}_{dd}$ as a perturbation to the Zeeman interaction, which holds in the case of rare earth ion-doped crystals with low doping concentrations. This allows one to use Fermi golden rule to calculate the flip-flop rate,

$$R_{\text{ff}} \sim |\langle \uparrow\downarrow| \hat{H}_{dd} |\downarrow\uparrow\rangle|^2 + |\langle \downarrow\uparrow| \hat{H}_{dd} |\uparrow\downarrow\rangle|^2, \qquad (4)$$

where $|\downarrow\uparrow\rangle$ and $|\uparrow\downarrow\rangle$ are degenerate eigenstates of the Zeeman Hamiltonian corresponding to antiparallel orientations of the spins. Due to the degeneracy, the transition between these two states (flip-flop transition) is possible without any energy transfer. This process is considered to be one of the main sources of transverse relaxation of spin systems, which reduces the coherence lifetime T_2 [5].

To calculate the flip-flop rate of the spins in an anisotropic media we assume that the magnetic field $\vec{B}$ is oriented in the plane containing two principal axes of the $\hat{g}$-tensor which consists of three different components noted g_x, g_y and g_z (3). The magnetic field in this case can be written $\vec{B} = B\{\cos(\theta), \sin(\theta), 0\}$, where θ is the angle with respect to x-axis. The magnetic moment for the case of an anisotropic $\hat{g}$-tensor stops to be oriented along the magnetic field and is accordingly to the anisotropy in the x, y plane. To integrate over the volume we assume that average distance r between the spins is constant while the orientation is random. The calculated flip-flop rate R_{ff} using Eq. (4) and integrated around the
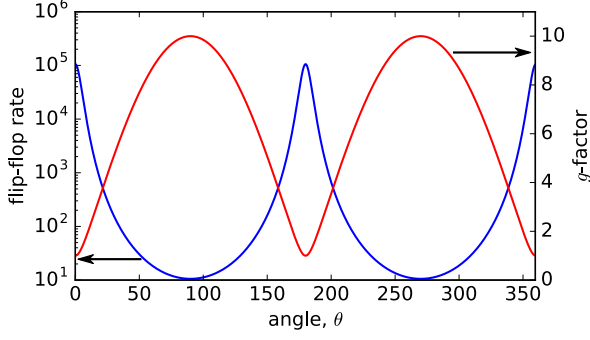
FIG. 1. Flip-flop rate in anisotropic media and g-factor as a function of magnetic field orientation in the plane containing two principal axes of the $\hat{g}$-tensor with $g_x = 1$, $g_y = 10$ and $g_z = 1$.

FIG. 2. Calculated flip-flop rate and g-factor as a function of magnetic field orientation in $\mathbf{D}_1 - \mathbf{D}_2$ plane for ground state of the Nd^{3+}:Y_2SiO_5 (site I).

sphere with radius r is expressed by

$$\beta_{\text{ff}} \sim \mu_B^4 \frac{2\pi \left(8g_x^4 g_y^4 + g_z^2(A+B)\right)}{5 \left(g_x^2 \cos^2(\theta) + g_y^2 \sin^2(\theta)\right)^2}, \quad (5)$$

where

$$A = (g_x^2 - g_y^2) \left(4 \left(g_z^2 \left(g_x^2 + g_y^2\right) - g_x^2 g_y^2\right) \cos(2\theta) + \quad (6)$$
$$+ g_z^2(g_x^2 - g_y^2) \cos(4\theta)\right)$$
$$B = 4g_x^2 g_y^2 \left(g_x^2 + g_y^2\right) + g_z^2 \left(3g_x^4 + 2g_x^2 g_y^2 + 3g_y^4\right). \quad (7)$$

In the case of an isotropic $\hat{g}$-tensor, the flip-flop rate is simply proportional to g^4. However, when $g_x \neq g_y$ and the g_z component is much smaller than one of the orthogonal components ($\hat{g}$-tensor has a "cigar"-shape) the reduction of the flip-flop rate is observed along the strongest component in x, y plane (Fig. 1). In this case, the general expression (5) can be written as

$$\beta_{\text{ff}} \sim \mu_B^4 \frac{16\pi g_x^4 g_y^4}{5 \left(g_x^2 \cos^2(\theta) + g_y^2 \sin^2(\theta)\right)^2}. \quad (8)$$

In the opposite situation, when g_z is much bigger than the other components the flip-flop rate ceases to depend on the orientation of the magnetic filed in x, y plane and is expressed as

$$\beta_{\text{ff}} \sim \mu_B^4 \frac{16\pi g_z^4}{5}. \quad (9)$$

Finally, we notice that this expression holds when $g_z \approx g_x$ (or $g_z \approx g_y$), and $g_z \gg g_y$ ($g_z \gg g_x$) (the $\hat{g}$-tensor has a "disc"-shape). This means that the "optimization" of the flip-flop rate in this situation is not possible in contrast to the "cigar" tensor shape.

The g-tensor of site I of the Nd^{3+}:Y_2SiO_5 crystal, for the $^4I_{9/2}$ ground state has been measured before and is strongly anisotropic [3]

$$\hat{g} = \begin{pmatrix} 1.33 & -0.57 & -0.23 \\ -0.57 & -2.13 & 1.63 \\ -0.23 & 1.63 & -2.9 \end{pmatrix}_{(D_1, D_2, b)} \quad (10)$$
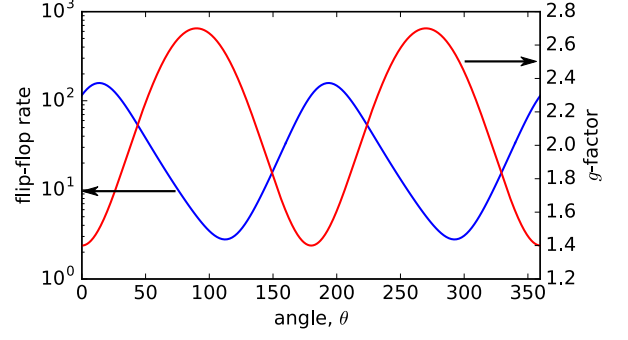
In our experiment the magnetic field was oriented in the $\mathbf{D}_1$-$\mathbf{D}_2$ plane. Since the magnetic field is not oriented along the principal axes one has to use the general form of the dipole-dipole interaction in order to calculate the flip-flop rate

$$\hat{H}_{dd} = \mu_B^2 r^{-3} \left[\hat{g}\vec{S}_i \hat{g}\vec{S}_j - 3r^{-2}(\hat{g}\vec{S}_i \vec{r})(\hat{g}\vec{S}_j \vec{r})\right]. \quad (11)$$

We performed a numerical simulation to calculate the variation of the flip-flop rate as a function of the angle θ between the $\mathbf{D}_1$ axis and the external magnetic field $\vec{B}$ applied in the $\mathbf{D}_1$-$\mathbf{D}_2$ plane (Fig. 2). The optimal orientation is expected around $\theta \approx 110°$ which coincides with the experimental observation, however the predicted angular variation of the flip-flop component was not observed in our experiment. Further investigation is required to explain this inconsistency, which could be attributed to additional relaxation processes. These possible processes could be observed by measuring spectral diffusion [6] on large timescales using for example three-pulse photon echo techniques.

The measurement of the spin resonance linewidth at different magnetic fields and different orientations would also simplify the search for the orientation with minimimal relaxation.

II. EXTRACTED RELAXATION RATES

In Table I we summarize extracted parameters for different magnetic filed orientations corresponding to different relaxation mechanisms: direct and cross relaxations. We also give the optimal values of magnetic filed amplitudes together with the maximum lifetimes obtained during the experiment.

TABLE I. Experimental results. Extracted values of SLR α_D and cross-relaxation γ_{FF} coupling from measured data as a function of magnetic field orientation θ with respect to $\mathbf{D}_1$ crystal axis. Maximum lifetimes $T_{\max}^{\mathrm{SHB}}$ together with corresponding optimal magnetic field amplitudes B^{opt} are given for every orientation. For this, the model described in the main text was used.

$\theta,°$	$\alpha_D(\times10^{-7})$, Hz$^{-4}\cdot$ T^5	γ_{FF}, Hz$\cdot$T	g	$T_{\max}^{\mathrm{SHB}}$, ms	B^{opt}, T
-30	20.97 ± 0.77	10.23 ± 1.74	1.82	51.7 ± 3.7	0.5
0	22.79 ± 0.65	6.62 ± 0.93	1.46	76.2 ± 405	0.65
30	70.23 ± 2.00	12.87 ± 5.79	1.89	29.9 ± 3.2	0.35
45	37.05 ± 1.11	13.13 ± 3.01	2.21	32.0 ± 2.5	0.5
60	51.39 ± 4.27	25.15 ± 0.88	2.49	17.5 ± 1.1	0.55
90	43.65 ± 0.48	6.86 ± 1.50	2.71	51.0 ± 5.7	0.3
115	27.37 ± 1.86	1.90 ± 0.25	2.51	144.4 ± 42.6	0.45
120	29.55 ± 0.19	2.06 ± 0.39	2.44	156.0 ± 6.1	0.4
125	18.49 ± 3.12	2.58 ± 0.74	2.35	92.6 ± 14.8	0.45

[1] T. Böttger, Y. Sun, C. W. Thiel, and R. L. Cone, Phys. Rev. B **74**, 075107 (2006).
[2] Y. Sun, T. Böttger, C. W. Thiel, and R. L. Cone, Phys. Rev. B **77**, 085124 (2008).
[3] G. Wolfowicz, H. Maier-Flaig, R. Marino, A. Ferrier, H. Vezin, J. J. L. Morton, and P. Goldner, Phys. Rev. Lett. **114**, 170503 (2015).
[4] S. Welinski, A. Ferrier, M. Afzelius, and P. Goldner, Phys. Rev. B **94**, 155116 (2016).
[5] A. Abragam and B. Bleaney, *Electronic Paramagnetic Resonance of Transition Ions* (Clarendon Press, Oxford UK, 1970).
[6] T. Böttger, C. W. Thiel, Y. Sun, and R. L. Cone, Phys. Rev. B **73**, 075101 (2006).